



HAL
open science

Propriétés effectives de matériaux architecturés

Justin Dirrenberger

► **To cite this version:**

Justin Dirrenberger. Propriétés effectives de matériaux architecturés. Autre. Ecole Nationale Supérieure des Mines de Paris, 2012. Français. ⟨NNT : 2012ENMP0045⟩. ⟨pastel-00797363⟩

HAL Id: pastel-00797363

<https://pastel.hal.science/pastel-00797363v1>

Submitted on 6 Mar 2013

HAL is a multi-disciplinary open access archive for the deposit and dissemination of scientific research documents, whether they are published or not. The documents may come from teaching and research institutions in France or abroad, or from public or private research centers.

L'archive ouverte pluridisciplinaire **HAL**, est destinée au dépôt et à la diffusion de documents scientifiques de niveau recherche, publiés ou non, émanant des établissements d'enseignement et de recherche français ou étrangers, des laboratoires publics ou privés.



HAL Authorization

École doctorale n°432: Sciences des Métiers de l'Ingénieur (SMI)

Doctorat ParisTech

T H È S E

pour obtenir le grade de docteur délivré par

l'École Nationale Supérieure des Mines de Paris

Spécialité "Science et Génie des Matériaux"

présentée et soutenue publiquement par

Justin DIRRENBARGER

le 10 décembre 2012

Propriétés effectives de matériaux architecturés

Effective properties of architected materials

Directeurs de thèse: **Samuel FOREST**
Dominique JEULIN

Jury

M. Yves BRÉCHET , Professeur, SIMAP, Grenoble-INP	Président
M. Albrecht BERTRAM , Professeur, Otto-von-Guericke-Universität Magdeburg	Rapporteur
M. Rémy DENDIEVEL , Professeur, SIMAP, Grenoble-INP	Rapporteur
M. Michel BORNERT , Ingénieur en Chef des Ponts, Eaux et Forêts, Navier, École des Ponts-ParisTech	Examineur
M. Pierre GILORMINI , Directeur de recherche, PIMM, Arts et Métiers-ParisTech / CNRS	Examineur
M. Marc THOMAS , Ingénieur de recherche, DMSM, ONERA	Examineur
M. François WILLOT , Chargé de recherche, CMM, MINES-ParisTech	Invité
M. Samuel FOREST , Directeur de recherche, CdM, MINES-ParisTech / CNRS	Directeur de thèse
M. Dominique JEULIN , Directeur de recherche, CMM, MINES-ParisTech	Directeur de thèse

MINES-ParisTech / CNRS UMR 7633

Centre des Matériaux

91003 EVRY Cedex, France

**T
H
È
S
E**

*Il ne s'agit plus de créer une belle œuvre,
il faut savoir s'organiser une belle réclame.*

— *Octave Mirbeau, Le Manuel du savoir-écrire (1889)*

Pour Flo...

Remerciements / Acknowledgements

Quelle meilleure introduction pour un manuscrit de thèse que la périlleuse épreuve des remerciements ? S'ils sont à l'image du candidat, je pense volontiers qu'ils reflètent aussi le contenu de la thèse. Je me suis alors senti obligé de faire preuve de bon sens, d'audace et d'honnêteté intellectuelle, tout en essayant, tant bien que mal, d'éviter les lieux communs et le piège des émotions.

Mes premiers remerciements vont à mon directeur de thèse Samuel Forest, qui a bien voulu m'accorder sa confiance alors qu'il n'avait que peu d'éléments pour le convaincre. Ce serait un euphémisme de dire que j'ai beaucoup appris à ses côtés. Tous ceux qui ont l'honneur d'avoir été ses élèves savent quelle déférente affection ils éprouvent pour le Maître si bienveillant qui les a guidés. Maître scientifique, mais aussi source d'inspiration. Samuel, veuillez trouver ici un trop faible témoignage de toute la considération que je vous porte.

J'aimerais de la même façon exprimer ma gratitude toute particulière envers mon autre directeur de thèse, Dominique Jeulin, qui a su partager son enthousiasme et son savoir sans bornes au profane curieux que j'étais et qui m'a ainsi fait découvrir cette discipline passionnante qu'est la morphologie mathématique. Ce fût un honneur de préparer mon doctorat sous votre direction.

Je souhaiterais maintenant remercier les membres de mon jury d'avoir accepté de se pencher sur mes travaux, en commençant par les rapporteurs. Ich danke Prof. Albrecht Bertram für das akribische Studium meiner Doktorarbeit und für seine einschlägigen Bemerkungen. Zudem danke ich ihm dafür, dass er mir durch sein Seminar an der École des Mines eine neue Sichtweise auf die Kontinuumsmechanik aufgezeigt hat. Un grand merci à Rémy Dendievel pour avoir accepté de rapporter sur ce travail à la dernière minute, et pour avoir constamment enrichi ma réflexion au cours de ces trois dernières années.

J'adresse mes plus sincères remerciements à Yves Bréchet pour avoir bien voulu présider mon jury de thèse. Je garderai un souvenir intense de nos discussions animées à propos du marquis de Condorcet ou de la bielle architecturée et autres moutons pentapodes.

Remerciements / Acknowledgements

Sans la contribution discrète de Michel Bornert, je n'aurais peut-être jamais entrepris une thèse en mécanique des matériaux. En effet, c'est en suivant son cours de master que je me suis intéressé à la question. Nos chemins se sont croisés à maintes reprises ces quatre dernières années, j'espère que ce n'est qu'un début ; je vous remercie d'avoir bien voulu juger mon travail. Merci à Pierre Gilormini de m'avoir fait l'honneur d'apporter, avec l'art et la manière, les précisions nécessaires à mon manuscrit lors de la soutenance. Je souhaiterais remercier chaleureusement Marc Thomas d'avoir participé en tant qu'examineur à mon jury de thèse, merci également à François Willot d'y avoir pris part.

Une thèse se résume parfois à trois années de frustration face à une expérience infructueuse ou à taper des lignes de code vertes sur un écran noir. Dans mon cas ça a aussi été l'occasion de participer à un certain nombre de réunions d'avancement du projet ANR MANSART et de côtoyer des gens avec qui j'ai apprécié travailler. Je remercie Marc Thomas et Yves Bréchet d'avoir si bien mené la barque du projet MANSART et fait émerger un environnement que je qualifierais d'exceptionnel pour les doctorants. Sans m'étendre davantage et sans ordre particulier, merci à Magali Dugué, Amélie Kolopp, Marion Amiot, Loïc Courtois, Pierre Leite, Christophe Bouvet, Dominique Poquillon, Valia Fascio, Yannick Girard, Sophie Gourdet, Cécile Davoine, Frank Simon, Eric Maire, Michel Perez, Marc Fivel, Pierrick Péchambert, Dominique Bissières, Anne Perwuelz, Maryline Lewandowski et Sjoerd van der Veen.

Ce travail a été préparé principalement au Centre des Matériaux à Evry, dont j'aimerais remercier les 3 directeurs successifs, Esteban Busso, Yves Bienvenu et Jacques Besson, pour m'avoir accueilli et fourni dans un environnement de travail lui aussi exceptionnel. Je souhaiterais remercier l'ensemble des membres du CdM pour leur convivialité et plus spécifiquement Olivier et Grégory pour le support informatique indispensable, Odile pour les références bibliographiques improbables, Véronique pour le support logistique, Liliane et Konaly pour la pré-soutenance. J'ai eu la chance de collaborer avec plusieurs équipes au CdM, merci donc à l'équipe SIP, notamment Jean-Dominique Bartout et Christophe Colin, merci à l'équipe VAL, notamment Djamel Missoum-Benziane pour ses Zébulonneries et Nikolay Osipov pour le maillage, et enfin un grand merci à l'équipe COCAS et ses membres distingués, Georges Cailletaud, David Ryckelynck et Matthieu Mazière. Merci à Anne-Françoise Gourgues-Lorenzon pour m'avoir incité à aller regarder la microstructure de mes échantillons. Merci à Jérôme Crépin pour ses précieux conseils que j'ai tenté de mettre en application tant bien que mal. Merci à Franck N'Guyen pour son aide en Matlab et en C++.

Merci aux camarades du bureau B127, Nicolas, Damien, Bahram, Édouard, Ozgur, Victor, Aurélien et Mouhcine. Merci aussi à Meriem, Anthony, Antonin, Xu, Olivier, Manu, Pierre, Duy, Laure-Line, Morgane, Arina, Prajwal, Arthur, Konstantin, Charlotte, Rémi, Mamane, Christophe, Guillaume, Julian, Laurent, Flora, Mélanie, Antoine, Jia, Judith, Philippe et Francesco au CdM, ainsi que Noémie, Alexandre et Dominique à l'ONERA. J'ai aussi eu la chance d'être accueilli par l'équipe du Centre de Morphologie Mathématique à Fontainebleau, je tiens à remercier tout particulièrement Charles Peyrega, Julie Escoda, Matthieu Faessel et Hellen Altendorf. Merci aussi aux compagnons de route des matériaux architecturés, Olivier Bouaziz, Laurent Laszczyk, Arthur Lebée, Sébastien Turcaud, Lorenzo Guiducci et John Dunlop. Je remercie chaleureusement Felix Fritzen pour ses passages, toujours enrichissants, au CdM.

Remerciements / Acknowledgements

J'aimerais aussi profiter de l'occasion pour remercier Clotilde Berdin de l'Université Paris-Sud pour m'avoir permis d'enseigner pendant ma thèse.

Je tiens aussi à remercier spécialement André Pineau pour nos nombreuses discussions à bâtons rompus sur l'industrie, la recherche, l'histoire des idées et, bien sûr, les aciers inoxydables, en espérant qu'il ne m'en veuille pas trop de partir étudier les bétons en Angleterre...

D'une manière générale, je tiens à remercier toutes les personnes qui m'ont accordé leur confiance ou qui m'ont laissé ma chance au cours de mes études, il aura fallu un invraisemblable concours de circonstances pour que je termine ce chapitre de ma vie. Sans nommer les acteurs de cette aventure, je leur rends ici hommage.

Merci à mes parents, à Lucas et à Matthieu pour leur soutien indéfectible depuis 1985.

Pour finir, mes sentiments les plus profonds et ma gratitude la plus sincère sont adressés à la best partner in crime ever, Flo. La réalisation de ce projet n'aurait jamais été possible sans ta patience et ton soutien continu depuis toutes ces années. Ta belle âme m'inspire quotidiennement, j'espère que tu voudras bien assumer cette responsabilité encore quelques décennies.

Paris, le 23 janvier 2013
Justin Dirrenberger

Abstract

Architected materials bring new possibilities in terms of structural and functional properties, filling gaps and pushing the boundaries of *Ashby's* materials maps. The term "architected materials" encompasses any microstructure designed in a thoughtful fashion, so that some of its materials properties have been improved. There are many examples: particulate and fibrous composites, foams, sandwich structures, woven materials, lattice structures, etc. One engineering challenge is to predict the effective properties of such materials. In this work, two types of microstructures are considered: periodic auxetic lattices and stochastic fibrous networks. Auxetics are materials with negative *Poisson's* ratio that have been engineered since the mid-1980s. Such materials have been expected to present enhanced mechanical properties such as shear modulus or indentation resistance. The stochastic fibrous networks considered in this work is made of 3D infinite interpenetrating fibers that are randomly distributed and oriented. This case of random structure is challenging regarding the determination of a volume element size that is statistically representative. For both materials, computational homogenization using finite element analysis is implemented in order to estimate the effective thermal and mechanical properties.

Keywords: Computational homogenization, Representative Volume Element, Auxetics, Random fibrous networks, Effective properties

Résumé

Les matériaux architecturés font émerger de nouvelles possibilités en termes de propriétés structurales et fonctionnelles, repoussant ainsi les limites des cartes d'*Ashby*. Le terme "matériaux architecturés" inclut toute microstructure conçue de façon astucieuse, de sorte que certaines de ses propriétés soient optimisées. Les exemples sont nombreux : composites fibreux et particuliers, matériaux cellulaires, structures sandwiches, matériaux tissés, structures treillis, etc. Un enjeu de taille pour l'emploi de tels matériaux est la prédiction de leurs propriétés effectives. Dans ce travail, deux types de microstructures sont considérés : des structures auxétiques périodiques et des milieux fibreux aléatoires. Les auxétiques sont des matériaux apparus au milieu des années 1980, présentant un coefficient de *Poisson* négatif. On attend des auxétiques qu'ils présentent des propriétés mécaniques améliorées, comme le module de cisaillement ou la résistance à l'indentation. Les milieux fibreux aléatoires considérés dans ce travail sont constitués de fibres 3D infinies interpénétrantes aléatoirement distribuées et orientées. Ce type de structure aléatoire est très défavorable à la détermination d'une taille de volume élémentaire statistiquement représentatif. Pour les deux types de matériaux, l'homogénéisation numérique à l'aide de la méthode des éléments finis est implémentée dans le but d'estimer les propriétés thermiques et mécaniques effectives.

Mots-clés : Homogénéisation numérique, Volume élémentaire représentatif, Auxétiques, Milieux fibreux stochastiques, Propriétés effectives

Contents

Remerciements / Acknowledgements	iii
Abstract (English/Français)	vii
List of notations	xv
Introduction	1
0 Architected Materials	3
0.1 A new class of materials	3
0.2 The MANSART project	6
0.3 The present study	7
0.4 From local heterogeneity to global response of materials	8
0.5 Summary	8
I Introduction to homogenization	9
1 Preliminary concepts	11
1.1 Constitutive thermal behavior	11
1.2 Principles for mechanical modeling	12
1.3 Constitutive mechanical behavior	12
1.3.1 Linear elasticity	12
1.3.2 Elastoplasticity	14
1.4 Additivity	16
2 Homogenization	17
2.1 Representative volume element	17
2.2 Averaging relations	19
2.2.1 Averaging thermal fields	19
2.2.2 Averaging mechanical fields	20
2.3 Boundary conditions	21
2.3.1 Thermal behavior	21

Contents

2.3.2	Mechanical behavior	22
2.3.3	Hill–Mandel condition	24
2.4	Effective properties vs. apparent properties	25
2.4.1	Linear conductivity	25
2.4.2	Linear elasticity	26
2.5	Some boundary value problems for the estimation of isotropic effective properties	29
2.5.1	Thermal properties	29
2.5.2	Elastic properties	30
3	Analytical estimates and bounds	33
3.1	Analytical estimates for thermal properties	33
3.1.1	Maxwell Garnett’s estimate	33
3.1.2	Bruggeman’s self-consistent model	34
3.2	Analytical bounds for thermal properties	35
3.2.1	Bounds of order 0	35
3.2.2	Bounds of order 1	35
3.2.3	Bounds of order 2	36
3.2.4	Bounds of order 3	37
3.2.5	Bounds of order 4	37
3.3	Analytical estimates for elastic properties	38
3.3.1	Einstein’s estimate	38
3.3.2	Eshelby’s model	38
3.3.3	Self-consistent scheme	41
3.4	Analytical bounds for elastic properties	43
3.4.1	Bounds of order 0	43
3.4.2	Bounds of order 1	43
3.4.3	Bounds of order 2	44
3.4.4	Bounds of order 3	46
3.4.5	Bounds of order 4	47
4	Computational homogenization	51
4.1	Computational homogenization using the finite element method	51
4.1.1	FE formulation of the principle of virtual work	52
4.1.2	Application to linear elasticity	53
4.1.3	The element DOF method with prescribed macroscopic strain	54
4.2	Statistical approach for determining a RVE size	56
4.2.1	Ergodicity hypothesis	56
4.2.2	Stationarity hypothesis	57
4.2.3	Statistical homogeneity hypothesis	57
4.2.4	RVE size determination for media with finite integral range	57
4.2.5	Generalization of the statistical approach to microstructures with non-finite integral range	60

II	Application to periodic media	65
5	Auxetics	67
5.1	Introduction to auxetics	67
5.2	Computational homogenization	69
5.3	Microstructures considered	70
5.3.1	Hexachiral lattice	70
5.3.2	Anti-tetrachiral lattice	71
5.3.3	Rotachiral lattice	72
5.3.4	Honeycomb lattice	72
5.4	Effective elastic properties	73
5.4.1	Hexachiral lattice	75
5.4.2	Anti-tetrachiral lattice	76
5.4.3	Rotachiral lattice	78
5.4.4	Honeycomb lattice	80
5.4.5	Discussion	80
5.5	Extension to elastoplasticity	82
5.5.1	Constitutive model considered	82
5.5.2	Comparison with the honeycomb lattice	86
5.5.3	Macroscopic modeling	87
5.5.4	Simulation and identification	90
5.5.5	Discussion	92
5.6	3D auxetic microstructure: the hexatruss lattice	92
5.7	Structural applications of auxetics	94
5.7.1	Spherical indentation: loading case 1	95
5.7.2	Spherical indentation: loading case 2	96
5.7.3	Cylindrical indentation	96
5.8	Experimental characterization of auxetics	102
5.9	Conclusions and prospects	102
III	Application to random media	107
6	Poisson fibers	109
6.1	Microstructural model	111
6.1.1	Poisson point process	111
6.1.2	Linear Poisson varieties	112
6.1.3	Boolean random sets	112
6.1.4	Generation of Poisson fiber virtual models	113
6.1.5	Discretization of microstructural models	114
6.1.6	Parameters of the simulation	116
6.1.7	Computational strategy	116
6.2	Boundary conditions	119

Contents

6.2.1	Thermal properties	121
6.2.2	Mechanical properties	128
6.3	Results	140
6.3.1	Morphological properties	140
6.3.2	Thermal properties	141
6.3.3	Elastic properties	143
6.4	Discussion	143
6.4.1	Morphological isotropy	145
6.4.2	Elastic isotropy	146
6.4.3	Thermal and mechanical fields	149
6.5	Determination of the statistical RVE size	151
6.5.1	Variance from simulation	151
6.5.2	Results	151
6.6	Conclusion	155
IV Conclusions & Outlook		159
V Appendices		169
A Finite element method for periodic homogenization		171
A.1	Case study #1: fiber-reinforced composite material	171
A.1.1	The MPC_periodic method	172
A.1.2	The element DOF method with prescribed macroscopic strain	175
A.1.3	The element DOF method with prescribed macroscopic stress	177
A.2	Case study #2: 3D grid	180
A.2.1	The MPC_periodic method	181
A.2.2	The element DOF method with prescribed macroscopic strain	182
A.2.3	The element DOF method with prescribed macroscopic stress	183
B Basics of mathematical morphology		189
B.1	Characterization of random structures	190
B.1.1	Minkowski functionals	190
B.1.2	Basic operations of mathematical morphology	190
B.1.3	Steiner formulae	191
B.1.4	Covariance	192
B.2	Models of random structures	193
B.2.1	Choquet capacity	193
B.2.2	Poisson point process	194
B.2.3	Poisson linear varieties	195
B.2.4	Boolean model	197
B.2.5	Boolean random varieties	198

B.2.6 Poisson fibres	199
C Experimental characterization of auxetics	201
C.1 Microstructural characterization	201
C.2 Macroscopic mechanical testing	203
C.3 X-ray microtomography	204
D Simulation results for Poisson fibers	209
References	214
Index	229
Academic genealogy	233

List of Notations

Tensors, tensor algebra and operators

x	0 th -order tensor (scalar)
\underline{x} or x_i	1 st -order tensor (vector)
$\underline{\underline{x}}$ or x_{ij}	2 nd -order tensor
$\underline{\underline{\underline{x}}}$ or x_{ijkl}	4 th -order tensor
\underline{I} or I_{ij}	2 nd -order identity tensor
$\underline{\underline{I}}$ or I_{ijkl}	4 th -order identity tensor
\underline{e}_i	Basis vector
$x = \underline{a} \cdot \underline{b}$	$x = a_i b_i$
$\underline{x} = \underline{a} \cdot \underline{b}$	$x_i = a_{ij} b_j$
$\underline{\underline{x}} = \underline{a} \cdot \underline{b}$	$x_{ij} = a_{ik} b_{kj}$
$x = \underline{a} : \underline{b}$	$x = a_{ij} b_{ij}$
$\underline{\underline{x}} = \underline{\underline{a}} : \underline{\underline{b}}$	$x_{ij} = a_{ijkl} b_{kl}$
$x = \underline{\underline{\underline{a}}} :: \underline{\underline{\underline{b}}}$	$x = a_{ijkl} b_{ijkl}$
$\underline{\underline{x}} = \underline{a} \otimes \underline{b}$	$x_{ij} = a_j b_j$
$\underline{\underline{\underline{x}}} = \underline{a} \otimes^s \underline{b} = \frac{1}{2} (\underline{a} \otimes \underline{b} + (\underline{a} \otimes \underline{b})^T)$	$x_{(ij)} = \frac{1}{2} (a_i b_j + a_j b_i)$
$\underline{\underline{\underline{x}}} = \underline{a} \otimes \underline{b}$	$x_{ijkl} = a_{ij} b_{kl}$
δ_{ij}	<i>Kronecker</i> symbol
$\ \underline{x}\ $	Euclidean norm of a vector
$I_1(\underline{x})$ or $\text{Tr } \underline{x}$ or x_{ii}	1 st invariant of a tensor (trace)
$I_2(\underline{x})$ or $\frac{1}{2} ((\text{Tr } \underline{x})^2 - \text{Tr}(\underline{x}^2))$	2 nd invariant of a tensor
$I_3(\underline{x})$ or $\text{Det } \underline{x}$	3 rd invariant of a tensor (determinant)
\underline{x}^{-1}	Inverse of an invertible tensor
\underline{x}^T	Transpose of a tensor
$\text{Div } \underline{x}$ or $\nabla \cdot \underline{x}$ or $x_{ij,j}$	Divergence of a tensor
$\nabla \underline{x}$ or $\nabla \otimes \underline{x}$	Gradient of a tensor
$\dot{\underline{x}} = \frac{d\underline{x}}{dt}$	Time derivative of a tensor
\underline{J}	Spherical projector for 2 nd -order symmetric tensors
$\underline{\underline{K}}$	Deviatoric projector for 2 nd -order symmetric tensors

Thermal and mechanical tensors

\mathcal{D}^{th}	Thermal dissipation rate density
$\underline{\mathbf{q}}$ or q_i	Heat flux vector
T	Temperature
∇T or $T_{,i}$	Temperature gradient
$\underline{\lambda}$ or λ_{ij}	Thermal conductivity tensor
$\underline{\rho}$ or ρ_{ij}	Thermal resistivity tensor
$\underline{\mathcal{E}}^{el}$	Elastic strain energy density
$\underline{\sigma}$ or σ_{ij}	<i>Cauchy</i> stress tensor
$\underline{\epsilon}$ or ϵ_{ij}	Engineering strain tensor
$\underline{\mathbf{c}}$ or c_{ijkl} or c_{IJ}	Elastic moduli tensor
$\underline{\mathbf{s}}$ or s_{ijkl} or s_{IJ}	Compliance tensor
$\underline{\sigma}^{sph} = \frac{1}{3}(\text{Tr } \underline{\sigma}) \underline{\mathbf{I}}$	Spherical stress tensor
$\underline{\sigma}^{dev} = \underline{\sigma} - \underline{\sigma}^{sph}$	Deviatoric stress tensor
$\underline{\mathbf{X}}$	Kinematic hardening tensor
$\underline{\mathbf{H}}$	<i>Hill</i> tensor
$\underline{\mathbf{v}}$	Velocity field
$\underline{\mathbf{u}}$	Displacement field
$\underline{\mathbf{f}}$	Body forces
$\underline{\mathbf{F}}$	Surface forces
\mathcal{P}_{int}	Power of internal forces
\mathcal{P}_{ext}	Power of external forces
$\underline{\boldsymbol{\tau}}$	Polarization stress tensor
$\underline{\mathbf{S}}^0$	<i>Eshelby</i> interaction tensor
$\underline{\mathbf{P}}^0$	<i>Hill</i> interaction tensor
$\underline{\mathbf{C}}^*$	<i>Hill</i> influence tensor
E	<i>Young's</i> modulus
μ	Shear modulus
k	Bulk modulus
ν	<i>Poisson's</i> ratio

Finite element notations

$[x]$	n -dimensional matrix
$\{x\}$	Column-vector
$[N]$	Shape function matrix
$[B]$	Deformation operator
$[K]$	Stiffness matrix

Mathematical morphology

A	Random closed set
A^c	Complementary set of A
$\check{A} = \{-x, x \in A\}$	Transposed set of A
$B(r)$	Closed ball with radius r
K	Compact set
P	Probability of an event
$p = P\{x \in A\}$	Probability of x to be in A
$q = P\{x \in A^c\} = 1 - p$	Probability of x to be in A^c
$C(h) = P\{x \in A, x + h \in A\}$	Covariance $C(h)$
$Q(h) = P\{x \in A^c, x + h \in A^c\}$	Covariance $Q(h)$
$T(K) = P\{K \cap A \neq \emptyset\} = 1 - Q(K)$	<i>Choquet's</i> capacity
$\overline{W}_2(x, x + h)$	2 nd order central correlation function
$A \oplus \check{K}$	Dilation by a compact K
$A \ominus \check{K}$	Erosion by a compact K
$A_K = A \ominus \check{K} \oplus K$	Opening by a compact K
$A^K = A \oplus \check{K} \ominus K$	Closing by a compact K
$\mu(A)$	Measure of A
μ_n	<i>Lebesgue</i> measure in \mathbb{R}^n
θ_k	<i>Radon</i> measure on locally compact topological spaces
$\mathcal{N}(A)$	Integral of total curvature or connectivity of A
$\mathcal{M}(A)$	Integral of mean curvature of A
$\mathcal{L}(A)$	Perimeter of A in \mathbb{R}^2
$\mathcal{A}(A)$	Area of A in \mathbb{R}^2
$\mathcal{S}(A)$	Area of A in \mathbb{R}^3
$\mathcal{V}(A)$	Volume of A
S_S	Surface fraction
V_V	Volume fraction
$Z(x)$	Random function or physical property
$E\{Z(x)\}$	Mathematical expectation of $Z(x)$
D_Z^2	Variance of $Z(x)$
D_Z	Standard deviation of $Z(x)$
$\overline{Z}(V)$	Average value over V of $Z(x)$
A_n	Integral range of dimension n
ϵ_{abs}	Absolute error
ϵ_{rel}	Relative error
θ	Intensity of a <i>Poisson</i> process
ω	Random orientation in \mathbb{R}^n
$V_k(\omega)$	<i>Poisson</i> variety with intensity $\theta(\omega)$
A'	Primary grain of a Boolean model
$K(h) = \overline{\mu}_n(A' \cap A'_{-h})$	Geometrical covariogram a Boolean model

Introduction Part

0 Architected Materials

*Accident is design
And design is accident
In a cloud of unknowing.*

— T. S. Eliot, *The Family Reunion* (1939)

0.1 A new class of materials

Architected materials are a rising class of materials that bring new possibilities in terms of functional properties, filling the gaps and pushing the limits of *Ashby's* materials performance maps [Ashby, 1999], as shown on Figure 1 [Ashby, 2013]. The term *architected materials* encompasses any microstructure designed in a thoughtful fashion, that some of its materials properties have been improved in comparison to those of its constituents [Ashby and Bréchet, 2003, Ashby, 2013, Bréchet and Embury, 2013]. There are many examples: particulate and fibrous composites, foams, sandwich structures, woven materials, lattice structures, etc. Most of them are shown on Figure 2, also taken from [Ashby, 2013]. One can play on many parameters to obtain architected materials, but all of them are related either to the microstructure or the geometry. Parameters related to the microstructure can be optimised for specific needs using a materials-by-design approach, which has been thoroughly developed by chemists, materials scientists and metallurgists. For instance, it is well-known among metallurgists that mechanically decreasing the average grain size of an alloy, as well as increasing the dislocation density, results in a higher yield strength. Stronger polymers can be engineered by changing interchain bounds or by optimizing the chain design. These improvements are intrinsically related to the synthesis and processing of materials and are therefore due to micro- and nanoscale phenomena, taking place at a scale ranging from 1 nm to 10 μm . This scale is below the scope of this work but has been extensively studied in the literature, see for instance [Brinker et al., 1994, Olson, 2001, Freeman, 2002, Embury and Bouaziz, 2010]. Processing is

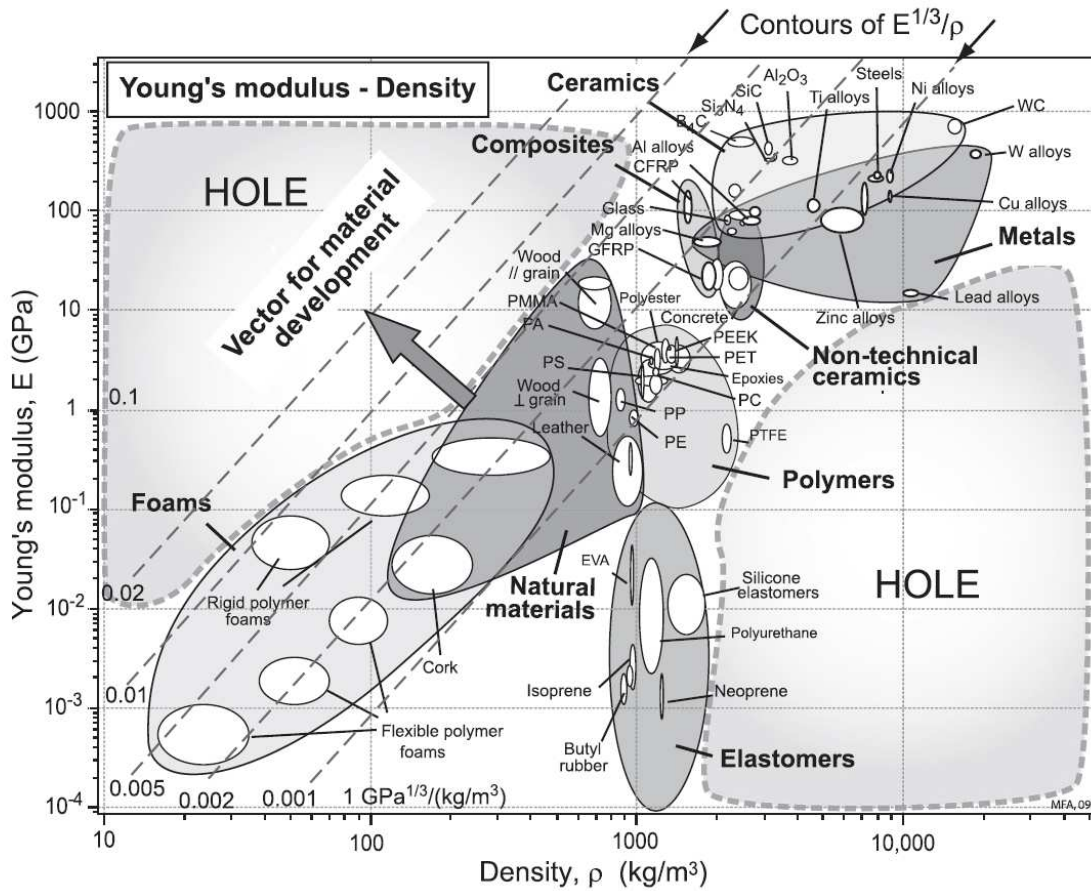


Figure 1: Ashby's material map for Young's modulus vs. density, from [Ashby, 2013]

the key technological lock for the development of architected materials, nevertheless progress is made every day to overcome this, as it was done in [Schaedler et al., 2011] by combining several processing techniques in order to fabricate ultralight metallic microlattice materials. From a macroscopic viewpoint, parameters related to the geometry have mainly been the responsibility of structural and civil engineers for centuries: to efficiently distribute materials within structures. An obvious example would be the many different strategies available for building bridges. Figure 3, taken from [Ashby and Bréchet, 2003], illustrates the basic strength of materials fact that one can optimize bending stiffness by modifying the geometry of the component, keeping the lineic mass (for beams) or surfacic mass (for plates) unchanged. On the other hand, one might need a lower flexural strength for the same lineic and surfacic masses. This can be achieved with stranded structures, as shown on Figure 4, also taken from [Ashby and Bréchet, 2003]. Architected materials thus lie between the microscale and the macroscale. This class of materials involves geometrically engineered distributions of microstructural phases at a scale comparable to the scale of the component, thus calling for new models in order to determine the effective properties of materials. One aim of the present work is to provide such models, in the case of mechanical and thermal properties.

0.1. A new class of materials

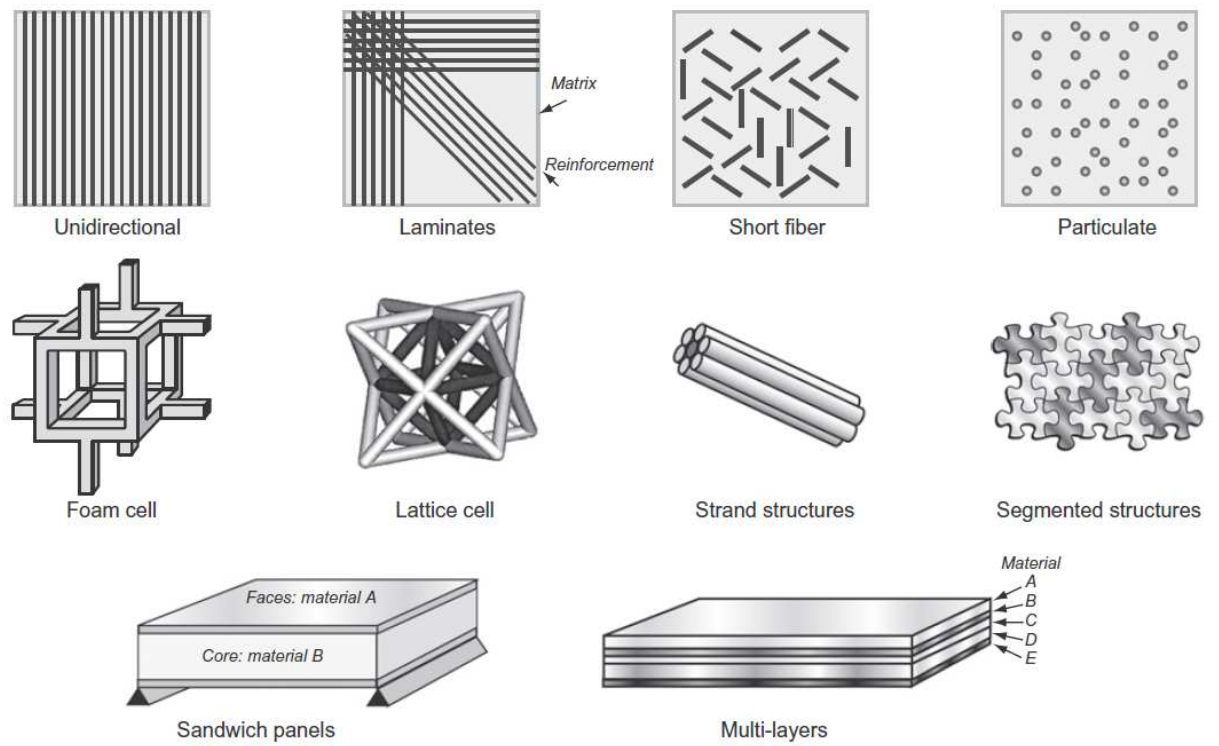


Figure 2: Examples of architected materials, from [Ashby, 2013]

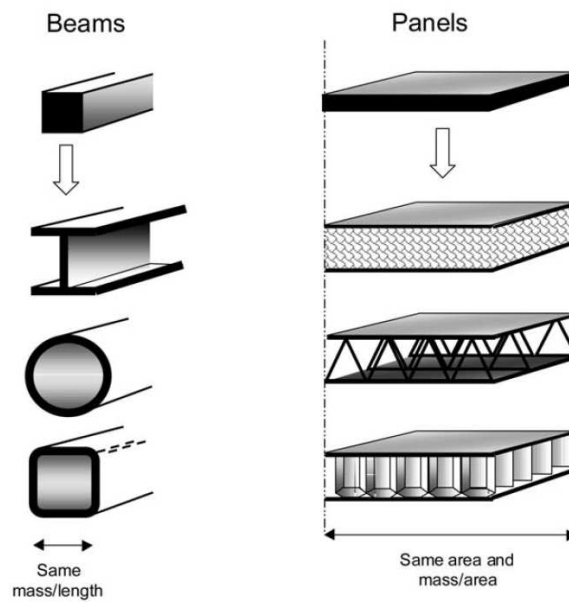


Figure 3: Shape as a parameter for increasing sectional bending stiffness, from [Ashby and Bréchet, 2003]

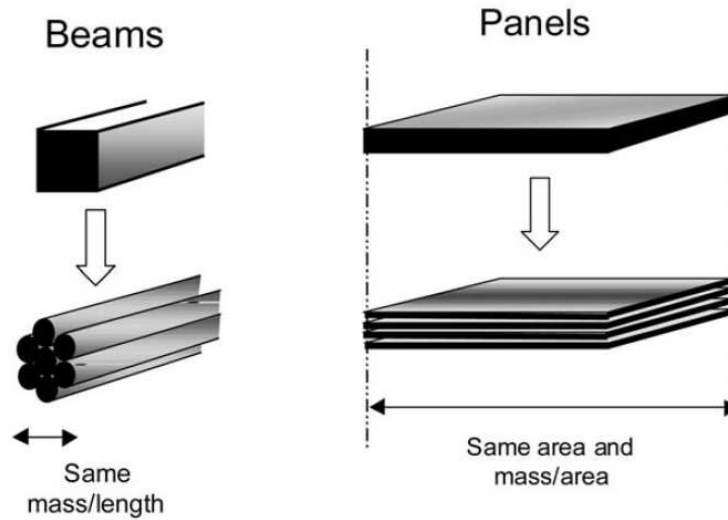


Figure 4: Shape as a parameter for decreasing sectional bending stiffness, from [Ashby and Bréchet, 2003]

0.2 The MANSART project

The MANSART (for MATériaux saNdwichES ARchiTecturés, or ARchiTectured saNdwichES MATerials) project aims at exploring new tools and approaches to develop such materials. The project is mostly funded by the French Agence Nationale pour la Recherche (ANR). Starting from January 2009, the project ran for 4 years, gathering 5 industrial (Airbus, EADS-IW, ONERA, Ateca, SMCI) and 6 academic partners (CdM/MINES-ParisTech, MATEIS/INSA Lyon, SIMAP/Grenoble-INP, GEMTEX/ENSAIT, ICA/ISAE, CIRIMAT/ENSIACET). It is subsequent to the previous ANR project MAPO (MATériaux POreux) and CNRS project MAM (MATériaux Architecturés Multifonctionnels). The applications considered in the MANSART project are mainly related to crashworthiness and mechanical properties at mid-range temperatures (*ca.* 300°C). The following architected materials were considered to fulfill industrial requirements: entangled monofilament of perlite steel (PhD work of *Loïc Courtois* at MATEIS/INSA Lyon [Courtois et al., 2011]), sandwich composite structures (PhD work of *Amélie Kolopp* at ICA/ISAE [Kolopp et al., 2011]), woven and non-woven textile composites (PhD work of *Marion Amiot* at GEMTEX/ENSAIT [Lewandowski et al., 2012]), segmented interlocking structures (PhD work of *Magali Dugué* at SIMAP/Grenoble-INP) and materials with negative *Poisson's* ratio (this work). Moreover, optimization of sandwich structures was also investigated (PhD work of *Pierre Leite* at ONERA [Leite et al., 2012b, Leite et al., 2012a]), as well as homogenization methods for predicting the effective properties of architected materials (this work).

0.3 The present study

This work is part of the MANSART project and was funded entirely by ANR. While most of the work was conducted at the Centre des Matériaux¹, which is a mixed research unit between MINES-ParisTech and CNRS located in Evry, some of it, especially most of the computational microstructural modeling, was done at the Centre de Morphologie Mathématique² of MINES-ParisTech in Fontainebleau.

The study is part of MANSART, with a focus on computational modeling as well as rapid prototyping of architected materials. As a matter of fact, one engineering challenge is to predict the effective properties of such materials; numerical homogenization using finite element analysis is a powerful tool to do so. A challenging candidate material was imagined for assessing the applicability of such methods to architected materials: stochastic random networks made of infinite fibers, more specifically Poissonian fibrous networks. The determination of the effective properties of *Poisson* fibers is not trivial, as it will be presented in Part III of this manuscript. The random fibrous media considered in this work do not exist *per se*, but their microstructure can be modeled computationally. The generation of such virtual specimens relies on a tridimensional *Poisson* point implantation process. Due to the long-range correlation induced by the model of random structures chosen, the size of the representative volume element is *a priori* unknown. One goal of this work was then to evaluate this size using numerical simulation. However, periodization of these microstructures is generally impossible, making the periodic homogenization tools ineffective. Very large virtual samples computations have to be performed in order to compute their representative volume element sizes *a posteriori* based on statistical arguments and finally predict their effective mechanical and thermal properties.

Another type of material was considered soon after we started the project: auxetics. Auxetic materials are a type of architected materials exhibiting a negative *Poisson's* ratio. They could present interesting advantages for both functional and structural applications in the future. They are presented in detail in Section 5.1. Auxetics considered in this work are halfway between lattice structures and foams. We worked on periodic structures, making their homogenization straightforward. A whole design-simulation-processing-characterization chain was developed for auxetics, making it possible for us to study numerically and experimentally auxetics from the literature, but also to develop new auxetic microstructures, using computer-aided design, results from homogenization, rapid prototyping with selective laser melting and mechanical testing. The results for auxetics are presented in Part II. By the means of homogenization technique coupled with finite elements, we were able to investigate anisotropy for both linear elasticity and elastoplasticity. Macroscopic modeling was performed and the simulation of indentation experiments was done using these models.

This work is aiming at helping us developing new architected materials by understanding the underlying processes taking place in auxetic periodic lattices structures and stochastic random

¹<http://www.mat.ensmp.fr/>

²<http://cmm.ensmp.fr/>

fibrous media. Rapid prototyping using selective laser melting allows us to be creative in terms of microstructural design. Our intention is also to demonstrate the ability of the computational homogenization using finite element analysis to be a powerful tool for designing, modeling and simulating future architected materials.

0.4 From local heterogeneity to global response of materials

Materials science comes from the following fact: microstructural heterogeneities play a critical role in the macroscopic behavior of a material. Constitutive modeling, thanks to an interaction between experiments and simulation, is usually able to describe the response of most materials in use. Such phenomenological models, including little to no information about the microstructure, cannot necessarily account for local fluctuation of properties. In that case, the material is considered as a homogeneous medium. Studying the behavior of heterogeneous materials involves developing enriched models including morphological information about the microstructure. These models should be robust enough to predict effective properties depending on statistical data (volume fraction, n -point correlation function, etc.) and the physical nature of each phase or constituent. As a matter of fact, advanced models are often restricted to a limited variety of materials. For instance, the behavior of a polycrystalline material without any particular texture, a multi-layered composite structure and a metallic ceramic exhibiting a composition gradient cannot be modeled using the same assumptions. Although isotropic and anisotropic polycrystalline metals have been extensively studied by the means of analytical and computational tools, architected materials bring up new challenges regarding the determination of effective properties. The core purpose of this work is to meet up these challenges by adapting existing homogenization methods to architected materials.

0.5 Summary

In this work, we intend on bringing up answers for the following questions:

- How to determine the effective properties of architected materials?
- How could we adapt existing computational tools for this purpose?
- Can rapid prototyping be useful to develop architected materials?
- What can be expected from negative *Poisson's* ratio materials?
- How could we assess the representativity of elementary volumes?

Those questions will be covered in the discussion taking place in Part [IV](#).

Introduction to homogenization Part I

1 Preliminary concepts

Experience is simply the name we give our mistakes.

— *Oscar Wilde, Lady Windermere's Fan (1892)*

Our scientific goal is the prediction of the mechanical and thermal effective properties for architected materials using computational homogenization. This first part aims at introducing homogenization methods and summarizing some approaches in this field, either analytical or computational.

Several considerations are necessary for implementing a homogenization scheme. They are presented hereafter.

A few assumptions have to be made regarding the physics of the materials studied in this work. They concern the constitutive thermal and mechanical behavior, as well as some related principles.

1.1 Constitutive thermal behavior

Thermal properties of architected materials are studied in this work. We assume that heat transfer takes place within the material to be defined locally according to *Fourier's* law [Fourier, 1822]:

$$\underline{q} = -\lambda \cdot \nabla T \tag{1.1}$$

Chapter 1. Preliminary concepts

with \underline{q} heat flux density vector, $\underline{\lambda}$ second-order symmetric tensor of thermal conductivity, and ∇T temperature gradient. Equation 1.1 can be written as follows using matrices and column-vectors:

$$\begin{bmatrix} q_1 \\ q_2 \\ q_3 \end{bmatrix} = - \begin{bmatrix} \lambda_{11} & \lambda_{12} & \lambda_{13} \\ \bullet & \lambda_{22} & \lambda_{23} \\ \bullet & \bullet & \lambda_{33} \end{bmatrix} \begin{bmatrix} \nabla T_1 \\ \nabla T_2 \\ \nabla T_3 \end{bmatrix} \quad (1.2)$$

It is also possible to express the temperature gradient as a function of the heat flux density using the second-order thermal resistivity tensor $\underline{\rho}$, which is defined as the inverse of tensor $\underline{\lambda}$:

$$-\nabla T = \underline{\rho} \cdot \underline{q} \quad \text{with, } \underline{\rho} \hat{=} \underline{\lambda}^{-1} \quad (1.3)$$

Also,

$$\underline{\rho} \cdot \underline{\lambda} = \underline{I} \quad (1.4)$$

with \underline{I} second-order identity tensor, defined as follows:

$$\underline{I} = \delta_{ij} \underline{e}_i \otimes \underline{e}_j \quad (1.5)$$

1.2 Principles for mechanical modeling

Small deformations hypothesis is considered in this work, as well as three classical principles used in mechanics for constitutive behavior modeling:

- the *principle of local action* implying that the local behavior defined at the material point \underline{x} depends only on variables defined at this material point, hence no effect of the neighboring points is taken into account.
- the *simple material* principle allowing only the use of the first gradient of the transformation within constitutive equations.
- the *material objectivity* principle making the constitutive behavior independent from the observer, in particular time cannot explicitly appear in constitutive equations.

1.3 Constitutive mechanical behavior

1.3.1 Linear elasticity

When heterogeneous materials are assumed to respond linearly to mechanical loading, constitutive relations are expressed locally for each phase in a linear elasticity framework using the generalized

Hooke's law [Hooke, 1678, Cauchy, 1827]:

$$\underline{\underline{\boldsymbol{\sigma}}} = \underline{\underline{\mathbf{c}}} : \underline{\underline{\boldsymbol{\varepsilon}}} \quad (1.6)$$

with $\underline{\underline{\boldsymbol{\sigma}}}$ second-order symmetric *Cauchy* stress tensor, $\underline{\underline{\boldsymbol{\varepsilon}}}$ second-order symmetric engineering strain tensor and $\underline{\underline{\mathbf{c}}}$, fourth-order positive definite tensor of elastic moduli, also known as the elastic stiffness tensor. It is possible to express strain as a function of stress using the compliance tensor $\underline{\underline{\mathbf{s}}}$, which is defined as the inverse of tensor $\underline{\underline{\mathbf{c}}}$:

$$\underline{\underline{\boldsymbol{\varepsilon}}} = \underline{\underline{\mathbf{s}}} : \underline{\underline{\boldsymbol{\sigma}}} \quad \text{with, } \underline{\underline{\mathbf{s}}} \triangleq \underline{\underline{\mathbf{c}}}^{-1} \quad (1.7)$$

such that,

$$\underline{\underline{\mathbf{s}}} \cdot \underline{\underline{\mathbf{c}}} = \underline{\underline{\mathbf{I}}} \quad (1.8)$$

with $\underline{\underline{\mathbf{I}}}$, fourth-order identity tensor operating on symmetric second-order tensors such that:

$$\underline{\underline{\mathbf{I}}} = \frac{1}{2} (\delta_{ik}\delta_{jl} + \delta_{il}\delta_{jk}) \underline{\mathbf{e}}_i \otimes \underline{\mathbf{e}}_j \otimes \underline{\mathbf{e}}_k \otimes \underline{\mathbf{e}}_l \quad (1.9)$$

The 81 components of c_{ijkl} can be thinned-down to 21 for the most anisotropic case (triclinic elasticity) due to symmetries of $\underline{\underline{\boldsymbol{\sigma}}}$ and $\underline{\underline{\boldsymbol{\varepsilon}}}$. By isomorphism, these 21 components can be written as a symmetric second-order tensor (matrix) c_{IJ} with 21 independent components using *Voigt* notation [Voigt, 1887]:

$$\begin{bmatrix} \sigma_{11} \\ \sigma_{22} \\ \sigma_{33} \\ \sigma_{23} \\ \sigma_{31} \\ \sigma_{12} \end{bmatrix} = \begin{bmatrix} c_{11} & c_{12} & c_{13} & c_{14} & c_{15} & c_{16} \\ \bullet & c_{22} & c_{23} & c_{24} & c_{25} & c_{26} \\ \bullet & \bullet & c_{33} & c_{34} & c_{35} & c_{36} \\ \bullet & \bullet & \bullet & c_{44} & c_{45} & c_{46} \\ \bullet & \bullet & \bullet & \bullet & c_{55} & c_{56} \\ \bullet & \bullet & \bullet & \bullet & \bullet & c_{66} \end{bmatrix} \begin{bmatrix} \varepsilon_{11} \\ \varepsilon_{22} \\ \varepsilon_{33} \\ \gamma_{23} \\ \gamma_{31} \\ \gamma_{12} \end{bmatrix} \quad (1.10)$$

Engineering shear strain is used in the strain column-vector:

$$\gamma_{23} = 2\varepsilon_{23}$$

$$\gamma_{31} = 2\varepsilon_{31}$$

$$\gamma_{12} = 2\varepsilon_{12}$$

Chapter 1. Preliminary concepts

The matrix form of the compliance tensor is obtained by inverting Equation 1.10:

$$\begin{bmatrix} \varepsilon_{11} \\ \varepsilon_{22} \\ \varepsilon_{33} \\ \gamma_{23} \\ \gamma_{31} \\ \gamma_{12} \end{bmatrix} = \begin{bmatrix} s_{11} & s_{12} & s_{13} & s_{14} & s_{15} & s_{16} \\ \bullet & s_{22} & s_{23} & s_{24} & s_{25} & s_{26} \\ \bullet & \bullet & s_{33} & s_{34} & s_{35} & s_{36} \\ \bullet & \bullet & \bullet & s_{44} & s_{45} & s_{46} \\ \bullet & \bullet & \bullet & \bullet & s_{55} & s_{56} \\ \bullet & \bullet & \bullet & \bullet & \bullet & s_{66} \end{bmatrix} \begin{bmatrix} \sigma_{11} \\ \sigma_{22} \\ \sigma_{33} \\ \sigma_{23} \\ \sigma_{31} \\ \sigma_{12} \end{bmatrix} \quad (1.11)$$

The finite element code used in this work is actually making use of the *Kelvin* notation presented in Equations 1.12 and 1.13:

$$\begin{bmatrix} \sigma_{11} \\ \sigma_{22} \\ \sigma_{33} \\ \sqrt{2}\sigma_{23} \\ \sqrt{2}\sigma_{31} \\ \sqrt{2}\sigma_{12} \end{bmatrix} = \begin{bmatrix} c_{11} & c_{12} & c_{13} & \sqrt{2}c_{14} & \sqrt{2}c_{15} & \sqrt{2}c_{16} \\ \bullet & c_{22} & c_{23} & \sqrt{2}c_{24} & \sqrt{2}c_{25} & \sqrt{2}c_{26} \\ \bullet & \bullet & c_{33} & \sqrt{2}c_{34} & \sqrt{2}c_{35} & \sqrt{2}c_{36} \\ \bullet & \bullet & \bullet & 2c_{44} & 2c_{45} & 2c_{46} \\ \bullet & \bullet & \bullet & \bullet & 2c_{55} & 2c_{56} \\ \bullet & \bullet & \bullet & \bullet & \bullet & 2c_{66} \end{bmatrix} \begin{bmatrix} \varepsilon_{11} \\ \varepsilon_{22} \\ \varepsilon_{33} \\ \sqrt{2}\varepsilon_{23} \\ \sqrt{2}\varepsilon_{31} \\ \sqrt{2}\varepsilon_{12} \end{bmatrix} \quad (1.12)$$

The matrix form of the compliance tensor is obtained by inverting Equation 1.12:

$$\begin{bmatrix} \varepsilon_{11} \\ \varepsilon_{22} \\ \varepsilon_{33} \\ \sqrt{2}\varepsilon_{23} \\ \sqrt{2}\varepsilon_{31} \\ \sqrt{2}\varepsilon_{12} \end{bmatrix} = \begin{bmatrix} s_{11} & s_{12} & s_{13} & \sqrt{2}s_{14} & \sqrt{2}s_{15} & \sqrt{2}s_{16} \\ \bullet & s_{22} & s_{23} & \sqrt{2}s_{24} & \sqrt{2}s_{25} & \sqrt{2}s_{26} \\ \bullet & \bullet & s_{33} & \sqrt{2}s_{34} & \sqrt{2}s_{35} & \sqrt{2}s_{36} \\ \bullet & \bullet & \bullet & 2s_{44} & 2s_{45} & 2s_{46} \\ \bullet & \bullet & \bullet & \bullet & 2s_{55} & 2s_{56} \\ \bullet & \bullet & \bullet & \bullet & \bullet & 2s_{66} \end{bmatrix} \begin{bmatrix} \sigma_{11} \\ \sigma_{22} \\ \sigma_{33} \\ \sqrt{2}\sigma_{23} \\ \sqrt{2}\sigma_{31} \\ \sqrt{2}\sigma_{12} \end{bmatrix} \quad (1.13)$$

In the isotropic case, $\underline{\underline{c}}$ can be rewritten as follows:

$$\underline{\underline{c}} = 3k\underline{\underline{J}} + 2\mu\underline{\underline{K}} \quad (1.14)$$

with k bulk modulus, μ shear modulus, $\underline{\underline{J}}$ and $\underline{\underline{K}}$ respectively spherical and deviatoric fourth-order tensorial projectors such that,

$$\underline{\underline{J}} = \frac{1}{3}\delta_{ij}\delta_{kl}\underline{\underline{e}}_i \otimes \underline{\underline{e}}_j \otimes \underline{\underline{e}}_k \otimes \underline{\underline{e}}_l \quad (1.15)$$

and

$$\underline{\underline{K}} = \underline{\underline{I}} - \underline{\underline{J}} \quad (1.16)$$

1.3.2 Elastoplasticity

Let us consider the strains as an additive combination of elastic and plastic strains such as,

$$\boldsymbol{\varepsilon} = \boldsymbol{\varepsilon}^{\text{el}} + \boldsymbol{\varepsilon}^{\text{p}} \quad (1.17)$$

The stress state rising from the mechanical loading is only governed by the elastic deformation:

$$\boldsymbol{\sigma} = \boldsymbol{\underline{c}} : \boldsymbol{\varepsilon}^{\text{el}} \quad (1.18)$$

The material considered now exhibits a yield stress R_0 corresponding to the elastic limit. Above this value, the local stress level will induce plasticity and hardening. The evolution of plasticity will depend on the considered nonlinear model. This model is characterized by a load function f . We consider a *Prager*-type function which reads as follows in the case of uniaxial loading:

$$f(\sigma, X) = |\sigma - X| - R_0 \quad (1.19)$$

with σ uniaxial stress, X kinematic hardening function and R_0 yield stress. Plastic flow will take place if and only if $f = 0$ and $\dot{f} = 0$. This yields the following condition:

$$\frac{\partial f}{\partial \sigma} \dot{\sigma} + \frac{\partial f}{\partial X} \dot{X} = 0 \quad (1.20)$$

The load function is considered over three domains:

- Elastic domain if $f(\sigma, X) < 0$ with $\dot{\varepsilon} = \dot{\sigma}/E$
- Elastic discharge if $f(\sigma, X) = 0$ and $\dot{f}(\sigma, X) < 0$ with $\dot{\varepsilon} = \dot{\sigma}/E$
- Plastic flow if $f(\sigma, X) = 0$ and $\dot{f}(\sigma, X) = 0$ with $\dot{\varepsilon} = \dot{\sigma}/E + \dot{\varepsilon}^{\text{p}}$

If $X = H\varepsilon^{\text{p}}$ with H the hardening modulus, one obtains the linear kinematic hardening function [[Prager, 1949](#)] which is characterized by a shift of the yield surface $f(\sigma, X)$. On the other hand, if one wishes to model an expansion of the elastic domain instead of a shift, the hardening function R should be centered on the origin as follows:

$$f(\sigma, X) = |\sigma| - R - R_0 \quad (1.21)$$

This is known as linear isotropic hardening [[Lemaitre and Chaboche, 1994](#)].

The shape of the nonlinear stress-strain curve is therefore given by the evolution of the hardening function R . In order to model more accurately the behavior of materials, nonlinear saturating hardening functions can be considered. Here is an example of exponential hardening function:

$$R = Qe^{-b\varepsilon^{\text{p}}} \quad (1.22)$$

Chapter 1. Preliminary concepts

with Q ultimate stress and b saturation rate parameter.

When dealing with multiaxial loading, it is mandatory to consider a yield criterion that is based on the stress tensor $\underline{\sigma}$ instead of the uniaxial stress σ . The *von Mises* criterion [von Mises, 1913] is one of the most common yield criterion for metallic materials. It makes use of the second invariant of the deviatoric stress tensor $I_2(\underline{\sigma}^{\text{dev}})$:

$$I_2(\underline{\sigma}^{\text{dev}}) = \frac{1}{2} \underline{\sigma}^{\text{dev}} : \underline{\sigma}^{\text{dev}} \quad (1.23)$$

For the sake of comparison, it is useful to obtain a criterion that is comparable with a uniaxial stress. Invariant J_2 is defined for this purpose:

$$J_2(\underline{\sigma}) = \sqrt{3I_2(\underline{\sigma}^{\text{dev}})} = \sqrt{\frac{3}{2} \underline{\sigma}^{\text{dev}} : \underline{\sigma}^{\text{dev}}} \quad (1.24)$$

The *von Mises* yield function (J_2 -plasticity) then reads as follows:

$$f(\underline{\sigma}) = J_2(\underline{\sigma}) - R_0 \quad (1.25)$$

Finally, the multiaxial *von Mises* yield function accounting for linear kinematic and isotropic hardening is expressed this way:

$$f(\underline{\sigma}, \underline{X}, R) = J_2(\underline{\sigma} - \underline{X}) - R - R_0 = \sqrt{\frac{3}{2} (\underline{\sigma}^{\text{dev}} - \underline{X}) : (\underline{\sigma}^{\text{dev}} - \underline{X})} - R - R_0 \quad (1.26)$$

with \underline{X} tensor accounting for kinematic hardening and R scalar for isotropic hardening.

1.4 Additivity

Throughout this work we will consider the following quantities to be additive, meaning also that their effective values can be determined by spatial average:

- Lengths, surfaces and volumes
- Thermal dissipation and associated heat flux and temperature fields
- Elastic energy and associated strain, stress, forces and displacement fields

2 Homogenization

To live effectively is to live with adequate information.

— Norbert Wiener, *The Human Use of Human Beings: Cybernetics and Society* (1954)

2.1 Representative volume element

Many definitions of what is a representative volume element (RVE) have been formulated for the past 50 years. A partial review on those can be found in [Gitman et al., 2007]. The classical definition of RVE is usually attributed to [Hill, 1963]. He stated that for a given material the RVE is a sample that is structurally typical of the whole microstructure, *i.e.* containing a sufficient number of heterogeneities for the macroscopic moduli to be independent of the boundary values of traction and displacement.

Later, [Beran, 1968] emphasized the role of statistical homogeneity, as defined in Section 4.2.3, especially in a volume-averaged sense. This also meant that the characteristic RVE size considered should be larger than a certain microstructural length for which moduli fluctuate.

[Hashin, 1983] made a review on analysis of composite materials, and referred to statistical homogeneity as a practical necessity. In the same article he proposed a scale separation principle formalized as follows: $\text{MICRO} \ll \text{MINI} \ll \text{MACRO}$, MICRO being the scale of microstructural heterogeneities, *e.g.* the size of a particle, a single crystal. MACRO is referring to the scale of the whole composite material, while MINI is the scale of the RVE, often called the mesoscale.

[Sab, 1992] considered that the classical RVE definition for a heterogeneous medium holds only if the homogenized moduli tend towards those of a similar periodic medium. This entails that the response over a RVE should be independent of boundary conditions. The ergodicity hypothesis (*cf.* Section 4.2.1) was stated by [Ostoja-Starzewski, 2002] as a requisite for the definition of the RVE, as well as statistical homogeneity. The author considers the RVE to be only definable over

Chapter 2. Homogenization

a periodic unit-cell or a non-periodic cell containing an infinite number of heterogeneities.

[Drugan and Willis, 1996] introduced explicitly the idea of minimizing the RVE size, meaning that the RVE would be the smallest material volume for which the apparent and effective properties coincide. Using the ergodicity hypothesis, [Kanit et al., 2003] proposed a method to compute that minimal RVE size for a given property Z , a given contrast of properties and a given precision in the estimate of effective properties.

Many definitions refer to the separation of scales as a necessary condition for the existence of a RVE. This condition is not always met, *i.e.* with percolating media or materials with microstructural gradient of properties. This separation of scale involves a comparison between different characteristic lengths:

- d , size of microstructural heterogeneities;
- l , size of the RVE considered;
- L , characteristic length of the applied load.

Previous considerations regarding characteristic lengths can be summarized as follow:

$$d \ll l \ll L \tag{2.1}$$

Nevertheless, Inequality 2.1 is a necessary but not sufficient condition for the applicability of homogenization. As a matter of fact, uniform loading, *i.e.* $l \ll L$, has to be enforced. Let us consider a measurable property, such as a mechanical strain field. The spatial average of its measured value over a finite volume V converges towards the mathematical expectation of its measured value over a series of samples smaller than V (ensemble average). It is the ergodicity hypothesis. Moreover, ergodicity implies that one sample (or realization) of volume $V \geq V_{\text{RVE}}$ contains all the statistical information necessary for the description of its microstructure. Also, this entails that heterogeneities are small enough in comparison to the RVE size, *i.e.* $d \ll l$. If and only if these two conditions are met ($d \ll l$ and $l \ll L$), the existence and uniqueness of an equivalent homogeneous medium for both cases of random and periodic materials can be rigorously proved [Sab, 1992]. Homogenization is therefore possible.

Besides, it is worth noticing that within one medium the RVE size for thermal conductivity is *a priori* different from the RVE size for elastic moduli. Thus, one has to consider a RVE that depends on the specific investigated property.

In this work, we adopt a restrictive, yet rigorous, definition for the RVE grounded on statistical arguments. We will ensure that the separability of scales is met and that the ergodicity and stationarity hypotheses are fulfilled for the materials studied. The definition of [Sab, 1992] is also taken into account: effective properties should be independent of boundary conditions. For the case of random media, RVE sizes are determined for mechanical and thermal properties based

on finite elements simulations. The statistical method for determining RVE sizes proposed in [Kanit et al., 2003] is presented in Section 4.2 and implemented in Section 6.5.

2.2 Averaging relations

In this chapter, voids and rigid inclusions are excluded for simplicity of presentation. In this work, we will however have to deal with porous media in both Parts II and III. The relations given hereafter will then be reconsidered to fit the studied problems.

2.2.1 Averaging thermal fields

Let us define a certain volume of interest $V \in \Omega$ and its boundary ∂V . In order to homogenize thermal properties, one has to consider the spatial average over V of the gradient of temperature ∇T :

$$\begin{aligned}
 \langle \nabla T \rangle &= \frac{1}{V} \int_V \nabla T dV = \frac{1}{V} \int_V T_{,i} dV \underline{e}_i \\
 &= \frac{1}{V} \int_{\partial V} T n_i dS \underline{e}_i \\
 &= \frac{1}{V} \int_{\partial V} T \underline{n} dS
 \end{aligned} \tag{2.2}$$

If one considers now the spatial average over V of a balanced steady-state heat flux vector \underline{q}^* , i.e. $\text{Div} \underline{q}^* = 0$ in V , it yields:

$$\begin{aligned}
 \langle \underline{q}^* \rangle &= \frac{1}{V} \int_V \underline{q}^* dV = \frac{1}{V} \int_V q_i^* dV \underline{e}_i \\
 &= \frac{1}{V} \int_V (q_j^* x_i)_{,j} dV \underline{e}_i \\
 &= \frac{1}{V} \int_{\partial V} q_j^* n_j x_i dS \underline{e}_i \\
 &= \frac{1}{V} \int_{\partial V} (\underline{q}^* \cdot \underline{n}) \underline{x} dS
 \end{aligned} \tag{2.3}$$

Finally, let us consider the thermal dissipation rate density \mathcal{D}^{th} that arises from the fields \underline{q}^* and

∇T for a reference temperature T_0 (linearized theory):

$$\begin{aligned}
 T_0 \mathcal{D}^{\text{th}} &= \langle -\underline{\mathbf{q}}^* \cdot \nabla T \rangle \\
 &= \frac{1}{V} \int_V -\underline{\mathbf{q}}^* \cdot \nabla T dV \\
 &= \frac{1}{V} \int_V -q_i^* T_{,i} dV \\
 &= \frac{1}{V} \int_V -(q_i^* T)_{,i} dV \\
 &= \frac{1}{V} \int_{\partial V} -q_i^* n_i T dS \\
 &= \frac{1}{V} \int_{\partial V} -T \underline{\mathbf{q}}^* \cdot \underline{\mathbf{n}} dS
 \end{aligned} \tag{2.4}$$

2.2.2 Averaging mechanical fields

Thus, in the context of continuum mechanics, if one considers the spatial average of a kinematically compatible strain field $\underline{\boldsymbol{\varepsilon}}'$ which is defined as the symmetric part of the gradient of the displacement field $\underline{\mathbf{u}}'$:

$$\begin{aligned}
 \langle \underline{\boldsymbol{\varepsilon}}' \rangle &= \frac{1}{V} \int_V \underline{\boldsymbol{\varepsilon}}' dV = \frac{1}{V} \int_V u'_{(i,j)} dV \underline{\mathbf{e}}_i \otimes \underline{\mathbf{e}}_j \\
 &= \frac{1}{V} \int_{\partial V} u'_{(i} n_j) dS \underline{\mathbf{e}}_i \otimes \underline{\mathbf{e}}_j \\
 &= \frac{1}{V} \int_{\partial V} \underline{\mathbf{u}}' \overset{s}{\otimes} \underline{\mathbf{n}} dS
 \end{aligned} \tag{2.5}$$

with $\underline{\mathbf{u}}' \overset{s}{\otimes} \underline{\mathbf{n}}$ and $u'_{(i,j)}$ denoting the symmetric part of the resulting tensor. If one considers now the spatial average of a statically admissible stress field $\underline{\boldsymbol{\sigma}}^*$, i.e. $\underline{\text{Div}} \underline{\boldsymbol{\sigma}}^* = \underline{\mathbf{0}}$ in V , it yields:

$$\begin{aligned}
 \langle \underline{\boldsymbol{\sigma}}^* \rangle &= \frac{1}{V} \int_V \underline{\boldsymbol{\sigma}}^* dV = \frac{1}{V} \int_V \sigma_{ij}^* dV \underline{\mathbf{e}}_i \otimes \underline{\mathbf{e}}_j \\
 &= \frac{1}{V} \int_V \sigma^*_{(ik} \delta_{j)k} dV \underline{\mathbf{e}}_i \otimes \underline{\mathbf{e}}_j \\
 &= \frac{1}{V} \int_V \sigma^*_{(ik} x_{j),k} dV \underline{\mathbf{e}}_i \otimes \underline{\mathbf{e}}_j \\
 &= \frac{1}{V} \int_{\partial V} \sigma^*_{(ik} n_k x_j) dS \underline{\mathbf{e}}_i \otimes \underline{\mathbf{e}}_j \\
 &= \frac{1}{V} \int_{\partial V} (\underline{\boldsymbol{\sigma}}^* \cdot \underline{\mathbf{n}}) \overset{s}{\otimes} \underline{\mathbf{x}} dS
 \end{aligned} \tag{2.6}$$

From these averaging relations, we can define the elastic strain energy density \mathcal{E}^{el} such that,

$$\begin{aligned}
 2\mathcal{E}^{\text{el}} &= \langle \underline{\boldsymbol{\sigma}}^* : \underline{\boldsymbol{\varepsilon}}' \rangle \\
 &= \frac{1}{V} \int_V \underline{\boldsymbol{\sigma}}^* : \underline{\boldsymbol{\varepsilon}}' dV \\
 &= \frac{1}{V} \int_V \sigma_{ij}^* u'_{(i,j)} dV \\
 &= \frac{1}{V} \int_V (\sigma^*_{ij} u'_i)_{,j} dV \\
 &= \frac{1}{V} \int_{\partial V} \sigma^*_{ij} n_j u'_i dS \\
 &= \frac{1}{V} \int_{\partial V} (\underline{\boldsymbol{\sigma}}^* \cdot \underline{\mathbf{n}}) \cdot \underline{\mathbf{u}}' dS
 \end{aligned} \tag{2.7}$$

2.3 Boundary conditions

2.3.1 Thermal behavior

It is necessary to prescribe values at the boundary of the domain of interest in order to solve the thermal constitutive equations. Let us consider a volume V , its boundary ∂V and three types of boundary conditions:

Uniform temperature gradient boundary conditions – UTG

Temperature T is prescribed for any material point $\underline{\mathbf{x}}$ on ∂V such that,

$$T = \underline{\mathbf{G}} \cdot \underline{\mathbf{x}} \quad \forall \underline{\mathbf{x}} \in \partial V \tag{2.8}$$

with $\underline{\mathbf{G}}$ macroscopic temperature gradient, independent of $\underline{\mathbf{x}}$. Then,

$$\langle \nabla T \rangle = \frac{1}{V} \int_V \nabla T dV = \underline{\mathbf{G}} \tag{2.9}$$

The macroscopic heat flux density vector can be defined as the spatial average of the local heat flux density field:

$$\underline{\mathbf{Q}} \hat{=} \langle \underline{\mathbf{q}} \rangle = \frac{1}{V} \int_V \underline{\mathbf{q}} dV \tag{2.10}$$

Chapter 2. Homogenization

Uniform heat flux boundary conditions – UHF

Heat flux density \underline{q} is prescribed for any material point \underline{x} on ∂V such that,

$$\underline{q} \cdot \underline{n} = \underline{Q} \cdot \underline{n}(\underline{x}) \quad \forall \underline{x} \in \partial V \quad (2.11)$$

with \underline{Q} macroscopic heat flux density vector, independent of \underline{x} . Then,

$$\langle \underline{q} \rangle = \frac{1}{V} \int_V \underline{q} dV = \underline{Q} \quad (2.12)$$

The macroscopic temperature gradient can be defined as the spatial average of the local temperature gradient field:

$$\underline{G} \triangleq \langle \nabla T \rangle = \frac{1}{V} \int_V \nabla T dV \quad (2.13)$$

Periodic thermal boundary conditions – PTBC

The volume V is considered periodic when it is possible to fill the space by duplicating and translating this volume. This volume can then be considered as a periodic unit-cell. Temperature T can be dissociated into a macroscopic temperature given by the macroscopic temperature gradient \underline{G} and a periodic fluctuation field for any material point \underline{x} of V , such that:

$$T = \underline{G} \cdot \underline{x} + \vartheta \quad \forall \underline{x} \in V \quad (2.14)$$

with ϑ temperature periodic fluctuation, *i.e.* taking the same value on two homologous points \underline{x}^+ and \underline{x}^- of ∂V . Moreover, the heat flux vector \underline{q} must be anti-periodic so that,

$$\underline{q}^+ \cdot \underline{n}^+ + \underline{q}^- \cdot \underline{n}^- = 0 \quad (2.15)$$

$$\vartheta^+ - \vartheta^- = 0 \quad (2.16)$$

Periodicity is denoted by # while anti-periodicity is denoted by -#.

2.3.2 Mechanical behavior

As for the thermal case, it is necessary to set boundary conditions to the volume V considered in order to solve the constitutive equations in the case of statics. Let us consider three types of boundary conditions:

Kinematic uniform boundary conditions – KUBC

Displacement $\underline{\mathbf{u}}$ is prescribed for any material point $\underline{\mathbf{x}}$ on the boundary ∂V such that,

$$\underline{\mathbf{u}} = \underline{\mathbf{E}} \cdot \underline{\mathbf{x}} \quad \forall \underline{\mathbf{x}} \in \partial V \quad (2.17)$$

with $\underline{\mathbf{E}}$ second-order macroscopic strain tensor, which is symmetric and independent of $\underline{\mathbf{x}}$. It follows from Equation 2.17:

$$\langle \underline{\boldsymbol{\varepsilon}} \rangle = \frac{1}{V} \int_V \underline{\boldsymbol{\varepsilon}} dV = \underline{\mathbf{E}} \quad (2.18)$$

The macroscopic stress tensor is then defined as the spatial average of the local stress field:

$$\underline{\boldsymbol{\Sigma}} \hat{=} \langle \underline{\boldsymbol{\sigma}} \rangle = \frac{1}{V} \int_V \underline{\boldsymbol{\sigma}} dV \quad (2.19)$$

Static uniform boundary conditions – SUBC

Traction $\underline{\mathbf{t}}$ is prescribed for any material point $\underline{\mathbf{x}}$ on ∂V such that,

$$\underline{\mathbf{t}} = \underline{\boldsymbol{\Sigma}} \cdot \underline{\mathbf{n}} \quad \forall \underline{\mathbf{x}} \in \partial V \quad (2.20)$$

with $\underline{\boldsymbol{\Sigma}}$ second-order macroscopic stress tensor, which is symmetric and independent of $\underline{\mathbf{x}}$. It follows from Equation 2.20:

$$\langle \underline{\boldsymbol{\sigma}} \rangle = \frac{1}{V} \int_V \underline{\boldsymbol{\sigma}} dV = \underline{\boldsymbol{\Sigma}} \quad (2.21)$$

The macroscopic strain tensor is then defined as the spatial average of the local strain field:

$$\underline{\mathbf{E}} \hat{=} \langle \underline{\boldsymbol{\varepsilon}} \rangle = \frac{1}{V} \int_V \underline{\boldsymbol{\varepsilon}} dV \quad (2.22)$$

Periodic boundary conditions – PBC

For PBC, the displacement field $\underline{\mathbf{u}}$ can be dissociated into a part given by the macroscopic strain tensor $\underline{\mathbf{E}}$ and a periodic fluctuation field for any material point $\underline{\mathbf{x}}$ of V , such that:

$$\underline{\mathbf{u}} = \underline{\mathbf{E}} \cdot \underline{\mathbf{x}} + \underline{\mathbf{v}} \quad \forall \underline{\mathbf{x}} \in V \quad (2.23)$$

with $\underline{\mathbf{v}}$ the periodic fluctuations vector, *i.e.* taking the same value on two homologous points $\underline{\mathbf{x}}^+$ and $\underline{\mathbf{x}}^-$ of ∂V . Furthermore, the traction vector $\underline{\mathbf{t}} = \underline{\boldsymbol{\sigma}} \cdot \underline{\mathbf{n}}$ fulfills anti-periodic conditions such

that,

$$\underline{\sigma}^+ \cdot \underline{n}^+ + \underline{\sigma}^- \cdot \underline{n}^- = \underline{\mathbf{0}} \quad (2.24)$$

$$\underline{v}^+ - \underline{v}^- = \underline{\mathbf{0}} \quad (2.25)$$

A dual approach exists; it consists in prescribing a macroscopic stress to the cell. However we do not develop this approach here, *cf.* [Michel et al., 1999] for details.

2.3.3 Hill–Mandel condition

Thermal behavior

Let us consider a volume V with two independent local fields $\nabla T'$ and \underline{q}^* . If \underline{q}^* verifies UHF, or $\nabla T'$ verifies UGT, or if \underline{q}^* and $\nabla T'$ verify simultaneously PTBC, then:

$$\langle -\underline{q}^* \cdot \nabla T' \rangle = \langle \underline{q}^* \rangle \cdot \langle -\nabla T' \rangle \quad (2.26)$$

Thus, one obtains the following equivalence for the three types of boundary conditions:

$$\langle -\underline{q} \cdot \nabla T \rangle = \langle \underline{q} \rangle \cdot \langle -\nabla T \rangle \quad (2.27)$$

which corresponds to the *Hill* macrohomogeneity condition [Hill, 1967] applied to the thermal problem. This ensures that the thermal dissipation rate density at the microscale is preserved while scaling up to the macroscopic level.

Mechanical behavior

Let us consider a volume V with two independent local fields $\underline{\epsilon}'$ and $\underline{\sigma}^*$ such that $\underline{\epsilon}'$ is kinematically compatible and $\underline{\sigma}^*$ is statically admissible. If $\underline{\sigma}^*$ verifies SUBC, or $\underline{\epsilon}'$ verifies KUBC, or if $\underline{\sigma}^*$ and $\underline{\epsilon}'$ verify simultaneously the periodic boundary conditions, then:

$$\langle \underline{\sigma}^* : \underline{\epsilon}' \rangle = \langle \underline{\sigma}^* \rangle : \langle \underline{\epsilon}' \rangle \quad (2.28)$$

Thus, one obtains the following equivalence for the three types of boundary conditions:

$$\langle \underline{\sigma} : \underline{\epsilon} \rangle = \langle \underline{\sigma} \rangle : \langle \underline{\epsilon} \rangle \quad (2.29)$$

which corresponds to the *Hill* macrohomogeneity condition [Hill, 1967]. This ensures that the mechanical work density at the microscale is preserved while scaling up to the macroscopic level.

2.4 Effective properties vs. apparent properties

When determining the properties of the volume V smaller than the RVE, apparent properties are considered. The apparent properties converge towards the effective properties once $V \geq V_{\text{RVE}}$.

2.4.1 Linear conductivity

The thermal problem admits a unique solution, up to a temperature offset, for the UHF and PTBC problems. One can define two second-order concentration tensors $\underline{\Phi}$ and $\underline{\Psi}$ accounting respectively for the temperature gradient localization (UTG problem) and the heat flux concentration (UHF problem), such that,

$$\nabla T(\underline{x}) = \underline{\Phi}(\underline{x}) \cdot \underline{G} \quad \forall \underline{x} \in V \text{ and } \forall \underline{G} \quad (2.30)$$

and

$$\underline{q}(\underline{x}) = \underline{\Psi}(\underline{x}) \cdot \underline{Q} \quad \forall \underline{x} \in V \text{ and } \forall \underline{Q} \quad (2.31)$$

such that,

$$\langle \underline{\Phi} \rangle = \langle \underline{\Psi} \rangle = \underline{I} \quad (2.32)$$

Let us consider the conductivity $\underline{\lambda}(\underline{x})$ and the resistivity $\underline{\rho}(\underline{x})$, then:

$$\underline{q}(\underline{x}) = -\underline{\lambda}(\underline{x}) \cdot \nabla T(\underline{x}) \quad \forall \underline{x} \in V \quad (2.33)$$

and

$$-\nabla T(\underline{x}) = \underline{\rho}(\underline{x}) \cdot \underline{q}(\underline{x}) \quad \forall \underline{x} \in V \quad (2.34)$$

Thus,

$$\underline{Q} = \langle \underline{q} \rangle = \langle -\underline{\lambda} \cdot \nabla T \rangle = \langle -\underline{\lambda} \cdot \underline{\Psi} \cdot \underline{G} \rangle = \langle -\underline{\lambda} \cdot \underline{\Psi} \rangle \cdot \underline{G} \quad (2.35)$$

and

$$\underline{G} = \langle \nabla T \rangle = \langle -\underline{\rho} \cdot \underline{q} \rangle = \langle -\underline{\rho} \cdot \underline{\Phi} \cdot \underline{Q} \rangle = \langle -\underline{\rho} \cdot \underline{\Phi} \rangle \cdot \underline{Q} \quad (2.36)$$

Let us then define $\underline{\Lambda}_G^{\text{app}}$ and $\underline{P}_Q^{\text{app}}$, second-order symmetric tensors respectively accounting for the apparent thermal conductivity and resistivity for an elementary volume V of the considered material so that,

$$\underline{\Lambda}_G^{\text{app}} = \langle \underline{\lambda} \cdot \underline{\Phi} \rangle \quad (2.37)$$

$$\underline{\underline{P}}_Q^{\text{app}} = \langle \underline{\underline{\rho}} \cdot \underline{\underline{\Psi}} \rangle \quad (2.38)$$

These equations highlight the fact that homogenized properties are generally not obtained by a simple mixture rule.

Also, one can define the apparent properties in the linear case from the thermal dissipation rate density \mathcal{D}^{th} for a given temperature T_0 :

$$T_0 \mathcal{D}^{th} = \langle -\underline{\underline{q}} \cdot \nabla T \rangle = \langle \nabla T \cdot \underline{\underline{\lambda}} \cdot \nabla T \rangle = \underline{\underline{G}} \cdot \langle \underline{\underline{\Phi}}^T \cdot \underline{\underline{\lambda}} \cdot \underline{\underline{\Phi}} \rangle \cdot \underline{\underline{G}} \quad (2.39)$$

and

$$T_0 \mathcal{D}^{th} = \langle -\underline{\underline{q}} \cdot \nabla T \rangle = \langle \underline{\underline{q}} \cdot \underline{\underline{\rho}} \cdot \underline{\underline{q}} \rangle = \underline{\underline{Q}} \cdot \langle \underline{\underline{\Psi}}^T \cdot \underline{\underline{\rho}} \cdot \underline{\underline{\Psi}} \rangle \cdot \underline{\underline{Q}} \quad (2.40)$$

$\underline{\underline{x}}^T$ denotes transposition of tensor $\underline{\underline{x}}$. This way, we obtain a new definition of the apparent thermal conductivity and resistivity:

$$\underline{\underline{\Lambda}}_G^{\text{app}} = \langle \underline{\underline{\Phi}}^T \cdot \underline{\underline{\lambda}} \cdot \underline{\underline{\Phi}} \rangle \quad (2.41)$$

and

$$\underline{\underline{P}}_Q^{\text{app}} = \langle \underline{\underline{\Psi}}^T \cdot \underline{\underline{\rho}} \cdot \underline{\underline{\Psi}} \rangle \quad (2.42)$$

This new definition justifies the symmetric nature of the apparent thermal conductivity and resistivity tensors. It can be shown using the *Hill–Mandel* lemma that the results of Equations 2.37 and 2.41 provide the same effective moduli. If one considers $V \geq V_{\text{RVE}}$, the apparent thermal conductivity and resistivity will converge towards the effective thermal properties.

2.4.2 Linear elasticity

As for the thermal problem, the micromechanical linear elastic problem admits a unique solution, up to a rigid body displacement for SUBC and a periodic translation for PBC. Let us consider two fourth-order tensors $\underline{\underline{A}}$ and $\underline{\underline{B}}$ accounting respectively for strain localization and for stress concentration:

$$\underline{\underline{\epsilon}}(\underline{\underline{x}}) = \underline{\underline{A}}(\underline{\underline{x}}) : \underline{\underline{E}} \quad \forall \underline{\underline{x}} \in V \text{ and } \forall \underline{\underline{E}} \quad (2.43)$$

and

$$\underline{\underline{\sigma}}(\underline{\underline{x}}) = \underline{\underline{B}}(\underline{\underline{x}}) : \underline{\underline{\Sigma}} \quad \forall \underline{\underline{x}} \in V \text{ and } \forall \underline{\underline{\Sigma}} \quad (2.44)$$

2.4. Effective properties vs. apparent properties

such that,

$$\langle \underline{\mathbf{A}} \rangle = \langle \underline{\mathbf{B}} \rangle = \underline{\mathbf{I}} \quad (2.45)$$

Let us consider the elastic moduli $\underline{\mathbf{c}}(\underline{\mathbf{x}})$ and the compliances $\underline{\mathbf{s}}(\underline{\mathbf{x}})$, then:

$$\underline{\boldsymbol{\sigma}}(\underline{\mathbf{x}}) = \underline{\mathbf{c}}(\underline{\mathbf{x}}) : \underline{\boldsymbol{\epsilon}}(\underline{\mathbf{x}}) \quad \forall \underline{\mathbf{x}} \in V \quad (2.46)$$

and

$$\underline{\boldsymbol{\epsilon}}(\underline{\mathbf{x}}) = \underline{\mathbf{s}}(\underline{\mathbf{x}}) : \underline{\boldsymbol{\sigma}}(\underline{\mathbf{x}}) \quad \forall \underline{\mathbf{x}} \in V \quad (2.47)$$

Thus,

$$\underline{\boldsymbol{\Sigma}} = \langle \underline{\boldsymbol{\sigma}} \rangle = \langle \underline{\mathbf{C}} : \underline{\boldsymbol{\epsilon}} \rangle = \langle \underline{\mathbf{c}} : \underline{\mathbf{A}} : \underline{\mathbf{E}} \rangle = \langle \underline{\mathbf{c}} : \underline{\mathbf{A}} \rangle : \underline{\mathbf{E}} \quad (2.48)$$

and

$$\underline{\mathbf{E}} = \langle \underline{\boldsymbol{\epsilon}} \rangle = \langle \underline{\mathbf{S}} : \underline{\boldsymbol{\sigma}} \rangle = \langle \underline{\mathbf{s}} : \underline{\mathbf{B}} : \underline{\boldsymbol{\Sigma}} \rangle = \langle \underline{\mathbf{s}} : \underline{\mathbf{B}} \rangle : \underline{\boldsymbol{\Sigma}} \quad (2.49)$$

We can define $\underline{\mathbf{C}}_{\underline{\mathbf{E}}}^{\text{app}}$ and $\underline{\mathbf{S}}_{\underline{\boldsymbol{\Sigma}}}^{\text{app}}$, fourth-order symmetric tensors, accounting respectively for the apparent elastic moduli and compliance of the volume V considered such that,

$$\underline{\mathbf{C}}_{\underline{\mathbf{E}}}^{\text{app}} = \langle \underline{\mathbf{c}} : \underline{\mathbf{A}} \rangle \quad (2.50)$$

and

$$\underline{\mathbf{S}}_{\underline{\boldsymbol{\Sigma}}}^{\text{app}} = \langle \underline{\mathbf{s}} : \underline{\mathbf{B}} \rangle \quad (2.51)$$

As for the thermal case, these equations show that homogenized properties are not usually obtained by a simple mixing rule.

Also, one can define the apparent properties from the elastic strain energy density \mathcal{E}^{el} :

$$\mathcal{E}^{el} = \frac{1}{2} \langle \underline{\boldsymbol{\sigma}} : \underline{\boldsymbol{\epsilon}} \rangle = \frac{1}{2} \langle \underline{\boldsymbol{\epsilon}} : \underline{\mathbf{c}} : \underline{\boldsymbol{\epsilon}} \rangle = \frac{1}{2} \underline{\mathbf{E}} : \langle \underline{\mathbf{A}}^T : \underline{\mathbf{c}} : \underline{\mathbf{A}} \rangle : \underline{\mathbf{E}} \quad (2.52)$$

and

$$\mathcal{E}^{el} = \frac{1}{2} \langle \underline{\boldsymbol{\sigma}} : \underline{\boldsymbol{\epsilon}} \rangle = \frac{1}{2} \langle \underline{\boldsymbol{\sigma}} : \underline{\mathbf{s}} : \underline{\boldsymbol{\sigma}} \rangle = \frac{1}{2} \underline{\boldsymbol{\Sigma}} : \langle \underline{\mathbf{B}}^T : \underline{\mathbf{s}} : \underline{\mathbf{B}} \rangle : \underline{\boldsymbol{\Sigma}} \quad (2.53)$$

This way, we obtain a new definition of the apparent elastic moduli and compliance:

$$\underline{\mathbf{C}}_{\underline{\mathbf{E}}}^{\text{app}} = \langle \underline{\mathbf{A}}^T : \underline{\mathbf{c}} : \underline{\mathbf{A}} \rangle \quad (2.54)$$

Chapter 2. Homogenization

and

$$\underset{\approx}{\mathbf{S}}_{\Sigma}^{\text{app}} = \langle \underset{\approx}{\mathbf{B}}^T : \underset{\approx}{\mathbf{s}} : \underset{\approx}{\mathbf{B}} \rangle \quad (2.55)$$

This new definition justifies the symmetric nature of the apparent elastic moduli and compliance tensors. By applying the *Hill–Mandel* lemma (*cf.* Section 2.3.3) one can prove the equivalence between direct and energetic definitions [Sanchez-Palencia and Zaoui, 1987].

According to [Sab, 1992], for an elementary volume V large enough ($V > V_{\text{RVE}}$), the apparent properties do not depend on the boundary conditions and match with the effective properties of the considered material, then:

$$\underset{\approx}{\mathbf{C}}_{\Sigma}^{\text{app}} = \underset{\approx}{\mathbf{S}}_{\Sigma}^{\text{app}-1} = \underset{\approx}{\mathbf{C}}_E^{\text{app}} = \underset{\approx}{\mathbf{S}}_E^{\text{app}-1} = \underset{\approx}{\mathbf{C}}^{\text{eff}} = \underset{\approx}{\mathbf{S}}^{\text{eff}-1} \quad (2.56)$$

For volumes ($V \geq V_{\text{RVE}}$), based on energetic considerations and the subadditivity property of the effective elastic moduli tensor, [Huet, 1990] proposed the so-called partition theorem. The effective properties can be bounded by the following inequalities:

$$\underset{\approx}{\mathbf{C}}_{\Sigma}^{\text{app}} \leq \underset{\approx}{\mathbf{C}}^{\text{eff}} \leq \underset{\approx}{\mathbf{C}}_E^{\text{app}} \quad (2.57)$$

$$\underset{\approx}{\mathbf{S}}_E^{\text{app}} \leq \underset{\approx}{\mathbf{S}}^{\text{eff}} \leq \underset{\approx}{\mathbf{S}}_{\Sigma}^{\text{app}} \quad (2.58)$$

These inequalities have to be considered in a quadratic form sense. For elementary volumes smaller than the RVE, using the same arguments but for partitions of different sizes, [Huet, 1990] derived hierarchical inequalities regarding apparent and effective properties. Coarse and fine partitions are considered and their respective statistical apparent properties are denoted by indices c and f :

$$\underset{\approx}{\mathbf{C}}^{\text{Reuss}} \leq \underset{\approx}{\mathbf{C}}_{\Sigma f}^{\text{app}} \leq \underset{\approx}{\mathbf{C}}_{\Sigma c}^{\text{app}} \leq \underset{\approx}{\mathbf{C}}^{\text{eff}} \leq \underset{\approx}{\mathbf{C}}_{Ec}^{\text{app}} \leq \underset{\approx}{\mathbf{C}}_{Ef}^{\text{app}} \leq \underset{\approx}{\mathbf{C}}^{\text{Voigt}} \quad (2.59)$$

$$\underset{\approx}{\mathbf{S}}^{\text{Voigt}} \leq \underset{\approx}{\mathbf{S}}_{Ef}^{\text{app}} \leq \underset{\approx}{\mathbf{S}}_{Ec}^{\text{app}} \leq \underset{\approx}{\mathbf{S}}^{\text{eff}} \leq \underset{\approx}{\mathbf{S}}_{\Sigma c}^{\text{app}} \leq \underset{\approx}{\mathbf{S}}_{\Sigma f}^{\text{app}} \leq \underset{\approx}{\mathbf{S}}^{\text{Reuss}} \quad (2.60)$$

$\underset{\approx}{\mathbf{C}}^{\text{Voigt}}$, $\underset{\approx}{\mathbf{S}}^{\text{Voigt}}$, $\underset{\approx}{\mathbf{C}}^{\text{Reuss}}$ and $\underset{\approx}{\mathbf{S}}^{\text{Reuss}}$ refer to the classical *Voigt* and *Reuss* bounds that are introduced in Section 3.4.2. The inequalities presented above can be used for verification of computational homogenization results, as it was done for instance in [Kanit et al., 2003, Kanit et al., 2006] for elastic and thermal properties. Moreover, the bounds $\underset{\approx}{\mathbf{C}}_{\Sigma}^{\text{app}}$ and $\underset{\approx}{\mathbf{C}}_E^{\text{app}}$ are usually far apart when the contrast of properties between phases is large. If the microstructure features a matrix phase, tighter bounds can be obtained by choosing elementary volumes including only the matrix at the boundary, as shown in [Salmi et al., 2012a, Salmi et al., 2012b].

2.5 Some boundary value problems for the estimation of isotropic effective properties

Boundary value problems are presented in this section for determining linear isotropic thermal and elastic properties: bulk modulus k , shear modulus μ and conductivity λ .

2.5.1 Thermal properties

In order to solve the thermal conduction problem, one can prescribe $\underline{\mathbf{G}}$ or $\underline{\mathbf{Q}}$ tensors by means of PTBC, UTG or UHF.

Thermal conductivity

For determining an apparent thermal conductivity λ^{app} over V , let us apply the following macroscopic gradient of temperature in order to solve the thermal UTG problem:

$$\underline{\mathbf{G}}_{\lambda} = \begin{bmatrix} \frac{1}{3} \\ \frac{1}{3} \\ \frac{1}{3} \end{bmatrix} \quad (2.61)$$

An apparent thermal conductivity λ^{app} can be defined from the thermal dissipation rate density using the macroscopic temperature gradient given by Equation 2.61 as follows:

$$\lambda^{\text{app}} \triangleq 3T_0 \mathcal{D}^{th}(\underline{\mathbf{G}}_{\lambda}) = 3\langle -\underline{\mathbf{q}} \cdot \nabla T \rangle = 3\langle \underline{\mathbf{q}} \rangle \cdot \langle -\nabla T \rangle = -3\underline{\mathbf{Q}} \cdot \underline{\mathbf{G}}_{\lambda} \quad (2.62)$$

$$= -(Q_1 + Q_2 + Q_3) \quad (2.63)$$

λ^{app} can be regarded as an estimate of λ^{eff} . Conversely the apparent thermal resistivity can be obtained from solving the thermal UHF problem. Let us apply the following macroscopic heat flux:

$$\underline{\mathbf{Q}}_{\rho} = \begin{bmatrix} \frac{1}{3} \\ \frac{1}{3} \\ \frac{1}{3} \end{bmatrix} \quad (2.64)$$

The apparent thermal resistivity ρ^{app} can be defined the same way using the macroscopic heat flux given in Equation 2.64 as follows:

$$\rho^{\text{app}} \triangleq 3T_0 \mathcal{D}^{th}(\underline{\mathbf{Q}}_{\rho}) = 3\lambda^{\text{app}-1} = 3\langle -\underline{\mathbf{q}} \cdot \nabla T \rangle = 3\langle \underline{\mathbf{q}} \rangle \cdot \langle -\nabla T \rangle = -3\underline{\mathbf{Q}}_{\lambda} \cdot \underline{\mathbf{G}} \quad (2.65)$$

$$= -(G_1 + G_2 + G_3) \quad (2.66)$$

ρ^{app} can be regarded as an estimate of ρ^{eff} .

2.5.2 Elastic properties

Let us consider an elastic strain energy density over a volume V as defined in Equation 2.52. One can prescribe specific $\underline{\underline{E}}$ and $\underline{\underline{\Sigma}}$ tensors for PBC and respectively for KUBC and SUBC.

Bulk modulus

For determining an apparent bulk modulus k^{app} over V , let us apply the following macroscopic strain tensor in order to solve the micromechanical KUBC problem:

$$\underline{\underline{E}}_k = \begin{bmatrix} \frac{1}{3} & 0 & 0 \\ 0 & \frac{1}{3} & 0 \\ 0 & 0 & \frac{1}{3} \end{bmatrix} \quad (2.67)$$

An apparent bulk modulus k^{app} can be defined from the elastic strain energy density for the macroscopic strain given in Equation 2.67 using the *Hill–Mandel* lemma, such that:

$$k^{\text{app}} \hat{=} 2\mathcal{E}^{el}(\underline{\underline{E}}_k) = \langle \underline{\underline{\sigma}} : \underline{\underline{\epsilon}} \rangle = \langle \underline{\underline{\sigma}} \rangle : \langle \underline{\underline{\epsilon}} \rangle = \underline{\underline{\Sigma}} : \underline{\underline{E}}_k \quad (2.68)$$

$$= \frac{1}{3} \text{Tr} \underline{\underline{\Sigma}} \quad (2.69)$$

k^{app} can be regarded as an estimate of k^{eff} . Conversely an apparent bulk modulus can be obtained from solving the micromechanical SUBC problem using the following macroscopic stress tensor:

$$\underline{\underline{\Sigma}}_k = \begin{bmatrix} 1 & 0 & 0 \\ 0 & 1 & 0 \\ 0 & 0 & 1 \end{bmatrix} \quad (2.70)$$

Then, again using the elastic strain energy density:

$$k^{\text{app}-1} \hat{=} 2\mathcal{E}^{el}(\underline{\underline{\Sigma}}_k) = \langle \underline{\underline{\sigma}} : \underline{\underline{\epsilon}} \rangle = \langle \underline{\underline{\sigma}} \rangle : \langle \underline{\underline{\epsilon}} \rangle = \underline{\underline{\Sigma}}_k : \underline{\underline{E}} \quad (2.71)$$

$$= \text{Tr} \underline{\underline{E}} \quad (2.72)$$

2.5. Some boundary value problems for the estimation of isotropic effective properties

Shear modulus

We consider the shear modulus μ^{app} over V , let us apply the following macroscopic strain tensor in order to solve the micromechanical KUBC problem:

$$\underline{\underline{E}}_{\mu} = \begin{bmatrix} 0 & \frac{1}{2} & 0 \\ \frac{1}{2} & 0 & 0 \\ 0 & 0 & 0 \end{bmatrix} \quad (2.73)$$

An apparent shear modulus μ^{app} can be defined from the elastic strain energy density for the macroscopic strain given in Equation 2.73 using the *Hill–Mandel* lemma, such that:

$$\mu^{\text{app}} \hat{=} 2\mathcal{E}^{el}(\underline{\underline{E}}_{\mu}) = \langle \underline{\underline{\sigma}} : \underline{\underline{\varepsilon}} \rangle = \langle \underline{\underline{\sigma}} \rangle : \langle \underline{\underline{\varepsilon}} \rangle = \underline{\underline{\Sigma}} : \underline{\underline{E}}_{\mu} \quad (2.74)$$

$$= \Sigma_{12} \quad (2.75)$$

μ^{app} can be regarded as an estimate of μ^{eff} . Conversely we can obtain an apparent shear modulus from the SUBC problem using the following macroscopic stress tensor:

$$\underline{\underline{\Sigma}}_{\mu} = \begin{bmatrix} 0 & 1 & 0 \\ 1 & 0 & 0 \\ 0 & 0 & 0 \end{bmatrix} \quad (2.76)$$

Then, again using the elastic strain energy density:

$$\mu^{\text{app-1}} \hat{=} 2\mathcal{E}^{el}(\underline{\underline{\Sigma}}_{\mu}) = \langle \underline{\underline{\sigma}} : \underline{\underline{\varepsilon}} \rangle = \langle \underline{\underline{\sigma}} \rangle : \langle \underline{\underline{\varepsilon}} \rangle = \underline{\underline{\Sigma}}_{\mu} : \underline{\underline{E}} \quad (2.77)$$

$$= 2E_{12} \quad (2.78)$$

The shear and bulk moduli are material parameters related to isotropic elasticity, which is an idealization of reality. Thus, we will have to verify carefully the isotropy hypothesis when computing these quantities, this is discussed in Section 6.3.

3 Analytical estimates and bounds

Qu'il ne faut point tâcher de comprendre l'infini, mais seulement penser que tout ce en quoi nous ne trouvons aucunes bornes est indéfini.

— René Descartes, *Principes de la philosophie* (1644)

Analytical methods are available for estimating the properties of heterogeneous materials. They usually involve assumptions regarding the microstructure. In the field of mechanics, asymptotic expansions [Sanchez-Palencia, 1974, Bensoussan et al., 1978] and variational bounds [Hashin and Shtrikman, 1962b, Beran, 1968] are examples of analytical approaches. For a heterogeneous elastic material, homogenization consists in solving the micromechanical problem of localization (for a prescribed strain) or concentration (for a prescribed stress). Formally, this means solving an implicit integral *Lippmann–Schwinger*-type equation. That can be done numerically, or analytically using some assumptions. This is how estimates and bounds have been developed. This chapter was written based on the following textbooks: [Bornert et al., 2001, Torquato, 2001, Besson et al., 2001, Milton, 2002], as well as the graduate course *Modélisation du comportement des matériaux hétérogènes et composites* taught at ENSTA-ParisTech by Profs. Bornert and Brenner.

3.1 Analytical estimates for thermal properties

3.1.1 Maxwell Garnett's estimate

In his treatise [Maxwell, 1873], *J. C. Maxwell* gave an approximation for the effective thermal conductivity of a single spherical inclusion embedded within an infinite matrix. Based on this result, *Maxwell's* son *J. C. Maxwell Garnett* proposed a d -dimensional extension to n spherical inclusions of conductivity λ^i and volume fraction V_V^i within an infinite matrix of conductivity λ^m , by assuming no interaction between the inclusions (high dilution assumption)

[Maxwell Garnett, 1904]. Thus, by superposition of the contribution of each inclusion, it yields:

$$\frac{\lambda^{\text{MG}} - \lambda^m}{\lambda^{\text{MG}} + (d-1)\lambda^m} = V_V^i \left(\frac{\lambda^i - \lambda^m}{\lambda^i + (d-1)\lambda^m} \right) \quad (3.1)$$

which can be rewritten as follows for $d = 3$:

$$\lambda^{\text{MG}} = \lambda^m \frac{\lambda^i (1 + 2V_V^i) - \lambda^m (2V_V^i - 2)}{\lambda^m (2 + V_V^i) + \lambda^i (1 - V_V^i)} \quad (3.2)$$

Equation 3.1 can be generalized to n spherical inclusions with different conductivities λ^r such that:

$$\frac{\lambda^{\text{MG}} - \lambda^m}{\lambda^{\text{MG}} + (d-1)\lambda^m} = \sum_{r=1}^n V_V^r \left(\frac{\lambda^r - \lambda^m}{\lambda^r + (d-1)\lambda^m} \right) \quad (3.3)$$

and again, one can rewrite it as follows for $d = 3$:

$$\lambda^{\text{MG}} = \sum_{r=1}^n \lambda^m \frac{\lambda^r (1 + 2V_V^r) - \lambda^m (2V_V^r - 2)}{\lambda^m (2 + V_V^r) + \lambda^r (1 - V_V^r)} \quad (3.4)$$

Equation 3.1 and 3.2 actually coincide with the *Hashin–Shtrikman* optimal bounds that are introduced in Section 3.2.3. Since *Maxwell Garnett's* estimate is not accounting for interaction between particles, its validity is restricted to small volume fractions.

3.1.2 Bruggeman's self-consistent model

Bruggeman proposed in [Bruggeman, 1935] a self-consistent model for determining the effective conductivity λ^{SC} of a medium made of n spherical particles of different conductivities λ^r and volume fractions V_V^r :

$$\sum_{r=1}^n V_V^r \frac{\lambda^r - \lambda^{\text{SC}}}{\lambda^r + (d-1)\lambda^{\text{SC}}} = 0 \quad (3.5)$$

For the case of d -dimensional two-phase materials, the solution of Equation 3.5 reads as follows:

$$\lambda^{\text{SC}} = \frac{\alpha + \sqrt{\alpha^2 + 4(d-1)\lambda^1\lambda^2}}{2(d-1)} \quad (3.6)$$

with $\alpha = \lambda^1 (dV_V^1 - 1) + \lambda^2 (dV_V^2 - 1)$. The self-consistent equation was extended to the d -dimensional case of a dilute distribution of spherical inclusions of conductivity λ^i and volume fraction V_V^i within a matrix of conductivity λ^m :

$$\frac{V_V^i (\lambda^i - \lambda^{\text{SC}})}{d\lambda^{\text{SC}}} + \frac{(1 - V_V^i) (\lambda^m - \lambda^{\text{SC}})}{\lambda^m + (d-1)\lambda^{\text{SC}}} = 0 \quad (3.7)$$

Since all phases are treated equally with the self-consistent estimate, its use for highly contrasted composites is not recommended.

3.2 Analytical bounds for thermal properties

We will now focus on rigorous bounds that can be defined based on variational principles and statistical information about the morphology of the material. Effective properties are included in-between these bounds. An analytical bound of order k is considered optimal if its definition uses all the statistical data of order k available. We will consider n -phase materials although each bound will be specialized for two-phase materials.

3.2.1 Bounds of order 0

Considering that $\underline{\lambda}^2 > \underline{\lambda}^1$, bounds of order 0 correspond to the properties of each phase. The homogenized tensor of conductivity $\underline{\lambda}^H$ is then bounded by the conductivities of the most conductive phase $\underline{\lambda}^2$ and the least conductive phase $\underline{\lambda}^1$ as follows:

$$\underline{\lambda}^1 \leq \underline{\lambda}^H \leq \underline{\lambda}^2 \quad (3.8)$$

These inequalities have to be considered in the sense of quadratic forms. Such bounds do not take volume fraction into account. As a matter of fact, they are of limited interest since they do not give any useful estimate of the homogenized properties.

3.2.2 Bounds of order 1

If information about the volume fraction is available, one should use it. *Wiener* bounds can then be obtained [Wiener, 1912]. They correspond respectively to the arithmetic and harmonic means of phase conductivities, balanced by V_V^r , the volume fraction of each phase r such that,

$$\underline{\lambda}^{W+} = \sum_{r=1}^n V_V^r \underline{\lambda}^r = (\underline{\rho}^{W+})^{-1} \quad (3.9)$$

and

$$\underline{\rho}^{W-} = \sum_{r=1}^n V_V^r \underline{\rho}^r = (\underline{\lambda}^{W-})^{-1} \quad (3.10)$$

One can thus bound $\underline{\lambda}^H$ and $\underline{\rho}^H$ as follows:

$$\underline{\lambda}^{W-} \leq \underline{\lambda}^H \leq \underline{\lambda}^{W+} \quad (3.11)$$

and

$$\underline{\rho}^{W+} \leq \underline{\rho}^H \leq \underline{\rho}^{W-} \quad (3.12)$$

3.2.3 Bounds of order 2

For the case of d -dimensional isotropic media, *i.e.* exhibiting an isotropic distribution of heterogeneities with isotropic thermal behavior, tighter bounds can be obtained. From variational principles of energy minimization for linear conductivity, *Hashin and Shtrikman* have defined the 2nd-order bounds [[Hashin and Shtrikman, 1962a](#)] for thermal conductivity in the case of a macroscopically isotropic material made of n isotropic phases with conductivity λ^r . The lowest conductivity is denoted by exponent 1 , the highest by exponent n . It is thus assumed that $\lambda^{n-1} < \lambda^n$. Exponent HS^+ denotes upper bounds while exponent HS^- denotes lower bounds:

$$\lambda^{HS^-} = \left(\sum_{r=1}^n V_V^r (\alpha_1 + \lambda^r)^{-1} \right)^{-1} - \alpha_1 \quad (3.13)$$

$$\lambda^{HS^+} = \left(\sum_{r=1}^n V_V^r (\alpha_n + \lambda^r)^{-1} \right)^{-1} - \alpha_n \quad (3.14)$$

with α_1 and α_n as follows:

$$\alpha_1 = V_V^1 \lambda^1 + V_V^r \lambda^r - \frac{V_V^1 V_V^r (\lambda^r - \lambda^1)^2}{\lambda^r V_V^1 + \lambda^1 V_V^r + (d-1) \lambda^1} \quad (3.15)$$

$$\alpha_n = V_V^r \lambda^r + V_V^n \lambda^n - \frac{V_V^r V_V^n (\lambda^n - \lambda^r)^2}{\lambda^n V_V^r + \lambda^r V_V^n + (d-1) \lambda^r} \quad (3.16)$$

with V_V^r , volume fraction of phase r . This way one can bound the effective thermal conductivity λ^H :

$$\lambda^{HS^-} \leq \lambda^H \leq \lambda^{HS^+} \quad (3.17)$$

Application to two-phase composites

$$\lambda^{HS^-} = V_V^1 \lambda^1 + V_V^2 \lambda^2 - \frac{V_V^1 V_V^2 (\lambda^2 - \lambda^1)^2}{\lambda^2 V_V^1 + \lambda^1 V_V^2 + (d-1) \lambda^1} \quad (3.18)$$

$$\lambda^{HS^+} = V_V^1 \lambda^1 + V_V^2 \lambda^2 - \frac{V_V^1 V_V^2 (\lambda^2 - \lambda^1)^2}{\lambda^2 V_V^1 + \lambda^1 V_V^2 + (d-1) \lambda^2} \quad (3.19)$$

which can be rewritten as follows for $d = 3$:

$$\lambda^{HS^-} = \lambda^1 + \frac{3V_V^2 \lambda^1 (\lambda^2 - \lambda^1)}{3\lambda^1 + V_V^1 (\lambda^2 - \lambda^1)} \quad (3.20)$$

$$\lambda^{HS^+} = \lambda^2 - \frac{3V_V^1 \lambda^2 (\lambda^2 - \lambda^1)}{3\lambda^2 - V_V^2 (\lambda^2 - \lambda^1)} \quad (3.21)$$

We will compare our simulation results in Chapter 6 with the *Hashin–Shtrikman* bounds for 3D two-phase materials.

3.2.4 Bounds of order 3

Higher-order bounds have been developed for random media based on three-point correlation functions. This was first achieved by *Beran* for conductivity properties [Beran, 1965].

3.2.5 Bounds of order 4

Milton proposed fourth-order bounds for elastic properties based on four-point correlation functions in [Milton and Phan-Thien, 1982].

In this work, we will not use bounds of order higher than 2. Considering a dispersion of inclusions within a matrix, *Hill's* lens for thermal conductivity is plotted on Figures 3.1 and 3.2, respectively for a contrast between phases of 4 and 100.

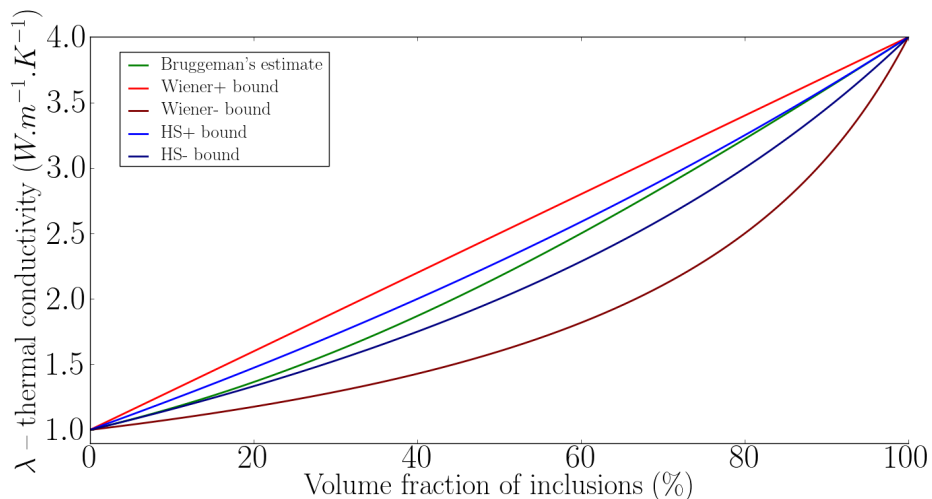


Figure 3.1: *Hill's* lens for thermal conductivity with contrast $c = 4$

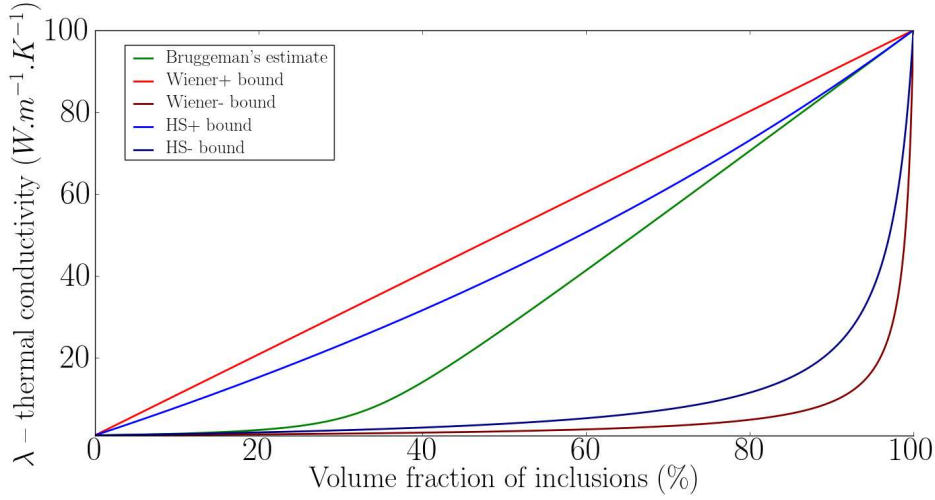


Figure 3.2: *Hill's lens* for thermal conductivity with contrast $c = 100$

3.3 Analytical estimates for elastic properties

3.3.1 Einstein's estimate

Estimates can be drawn from reasonable assumptions in the case of biphasic materials, as *Einstein* did while studying the viscous properties of a fluid with incompressible spherical particles [Einstein, 1906, Einstein, 1911]. Small concentration of particles is assumed (*high dilution assumption* or *HD*). For a weakly viscous fluid M with dilute incompressible particles P of volume fraction V_V^P , *Einstein's* estimate for the shear modulus μ^{Einstein} yields:

$$\mu^{\text{Einstein}} = \mu^M (1 + 2.5V_V^P) \quad (3.22)$$

3.3.2 Eshelby's model

As for *Einstein's*, *Eshelby's* model neglects interactions between inclusions. The response of each inclusion is the same as the one of a unique inclusion surrounded by a quasi-infinite elastic matrix domain Ω . *Eshelby* gave the analytical expressions of the elastic fields for an ellipsoidal inclusion [Eshelby, 1957]. He first considers a homogeneous problem: an ellipsoidal inclusion with moduli $\underline{\underline{C}}^0$ and compliance $\underline{\underline{S}}^0$, embedded within an infinite matrix with the same elastic properties. The inclusion is subject to eigen-strain $\underline{\underline{\epsilon}}^f = -\underline{\underline{S}}^0 : \underline{\underline{\tau}}$, with $\underline{\underline{\tau}} = -\underline{\underline{C}}^0 : \underline{\underline{\epsilon}}^f$ polarization stress tensor. The constitutive behavior is described as follows:

$$\begin{cases} \underline{\underline{\sigma}} = \underline{\underline{C}}^0 : \underline{\underline{\epsilon}} & \text{outside the inclusion} \\ \underline{\underline{\sigma}} = \underline{\underline{C}}^0 : (\underline{\underline{\epsilon}} - \underline{\underline{\epsilon}}^f) = \underline{\underline{C}}^0 : \underline{\underline{\epsilon}} + \underline{\underline{\tau}} & \text{inside the inclusion} \end{cases}$$

The actual strain field $\underline{\boldsymbol{\varepsilon}}^i$ in the inclusion is given by:

$$\underline{\boldsymbol{\varepsilon}}^i = \underline{\mathbf{S}}_i^0 : \underline{\boldsymbol{\varepsilon}}^f = -\underline{\mathbf{P}}_i^0 : \underline{\boldsymbol{\tau}} \quad (3.23)$$

with $\underline{\mathbf{S}}_i^0$, the dimensionless *Eshelby* interaction tensor and $\underline{\mathbf{P}}_i^0$, the *Hill* interaction tensor, symmetric positive definite, both depending on $\underline{\mathbf{C}}^0$ and the shape of the inclusion. These tensors are related in this way:

$$\underline{\mathbf{P}}_i^0 = \underline{\mathbf{S}}_i^0 : \underline{\mathbf{S}}_i^0 \quad (3.24)$$

If one considers now the same problem with kinematic boundary condition (prescribed displacement $\underline{\mathbf{u}}^0$, yielding homogeneous strain $\underline{\boldsymbol{\varepsilon}}^0$) at the boundary $\partial\Omega$ of the quasi-infinite domain, the strain field seen by the inclusion can be deduced from the previous result by superposition:

$$\underline{\boldsymbol{\varepsilon}}^i = \underline{\boldsymbol{\varepsilon}}^0 - \underline{\mathbf{P}}_i^0 : \underline{\boldsymbol{\tau}} \quad (3.25)$$

Eshelby showed that the solution he proposed for the homogeneous problem was applicable to the inhomogeneous problem involving an ellipsoidal inclusion with different elastic properties from the quasi-infinite matrix. Let us consider the previous problem, with an ellipsoidal inclusion now with moduli $\underline{\mathbf{C}}^i$. *Hooke's* law outside and inside the inclusion reads as follows:

$$\begin{cases} \underline{\boldsymbol{\sigma}} = \underline{\mathbf{C}}^0 : \underline{\boldsymbol{\varepsilon}} & \text{outside the inclusion} \\ \underline{\boldsymbol{\sigma}} = \underline{\mathbf{C}}^i : \underline{\boldsymbol{\varepsilon}} & \text{inside the inclusion} \end{cases}$$

which can be rewritten such that:

$$\begin{cases} \underline{\boldsymbol{\sigma}} = \underline{\mathbf{C}}^0 : \underline{\boldsymbol{\varepsilon}} & \text{outside the inclusion} \\ \underline{\boldsymbol{\sigma}} = \underline{\mathbf{C}}^0 : \underline{\boldsymbol{\varepsilon}} + \underbrace{(\underline{\mathbf{C}}^i - \underline{\mathbf{C}}^0)}_{\underline{\boldsymbol{\tau}}'} : \underline{\boldsymbol{\varepsilon}} & \text{inside the inclusion} \end{cases}$$

If $\underline{\boldsymbol{\tau}}'$ is considered homogeneous within the inclusion, the inhomogeneous problem becomes similar to the homogeneous problem, the strain in the inclusion is homogeneous and is given by Equation 3.25, which yields:

$$\underline{\boldsymbol{\varepsilon}}^i = \underline{\boldsymbol{\varepsilon}}^0 - \underline{\mathbf{P}}_i^0 : \underline{\boldsymbol{\tau}}' = \underline{\boldsymbol{\varepsilon}}^0 - \underline{\mathbf{P}}_i^0 : (\underline{\mathbf{C}}^i - \underline{\mathbf{C}}^0) : \underline{\boldsymbol{\varepsilon}}^i \quad (3.26)$$

which can be rewritten in this way:

$$\begin{aligned}
 \left(\mathbb{I} + \mathbb{P}_i^0 : \left(\mathbb{C}^i - \mathbb{C}^0 \right) \right) : \boldsymbol{\varepsilon}^i &= \boldsymbol{\varepsilon}^0 \\
 \left(\left(\mathbb{P}_i^0 \right)^{-1} - \mathbb{C}^0 + \mathbb{C}^i \right) : \boldsymbol{\varepsilon}^i &= \left(\mathbb{P}_i^0 \right)^{-1} : \boldsymbol{\varepsilon}^0 \\
 \left(\mathbb{C}_i^* + \mathbb{C}^i \right) : \boldsymbol{\varepsilon}^i &= \left(\mathbb{C}_i^* + \mathbb{C}^0 \right) : \boldsymbol{\varepsilon}^0 \\
 \boldsymbol{\varepsilon}^i &= \left(\mathbb{C}_i^* + \mathbb{C}^i \right)^{-1} : \left(\mathbb{C}_i^* + \mathbb{C}^0 \right) : \boldsymbol{\varepsilon}^0
 \end{aligned} \tag{3.27}$$

with $\mathbb{C}_i^* = \left(\mathbb{P}_i^0 \right)^{-1} - \mathbb{C}^0 = \mathbb{C}^0 : \left(\left(\mathbb{S}_i^0 \right)^{-1} - \mathbb{I} \right)$, the *Hill* influence tensor, symmetric positive definite, which only depends on \mathbb{C}^0 and on the shape of the inclusion. This tensor is accounting for the reaction of the quasi-infinite matrix on the inclusion. Finally, by homogenization one obtains the estimate of tensor of elastic moduli (resp. compliance) using the approach with prescribed strain (resp. stress), for a high dilution (HD) of inclusions without any interaction:

$$\mathbb{C}^{\text{HD}} = \mathbb{C}^0 + V_V^i \mathbb{T}_i^0 \tag{3.28}$$

$$\mathbb{S}^{\text{HD}} = \mathbb{S}^0 - V_V^i \left(\mathbb{S}^0 : \mathbb{T}_i^0 : \mathbb{S}^0 \right) \tag{3.29}$$

with \mathbb{T}_i^0 , tensor relating the polarization stress tensor $\boldsymbol{\tau}'$ within the inclusion to the homogeneous strain $\boldsymbol{\varepsilon}^0$ outside of the inclusion, which can be obtain as follows:

$$\mathbb{T}_i^0 = \left(\mathbb{C}^i - \mathbb{C}^0 \right) : \left(\mathbb{C}_i^* + \mathbb{C}^i \right)^{-1} : \left(\mathbb{C}_i^* + \mathbb{C}^0 \right) = \left(\mathbb{C}^i - \mathbb{C}^0 \right) - \left(\mathbb{C}^i - \mathbb{C}^0 \right) : \left(\mathbb{C}_i^* + \mathbb{C}^i \right)^{-1} : \left(\mathbb{C}^i + \mathbb{C}^0 \right) \tag{3.30}$$

For an elastically isotropic matrix reinforced with a highly dilute dispersion of elastically isotropic spherical particles, one can analytically compute the *Hill* influence tensor:

$$\mathbb{C}_i^* = \{3k^*, 2\mu^*\} = \left\{ 4\mu^0, \frac{\mu^0(9k^0 + 8\mu^0)}{3(k^0 + 2\mu^0)} \right\} = \mu^0 \left\{ 4, \frac{7 - 5\nu^0}{4 - 5\nu^0} \right\} \tag{3.31}$$

Then, when applied to the shear and bulk moduli, it yields:

$$\mu_E^{\text{HD}} = \mu^0 + V_V^i \frac{(\mu^i - \mu^0)(\mu_i^* + \mu^0)}{\mu_i^* + \mu^i} = \mu^0 + V_V^i \frac{(\mu^i - \mu^0) \left(\frac{\mu^0(9k^0 + 8\mu^0)}{6(k^0 + 2\mu^0)} + \mu^0 \right)}{\frac{\mu^0(9k^0 + 8\mu^0)}{6(k^0 + 2\mu^0)} + \mu^i} \quad (3.32)$$

$$\frac{1}{\mu_\Sigma^{\text{HD}}} = \frac{1}{\mu^0} + V_V^i \frac{\left(\frac{1}{\mu^i} - \frac{1}{\mu^0} \right) \left(\frac{1}{\mu_i^*} + \frac{1}{\mu^0} \right)}{\frac{1}{\mu_i^*} + \frac{1}{\mu^i}} = \frac{1}{\mu^0} + V_V^i \frac{\left(\frac{1}{\mu^i} - \frac{1}{\mu^0} \right) \left(\frac{6(k^0 + 2\mu^0)}{\mu^0(9k^0 + 8\mu^0)} + \frac{1}{\mu^0} \right)}{\frac{6(k^0 + 2\mu^0)}{\mu^0(9k^0 + 8\mu^0)} + \frac{1}{\mu^i}} \quad (3.33)$$

$$k_E^{\text{HD}} = k^0 + V_V^i \frac{(k^i - k^0)(k_i^* + k^0)}{k_i^* + k^i} = k^0 + V_V^i \frac{(k^i - k^0) \left(\frac{4\mu^0}{3} + k^0 \right)}{\frac{4\mu^0}{3} + k^i} \quad (3.34)$$

$$\frac{1}{k_\Sigma^{\text{HD}}} = \frac{1}{k^0} + V_V^i \frac{\left(\frac{1}{k^i} - \frac{1}{k^0} \right) \left(\frac{1}{k_i^*} + \frac{1}{k^0} \right)}{\frac{1}{k_i^*} + \frac{1}{k^i}} = \frac{1}{k^0} + V_V^i \frac{\left(\frac{1}{k^i} - \frac{1}{k^0} \right) \left(\frac{3}{4\mu^0} + \frac{1}{k^0} \right)}{\frac{3}{4\mu^0} + \frac{1}{k^i}} \quad (3.35)$$

3.3.3 Self-consistent scheme

The self-consistent scheme applied to elastic moduli was first proposed by *Budiansky* [Budiansky, 1965] and *Hill* [Hill, 1965]. This approach is taking into account the interaction between particles by simplifying the problem such that the average of neighboring effects seen by each particle can be accounted for by replacing the reference medium (matrix) properties $\underline{\underline{\mathbf{C}}}^0$ by the estimated ones $\underline{\underline{\mathbf{C}}}^{\text{SC}}$. Let us rewrite Equation 3.27 in the case of spherical phases such that:

$$\underline{\underline{\boldsymbol{\varepsilon}}}^i = \left(\underline{\underline{\mathbf{C}}}_i^* + \underline{\underline{\mathbf{C}}}^i \right)^{-1} : \left(\underline{\underline{\mathbf{C}}}_i^* + \underline{\underline{\mathbf{C}}}^{\text{SC}} \right) : \underline{\underline{\boldsymbol{\varepsilon}}}^0 \quad (3.36)$$

Thus, by considering the spatial average over the whole domain Ω :

$$\langle \underline{\underline{\boldsymbol{\varepsilon}}}^i \rangle = \left\langle \left(\underline{\underline{\mathbf{C}}}_i^* + \underline{\underline{\mathbf{C}}}^i \right)^{-1} : \left(\underline{\underline{\mathbf{C}}}_i^* + \underline{\underline{\mathbf{C}}}^{\text{SC}} \right) \right\rangle : \underline{\underline{\boldsymbol{\varepsilon}}}^0 \quad (3.37)$$

As for *Eshelby's* problems, the overall spatial average of the elastic strain field $\langle \underline{\underline{\boldsymbol{\varepsilon}}}^i \rangle$ converges towards the value of the strain $\underline{\underline{\boldsymbol{\varepsilon}}}^0$ prescribed on $\partial\Omega$. Hence, it yields:

$$1 = \left\langle \left(\underline{\underline{\mathbf{C}}}_i^* + \underline{\underline{\mathbf{C}}}^i \right)^{-1} \right\rangle : \left(\underline{\underline{\mathbf{C}}}_i^* + \underline{\underline{\mathbf{C}}}^{\text{SC}} \right) \quad (3.38)$$

which is the self-consistent equation. Solving this equation by finding $\underline{\underline{\mathbf{C}}}^{\text{SC}}$ is usually done computationally. It is worth noting that with this model, the contribution of each phase is treated equally, making it interesting for studying polycrystalline materials but not so much for reinforced composites with large contrast of properties between phases.

Chapter 3. Analytical estimates and bounds

For the case of isotropic d -dimensional materials made of n different spherical isotropic particles with bulk modulus k^n and shear modulus μ^n , Equation 3.38 can be rewritten as follows for the bulk modulus k^{SC} :

$$\sum_{r=1}^n V_V^r \frac{k^r - k^{\text{SC}}}{k^r + \frac{2(d-1)}{d} \mu^{\text{SC}}} = 0 \quad (3.39)$$

The bulk modulus estimate obtained using the self-consistent scheme depends on the estimate of the shear modulus μ^{SC} :

$$\sum_{r=1}^n V_V^r \frac{\mu^r - \mu^{\text{SC}}}{\mu^r + h^{\text{SC}}} = 0 \quad (3.40)$$

with

$$h^{\text{SC}} \triangleq \mu^{\text{SC}} \frac{\frac{dk^{\text{SC}}}{2} + \frac{(d+1)(d-2)\mu^{\text{SC}}}{d}}{k^{\text{SC}} + 2\mu^{\text{SC}}} \quad (3.41)$$

Let us now apply these formulae to 3D 2-phase composites.

Application to two-phase composites

$$V_V^1 \frac{k^1 - k^{\text{SC}}}{k^1 + \frac{4}{3} \mu^{\text{SC}}} + V_V^2 \frac{k^2 - k^{\text{SC}}}{k^2 + \frac{4}{3} \mu^{\text{SC}}} = 0 \quad (3.42)$$

$$V_V^1 \frac{\mu^1 - \mu^{\text{SC}}}{\mu^1 + h^{\text{SC}}} + V_V^2 \frac{\mu^2 - \mu^{\text{SC}}}{\mu^2 + h^{\text{SC}}} = 0 \quad (3.43)$$

with

$$h^{\text{SC}} \triangleq \mu^{\text{SC}} \frac{\frac{3}{2} k^{\text{SC}} + \frac{4}{3} \mu^{\text{SC}}}{k^{\text{SC}} + 2\mu^{\text{SC}}} \quad (3.44)$$

and

$$V_V^2 = 1 - V_V^1 \quad (3.45)$$

After calculation, it yields:

$$k^{\text{SC}} = \frac{k^1 k^2 + (V_V^1 k^1 + V_V^2 k^2) \frac{4}{3} \mu^{\text{SC}}}{V_V^2 k^1 + V_V^1 k^2 + \frac{4}{3} \mu^{\text{SC}}} \quad (3.46)$$

$$\mu^{\text{SC}} = \frac{\mu^1 \mu^2 + (V_V^1 \mu^1 + V_V^2 \mu^2) \frac{\mu^{\text{SC}} (\frac{3}{2} k^{\text{SC}} + \frac{4}{3} \mu^{\text{SC}})}{k^{\text{SC}} + 2\mu^{\text{SC}}}}{V_V^2 \mu^1 + V_V^1 \mu^2 + \frac{\mu^{\text{SC}} (\frac{3}{2} k^{\text{SC}} + \frac{4}{3} \mu^{\text{SC}})}{k^{\text{SC}} + 2\mu^{\text{SC}}}} \quad (3.47)$$

A unique solution can be found for Equations 3.46 and 3.47 using a fixed-point algorithm.

3.4 Analytical bounds for elastic properties

As for the thermal conductivity, rigorous bounds can be defined for the elastic properties.

3.4.1 Bounds of order 0

Considering that one phase is stiffer than the other, bounds of order 0 correspond to the properties of each phase. The homogenized tensor of elasticity moduli $\underline{\underline{\mathbf{C}}}^H$ is then bounded by the moduli of the hardest phase $\underline{\underline{\mathbf{C}}}^2$ and the softest phase $\underline{\underline{\mathbf{C}}}^1$ as follows:

$$\underline{\underline{\mathbf{C}}}^1 \leq \underline{\underline{\mathbf{C}}}^H \leq \underline{\underline{\mathbf{C}}}^2 \quad (3.48)$$

These inequalities have to be considered in the sense of quadratic forms. Such bounds do not take volume fraction into account. As a matter of fact, they are of limited interest since they do not give any useful estimate of the homogenized properties.

3.4.2 Bounds of order 1

If information about the volume fraction is available, one should use it. *Voigt* and *Reuss* bounds can then be obtained [Voigt, 1889, Reuss, 1929]. *Voigt*'s assumption is that the strain field is homogeneous throughout the medium, while *Reuss*' correspond to a homogeneous stress field. They correspond respectively to the arithmetic and harmonic means of phase properties, balanced by V_V^r , the volume fraction of each phase r such that,

$$\underline{\underline{\mathbf{C}}}^{\text{Voigt}} = \sum_{r=1}^n V_V^r \underline{\underline{\mathbf{C}}}^r = \left(\underline{\underline{\mathbf{S}}}^{\text{Voigt}} \right)^{-1} \quad (3.49)$$

and

$$\underline{\underline{\mathbf{S}}}^{\text{Reuss}} = \sum_{r=1}^n V_V^r \underline{\underline{\mathbf{S}}}^r = \left(\underline{\underline{\mathbf{C}}}^{\text{Reuss}} \right)^{-1} \quad (3.50)$$

One can thus bound $\underline{\underline{\mathbf{C}}}^H$ and $\underline{\underline{\mathbf{S}}}^H$ as follows:

$$\underline{\underline{\mathbf{C}}}^{\text{Reuss}} \leq \underline{\underline{\mathbf{C}}}^H \leq \underline{\underline{\mathbf{C}}}^{\text{Voigt}} \quad (3.51)$$

and

$$\underline{\underline{\mathbf{S}}}^{\text{Voigt}} \leq \underline{\underline{\mathbf{S}}}^H \leq \underline{\underline{\mathbf{S}}}^{\text{Reuss}} \quad (3.52)$$

3.4.3 Bounds of order 2

For the case of two-dimensional isotropic media, *i.e.* exhibiting an isotropic distribution of heterogeneities with isotropic elastic behavior, tighter bounds can be obtained. From variational principles of energy minimization for linear elasticity, *Hashin and Shtrikman* have defined 2nd-order bounds for bulk modulus k and shear modulus μ [[Hashin and Shtrikman, 1963](#)]. Lowest moduli are denoted by exponents ¹, highest moduli by exponents ^{*n*}. It is thus assumed that $k^{n-1} < k^n$ and $\mu^{n-1} < \mu^n$. Exponent ^{*HS+*} denotes upper bounds while exponent ^{*HS-*} denotes lower bounds. Let us define the bounds for the bulk modulus K ,

$$k^{HS^-} = k^1 + \frac{A_1}{1 + \alpha_1 A_1} \quad (3.53)$$

$$k^{HS^+} = k^n + \frac{A_n}{1 + \alpha_n A_n} \quad (3.54)$$

with α_1 , α_n , A_1 and A_n as follows:

$$\alpha_1 = -\frac{3}{3k^1 + 4\mu^1} \quad (3.55)$$

$$\alpha_n = -\frac{3}{3k^n + 4\mu^n} \quad (3.56)$$

$$A_1 = \sum_{r=2}^n \frac{A_A^r}{\frac{1}{k^r - k^1} - \alpha_1} \quad (3.57)$$

$$A_n = \sum_{r=1}^{n-1} \frac{A_A^r}{\frac{1}{k^r - k^n} - \alpha_n} \quad (3.58)$$

3.4. Analytical bounds for elastic properties

with A_A^r , surface fraction of phase r in \mathbb{R}^2 or V_V^r , volume fraction of phase r in \mathbb{R}^3 . This way one can bound the homogenized bulk modulus k^H :

$$k^{HS^-} \leq k^H \leq k^{HS^+} \quad (3.59)$$

Let us now consider the shear modulus μ :

$$\mu^{HS^-} = \mu^1 + \frac{1}{2} \frac{B_1}{1 + \beta_1 B_1} \quad (3.60)$$

$$\mu^{HS^+} = \mu^n + \frac{1}{2} \frac{B_n}{1 + \beta_n B_n} \quad (3.61)$$

with β_1 , β_n , B_1 and B_n as follows:

$$\beta_1 = -\frac{3(k^1 + 2\mu^1)}{5\mu^1(3k^1 + 4\mu^1)} \quad (3.62)$$

$$\beta_n = -\frac{3(k^n + 2\mu^n)}{5\mu^n(3k^n + 4\mu^n)} \quad (3.63)$$

$$B_1 = \sum_{r=2}^n \frac{A_A^r}{\frac{1}{2(\mu^r - \mu^1)} - \beta_1} \quad (3.64)$$

$$B_n = \sum_{r=1}^{n-1} \frac{A_A^r}{\frac{1}{2(\mu^r - \mu^n)} - \beta_n} \quad (3.65)$$

Thus bounds for the homogenized shear modulus μ^H can be defined:

$$\mu^{HS^-} \leq \mu^H \leq \mu^{HS^+} \quad (3.66)$$

Application to two-phase composites in \mathbb{R}^2

$$\mu^{HS^-} = \mu^1 + \frac{A_A^2}{\frac{1}{\mu^2 - \mu^1} + \frac{6(k^1 + 2\mu^1)A_A^1}{5\mu^1(3k^1 + 4\mu^1)}} \quad (3.67)$$

$$\mu^{HS^+} = \mu^2 + \frac{A_A^1}{\frac{1}{\mu^1 - \mu^2} + \frac{6(k^2 + 2\mu^2)A_A^2}{5\mu^2(3k^2 + 4\mu^2)}} \quad (3.68)$$

$$k^{HS^-} = k^1 + \frac{A_A^2}{\frac{1}{k^2 - k^1} + \frac{3A_A^1}{3k^1 + 4\mu^1}} \quad (3.69)$$

$$k^{HS^+} = k^2 + \frac{A_A^1}{\frac{1}{k^1 - k^2} + \frac{3A_A^2}{3k^2 + 4\mu^2}} \quad (3.70)$$

The *Hashin–Shtrikman* bounds are also available for bounding the properties of 3-dimensional isotropic microstructures, they are presented hereafter for the case of a two-phase composite.

Hashin–Shtrikman bounds for 3D two-phase materials

$$\mu_{3D}^{HS^-} = \mu^1 + \frac{V_V^2}{\frac{1}{\mu^2 - \mu^1} + \frac{2(k^1 + 2\mu^1)V_V^1}{5\mu^1(k^1 + \frac{4}{3}\mu^1)}} \quad (3.71)$$

$$\mu_{3D}^{HS^+} = \mu^2 + \frac{V_V^1}{\frac{1}{\mu^1 - \mu^2} + \frac{2(k^2 + 2\mu^2)V_V^2}{5\mu^2(k^2 + \frac{4}{3}\mu^2)}} \quad (3.72)$$

$$k_{3D}^{HS^-} = \frac{1}{\frac{V_V^2}{k^2 + \frac{4\mu^2}{3}} + \frac{V_V^1}{k^1 + \frac{4\mu^1}{3}}} - \frac{4\mu^2}{3} \quad (3.73)$$

$$k_{3D}^{HS^+} = \frac{1}{\frac{V_V^2}{k^2 + \frac{4}{3\mu^2}} + \frac{V_V^1}{k^1 + \frac{4}{3\mu^1}}} - \frac{4}{3\mu^2} \quad (3.74)$$

It is worth noting that for an isotropic dilute distribution of hard spherical inclusions in a soft matrix considered as the reference medium, the lower HS bound is equivalent to the *Mori–Tanaka* estimate [Mori and Tanaka, 1973]. We will compare our simulation results in Chapter 6 with the *Hashin–Shtrikman* bounds for 3D two-phase materials.

3.4.4 Bounds of order 3

Higher-order bounds have been developed for random media based on three-point correlation functions. The third-order bounds were proposed in [Beran and Molyneux, 1966] for the elastic bulk modulus, and in [McCoy, 1970] for the shear modulus. *Jeulin* developed third-order bounds for specific models of random structures [Jeulin and Ostoja-Starzewski, 2001].

3.4.5 Bounds of order 4

Milton proposed fourth-order bounds for elastic properties based on four-point correlation functions in [[Milton and Phan-Thien, 1982](#)].

In this work, we will not use bounds of order higher than 2. There are many other bounds and estimates available. An extensive literature exist on the topic of analytical homogenization, for a comprehensive review readers should consult these references: [[Sanchez-Palencia and Zaoui, 1987](#), [Mura, 1987](#), [Besson et al., 2001](#), [Bornert et al., 2001](#), [Jeulin and Ostoja-Starzewski, 2001](#), [Torquato, 2001](#), [Milton, 2002](#)].

Considering a dispersion of inclusions within a matrix, *Hill's* lens for bulk and shear moduli are plotted on Figures 3.3 to 3.6, for two contrasts of properties between phases.

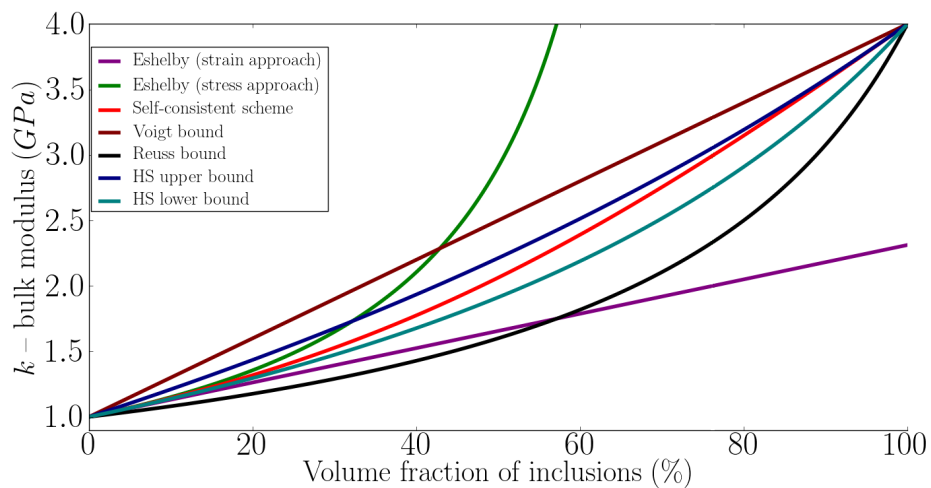


Figure 3.3: *Hill's* lens for bulk modulus with contrast $c = 4$

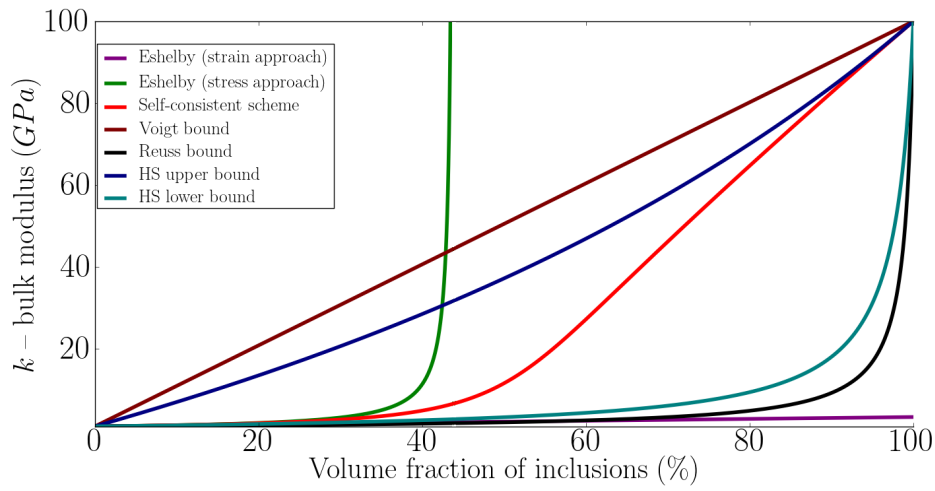


Figure 3.4: *Hill's lens* for bulk modulus with contrast $c = 100$

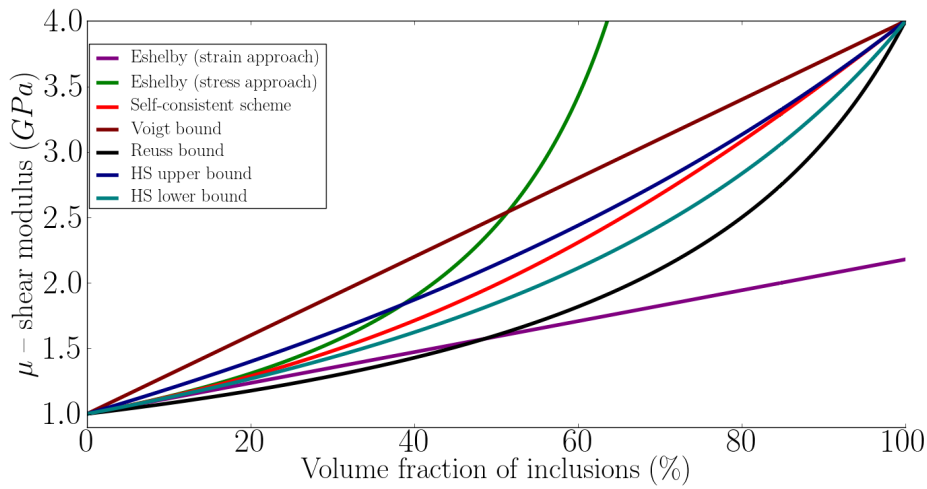


Figure 3.5: *Hill's lens* for shear modulus with contrast $c = 4$

3.4. Analytical bounds for elastic properties

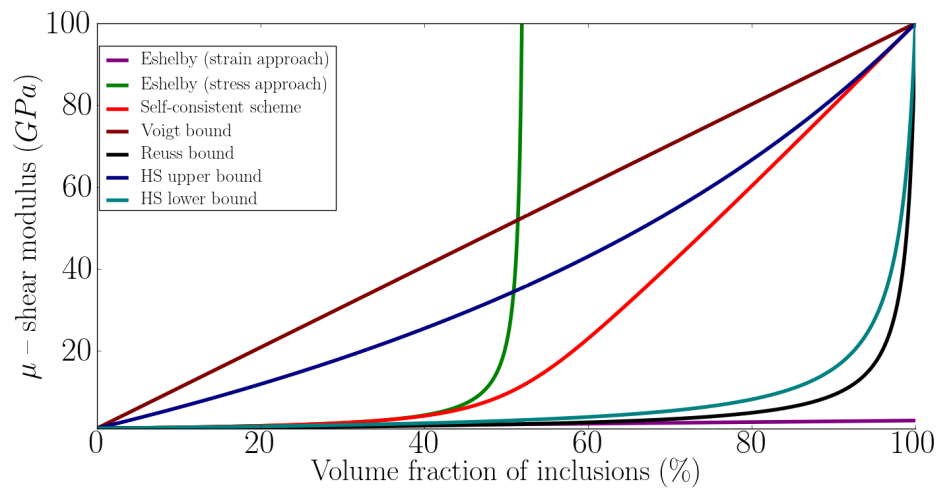


Figure 3.6: *Hill's lens* for shear modulus with contrast $c = 100$

4 Computational homogenization

*The liberating force of technology—the instrumentalization of things—turns into...
the instrumentalization of man.*

— Herbert Marcuse, *One-dimensional man* (1964)

4.1 Computational homogenization using the finite element method

There are many computational homogenization techniques available for predicting effective properties. In this work we will primarily focus on full-field approaches using the finite element (FE) method.

In order to determine homogenized mechanical properties for a given microstructure, one has to solve boundary value problems in statics. The finite element method has proved to be a quite efficient technique to solve this kind of problems even in the case of highly nonlinear phenomena [Besson et al., 2001, Cailletaud et al., 2003]. The complex and heterogeneous nature of microstructures brings up systems to solve including millions of degrees of freedom (DOFs). Every FE computation in this work has been done using `Z-Set` code¹ which is flexible and robust enough for our purpose. The content of this section is based on reference [Besson et al., 2001] and on the graduate course *Nonlinear computational mechanics* given by Profs. *Cailletaud* and *Chaboche* at École Nationale Supérieure des Mines de Paris². This section is limited to the FE method for determining mechanical properties, a similar approach can be drawn for computing thermal properties.

¹<http://www.zset-software.com>

²<http://mms2.ensmp.fr>

4.1.1 FE formulation of the principle of virtual work

Galerkin's approach [Galerkin, 1915] for continuum mechanics is implemented and used with the principle of virtual work. In each of the n elements e , knowing the nodal displacements $\{u_e^*\}$, one can compute the virtual displacement field \underline{u}^* and the strain tensor $\underline{\epsilon}$ as follows:

$$\underline{u}^* = [N] \{u_e^*\} \quad (4.1)$$

and,

$$\underline{\epsilon} = [B] \{u_e^*\} \quad (4.2)$$

with $[N]$, the shape function matrix and $[B]$, the matrix of shape function derivatives. Then, for all $\{u_e^*\}$ with prescribed body forces \underline{f} and surface forces \underline{F} :

$$\sum_{e=1}^n \left(\int_{\Omega} \underline{\sigma}(\{u_e^*\}) [B] \{u_e^*\} dV \right) = \sum_{e=1}^n \left(\int_{\Omega} \underline{f} [N] \{u_e^*\} dV + \int_{\partial\Omega} \underline{F} [N] \{u_e^*\} dS \right) \quad (4.3)$$

Thus,

$$\sum_{e=1}^n \left(\{ \mathcal{F}_e^{\text{int}} \} - \{ \mathcal{F}_e^{\text{ext}} \} \right) \{u_e^*\} = 0 \quad (4.4)$$

with $\{ \mathcal{F}_e^{\text{int}} \}$ and $\{ \mathcal{F}_e^{\text{ext}} \}$ respectively internal and external forces, in each element e , such that:

$$\{ \mathcal{F}_e^{\text{int}} \} = \int_{\Omega} [B]^T \underline{\sigma}(\{u_e^*\}) dV \quad (4.5)$$

and,

$$\{ \mathcal{F}_e^{\text{ext}} \} = \int_{\Omega} [N]^T \underline{f} dV + \int_{\partial\Omega} [N]^T \underline{F} dS \quad (4.6)$$

Balance between internal and external forces is achieved with a *Newton* iterative algorithm using the element stiffness matrix $[K_e]$:

$$\begin{aligned} [K_e] &= \frac{\partial \{ \mathcal{F}_e^{\text{int}} \}}{\partial \{u_e^*\}} \\ &= \int_e [B]^T \frac{\partial \{ \sigma \}}{\partial \{ \epsilon \}} \frac{\partial \{ \epsilon \}}{\partial \{u_e^*\}} dV \\ &= \int_e [B]^T \frac{\partial \{ \sigma \}}{\partial \{ \epsilon \}} [B] dV \end{aligned} \quad (4.7)$$

4.1. Computational homogenization using the finite element method

which yields, for linear elastic problems:

$$[K_e] = \int_e [B]^T [\underline{\underline{c}}] [B] dV \quad (4.8)$$

4.1.2 Application to linear elasticity

In the case of linear elasticity within a volume V fulfilling RVE requirements, one can compute the effective elastic moduli $\underline{\underline{C}}$ or compliances $\underline{\underline{S}}$ using Equation 1.10 by prescribing either the macroscopic strain $\underline{\underline{E}}$ or macroscopic stress $\underline{\underline{\Sigma}}$:

$$\begin{bmatrix} \Sigma_{11} \\ \Sigma_{22} \\ \Sigma_{33} \\ \Sigma_{23} \\ \Sigma_{31} \\ \Sigma_{12} \end{bmatrix} = \begin{bmatrix} C_{11} & C_{12} & C_{13} & C_{14} & C_{15} & C_{16} \\ - & C_{22} & C_{23} & C_{24} & C_{25} & C_{26} \\ - & - & C_{33} & C_{34} & C_{35} & C_{36} \\ - & - & - & C_{44} & C_{45} & C_{46} \\ - & - & - & - & C_{55} & C_{56} \\ - & - & - & - & - & C_{66} \end{bmatrix} \begin{bmatrix} E_{11} \\ E_{22} \\ E_{33} \\ 2E_{23} \\ 2E_{31} \\ 2E_{12} \end{bmatrix} \quad (4.9)$$

$$\begin{bmatrix} E_{11} \\ E_{22} \\ E_{33} \\ 2E_{23} \\ 2E_{31} \\ 2E_{12} \end{bmatrix} = \begin{bmatrix} S_{11} & S_{12} & S_{13} & S_{14} & S_{15} & S_{16} \\ - & S_{22} & S_{23} & S_{24} & S_{25} & S_{26} \\ - & - & S_{33} & S_{34} & S_{35} & S_{36} \\ - & - & - & S_{44} & S_{45} & S_{46} \\ - & - & - & - & S_{55} & S_{56} \\ - & - & - & - & - & S_{66} \end{bmatrix} \begin{bmatrix} \Sigma_{11} \\ \Sigma_{22} \\ \Sigma_{33} \\ \Sigma_{23} \\ \Sigma_{31} \\ \Sigma_{12} \end{bmatrix} \quad (4.10)$$

Linear relations thus appear between macroscopic stress and strain. For instance, if $E_{22} = E_{33} = E_{23} = E_{31} = E_{12} = 0$ and $E_{11} = 1$, then:

$$\begin{bmatrix} \Sigma_{11} \\ \Sigma_{22} \\ \Sigma_{33} \\ \Sigma_{23} \\ \Sigma_{31} \\ \Sigma_{12} \end{bmatrix} = \begin{bmatrix} C_{11} & C_{12} & C_{13} & C_{14} & C_{15} & C_{16} \\ - & C_{22} & C_{23} & C_{24} & C_{25} & C_{26} \\ - & - & C_{33} & C_{34} & C_{35} & C_{36} \\ - & - & - & C_{44} & C_{45} & C_{46} \\ - & - & - & - & C_{55} & C_{56} \\ - & - & - & - & - & C_{66} \end{bmatrix} \begin{bmatrix} E_{11} \\ 0 \\ 0 \\ 0 \\ 0 \\ 0 \end{bmatrix} = \begin{bmatrix} C_{11} \\ C_{12} \\ C_{13} \\ C_{14} \\ C_{15} \\ C_{16} \end{bmatrix} \quad (4.11)$$

which can be rewritten such as:

$$\Sigma_{11} = C_{11}, \quad \Sigma_{22} = C_{12}, \quad \Sigma_{33} = C_{13}, \quad \Sigma_{23} = C_{14}, \quad \Sigma_{31} = C_{15}, \quad \Sigma_{12} = C_{16} \quad (4.12)$$

Using these linear relations, one can build up effective compliance and elastic moduli tensors for a given microstructure. The formalism is similar for any linear property, *e.g.* thermal conductivity. Such an approach has been successfully implemented in [Kanit et al., 2003, Kanit, 2003, Madi et al., 2005, Kanit et al., 2006, Madi, 2006, Jean, 2009, Jean and Engelmayer, 2010].

4.1.3 The element DOF method with prescribed macroscopic strain

In the case of periodic boundary conditions (*cf.* Section 2.3.2), there is an alternative to the FE formulation presented in Section 4.1.1. It consists in adding DOFs at the scale of the element. These DOFs correspond to the macroscopic strain E_{ij} , in addition to nodal DOFs for displacement u_i . The balance equations can thus be written as follows:

$$\begin{aligned}
 \int_V \sigma_{ij} u_{i,j} dV &= \int_V \sigma_{ij} (E_{ik} x_k + v_i)_{,j} dV \\
 &= \int_V \sigma_{ij} E_{ij} dV + \int_V \sigma_{ij} v_{i,j} dV \\
 &= \int_V \sigma_{ij} E_{ij} dV + \int_V (\sigma_{ij} v_i)_{,j} dV \\
 &= \int_V \sigma_{ij} E_{ij} dV + \underbrace{\int_{\partial V} \sigma_{ij} v_i n_j dS}_{=0} \\
 &= \int_V \sigma_{ij} dV E_{ij} \\
 &= V \Sigma_{ij} E_{ij} \\
 &= R E_{ij} E_{ij}
 \end{aligned} \tag{4.13}$$

The FE problem left to solve concerns the homogeneous strain tensor E_{ij} and its dual $R E_{ij}$, which corresponds to the macroscopic reaction stress. Prescribing E_{ij} corresponds to the macroscopic strain approach, while prescribing $R E_{ij}$ leads to the macroscopic stress approach. The product $R E_{ij} E_{ij}$ is developed in this way:

$$\begin{aligned}
 R E_{ij} E_{ij} &= R E_{11} E_{11} + R E_{22} E_{22} + \dots + R E_{33} E_{33} \\
 &\quad + 2 R E_{12} E_{12} + 2 R E_{31} E_{31} + 2 R E_{23} E_{23}
 \end{aligned} \tag{4.14}$$

Implementation of additional degrees of freedom in the FE framework is done as follows:

$$\{\boldsymbol{\epsilon}\} = [B] \{u\} + \{\boldsymbol{E}\} \tag{4.15}$$

Also,

$$\{\boldsymbol{\epsilon}\} = [B'] \{u'\} \tag{4.16}$$

$$E_{12} = \langle \varepsilon_{12} \rangle = 1, \quad E_{11} = E_{22} = E_{33} = E_{23} = E_{31} = 0$$

$$\Rightarrow \Sigma_{11} = C_{16} 2E_{12}$$

...

$$\Sigma_{12} = C_{66} 2E_{12}$$

By computing $\langle \sigma_{ij} \rangle$, it yields:

$$C_{16} = \frac{\Sigma_{11}}{2E_{12}} = \frac{\langle \sigma_{11} \rangle}{2}$$

...

$$C_{66} = \frac{\Sigma_{12}}{2E_{12}} = \frac{\langle \sigma_{12} \rangle}{2}$$

A similar approach with prescribed macroscopic stress is given in Appendix A, as well as a simplified method for determining elastic properties without having to compute spatial averages. We will now introduce the statistical computational homogenization approach for determining RVE sizes for random media.

4.2 Statistical approach for determining a RVE size

This approach, already mentioned in Section 2.1, was applied on materials for the first time in [Kanit et al., 2003], albeit it was based on a seminal work on representativity: [Cailletaud et al., 1994]. The problem of representativity of samples is addressed by means of a probabilistic approach giving size-dependent intervals of confidence, which is a well-known approach used in geostatistics [Matheron, 1971]. It is based on the scaling effect on the variance of effective properties in simulations of random media. Several assumptions have to be considered regarding the statistics of the microstructures we intend to study.

4.2.1 Ergodicity hypothesis

The ergodicity hypothesis is fulfilled for a property or a random function Z when the statistical properties of its measured value (mathematical expectation, variance, etc.) over a finite volume V (spatial average) converge to those estimated over series of independent samples smaller than V (ensemble average), when the volume V goes to infinity. Ergodicity implies that one realization of a volume $V \geq V_{\text{RVE}}$ contains all the statistical information necessary to the description of its microstructure.

4.2.2 Stationarity hypothesis

The stationarity hypothesis is assumed for a property or a random function Z when its mathematical expectation is constant with respect to time and space.

4.2.3 Statistical homogeneity hypothesis

A random structure is considered statistically homogeneous when the statistical description of its morphology, by the means of n -point correlation functions, is invariant by translation.

4.2.4 RVE size determination for media with finite integral range

Let us consider a microstructure that fulfills the ergodicity and stationarity conditions for a given physical quantity $Z(x)$ regarded as a random function with mathematical expectation $E\{Z(x)\}$ and point variance D_Z^2 . The variance $D_Z^2(V)$ of its average value $\bar{Z}(V)$ over the domain Ω with volume V can be obtained using the centered second-order correlation function \bar{W}_2 (cf. Appendix B.1.4) in this way:

$$D_Z^2(V) = \frac{1}{V} \iint_{\Omega} \bar{W}_2(x-y) dx dy \quad (4.19)$$

with

$$\bar{W}_2(h) = E\left\{\left(Z(x) - \bar{Z}\right)\left(Z(x+h) - \bar{Z}\right)\right\} \quad (4.20)$$

For determining the RVE size for the physical property Z one can rely on the geostatistical notion of integral range [Matheron, 1975, Lantuéjoul, 1991, Cailletaud et al., 1994, Jeulin, 2001, Jeulin and Ostoja-Starzewski, 2001, Lantuéjoul, 2002]. The integral range A_n is homogeneous to a volume of dimension n in \mathbb{R}^n . For $n = 3$, the integral range is given by:

$$A_3 = \frac{1}{D_Z^2} \int_{\mathbb{R}^3} \bar{W}_2(h) dh \quad (4.21)$$

The physical interpretation of the integral range is such that for a given volume V , one can define $n = \frac{V}{A_3}$ volume elements for which the i average values $Z_i(V')$ over the n sub-volumes $V' = \frac{V}{n}$ are uncorrelated random variables. Hence, for a large specimen, *i.e.* $V \gg A_3$, Equation 4.19 can be rewritten introducing the point variance of Z , D_Z^2 as follows:

$$D_Z^2(V) = D_Z^2 \frac{A_3}{V} \quad (4.22)$$

Let us analyze this asymptotic relation. First, in general one has no guarantee on the finiteness

Chapter 4. Computational homogenization

of point variance D_Z^2 [Matheron, 1971]: let us consider a large domain Ω and a smaller domain $V \subset \Omega$ that is attainable by means of experimentation or computation, one can then compute an experimental variance which is in fact a function of Ω supported by V , that will increase with Ω . If the variance over V is finite, it should be regarded as a limit of the experimental variance for $\Omega \rightarrow +\infty$. D_Z^2 can be computed over V as follows:

$$\begin{aligned}
 D_Z^2 &= \frac{1}{V} \int_V \left(Z(x) - \bar{Z} \right)^2 dV \\
 &= \frac{1}{V} \int_V Z^2(x) - \bar{Z}^2 dV \\
 &= \frac{1}{V} \int_V Z^2(x) dV - \left(\frac{1}{V} \int_V Z(x) dV \right)^2
 \end{aligned} \tag{4.23}$$

On the other hand, the ensemble variance $D_Z^2(V')$ is computed from the average values \bar{Z}_i over n sub-volumes:

$$\begin{aligned}
 D_Z^2(V') &= \frac{1}{n} \sum_{i=1}^n \left(Z_i(V') - \bar{Z}_i \right)^2 \\
 &= \frac{1}{n} \sum_{i=1}^n Z_i^2(V') - \bar{Z}_i^2 \\
 &= \frac{1}{n} \sum_{i=1}^n Z_i^2(V') - \left(\frac{1}{n} \sum_{i=1}^n Z_i(V') \right)^2
 \end{aligned} \tag{4.24}$$

Equation 4.24 uses the average value of the average values \bar{Z}_i over n sub-volumes V' , which is expected to converge towards the effective property Z_{eff} when $V \rightarrow +\infty$. If Z_{eff} is already known, it might be of interest to use it instead of \bar{Z}_i in order to obtain a better estimate.

If $Z(x)$ is the indicator function of the random set A , then one can obtain analytically the variance of the local volume fraction as a function of the point variance as follows:

$$D_Z^2 = p - p^2 = p(1 - p) \tag{4.25}$$

with p , probability for a point x to belong to the random set A , which is equivalent to the volume fraction of A in V .

The asymptotic scaling law given in Equation 4.22 can be used for any additive variable Z over the domain Ω . In the case of elastic properties for instance, average stress $\langle \boldsymbol{\sigma} \rangle$ or strain $\langle \boldsymbol{\epsilon} \rangle$ fields have to be computed. For determining the RVE size for a given property Z , one thus has to know its integral range A_3 . There is no theoretical covariance for mechanical fields. However, there are

4.2. Statistical approach for determining a RVE size

two ways to estimate it; first by assuming that \bar{Z} is equal to the arithmetic average of properties (mixing rule) for a biphasic medium, hence Equation 4.23 yields:

$$D_Z^2 = p(1-p)(Z_1 - Z_2)^2 \quad (4.26)$$

with Z_1 and Z_2 , respectively property Z of phase 1 and 2. D_Z^2 can also be estimated computationally on the largest virtual sample available, in order to minimize boundary layer effects and obtain a converged value. The approach proposed by [Pascal et al., 2010, di Paola, 2010] consists in taking only into account the inner part of the simulation volume. This could present an advantage for determining point variance.

Once the point variance has been estimated for a given property, the integral range can be obtained using the procedure proposed by [Matheron, 1989] for any random function: consider realizations of domains Ω with an increasing volume V (or non-overlapping sub-domains of large simulations, with a wide range of sizes), the parameter A_3 can be estimated by fitting the obtained variance according to Equation 4.22:

$$\log D_Z^2(V) = \log D_Z^2 + \log A_3 - \log V \quad (4.27)$$

Following the method proposed in [Kanit et al., 2003], considering a large number n of realizations (or sub-volumes), the following sampling error in the estimation of the effective properties arises:

$$\epsilon_{\text{abs}} = \frac{2D_Z(V)}{\sqrt{n}} \quad (4.28)$$

From which the relative error ϵ_{rel} can be defined:

$$\epsilon_{\text{rel}} = \frac{\epsilon_{\text{abs}}}{\bar{Z}} = \frac{2D_Z(V)}{\bar{Z}\sqrt{n}} \Rightarrow \epsilon_{\text{rel}}^2 = \frac{4D_Z^2 A_3}{\bar{Z}^2 n V} \quad (4.29)$$

Hence a volume size that we will consider statistically representative can be defined for a prescribed property Z , number of realizations n and relative error (e.g. 5%):

$$V_{\text{RVE}} = \frac{4D_Z^2 A_3}{\epsilon_{\text{rel}}^2 \bar{Z}^2 n} \quad (4.30)$$

This RVE size then depends on the point variance D_Z^2 , integral range A_3 and mean value \bar{Z} , 3 parameters that are estimated from simulations.

4.2.5 Generalization of the statistical approach to microstructures with non-finite integral range

The method presented above is now adapted and generalized to the case of media with non-finite integral range, especially *Poisson* linear varieties and Boolean random models made of *Poisson* linear varieties, *e.g.* *Poisson* fibers. Since the integral range of linear *Poisson* varieties is not finite [Jeulin, 1991a], Equation 4.22 does not apply anymore. It was proposed in [Lantuéjoul, 1991] to use a modified scaling law with exponent $\gamma < 1$. The variance can thus be rewritten as follows [Jeulin, 2011]:

$$D_Z^2(V) = D_Z^2 \left(\frac{A_3^*}{V} \right)^\gamma \quad (4.31)$$

which yields by linearization,

$$\log D_Z^2(V) = \log D_Z^2 + \gamma \log A_3^* - \gamma \log V \quad (4.32)$$

A_3^* is not the integral of the centered second-order correlation function $\overline{W}_2(h)$ anymore, as defined before in Equation 4.21. Nonetheless, it is homogeneous to a volume of material and can readily be used to determine RVE sizes which can then be obtained by updating the previous definition for relative error:

$$\epsilon_{\text{rel}} = \frac{\epsilon_{\text{abs}}}{\overline{Z}} = \frac{2D_Z(V)}{\overline{Z}\sqrt{n}} \Rightarrow \epsilon_{\text{rel}}^2 = \frac{4D_Z^2 A_3^{*\gamma}}{\overline{Z}^2 n V \gamma} \quad (4.33)$$

Hence yielding an updated definition of the RVE size:

$$V_{\text{RVE}} = A_3^{*\gamma} \sqrt{\frac{4D_Z^2}{\epsilon_{\text{rel}}^2 \overline{Z}^2 n}} \quad (4.34)$$

The generalized integral range A_3^* and scaling-law exponent γ can be estimated from simulations as it was done in [Kanit et al., 2003] and [Altendorf, 2011]. Some results from those sources are gathered in Table 4.1. For a *Voronoi* tessellation, the variance on the morphological properties, *i.e.* the volume fraction of each phase, is inversely proportional to the volume considered, $\gamma = 1$. It can also be observed that for the bulk modulus k^{app} , with a volume fraction of 70% for the phase considered and a contrast of properties of 100, the integral range is smaller for PBC than for SUBC and KUBC. On the other hand, the convergence of the variance with the simulation size is slower with PBC than with SUBC and KUBC. We will study infinite fibers in this work, results from [Altendorf, 2011] are thus of interest for us since they correspond to long-fibers that are randomly distributed in 3D. Interestingly, the convergence of the variance on the volume fraction of fibers is following a scaling law with exponent $\gamma = 0.87$, which is in between the values for infinite fibers ($\gamma = \frac{2}{3}$, *cf.* [Jeulin, 2011]) and short-fibers, or a random distribution of spheres in the extreme case of a shape factor equal to 1, for which $\gamma = 1$ as shown from simulations in

4.2. Statistical approach for determining a RVE size

Source	Morphology	Z	BC	A_3^*	γ
[Kanit et al., 2003]	Voronoi	$V_V (0.5)$	-	1.178	1
[Kanit et al., 2003]	Voronoi	$V_V (0.7)$	-	1.111	1
[Kanit et al., 2003]	Voronoi	$V_V (0.9)$	-	1.177	1
[Kanit et al., 2003]	Voronoi	$k^{\text{app}} (V_V = 0.5, \frac{E_1}{E_2} = 10^2)$	PBC	1.589	0.875
[Kanit et al., 2003]	Voronoi	$k^{\text{app}} (V_V = 0.7, \frac{E_1}{E_2} = 10^2)$	PBC	1.020	0.780
[Kanit et al., 2003]	Voronoi	$k^{\text{app}} (V_V = 0.7, \frac{E_1}{E_2} = 10^2)$	SUBC	1.267	0.915
[Kanit et al., 2003]	Voronoi	$k^{\text{app}} (V_V = 0.7, \frac{E_1}{E_2} = 10^2)$	KUBC	2.088	1.029
[Kanit et al., 2003]	Voronoi	$\mu^{\text{app}} (V_V = 0.7, \frac{E_1}{E_2} = 10^2)$	PBC	1.322	0.763
[Kanit et al., 2003]	Voronoi	$\mu^{\text{app}} (V_V = 0.7, \frac{E_1}{E_2} = 10^3)$	PBC	2.097	0.862
[Altendorf, 2011]	Isotropic fibers	V_V	-	1.743	0.87
[Altendorf, 2011]	Isotropic fibers	μ^{app}	PBC	1.718	0.84
[Altendorf, 2011]	Isotropic fibers	k^{app}	PBC	0.932	0.77

Table 4.1: Estimates of A_3 and γ for various properties, morphologies and boundary conditions

[Jean et al., 2011a]. When considering statistical RVE sizes of microstructures with non-finite integral range for other properties than morphological ones, for which there is no information about the theoretical value of the point variance D_Z^2 , it may be useful to reformulate Equation 4.31 as follows:

$$D_Z^2(V) = KV^{-\gamma} \quad (4.35)$$

with $K = D_Z^2 A_3^{\gamma}$, leaving only 2 parameters to identify from the statistical data obtained by simulation. We will adopt this formulation when studying *Poisson* fibers in Part III.

The method for determining statistical RVE sizes has been studied and used for media with finite integral range in the references [Kanit, 2003, Kanit et al., 2003, Kanit et al., 2006, Madi et al., 2005, Madi, 2006, Madi et al., 2007, Jean, 2009, Jean et al., 2011a, Oumarou et al., 2011]. We implement this approach for media with infinite integral range, *i.e.* *Poisson* fibers, in Section 6.5.

We presented an introduction to analytical and computational homogenization and its implementation using finite elements. We will now apply this technique to study two classes of architected materials: auxetic periodic lattices and stochastic *Poisson* fiber networks, respectively in Part II and Part III.

Résumé

La première partie de ce mémoire est constituée principalement de rappels bibliographiques et de remarques préliminaires concernant l'homogénéisation de milieux hétérogènes. Les lois de comportement thermique et mécanique sont présentées, ainsi que le principe des puissances virtuelles. La notion de volume élémentaire représentatif est discutée à partir de définitions provenant de la littérature. Les conditions aux limites des problèmes d'homogénéisation sont ensuite analysées. Afin de pouvoir comparer les résultats provenant de l'homogénéisation numérique, les estimateurs et autres bornes analytiques sont aussi introduites. Enfin, l'implémentation de l'homogénéisation numérique en utilisant la méthode des éléments finis est présentée, ainsi que la méthode statistique de détermination de la taille du volume élémentaire représentatif dans le cas de milieux aléatoires. Toutes ces notions sont mises à contribution dans les applications des Chapitres 5 et 6.

Application to periodic media Part II

5 Auxetics

The only way to discover the limits of the possible is to go beyond them into the impossible.

— Arthur C. Clarke, *Profiles of the Future* (1973)

This part deals with the determination of the effective mechanical properties of some negative *Poisson's* ratio (NPR) materials. First, an introduction to NPR materials is given in Section 5.1. The computational homogenization procedure presented in Chapter 4 is adapted to the case of cellular materials in Section 5.2. Geometries of the microstructures considered and the classical honeycomb cell are presented in Section 5.3. Volumic FE coupled with periodic homogenization techniques are then used in Section 5.4 to compute the elastic moduli. Anisotropy is then characterized and a comparison is made between the different microstructures considered. An extension of this study to elastoplasticity for the hexachiral lattice is provided in Section 5.5, influence of the hardening modulus is investigated, as well as macroscopic modeling of the plastic compressible behaviour. A new tridimensional auxetic periodic microstructure is proposed and studied in Section 5.6. Structural applicability of auxetics is validated in Section 5.7 with the simulation of spherical and cylindrical elastic indentation tests. Experimental characterization was conducted on auxetic samples manufactured using rapid prototyping, results are presented in Section 5.8. Finally the use of such materials in terms of design and engineering applications is put into perspective in Section 5.9.

5.1 Introduction to auxetics

In the case of isotropic elasticity, mechanical behavior is described by any couple of parameters among these: *Young's* modulus E , *Poisson's* ratio ν , the bulk modulus k and *Lamé's* coefficients λ and μ (also referred to as the shear modulus). *Poisson's* ratio is defined as the ratio of the contraction in the transverse direction to the extension in the longitudinal direction. Material stability requires the tensor of elastic moduli to be positive definite, resulting in a positive *Young's*

modulus E and a *Poisson's* ratio ν ranging from -1 , for unshearable materials, and 0.5 for incompressible or rubber-like materials. Most materials naturally present a positive *Poisson's* ratio, although negative *Poisson's* ratio materials, or auxetics [Evans et al., 1991], have been engineered since the mid-1980s with the pioneering works of [Herakovich, 1984, Almgren, 1985] and [Lakes, 1987]. This new class of materials has been drawing more and more attention since then [Bathurst and Rothenburg, 1988, Caddock and Evans, 1989, Lakes, 1991, Rothenburg et al., 1991, Milton, 1992, Prall and Lakes, 1997, Evans and Alderson, 2000, Yang et al., 2004, Gaspar et al., 2005, Hughes et al., 2010, Alderson et al., 2010], as well as their potential applications [Evans, 1991, Choi and Lakes, 1991, Martin et al., 2008, Spadoni, 2008].

Let us consider several mechanical models involving the *Poisson* ratio ν . First, let us consider the classical formula of isotropic elasticity relating the shear modulus to *Young's* modulus and *Poisson's* ratio:

$$\mu = \frac{E}{2(1 + \nu)} \quad (5.1)$$

For $\nu \rightarrow -1$, the shear modulus μ tends towards $+\infty$. This relationship holds only for isotropic materials, or transversely isotropic materials when the in-plane shear modulus is considered. Another interesting property is the elastic indentation resistance F which is classically related to *Poisson's* ratio by the following formula [Timoshenko and Goodier, 1951]:

$$F \propto (1 - \nu^2)^{-x} \quad (5.2)$$

with exponent x depending on the indentation problem considered. For the classical sphere-to-sphere contact, $x = \frac{2}{3}$ [Hertz, 1881], whereas $x = 1$ for the contact between two cylinders of parallel axes, or for the spherical indentation of a semi-infinite solid. Clearly, an isotropic material with ν close to -1 would exhibit an increased elastic indentation resistance in comparison with the same material (same *Young's* modulus), but with a positive *Poisson's* ratio. This was discussed in the literature and shown from experiments in [Lakes, 1993, Alderson et al., 1994, Alderson et al., 2000]. If one now considers the growth of a penny-shaped crack within an isotropic elastic brittle material under plane-strain conditions, the fracture toughness K_c is related to *Poisson's* ratio as follows [Irwin, 1957]:

$$K_c = \sqrt{\frac{2E\gamma}{1 - \nu^2}} \quad (5.3)$$

with γ the surface energy. Thus, a material with a *Poisson* ratio of -0.3 would exhibit a fracture toughness similar to those of typical metallic materials. Nevertheless, with *Poisson's* ratio close to -1 and same *Young's* modulus and surface energy, this value would increase dramatically. This particular property was investigated in [Choi and Lakes, 1996] for the case of auxetic copper foams. Finally, if one considers the deflection of an isotropic elastic plate subject to a prescribed curvature along direction 1, the associated curvature along direction 2 is due to the *Poisson* effect,

thus yielding [Timoshenko and Goodier, 1951]:

$$R_2 = -\frac{R_1}{\nu} \quad (5.4)$$

with R_1 and R_2 the radii of curvature of the plate respectively along directions 1 and 2. For conventional materials, this yields anticlastic (saddle-shaped) curvature, whereas for auxetic materials, ν being negative, it yields synclastic (dome-shaped) curvature. This enables one to manufacture curved sandwich panels without core buckling. The synclastic curvature property was studied in [Evans, 1991].

Auxetic materials have also been expected to present enhanced acoustic damping [Lipsett and Beltzer, 1988]; this was shown experimentally in [Chen and Lakes, 1996, Chekkal et al., 2010]. The use of auxetics as building blocks for wave-guiding metamaterials has also been investigated in [Spadoni et al., 2009]. Moreover, experiments on auxetic foams seem to provide evidence of better resistance to crash compared to conventional cellular materials [Scarpa et al., 2002].

Poisson's ratio is defined only for isotropic elastic materials. In the anisotropic case, negative apparent *Poisson's* ratio can be defined as the opposite of the ratio between transverse and longitudinal strains for a given specific direction. There is no restriction anymore on the values of the apparent *Poisson* ratio ν^* . We call anisotropic auxetics, materials for which negative apparent *Poisson's* ratio is observed for a sufficiently large set of tensile directions.

5.2 Computational homogenization

The computational framework used for homogenization has been presented in Chapter 4.1. For this application, effective mechanical properties are computed over a unit-cell (defined by its periodicity vectors $\underline{\mathbf{v}}_i$) with periodic boundary conditions (PBC) using FE. Homogenization requires separation between micro and macro scales. In the case of periodic homogenization, the computed effective properties correspond to those of an infinite continuum made of periodic tiles.

Let us consider an elementary volume V including a solid phase V_s and porous one V_p . In the latter, the stress field is extended by setting $\underline{\boldsymbol{\sigma}} = \mathbf{0}$ in V_p . Practically, the macroscopic strain $\underline{\mathbf{E}}$ and stress $\underline{\boldsymbol{\Sigma}}$ are computed by averaging the local fields $\underline{\boldsymbol{\epsilon}}$ and $\underline{\boldsymbol{\sigma}}$. Within the porous phase, stresses are assumed to be equal to zero. Using periodic boundary conditions, and applying a homogeneous

macroscopic strain field $\underline{\mathbf{E}}$ (cf. Section A.1.2), it yields:

$$\begin{aligned}
 \underline{\Sigma} &= \langle \underline{\sigma} \rangle = \frac{1}{V} \int_V \underline{\sigma} dV \\
 &= \frac{1}{V} \int_{V_s} \underline{\sigma} dV + \underbrace{\frac{1}{V} \int_{V_p} \underline{\sigma} dV}_{=0} \\
 &= \frac{V_s}{V} \frac{1}{V_s} \int_{V_s} \underline{\sigma} dV \\
 &= V_V^s \langle \underline{\sigma} \rangle_s
 \end{aligned} \tag{5.5}$$

$$\tag{5.6}$$

with V_V^s , volume fraction of the solid phase. Let us now consider the case of a prescribed homogeneous macroscopic stress $\underline{\Sigma}$:

$$\begin{aligned}
 \underline{\mathbf{E}} &= \langle \underline{\epsilon} \rangle = \frac{1}{V} \int_V \underline{\epsilon} dV \\
 &= \frac{1}{V} \int_{V_s} \underline{\epsilon} dV + \frac{1}{V} \int_{V_p} \underline{\epsilon} dV \\
 &= \frac{V_s}{V} \frac{1}{V_s} \int_{V_s} \underline{\epsilon} dV + \frac{V_p}{V} \frac{1}{V_p} \int_{V_p} \underline{\epsilon} dV \\
 &= V_V^s \langle \underline{\epsilon} \rangle_s + V_V^p \langle \underline{\epsilon} \rangle_p
 \end{aligned} \tag{5.7}$$

with V_V^p , volume fraction of the porous phase.

5.3 Microstructures considered

5.3.1 Hexachiral lattice

This chiral microstructure was first proposed by Lakes in 1991 [Lakes, 1991], then studied in [Prall and Lakes, 1997, Spadoni, 2008, Alderson et al., 2010, Dirrenberger et al., 2011]. Based on the parameters defined in reference [Alderson et al., 2010], cell geometry can be described in this way: the circular nodes have radius r , the ligaments have length L , and both have in common wall thickness t (cf. figure 5.1(a)) as well as depth d , which in our case is considered infinite due to periodicity conditions along direction 3. Hence, three dimensionless parameters can be derived as shown in Equations 5.8 to 5.10. On Figure 5.1(b), $\alpha = 5$, $\beta = 0.25$ and $\gamma \rightarrow +\infty$. These parameters correspond to a volume fraction of 15%. The microstructure is invariant by a rotation of order 6, which provides transverse hemitropy, which is equivalent to transverse isotropy in the case of linear elasticity. An in-depth study of symmetries in architected materials was

conducted in [Auffray, 2008a, Auffray, 2008b].

$$\alpha = L/r \tag{5.8}$$

$$\beta = t/r \tag{5.9}$$

$$\gamma = d/r \tag{5.10}$$

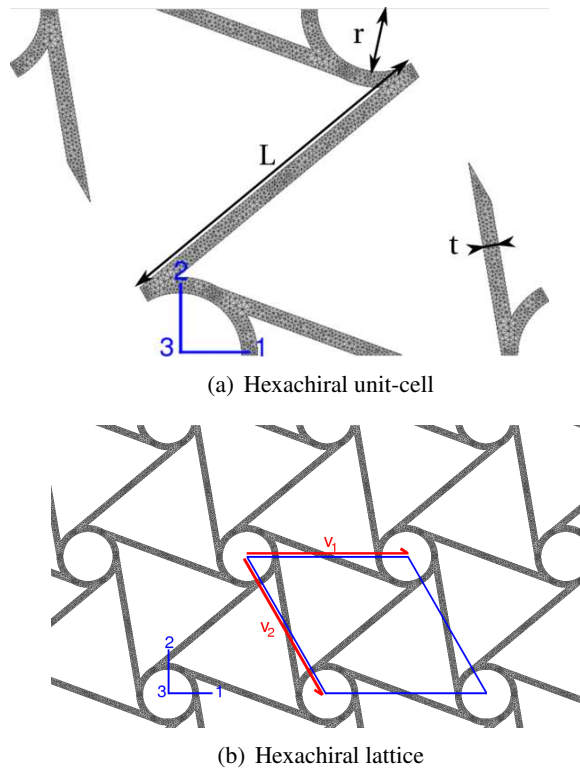


Figure 5.1: (a) Periodic cell with geometric parameters. (b) Hexachiral lattice with unit-cell (blue) and periodicity vectors \underline{v}_1 and \underline{v}_2 (red).

5.3.2 Anti-tetrachiral lattice

This microstructure was proposed and studied in [Alderson et al., 2010]. Cell geometry can be described exactly as for the hexachiral lattice, *cf.* Figure 5.2(a). Here, $\alpha = 11$, $\beta = 0.06$ and $\gamma \rightarrow +\infty$, *cf.* Figure 5.2(b). Volume fraction is 15%. The cell is invariant by a rotation in-plane of order 4, thus giving rise to quadratic elasticity.

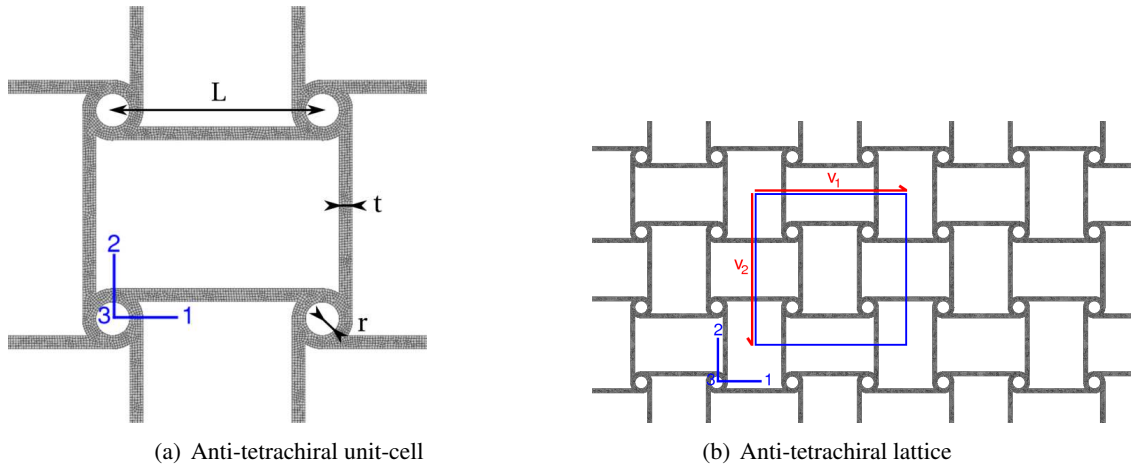


Figure 5.2: (a) Periodic cell with geometric parameters. (b) Anti-tetrachiral lattice with unit-cell (blue) and periodicity vectors \underline{v}_1 and \underline{v}_2 (red).

5.3.3 Rotachiral lattice

This chiral microstructure, initially proposed in [Dirrenberger et al., 2011], has been designed based on ideas from [Prall and Lakes, 1997] and [Gaspar et al., 2005], the aim was to study the impact of ligaments geometry on auxeticity for chiral lattices. It was also investigated in [Alvarez Elipe and Diaz Lantada, 2012]. Cell geometry is similar to the hexachiral case, except for the straight ligaments that have been replaced by circular ones with diameter D , cf. Figure 5.3(a). A new dimensionless parameter is defined by:

$$\delta = D/r \quad (5.11)$$

As shown on Figure 5.3(b), $\delta = 2.4$, $\beta = 0.1$ and $\gamma \rightarrow +\infty$. Volume fraction is 15%. As for the hexachiral lattice, the 6-fold symmetry provides transverse isotropy.

5.3.4 Honeycomb lattice

For the purpose of this work, the classical honeycomb lattice is considered as a comparison medium. The 6-fold symmetry provides transverse isotropy. Geometry can be described using the same parameters as for the rotachiral lattice. For a regular hexagonal honeycomb cell, r and D are not independent and $\delta = \sqrt{3}$, cf. Figure 5.4(a). Also, $\beta = 0.15$ and $\gamma \rightarrow +\infty$, which corresponds to 15% of volume fraction as for the other microstructures considered in this work. Unit-cell for this microstructure has been chosen hexagonal but it could have been square or rhomboid shaped as for the previous lattices, cf. Figure 5.4(b).

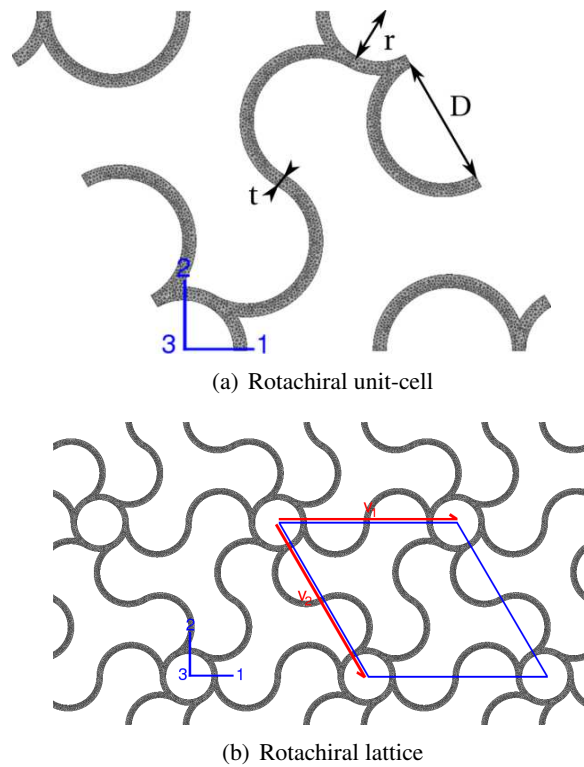


Figure 5.3: (a) Periodic cell with geometric parameters. (b) Rotachiral lattice with unit-cell (blue) and periodicity vectors \underline{v}_1 and \underline{v}_2 (red).

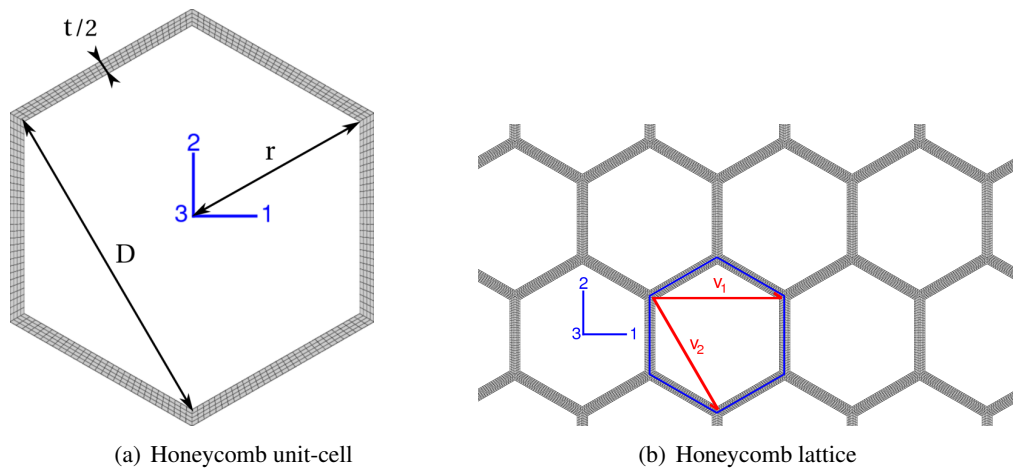


Figure 5.4: (a) Periodic cell with geometric parameters. (b) Honeycomb lattice with unit-cell (blue) and periodicity vectors \underline{v}_1 and \underline{v}_2 (red).

5.4 Effective elastic properties

The tensor of elastic moduli $\underline{\underline{C}}$ is computed over a periodic unit-cell for each microstructure using Z-Set FE software¹. Meshes are composed of volumic fully-integrated quadratic elements, such

¹<http://www.zset-software.com/>

as 10-node tetrahedra and 20-node hexahedra. Using the *Euler–Bunge* [Bunge, 1982] angles ϕ , θ and ψ as shown on Figure 5.5, let us define 3 orthogonal vectors \underline{l} , \underline{m} and \underline{n} , such that:

$$[\underline{l}] = \begin{bmatrix} \cos(\phi) \cos(\psi) - \sin(\phi) \sin(\psi) \cos(\theta) \\ \sin(\phi) \cos(\psi) + \cos(\phi) \sin(\psi) \cos(\theta) \\ \sin(\psi) \sin(\theta) \end{bmatrix} \quad (5.12)$$

$$[\underline{m}] = \begin{bmatrix} -\cos(\phi) \sin(\psi) - \sin(\phi) \cos(\psi) \cos(\theta) \\ -\sin(\phi) \sin(\psi) + \cos(\phi) \cos(\psi) \cos(\theta) \\ \cos(\psi) \sin(\theta) \end{bmatrix} \quad (5.13)$$

$$[\underline{n}] = \begin{bmatrix} \sin(\phi) \sin(\theta) \\ -\cos(\phi) \sin(\theta) \\ \cos(\theta) \end{bmatrix} \quad (5.14)$$

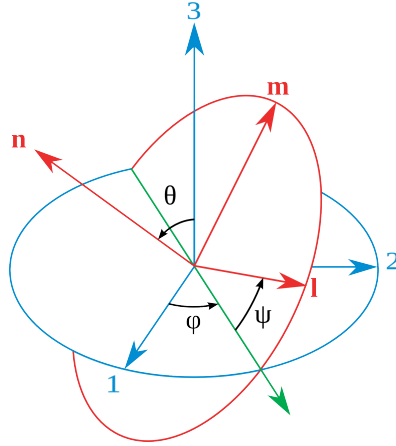


Figure 5.5: *Euler–Bunge* angles

Using macroscopic strain and stress tensors $\underline{E}(\phi, \theta, \psi)$ and $\underline{\Sigma}(\phi, \theta, \psi)$, one can now define the *Young* modulus E and effective *Poisson* ratio ν^* for any uniaxial tensile test along direction \underline{l} , and the shear modulus μ for any shear test within directions $(\underline{l}, \underline{m})$ as follows:

$$E(\underline{l}) = \frac{\underline{l} \cdot \underline{\Sigma} \cdot \underline{l}}{\underline{l} \cdot \underline{E} \cdot \underline{l}} \quad (5.15)$$

$$\mu(\underline{l}, \underline{m}) = \frac{\underline{l} \cdot \underline{\Sigma} \cdot \underline{m}}{\underline{l} \cdot \underline{E} \cdot \underline{m}} \quad (5.16)$$

$$\nu^*(\underline{\mathbf{l}}, \underline{\mathbf{m}}) = -\frac{\underline{\mathbf{m}} \cdot \underline{\mathbf{E}} \cdot \underline{\mathbf{m}}}{\underline{\mathbf{l}} \cdot \underline{\mathbf{E}} \cdot \underline{\mathbf{l}}} \quad (5.17)$$

For $\theta = \psi = 0$, elastic moduli and *Poisson's* ratios are obtained in the plane (1,2) as functions of ϕ , we will refer to those as in-plane elastic properties. On the other hand, when $\phi = 0$ and $\theta = \frac{\pi}{2}$, one obtains moduli and *Poisson's* ratios within plane (1,3) as functions of ψ . These values will be considered as out-of-plane elastic properties.

For comparison purposes, normalized elastic moduli are defined using V_V^s , volume fraction of solid phase, local constitutive isotropic elastic material parameters such as E_0 (*Young's* modulus) and μ_0 . Shear modulus μ_0 is defined from E_0 and *Poisson's* ratio ν_0 as follows:

$$\mu_0 = \frac{E_0}{2(1 + \nu_0)} \quad (5.18)$$

Thus, normalized *Young's* modulus E^* is obtained as follows:

$$E^*(\underline{\mathbf{l}}) = \frac{1}{E_0 V_V^s} E(\underline{\mathbf{l}}) \quad (5.19)$$

Normalized shear modulus μ^* is defined in this way:

$$\mu^*(\underline{\mathbf{l}}, \underline{\mathbf{m}}) = \frac{1}{\mu_0 V_V^s} \mu(\underline{\mathbf{l}}, \underline{\mathbf{m}}) \quad (5.20)$$

In-plane elastic properties are shown in Table 5.1 and plotted against ϕ for the anti-tetrachiral cell on Figures 5.8 and 5.9 (polar plots). The use of auxetic lattices in engineering applications might involve out-of-plane loading. Hence, $\nu^*(\underline{\mathbf{l}}, \underline{\mathbf{m}})$, $E^*(\underline{\mathbf{l}})$ and $\mu^*(\underline{\mathbf{l}}, \underline{\mathbf{m}})$ were also plotted against ψ on Figures 5.6 to 5.15. For this work, $E_0 = 210000$ MPa and $\nu_0 = 0.3$. The resulting elastic moduli tensors are presented in Equations 5.21 for the hexachiral lattice, 5.22 for the anti-tetrachiral lattice, 5.23 for the rotachiral lattice and 5.24 for the honeycomb lattice. Components are expressed in MPa.

5.4.1 Hexachiral lattice

Transverse isotropy is verified since $\frac{C_{11} - C_{12}}{2} = C_{66}$. Components were used to obtain the in-plane properties gathered in Table 5.1. $\nu^*(\underline{\mathbf{l}}, \underline{\mathbf{m}})$ is underestimated compared to the value from [Alderson et al., 2010], while our estimation of the normalized *Young's* modulus $E^*(\underline{\mathbf{l}})$ is higher. This is discussed later. Figure 5.6 shows an increase of $E^*(\underline{\mathbf{l}})$ when the material is stretched out-of-plane, while reaching its maximum value along direction 3 ($\psi = \frac{\pi}{2}$). Figure 5.7 shows that *Poisson's* ratio $\nu^*(\underline{\mathbf{l}}, \underline{\mathbf{m}})$ is always negative, except for $\psi = 0$ where $\nu^*(\underline{\mathbf{l}}, \underline{\mathbf{m}})$ is close

to 0, and $\psi = \frac{\pi}{2}$ where it takes the constitutive material value 0.3. Normalized shear modulus $\mu^*(\underline{\mathbf{l}}, \underline{\mathbf{m}})$ fluctuates in a decade around the in-plane value depending on angle ψ . A similar kind of 6-fold symmetric chiral lattice was proposed and studied in [Mitschke et al., 2011], yielding the same value for the value for in-plane effective *Poisson's* ratio.

$$[C] = \begin{bmatrix} 1650 & -1218 & 130 & 0 & 0 & 0 \\ -1218 & 1650 & 130 & 0 & 0 & 0 \\ 130 & 130 & 31968 & 0 & 0 & 0 \\ 0 & 0 & 0 & 5075 & 0 & 0 \\ 0 & 0 & 0 & 0 & 5075 & 0 \\ 0 & 0 & 0 & 0 & 0 & 1434 \end{bmatrix} \quad (5.21)$$

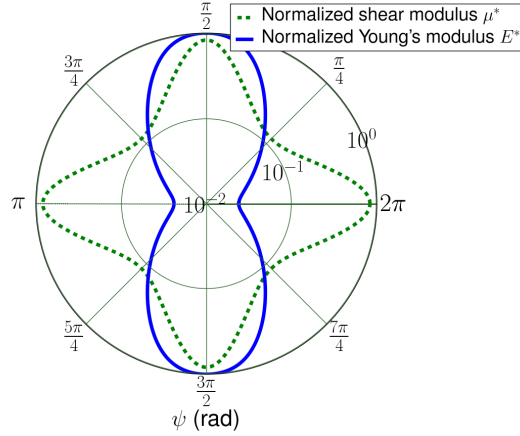


Figure 5.6: Hexachiral lattice ($\theta = \frac{\pi}{2}$, $\phi = 0$)

5.4.2 Anti-tetrachiral lattice

The tensor given below verifies quadratic elasticity (invariant by rotation of $\frac{\pi}{2}$ in plane). Figure 5.9 shows that in the cell's principal directions, $\nu^*(\underline{\mathbf{l}}, \underline{\mathbf{m}})$ is lower than the value from [Alderson et al., 2010], for the same lattice with approximately the same geometric parameters, but the normalized *Young* modulus $E^*(\underline{\mathbf{l}})$ is higher as shown on Figure 5.8. Besides, $\mu^*(\underline{\mathbf{l}}, \underline{\mathbf{m}})$ fluctuates over 2 decades and reaches its minimum when $\nu^*(\underline{\mathbf{l}}, \underline{\mathbf{m}})$ is close to -1 . $\nu^*(\underline{\mathbf{l}}, \underline{\mathbf{m}})$ is negative for short angle intervals around the principal directions of the cell. $E^*(\underline{\mathbf{l}})$ is varying over less than one order of magnitude depending on ϕ . Normalized out-of-plane moduli are plotted on Figure 5.10, which is very comparable with Figure 5.6 in terms of values and angles. $E^*(\underline{\mathbf{l}})$ is higher than or equal to in-plane values. $\nu^*(\underline{\mathbf{l}}, \underline{\mathbf{m}})$ is always negative as shown on Figure 5.11, except for $\psi = 0$ where $\nu^*(\underline{\mathbf{l}}, \underline{\mathbf{m}})$ is close to 0, and $\psi = \frac{\pi}{2}$ where it takes the bulk material value

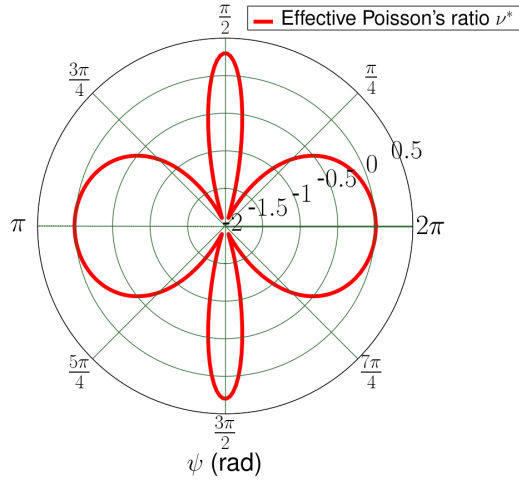


Figure 5.7: Hexachiral lattice ($\theta = \frac{\pi}{2}$, $\phi = 0$)

0.3 as for the hexachiral lattice. $\mu^*(\underline{l}, \underline{m})$ fluctuates less with ϕ than with ψ .

$$[C] = \begin{bmatrix} 5474 & -5040 & 130 & 0 & 0 & 0 \\ -5040 & 5474 & 130 & 0 & 0 & 0 \\ 130 & 130 & 31233 & 0 & 0 & 0 \\ 0 & 0 & 0 & 5184 & 0 & 0 \\ 0 & 0 & 0 & 0 & 5184 & 0 \\ 0 & 0 & 0 & 0 & 0 & 39 \end{bmatrix} \quad (5.22)$$

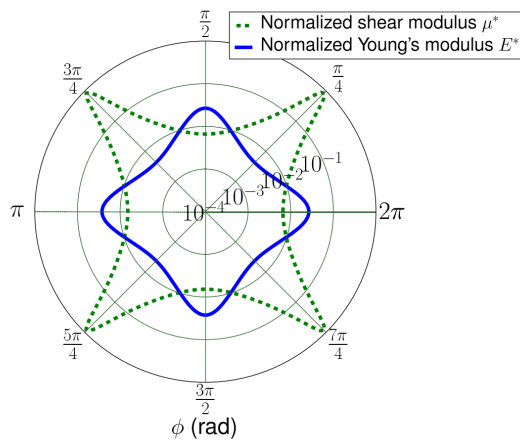


Figure 5.8: Anti-tetrachiral lattice ($\theta = 0$, $\psi = 0$)

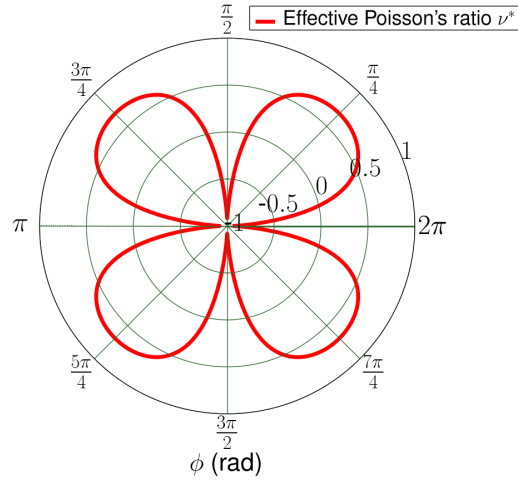


Figure 5.9: Anti-tetrachiral lattice ($\theta = 0, \psi = 0$)

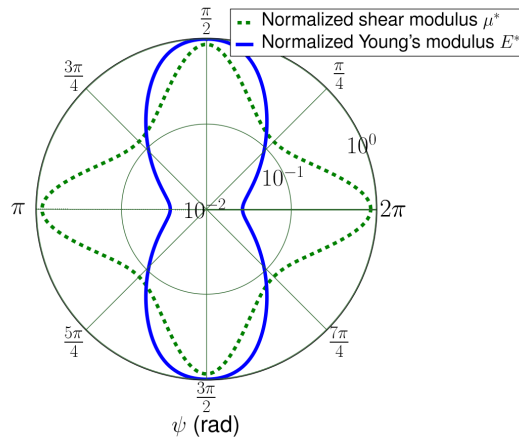


Figure 5.10: Anti-tetrachiral lattice ($\theta = \frac{\pi}{2}, \phi = 0$)

5.4.3 Rotachiral lattice

Elastic moduli tensor components for the rotachiral lattice are given in Equation 5.23. As for the hexachiral lattice, transverse isotropy is verified by the following relationship $\frac{C_{11} - C_{12}}{2} = C_{66}$. The in-plane normalized moduli and effective *Poisson* ratio are listed in Table 5.1. $E^*(\underline{l})$ and $\mu^*(\underline{l}, \underline{m})$ are about one order of magnitude lower than for the hexachiral lattice. Figure 5.12 shows an increase of $E^*(\underline{l})$ which fluctuates over 3 orders of magnitude when the material is stretched out-of-plane. $\nu^*(\underline{l}, \underline{m})$ is always negative as shown on Figure 5.13, except for $\psi = 0$ or $\psi = \pi$ where $\nu^*(\underline{l}, \underline{m})$ is close to 0, and $\psi = \frac{\pi}{2}$ or $\psi = \frac{3\pi}{2}$ where it reaches 0.3, which is the constituent value. Normalized shear modulus $\mu^*(\underline{l}, \underline{m})$ is always higher than its in-plane

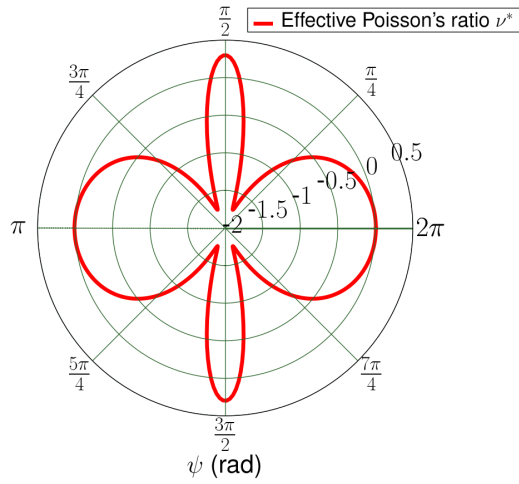


Figure 5.11: Anti-tetrachiral lattice ($\theta = \frac{\pi}{2}$, $\phi = 0$)

counterpart.

$${}_{\alpha}[\mathbf{C}] = \begin{bmatrix} 93 & -24 & 20 & 0 & 0 & 0 \\ -24 & 93 & 20 & 0 & 0 & 0 \\ 20 & 20 & 31617 & 0 & 0 & 0 \\ 0 & 0 & 0 & 3605 & 0 & 0 \\ 0 & 0 & 0 & 0 & 3605 & 0 \\ 0 & 0 & 0 & 0 & 0 & 59 \end{bmatrix} \quad (5.23)$$

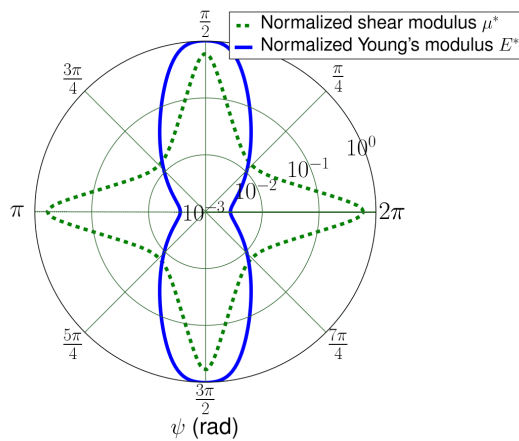


Figure 5.12: Rotachiral lattice ($\theta = \frac{\pi}{2}$, $\phi = 0$)

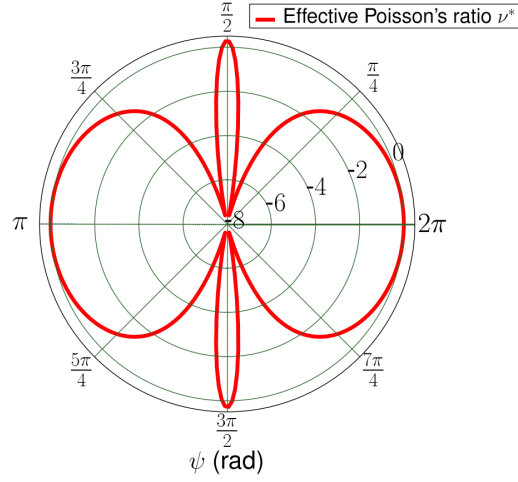


Figure 5.13: Rotachiral lattice ($\theta = \frac{\pi}{2}$, $\phi = 0$)

5.4.4 Honeycomb lattice

Transverse isotropy is verified since $\frac{C_{11} - C_{12}}{2} = C_{66}$. Components were used to obtain the in-plane properties gathered in Table 5.1. $\nu^*(\underline{\mathbf{l}}, \underline{\mathbf{m}})$ differs from the theoretical value of 1, due to the beams infinite slenderness hypothesis which is not fulfilled in our full-field simulations. Figure 5.14 shows an increase of $E^*(\underline{\mathbf{l}})$ when the material is stretched out-of-plane. Surprisingly, out-of-plane, the effective *Poisson's* ratio $\nu^*(\underline{\mathbf{l}}, \underline{\mathbf{m}})$ shown on Figure 5.15 is almost always negative for the honeycomb lattice, except for $\psi = 0$ or $\psi = \pi$ where $\nu^*(\underline{\mathbf{l}}, \underline{\mathbf{m}})$ is close to 0, and along direction 3 ($\psi = \frac{\pi}{2}$ or $\psi = \frac{3\pi}{2}$) where it takes the bulk material value 0.3 as for the other microstructures. Out-of-plane $\mu^*(\underline{\mathbf{l}}, \underline{\mathbf{m}})$ and $E^*(\underline{\mathbf{l}})$ are always equal or higher than their in-plane counterparts.

$$[\underline{\underline{\mathbf{C}}}] = \begin{bmatrix} 9945 & 9259 & 5761 & 0 & 0 & 0 \\ 9259 & 9945 & 5761 & 0 & 0 & 0 \\ 5761 & 5761 & 35070 & 0 & 0 & 0 \\ 0 & 0 & 0 & 6512 & 0 & 0 \\ 0 & 0 & 0 & 0 & 6512 & 0 \\ 0 & 0 & 0 & 0 & 0 & 343 \end{bmatrix} \quad (5.24)$$

5.4.5 Discussion

Values obtained in this work for $E^*(\underline{\mathbf{l}})$ (cf. Table 5.1) exceed those from [Alderson et al., 2010]. This is due to the boundary conditions of the FE problem. The nodal force loading prescribed

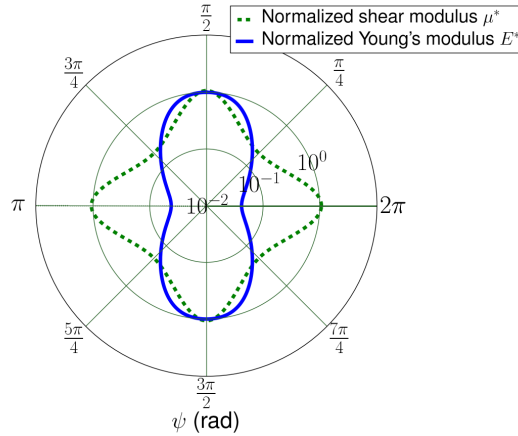


Figure 5.14: Honeycomb lattice ($\theta = \frac{\pi}{2}$, $\phi = 0$)

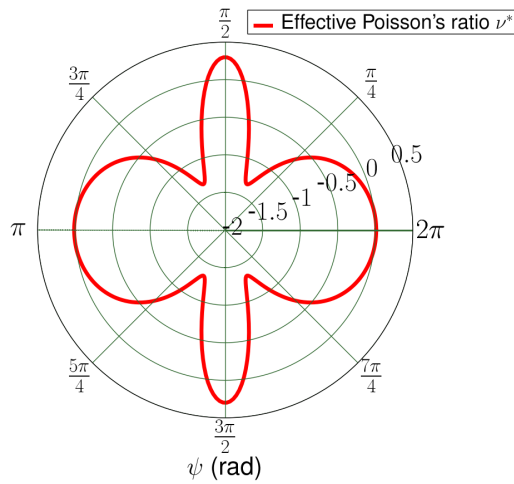


Figure 5.15: Honeycomb lattice ($\theta = \frac{\pi}{2}$, $\phi = 0$)

in [Alderson et al., 2010] actually corresponds to a static uniform boundary conditions (SUBC) micromechanical problem, which is known for underestimating elastic moduli. On the other hand, the periodic boundary conditions used in this work give exact results for a linear elastic infinite medium. While the honeycomb cell exhibits the higher normalized in-plane *Young* modulus, the hexachiral lattice presents a normalized shear modulus $\mu^*(\underline{l}, \underline{m})$ about 4 times higher. The hexachiral, anti-tetrachiral, rotachiral and honeycomb lattices all present a strong anisotropy when loaded out-of-plane (cf. Figures 5.6, 5.10, 5.12 and 5.14). An extreme *Poisson's* ratio value of -8 can be reached for the rotachiral lattice as shown on figure 5.13. It is worth noting that the anti-tetrachiral lattice presents a negative in-plane *Poisson's* ratio only for quite small angle intervals. Interestingly, for each microstructure, even the honeycomb lattice, $\nu^*(\underline{l}, \underline{m})$ is almost always negative when a function of angle ψ . The hexachiral, anti-tetrachiral and honeycomb lattices show comparable values in terms of magnitude for normalized elastic moduli as functions

	Hexachiral	Anti-tetrachiral	Rotachiral	Honeycomb
$\nu^*(\underline{\mathbf{l}}, \underline{\mathbf{m}})$	-0.73	[-0.92; 0.69]	-0.26	0.92
$E^*(\underline{\mathbf{l}})$	2.3×10^{-2}	$[4.3 \times 10^{-3}; 2.7 \times 10^{-2}]$	2.7×10^{-3}	4.2×10^{-2}
$\mu^*(\underline{\mathbf{l}}, \underline{\mathbf{m}})$	2.3×10^{-1}	$[6.6 \times 10^{-3}; 8.8 \times 10^{-1}]$	9.6×10^{-3}	5.6×10^{-2}

Table 5.1: In-plane *Poisson's* ratio and normalized elastic moduli

of ψ . For the same volume fraction, the impact on in and out-of-plane mechanical properties from the change in ligaments geometry between hexachiral and rotachiral lattices is critical: circular ligaments give values which are more than one order of magnitude lower for both $E^*(\underline{\mathbf{l}})$ and $\mu^*(\underline{\mathbf{l}}, \underline{\mathbf{m}})$.

5.5 Extension to elastoplasticity

We are now interested in the interaction between auxeticity and plasticity. Computational experiments are carried out on the hexachiral cell, which was presented in Section 5.3.1.

5.5.1 Constitutive model considered

In the case of elastoplasticity, the strain rate can be decomposed in an elastic strain rate part $\dot{\underline{\boldsymbol{\epsilon}}}^{\text{el}}$ and a plastic strain rate part $\dot{\underline{\boldsymbol{\epsilon}}}^{\text{pl}}$, such that:

$$\dot{\underline{\boldsymbol{\epsilon}}} = \dot{\underline{\boldsymbol{\epsilon}}}^{\text{el}} + \dot{\underline{\boldsymbol{\epsilon}}}^{\text{pl}} \quad (5.25)$$

Let us consider the following yield function $f(\underline{\boldsymbol{\sigma}})$:

$$f(\underline{\boldsymbol{\sigma}}) = \sigma^{\text{eq}} - \tau \quad (5.26)$$

with the *von Mises* equivalent stress,

$$\sigma^{\text{eq}} = \sqrt{\frac{3}{2} \underline{\boldsymbol{\sigma}}^{\text{dev}} : \underline{\boldsymbol{\sigma}}^{\text{dev}}} \quad (5.27)$$

where $\underline{\boldsymbol{\sigma}}^{\text{dev}}$ is the deviatoric part of the stress tensor. Based on experimental evidence obtained in [Deshpande and Fleck, 2000] for metallic foams, associated plasticity is assumed. The plastic strain rate can then be defined in this way:

$$\dot{\underline{\boldsymbol{\epsilon}}}^{\text{pl}} = \dot{p} \frac{3}{2} \frac{\underline{\boldsymbol{\sigma}}^{\text{dev}}}{\sigma^{\text{eq}}} \quad (5.28)$$

Yield stress (MPa)	100
Hardening modulus (MPa)	{100, 1000, 10000}

Table 5.2: Constitutive plastic parameters

and the cumulative plastic strain rate \dot{p} :

$$\dot{p} = \sqrt{\frac{2}{3} \dot{\underline{\epsilon}}^{\text{pl}} : \dot{\underline{\epsilon}}^{\text{pl}}} \quad (5.29)$$

A linear isotropic hardening rule is adopted:

$$r = r_0 + hp \quad (5.30)$$

where r_0 is the yield stress, h the hardening modulus and p the cumulative plastic strain.

Local material is now considered isotropic *von Mises* elastoplastic. Plastic material parameters are shown in Table 5.2.

First, the auxetic behavior is investigated. Although the parameters given in Table 5.2 will be used in the following sections, a short parametric study has been performed in order to assess the effect of the hardening modulus on the *Poisson* ratio. Uniaxial strain-controlled tensile test is performed along direction 1 until 4% of total macroscopic strain. The homogenized cell exhibits a nonlinear elastoplastic behavior, *cf.* Figure 5.19. Now, if one considers the ratio of transverse over longitudinal macroscopic strains, an apparent *Poisson's* ratio can be defined in the nonlinear regime as defined in Equation 5.31 and plotted on Figure 5.19. From these curves we observe that the auxetic nature of the lattice is kept with plasticity. The effect is even stronger than in elasticity when the hardening modulus is in the range $h = 100\text{--}1000$ MPa. The auxetic effect is dependent on the size of the plastic zone in the unit cell. If the plastic zone is confined to a small domain around the junction between the rotating nodes and the connecting beams, as shown on Figure 5.16 and 5.17 for low values of the hardening modulus, the auxetic deformation mechanism is strengthened. For $h = 10000$ MPa, the plastic zone spreads almost over the entire cell (*cf.* Figure 5.18), thus fading the effect of plasticity on the auxetic behavior. The hardening modulus value, $h = 1000$ MPa, is kept for the rest of this work since it is of the same order of magnitude as the hardening modulus of many common alloys.

$$v^{\text{app}} = -\frac{E_{22}}{E_{11}} \quad (5.31)$$

Now, anisotropy in the plastic regime is investigated. As a matter of fact, there is no guarantee for

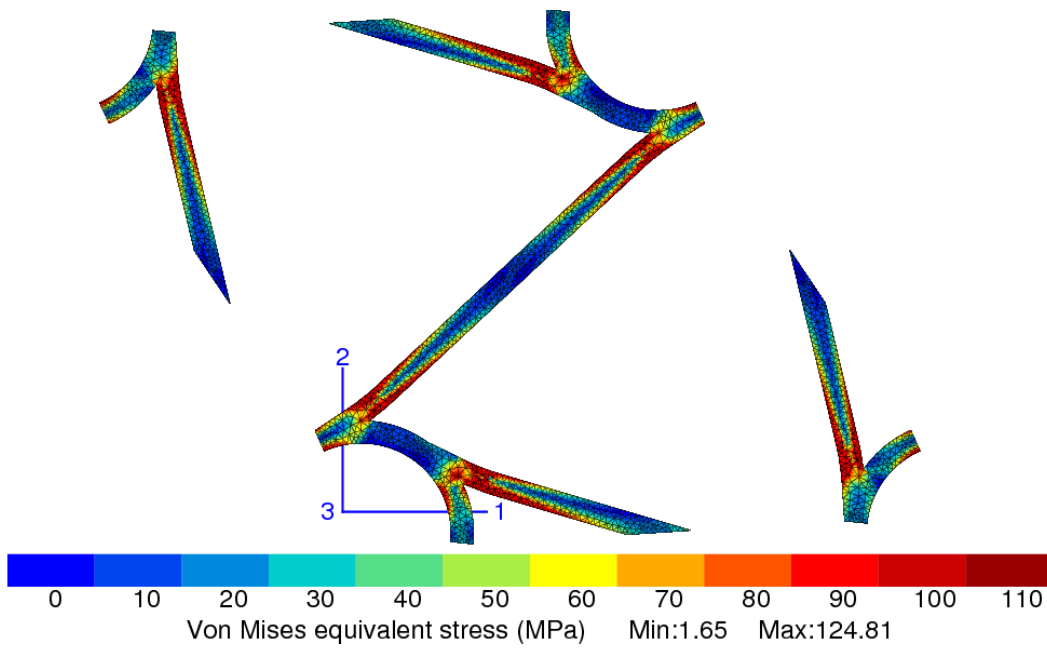


Figure 5.16: Deformed shape of unit-cell after 4% of total strain for a uniaxial tensile test along direction 1, with *von Mises* equivalent stress map ($h = 100$ MPa)

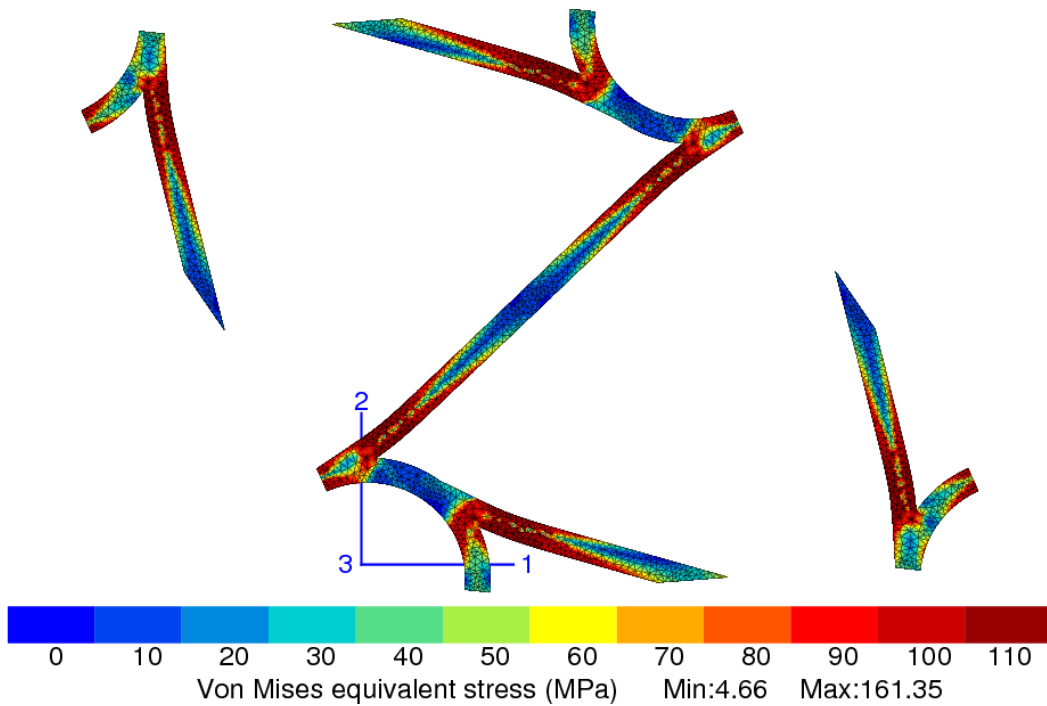


Figure 5.17: Deformed shape of unit-cell after 4% of total strain for a uniaxial tensile test along direction 1, with *von Mises* equivalent stress map ($h = 1000$ MPa)

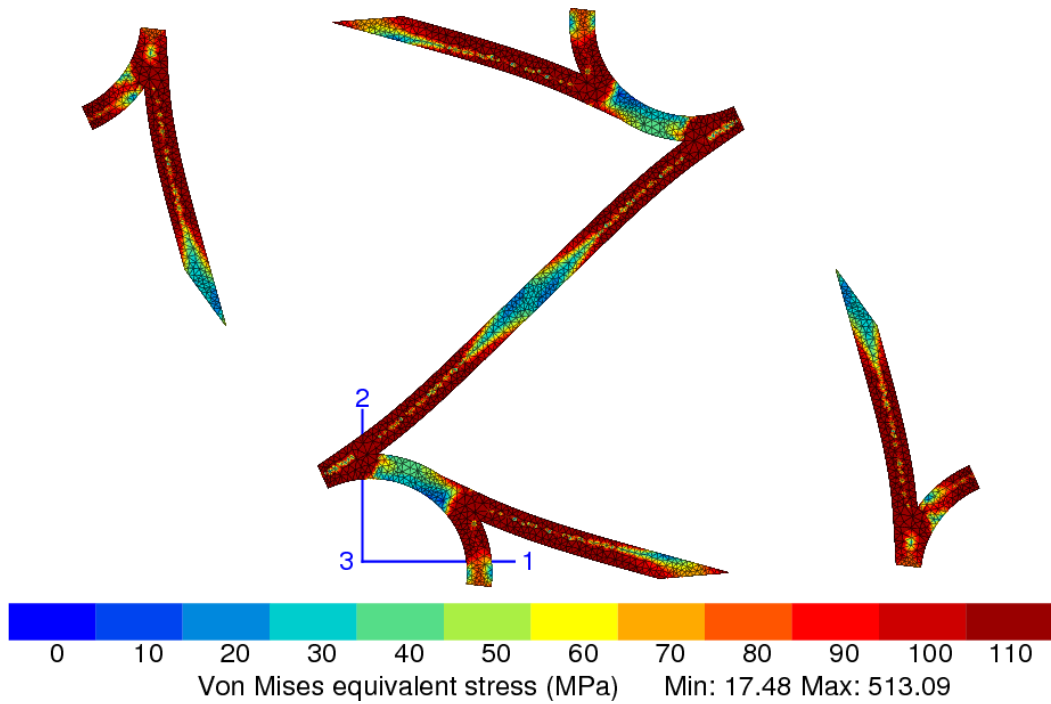


Figure 5.18: Deformed shape of unit-cell after 4% of total strain for a uniaxial tensile test along direction 1, with *von Mises* equivalent stress map ($h = 10000$ MPa)

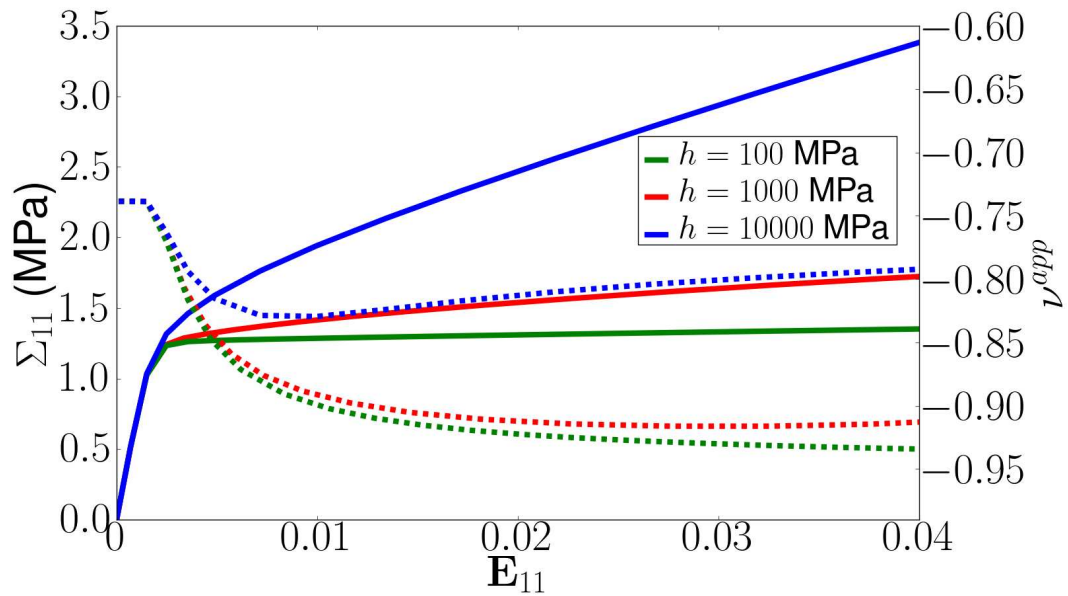


Figure 5.19: Stress and apparent *Poisson's* ratio vs. strain response for the HC cell

the 6-fold symmetric material to behave isotropically in the plastic regime. Polar plots shown on Figures 5.20, 5.21 and 5.22 are obtained from uniaxial tensile and shear tests in every direction of the plane (1,2). Each point corresponds to a test for a different direction with angle ϕ from the

principal direction 1 of the structure defined on Figure 5.16. Figures 5.20 and 5.22 shows stress level versus angle ϕ for three given strain states: respectively 0.2% (green), 1% (red) and 4% (blue) total strain for tension, and 0.1%, 0.5% and 2% for shear. Figure 5.21 uses the same color code but for the apparent *Poisson's* ratio versus angle ϕ for the same given tension states. The three plots show a quasi-transversely isotropic response for the hexachiral lattice with plasticity.

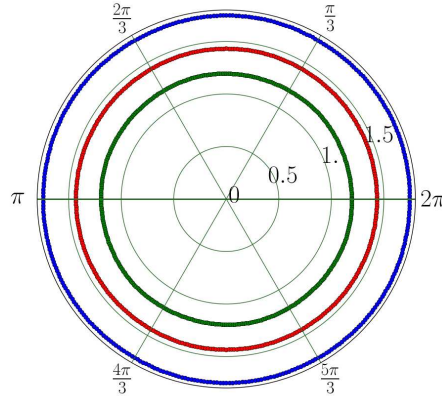


Figure 5.20: Stress level (MPa) for 0.2% (green), 1% (red) and 4% (blue) total strain for the HC cell

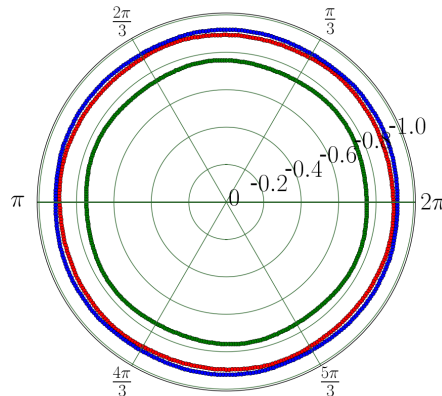


Figure 5.21: Apparent *Poisson's* ratio for 0.2% (green), 1% (red) and 4% (blue) total strain for the HC cell

5.5.2 Comparison with the honeycomb lattice

Starting from the results presented above, a comparison was made with the honeycomb lattice, which was introduced in Section 5.3.4. As for the hexachiral lattice, there is no guarantee for a material that is transversely isotropic in the elastic regime to behave the same with plasticity. Polar plots shown on Figures 5.23, 5.24 and 5.25 are obtained from uniaxial tensile and shear tests in every direction of the plane (1,2). Figures 5.23 and 5.25 show stress level versus angle ϕ for three given strain states: respectively 0.2% (green), 1% (red) and 4% (blue) total strain

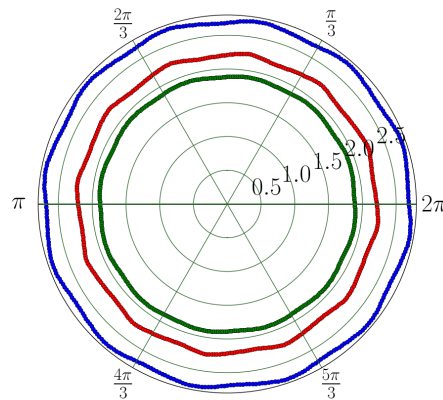


Figure 5.22: Stress level (MPa) for 0.1% (green), 0.5% (red) and 2% (blue) total shear strain for the HC cell

for tension, and 0.1%, 0.5% and 2% for shear. Figure 5.24 uses the same color code but for the apparent *Poisson's* ratio versus angle ϕ for the same given tension states. Regarding stress levels, the honeycomb develops a higher stress than the hexachiral cell in traction. However, the shear stress is as much as 3 times higher for the hexachiral cell than for the honeycomb lattice, this is mainly due to the auxetic nature of the cell. The three plots show a loss of transverse isotropy with plasticity. The honeycomb lattice behaves more anisotropically in the plastic regime in comparison with the hexachiral cell. Nevertheless, as for the hexachiral lattice, the anisotropy is fading with plastic saturation.

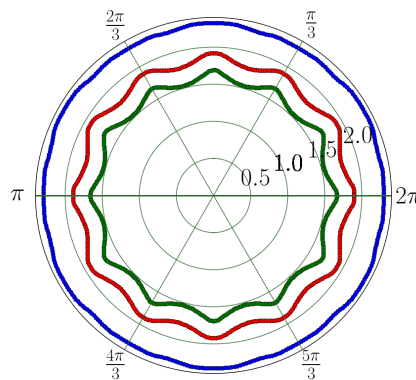


Figure 5.23: Stress level (MPa) for 0.2% (green), 1% (red) and 4% (blue) total strain for the honeycomb lattice

5.5.3 Macroscopic modeling

An additional upscaling is performed. The mesoscopic elastoplastic behavior shown on Figure 5.19 is now modelled as the constitutive behavior of an homogeneous equivalent medium for

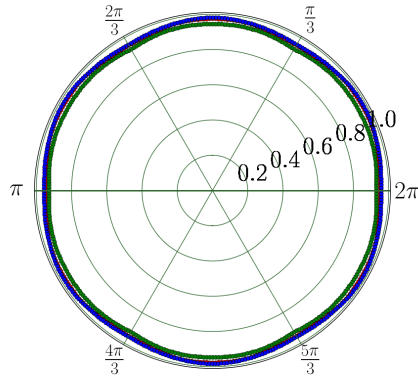


Figure 5.24: Apparent *Poisson's* ratio for 0.2% (green), 1% (red) and 4% (blue) total strain for the honeycomb lattice

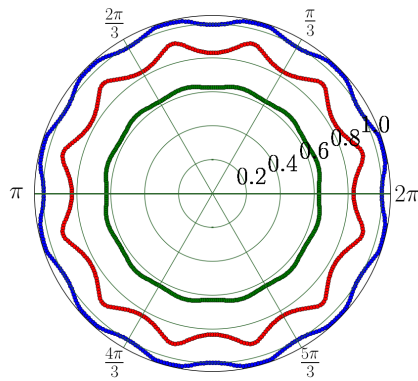


Figure 5.25: Stress level (MPa) for 0.1% (green), 0.5% (red) and 2% (blue) total shear strain for the honeycomb lattice

further use in structural computations. First, let us consider an isotropic compressible plasticity model such as those developed by [Green, 1972] and [Abouaf et al., 1988] for porous metals, and by [Miller, 2000] and [Deshpande and Fleck, 2000] for cellular materials. An extension to the anisotropic case was proposed in [Badiche et al., 2000] and [Forest et al., 2005].

Let us now consider a yield function $f(\Sigma)$ such that,

$$f(\Sigma) = \Sigma_{\text{eq}} - R \tag{5.32}$$

where R is the macroscopic yield stress. Moreover, let us adopt the following equivalent yield

stress:

$$\underline{\Sigma}_{\text{eq}} = \sqrt{\frac{3}{2} \mathbf{C} \underline{\Sigma}^{\text{dev}} : \underline{\Sigma}^{\text{dev}} + F (\text{Tr} \underline{\Sigma})^2} \quad (5.33)$$

where $\text{Tr} \underline{\Sigma}$ is the trace of the stress tensor. \mathbf{C} and F are weighting coefficients accounting for the relative influence of deviatoric and hydrostatic stress, they are usually expressed as functions of the porosity ρ for isotropic porous materials.

Associated plasticity is assumed, such that the macroscopic plastic strain rate is:

$$\dot{\underline{\mathbf{E}}}^{\text{p}} = \dot{\rho} \frac{\partial f}{\partial \underline{\Sigma}} = \frac{\dot{\rho}}{\sigma_{\text{eq}}} \left(\frac{3}{2} \mathbf{C} \underline{\Sigma}^{\text{dev}} + F (\text{Tr} \underline{\Sigma}) \underline{\mathbf{I}} \right) \quad (5.34)$$

In the case of uniaxial tension, we define the in-plane plastic *Poisson* ratio:

$$\nu^{\text{p}} = -\frac{\dot{\mathbf{E}}_{22}^{\text{p}}}{\dot{\mathbf{E}}_{11}^{\text{p}}} = -\frac{F - \frac{\mathbf{C}}{2}}{\mathbf{C} + F} = \frac{\frac{\mathbf{C}}{2} - F}{\mathbf{C} + F} \quad (5.35)$$

When $F = 0$, incompressible plasticity is recovered. If $\mathbf{C} = 1$, then $\nu^{\text{p}} < 0$ for $F > \frac{1}{2}$ and $\lim_{F \rightarrow +\infty} \nu^{\text{p}} = -1$. ν^{p} as a function of F is plotted on Figure 5.26.

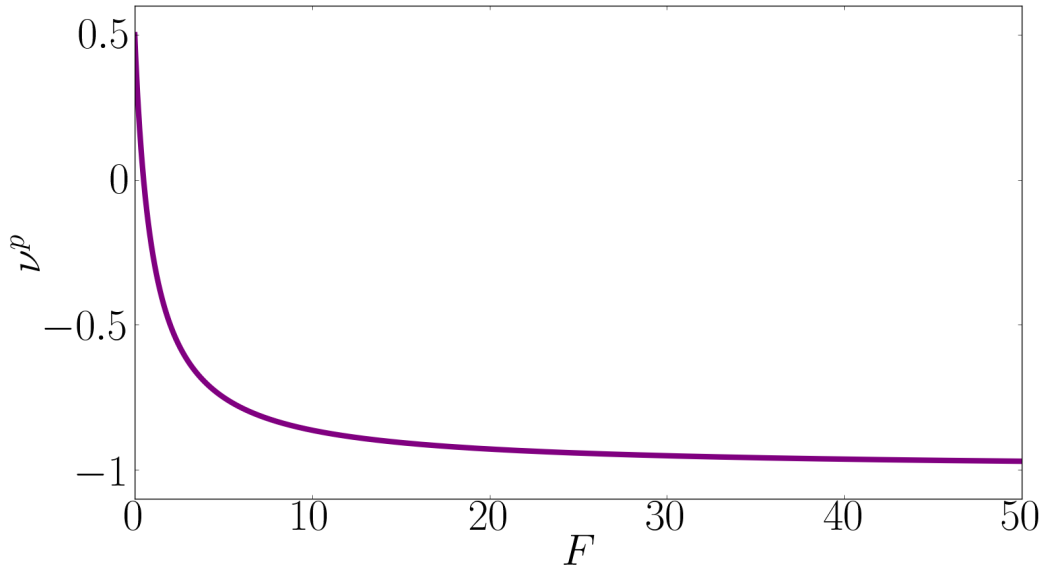


Figure 5.26: Plastic Poisson's ratio for an isotropic material as a function of parameter F , with $\mathbf{C} = 1$

Such a plasticity model is not fully capable of describing the anisotropic behavior of our microstructure along direction 3, especially the transverse contraction when tension is applied

in plane (1,2). In order to simplify the model, instead of using a fully anisotropic *Hill* tensor [Hill, 1950] applied to the deviatoric stress tensor and a separate contribution of the hydrostatic stress, we consider here a generalized *Hill* tensor applied to the *Cauchy* stress tensor².

We consider the same yield function $f(\underline{\Sigma})$ as in Equation 5.32 with the following equivalent yield stress:

$$\Sigma^{\text{eq}} = \sqrt{\underline{\Sigma} : \underline{\underline{H}} : \underline{\Sigma}} \quad (5.36)$$

where $\underline{\underline{H}}$ is the applied generalized *Hill* fourth-rank tensor.

For the hardening rule, we consider an isotropic hardening function with a nonlinear potential and a linear part:

$$R = R_0 + Hp + Q(1 - e^{-bp}) \quad (5.37)$$

5.5.4 Simulation and identification

In order to determine parameters for the model, we first estimate some of them from reference curves obtained by periodic simulations of the unit-cell. Then comparison between reference data with results computed on a RVE is made and optimization of macroscopic material parameters is run using a *Nelder–Mead* (simplex) algorithm. The experimental database includes tensile, shear and *Poisson's* ratio curves. While loading in tension, we consider out-of-plane contraction. However, we do not take into account tension in direction 3 and out-of-plane shear. Tensorial components of $\underline{\underline{H}}$ (cf. Equation 5.41) and parameters for the hardening rule (5.37) are thus identified:

$$R = 1.40 + 8.61p + 0.1(1 - e^{-140p}) \quad (5.38)$$

Identification of the hardening rule was also performed for the two other constitutive hardening moduli: $h = 100$ MPa (Equation 5.39) and $h = 10000$ MPa (Equation 5.40) in order to test the robustness of the identification scheme and to verify the effect of the local hardening modulus on the macroscopic hardening rule:

$$R = 1.26 + 0.62p + 0.1(1 - e^{-160p}) \quad (5.39)$$

²Although the *Hill* tensor is named after the work of *Rodney Hill* after World War II, its actual origin goes back to June 1928 and the paper of *Richard von Mises* in the *Zeitschrift für Angewandte Mathematik und Mechanik* [von Mises, 1928]. One could argue that *von Mises* describes a *Spannungsfunktionen*, a strain function using yielding compliance tensor components, instead of a stress criterion using yielding moduli tensor components. It seems likely that this oversight of the literature was a consequence of the geopolitical environment at the time.

$$R = 1.28 + 25.9p + 1.07(1 - e^{-86p}) \quad (5.40)$$

We observe that linear hardening modulus in the macroscopic rule increases with the local hardening modulus.

Comparison between curves from full-field simulations and the identified macroscopic model provides a good correlation as shown on the tensile stress and apparent *Poisson* ratio vs. strain curve (cf. Figure 5.27), the shear stress vs. strain curve (cf. Figure 5.28) and the transverse strain vs. longitudinal strain curve, cf. Figure 5.29.

$$[\underline{\underline{H}}] = \begin{bmatrix} 1.00 & 0.9294 & -0.00031 & 0.0006 & 0 & 0 \\ 0.9294 & 0.99 & -0.00027 & -0.00067 & 0 & 0 \\ -0.00031 & -0.00027 & \times & 0 & 0 & 0 \\ 0.0006 & -0.00067 & 0 & 0.11554 & 0 & 0 \\ 0 & 0 & 0 & 0 & \times & 0 \\ 0 & 0 & 0 & 0 & 0 & \times \end{bmatrix} \quad (5.41)$$

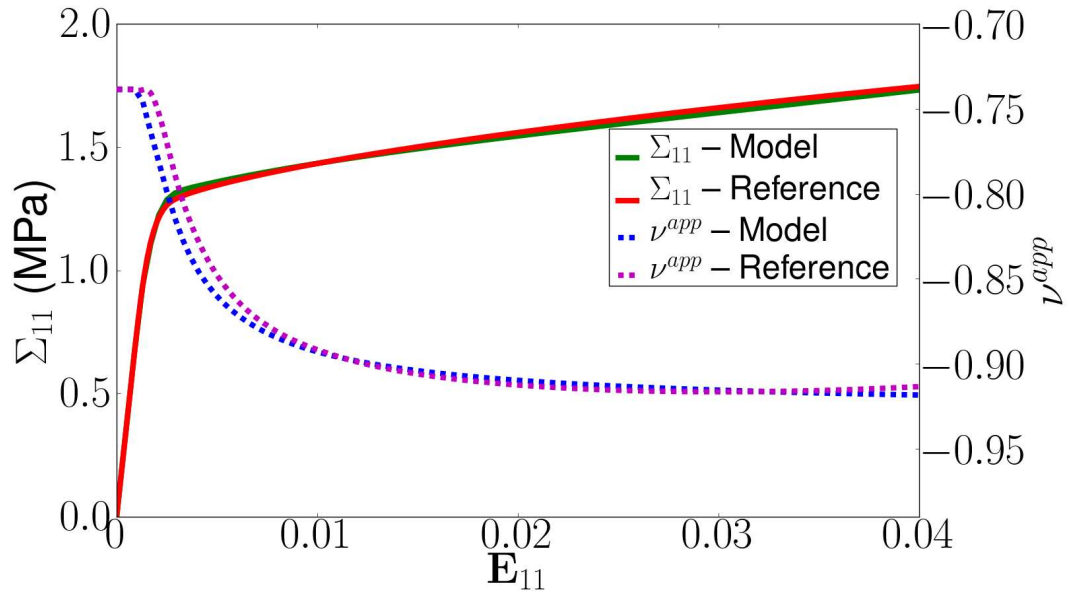


Figure 5.27: Stress and apparent *Poisson*'s ratio vs. strain for full-field simulation and macroscopic model for an uniaxial tensile test along direction 1 for the hexachiral lattice ($h = 1000$ MPa)

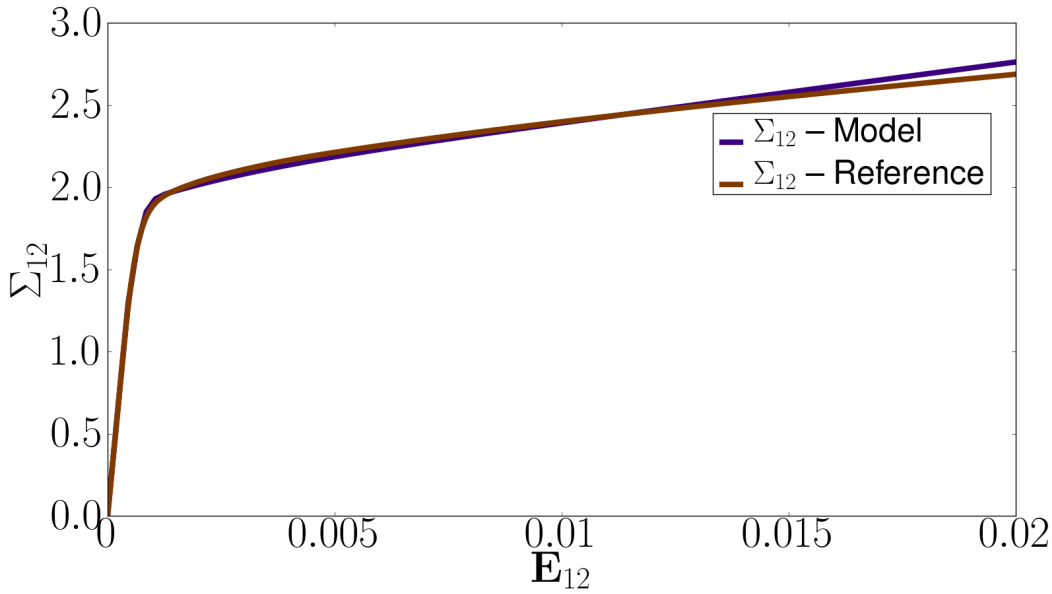


Figure 5.28: Stress vs. strain for full-field simulation and macroscopic model for an pure shear test in plane (1,2) for the hexachiral lattice ($h = 1000$ MPa)

5.5.5 Discussion

Full-field simulations and macroscopic modeling using an anisotropic compressible plasticity framework have been performed for an auxetic microstructure: the hexachiral lattice. Plasticity of auxetics has been explored, showing that the auxetic effect persists and becomes even stronger with plastic yielding. It was also shown that the strengthening effect of plasticity on auxeticity fades with the expansion of the plastic zone. The plastic response anisotropy for this 6-fold symmetric lattice is becoming weaker with hardening. The proposed fully anisotropic *Hill* criterion seems to be suitable for modeling architected cellular materials as it was able to catch negative *Poisson's* ratios, transverse contractions, and volume changes. Further work could include the modeling of other auxetic microstructures, a parametric study of the influence of the yield stress and the local hardening rule on the homogenized plastic behavior and the simulation of an indentation test using the macroscopic model developed in this work. This study on elastoplasticity and compressible plasticity modeling of auxetics was published in [Dirrenberger et al., 2012].

5.6 3D auxetic microstructure: the hexatruss lattice

The hexatruss lattice is an extension of auxetic lattices to 3D. It was first proposed in [Dirrenberger et al., 2013] but is very comparable with the unit-cell used in [Doyoyo and Hu, 2006] for modeling auxetic foams. The geometry of the cell is cubic, the principal directions are all equivalent as shown on Figure 5.30. The geometry can be described by lengths L , l , t and angle ω as shown on Figure 5.31. A new dimensionless parameter is defined in

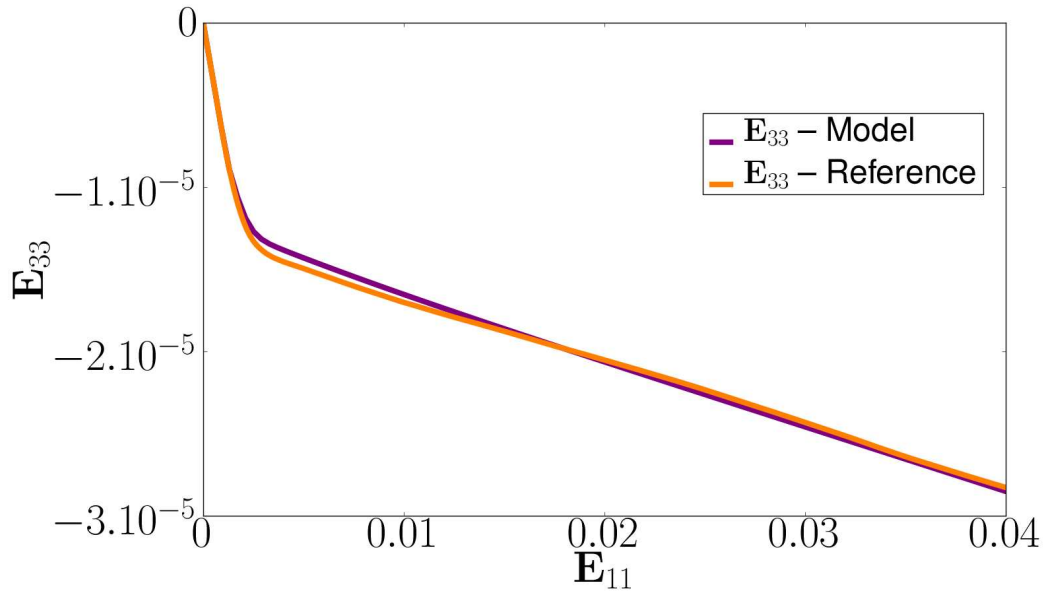


Figure 5.29: Transverse strain vs. longitudinal strain for full-field simulation and macroscopic model for an uniaxial tensile test along direction 1 for the hexachiral lattice ($h = 1000$ MPa)

Equation 5.42. L is not independent from l and ω , they are related to each other by the following equation: $L = 2l \cos^2 \omega$. For this work, $\omega = \frac{\pi}{5}$ and $\zeta = 15$, this corresponds to a volume fraction of 2.0%.

$$\zeta = \frac{l}{t} \tag{5.42}$$

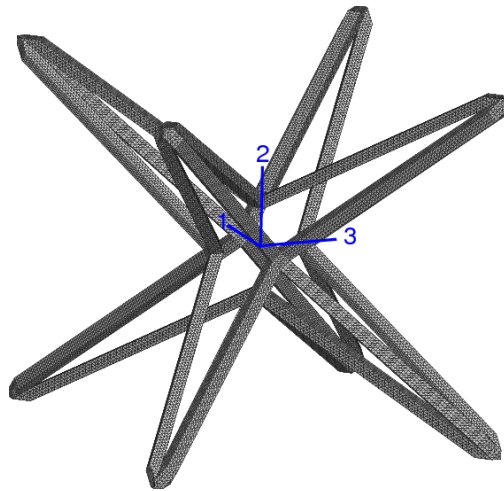


Figure 5.30: Hexatruss unit-cell

Cubic elasticity is verified since $C_{11} = C_{22} = C_{33}$, $C_{44} = C_{55} = C_{66}$ and $C_{12} = C_{23} = C_{31}$. Components were used to plot elastic properties on Figures 5.32 and 5.33. $\nu^*(\underline{l}, \underline{m})$ is negative for

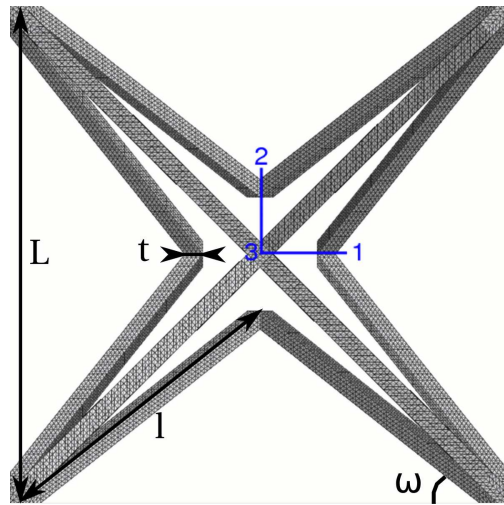


Figure 5.31: Hexatruss periodic unit-cell with geometric parameters

a large angle range, except near the principal directions of the cell, it reaches a minimal value of -0.97 for $\psi = \frac{\pi}{4}$. Figure 5.32 shows a massive increase of $\mu^*(\underline{l}, \underline{m})$ along the principal directions of the cell with a maximal normalized value of 0.5. $E^*(\underline{l})$ is higher in diagonal directions than in the principal directions. Overall, the elastic behavior of the hexatruss is strongly anisotropic, as shown in Equation 5.43:

$$[\underline{C}] = \begin{bmatrix} 6.12 & 1.62 & 1.62 & 0 & 0 & 0 \\ 1.62 & 6.12 & 1.62 & 0 & 0 & 0 \\ 1.62 & 1.62 & 6.12 & 0 & 0 & 0 \\ 0 & 0 & 0 & 227 & 0 & 0 \\ 0 & 0 & 0 & 0 & 227 & 0 \\ 0 & 0 & 0 & 0 & 0 & 227 \end{bmatrix} \quad (5.43)$$

5.7 Structural applications of auxetics

In order to conclude on the potential use of auxetic materials in engineering applications, we performed simulations of both elastic spherical and cylindrical indentation test on macroscopic homogenized models using elastic moduli determined in Sections 5.4 and 5.6. Since anisotropy is being investigated, we considered tridimensional meshes for the spherical indentation, as shown on Figure 5.34. In order to reduce computation time, symmetry conditions were prescribed at face boundaries so that the FE problem is equivalent to a full spherical indentation simulation. Also, for the sake of simplicity, 8-node hexahedral and 6-node tetrahedral linear elements were chosen for this computation. Two sets of boundary conditions have been considered. For each set

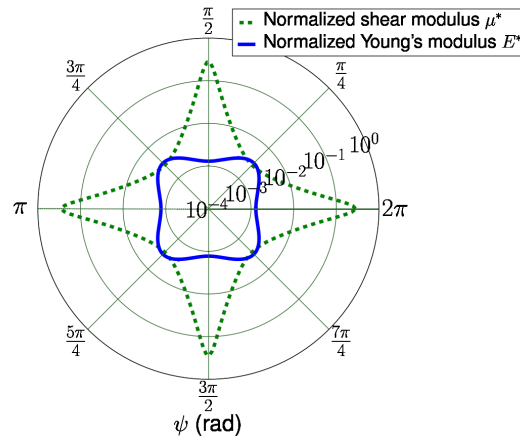


Figure 5.32: Hexatruss lattice ($\theta = \frac{\pi}{2}$, $\phi = 0$)

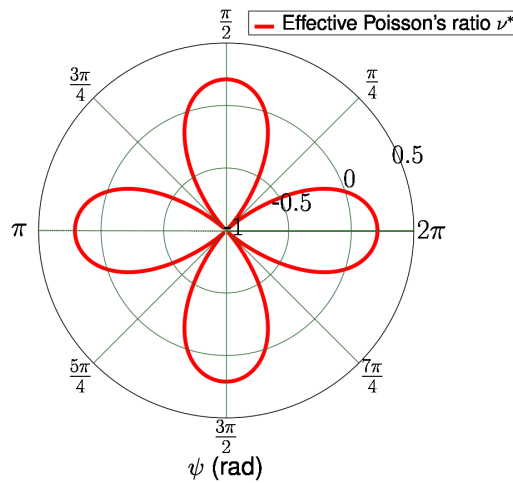


Figure 5.33: Hexatruss lattice ($\theta = \frac{\pi}{2}$, $\phi = 0$)

and each microstructure, indentation was performed along direction 2 in plane (1,2) and direction 3 in plane (1,3), respectively corresponding to in-plane and out-of-plane indentation tests. Radius of the indenter $R = 1$ mm and maximum indentation depth $h_s = 0.2$ mm.

5.7.1 Spherical indentation: loading case 1

The first loading case corresponds to the classical indentation test with prescribed displacement at the base of the indented medium along the direction of indentation, and symmetry conditions in the plane transverse to the direction of indentation. Loading is controlled by the displacement of the indenter. Force vs. indentation depth curves are shown on Figure 5.35 for in-plane indentation and Figure 5.36 for out-of-plane indentation. For both in-plane and out-of-plane indentations, the

honeycomb cell exhibits the higher strength. Both hexachiral and anti-tetrachiral lattices develop a slightly lower but reasonable strength. On the other hand, the rotachiral lattice does not seem adequate for such applications. The hexatruss lattice exhibits very low indentation resistance in comparison with the extruded 2D geometries for both orientations, although the difference in volume fraction has to be taken into account.

5.7.2 Spherical indentation: loading case 2

The second loading case differs by its boundary conditions. Here, the bottom base of the indented medium is free and the displacement is prescribed at the external circumferential border of the cylinder. These boundary conditions are closer to those of an impact test, which relates more to what an hypothetical architected sandwich panel would endure in use. Force *vs.* indentation depth curves are shown on Figure 5.37 for in-plane indentation and Figure 5.38 for out-of-plane indentation. Once again, the honeycomb cell exhibits the higher strength for both orientations, and the hexachiral and anti-tetrachiral lattices are still competitive, at least in its principal directions for the latter. The rotachiral lattice is definitely inadequate as far as elastic energy is concerned. Again, the hexatruss cell seems inadequate as is for structural design.

5.7.3 Cylindrical indentation

In order to emphasize the structural applicability of auxetics, we performed an elastic cylindrical indentation test using the same loading conditions as before. Unlike for the spherical indentation, a 2D-mesh was used for the cylindrical indentation as shown on Figure 5.39. Computations were done for both plane-strain and plane-stress assumptions. Force *vs.* indentation depth curves for both in-plane and out-of-plane cylindrical indentations for both loading cases are presented in Figures 5.40 to 5.43. Plain lines denote plane-strain assumption while dashed lines denote plane-stress. It is clear from Figures 5.40 and 5.42 that the rotachiral and hexatruss lattices are not good candidates for in-plane structural applications. On the other hand, results for the honeycomb cell are constantly good. For the second loading case, the hexachiral cell develops a higher strength in-plane than the honeycomb for $h_s = 0.2$ mm, this would advocate for the potential use of hexachiral cells for in-plane applications. The in-plane performance of the anti-tetrachiral cell is not as high as expected from spherical indentation tests. If we now consider the out-of-plane performance of auxetics (*cf.* Figures 5.41 and 5.43), it is interesting to note that again, the hexatruss lattice exhibits very low indentation resistance in comparison with the extruded 2D cells. Nevertheless, its small volume fraction could be an obvious cause for such behavior. The anti-tetrachiral cell exhibits high out-of-plane strength, comparable with the honeycomb strength level, for both loading cases. There are very strong discrepancies for the out-of-plane response of the rotachiral cell between loading cases 1 and 2.

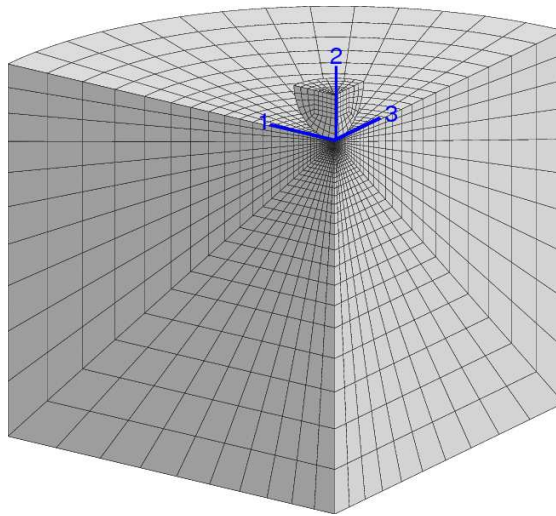


Figure 5.34: Cross sectional view of FE mesh used for spherical indentation tests, here with orientation for in-plane indentation

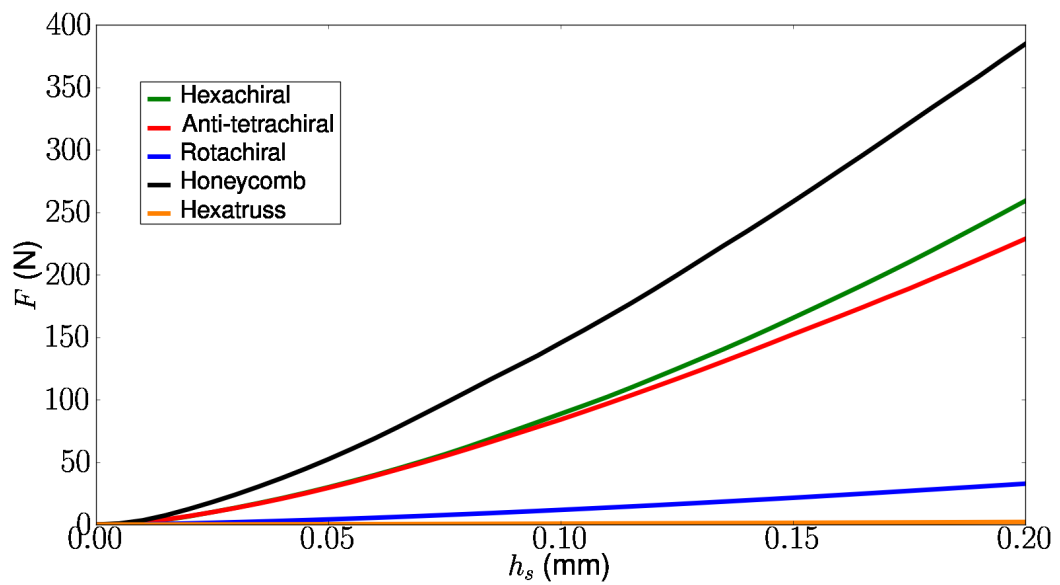


Figure 5.35: Force vs. indentation depth curves for spherical loading case 1 with (1,2) orientation

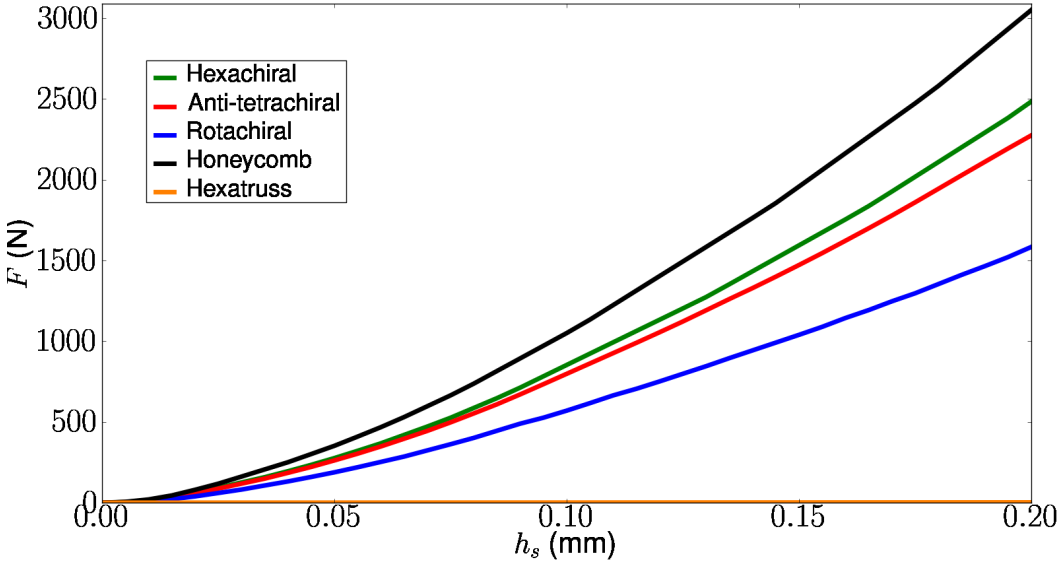


Figure 5.36: Force vs. indentation depth curves for spherical loading case 1 with (1,3) orientation

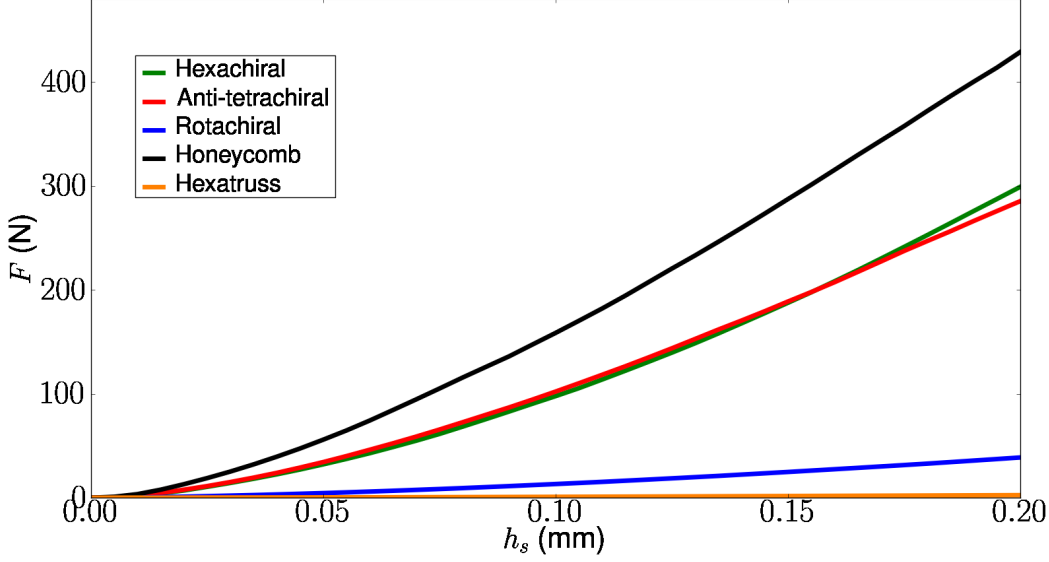


Figure 5.37: Force vs. indentation depth curves for spherical loading case 2 with (1,2) orientation

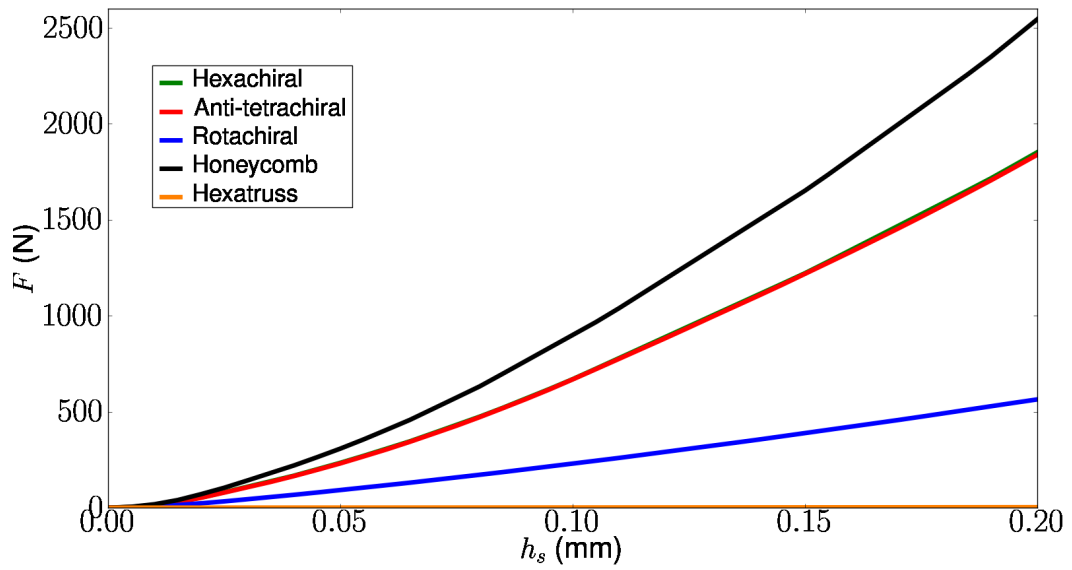


Figure 5.38: Force vs. indentation depth curves for spherical loading case 2 with (1,3) orientation

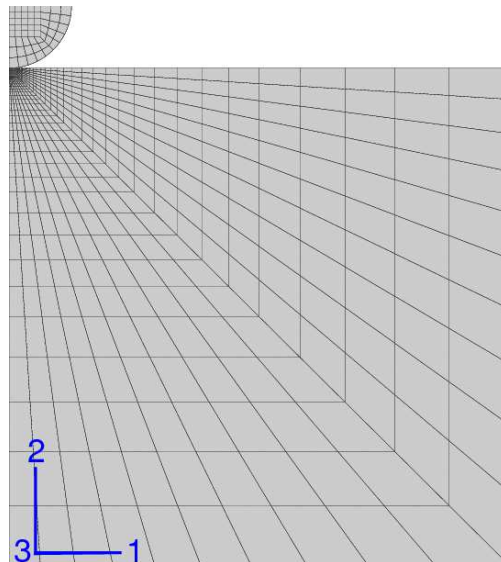


Figure 5.39: FE mesh used for cylindrical indentation tests, here with orientation for in-plane indentation

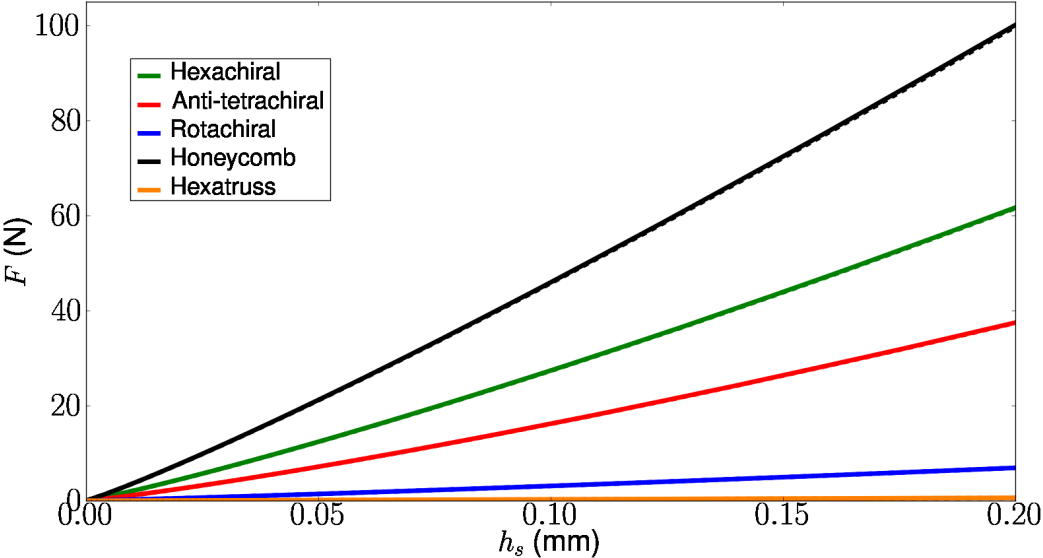


Figure 5.40: Force vs. indentation depth curves for cylindrical loading case 1 with (1,2) orientation

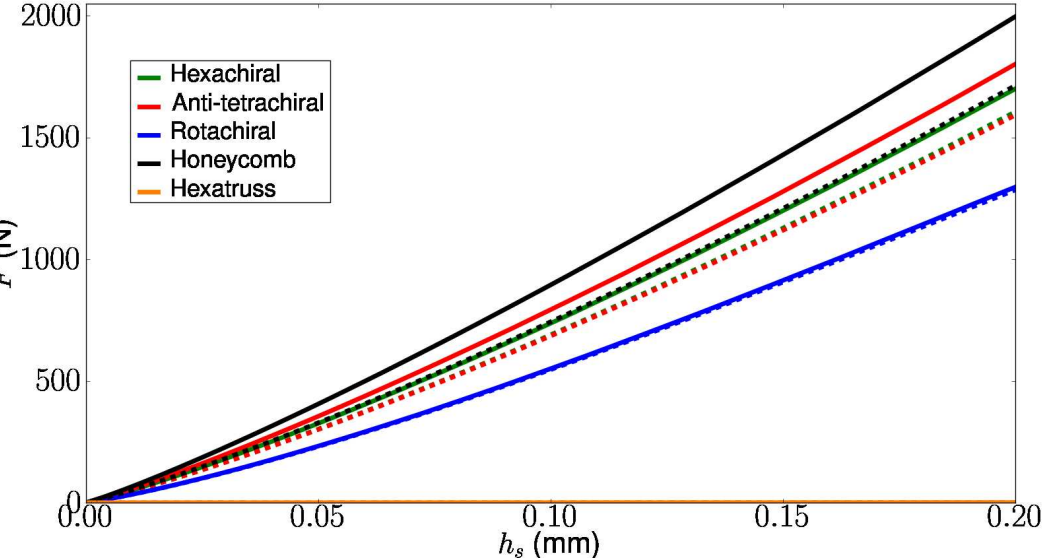


Figure 5.41: Force vs. indentation depth curves for cylindrical loading case 1 with (1,3) orientation

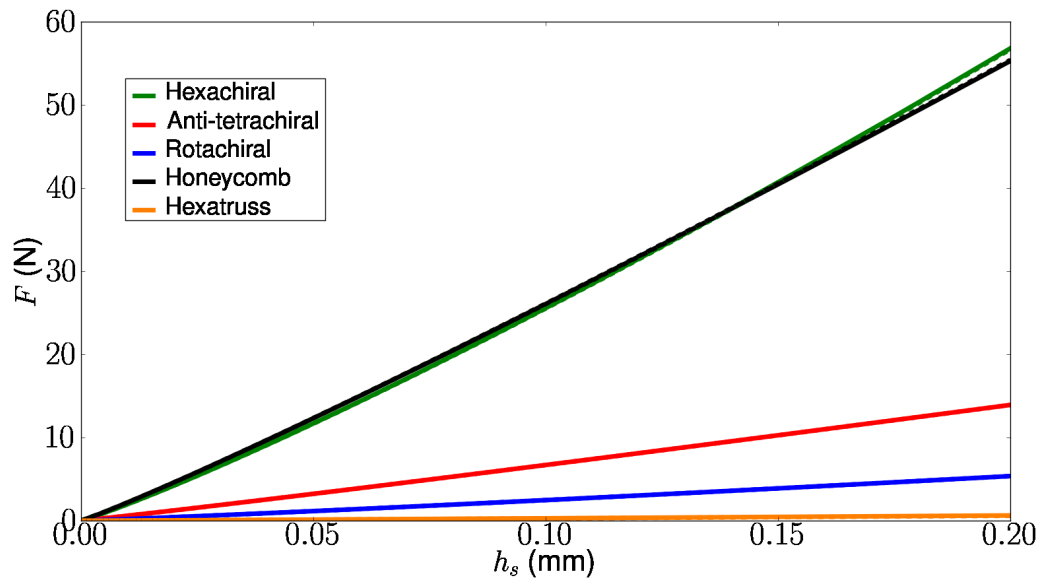


Figure 5.42: Force vs. indentation depth curves for cylindrical loading case 2 with (1,2) orientation

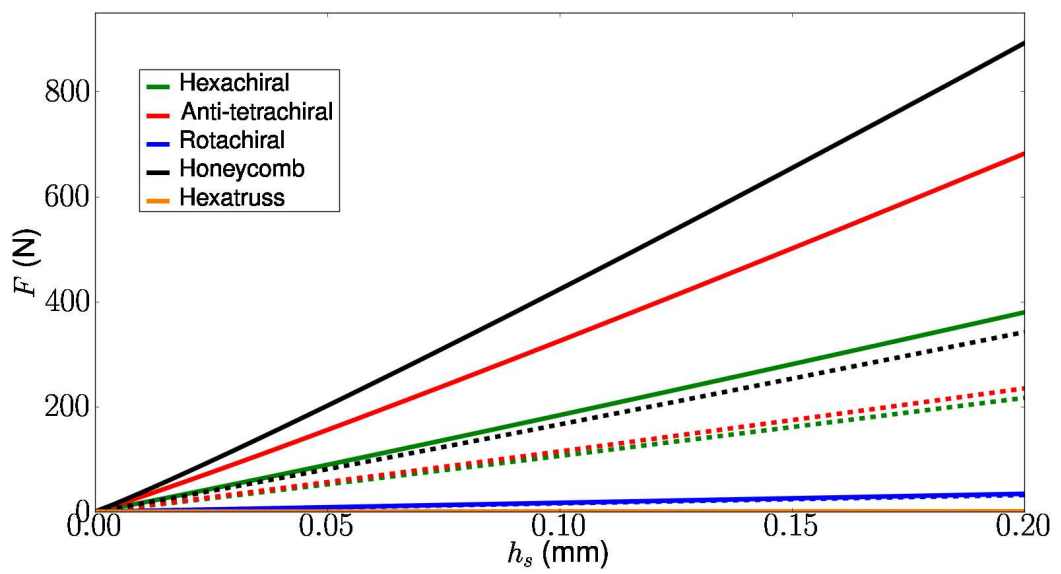


Figure 5.43: Force vs. indentation depth curves for cylindrical loading case 2 with (1,3) orientation

5.8 Experimental characterization of auxetics

In this work, metallic and polymeric auxetic samples were manufactured using the rapid prototyping method of selective laser melting (SLM). This method has been used successfully by others for auxetics [Huang and Blackburn, 2002, Schwerdtfeger et al., 2010, Mitschke et al., 2011]. Several experiments were conducted on auxetic samples in the context of mini-projects with students from MINES-ParisTech: the main goal was to investigate the effect of SLM on the resulting microstructure, as well as measure the auxetic effect experimentally.

For the case of a 316L stainless steel bulk sample made with SLM, micrographs revealed a surface fraction of porosity of about 4%, which makes SLM samples quite dense in comparison with other powder metallurgy processes, *cf.* Figure C.1. However, porosities are located at the boundary between two neighboring melting beds. The effects of such defaults are partly counterbalanced during the process by the laser beam path which alternates between x and y directions, thus disconnecting the initial voids. Unfortunately, this does not apply for truss structures with very thin struts, say 200 μm in diameter. Therefore, we suspect our auxetic samples to be sensibly more porous than the bulk samples made using SLM. This assertion was validated by microstructural characterization made using X-ray microtomography, as discussed in Section C.3. Further investigation of the microstructure showed a strong grain anisotropy, with very elongated grains up to a few millimeters long, *cf.* Figures C.2. On the same figure, as well as on Figures C.3 and C.4, we can observe that the grain growth occurred across many melting bed layers.

The rest of the experiments were macroscopic mechanical tests performed in order to determine the *Poisson* ratio of the samples studied. Due to lack of time and to the very strong heterogeneity of the microstructures considered, a full digital image correlation approach was not implemented. Instead, macroscopic strain values were evaluated from the discrepancies between two photographs corresponding respectively to the undeformed and deformed states. For instance, from Figure 5.44 a *Poisson* ratio of -1 was estimated on one cell. Although, this value fluctuates between -1 and -0.2 depending on local buckling and failure, it is comparable to the value $\nu = -0.97$ obtained from the simulation for an ideal elastic medium. All the experimental data acquired for auxetics is gathered in Appendix C.

5.9 Conclusions and prospects

Elastic moduli for three periodic auxetic 2D lattices, a 15% volume fraction honeycomb cell and a new 3D auxetic microstructure, have been computed using periodic homogenization technique coupled with finite elements. Anisotropy of in-plane and out-of-plane normalized elastic parameters was investigated. While the honeycomb cell exhibits a constantly high indentation strength, auxetic lattices can be competitive if shear is involved, especially the hexachiral and anti-tetrachiral lattices. With its circular (or elliptic) ligaments, the rotachiral lattice provides an additional parameter for tuning the microstructure for specific absorption

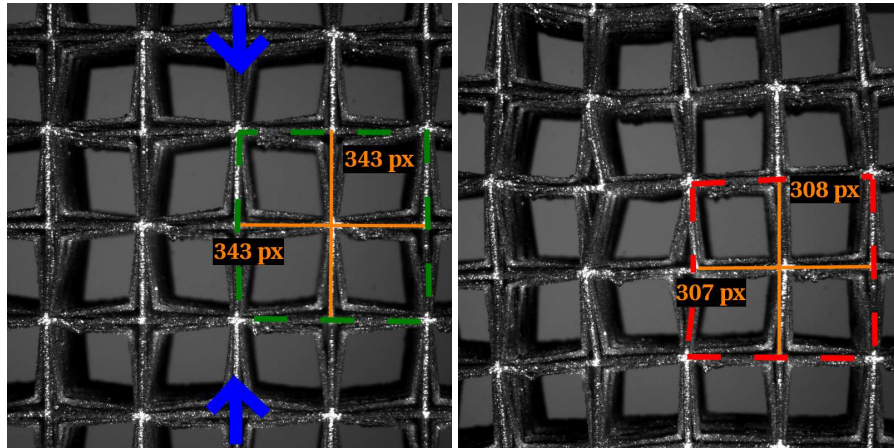


Figure 5.44: Initial (a) and final (b) states for a hexatruss 316L sample under compressive loading along the vertical direction ($\phi = \frac{\pi}{2}$, $\theta = 0$ and $\psi = \frac{\pi}{4}$). *Poisson's* ratio is estimated from discrepancies in pixel sizes.

properties. This lattice can exhibit highly negative *Poisson's* ratios when loaded out-of-plane. The quadratic elasticity of the anti-tetrachiral lattice was investigated numerically, showing higher normalized *Young's* modulus $E^*(\underline{l})$ in the principal directions of the cell, while in-plane auxetic effects are restricted to short angle intervals around these directions. Such lattices could be used in replacement of traditional honeycomb-core for sandwich panels, especially if produced by extrusion. In the context of this work, panels are being produced this way by SMCI³, which is an industrial partner of the MANSART project.

Results from structural computations were presented, advocating for further developments in the field of structural auxetics. Nevertheless, due to the importance of sandwich skins in the strength of composite structures, those will be taken into account and their influence investigated in subsequent works. The hexatruss 3D lattice gave not so promising results in terms of indentation strength. This is partly due to its very small volume fraction in comparison with the other microstructures studied in this work. Our simulations demonstrate the impact of elastic anisotropy on the loss of structural properties for architected materials. It would be interesting to compare the hexatruss mechanical performance with those of other tridimensional struts lattices with same densities. Auxetic samples were made using selective laser melting (SLM), an additive powder metallurgy process, extending one's microstructural design spectrum from 2D to 3D. The microstructure of the processed samples was investigated using optical microscopy and scanning electron microscopy, showing a very strong anisotropy in grain sizes and orientation. The crystallographic orientation distribution was not measured since it was out of the spectrum of the present study. The heterogeneous nature of the constitutive microstructure of our samples is conflicting with the assumption of homogeneous isotropy made in the simulation. In order to develop more realistic models, microstructural and crystallographic information has to be taken

³<http://www.klege-europ-smci.com/>

into account in the computation. This would advocate for modeling the actual process of selective laser melting to have a full understanding of the underlying phenomena taking place within the material. At a macroscopic scale, mechanical experiments were performed in compression and *Poisson's* ratio was estimated, yielding a fair accordance between simulation and experiments. Further characterization could be actual indentation experiments in order to compare the obtained data with our FE results.

Regarding plasticity, full-field simulations and macroscopic modeling using an anisotropic compressible plasticity framework have also been performed for the auxetic hexachiral lattice and compared with the honeycomb lattice. Elastoplasticity of auxetics has been explored, showing that the auxetic effect persists and becomes even stronger with plastic yielding. Transverse isotropy was preserved within the plastic domain for the hexachiral lattice unlike the honeycomb. The hexachiral cell exhibits an in-plane plastic shear stress that is about 3 times higher than for the honeycomb lattice, this is due to its auxetic properties. The plastic response anisotropy for this 6-fold symmetric lattice is becoming weaker with plastic saturation. The proposed fully anisotropic *Hill* criterion seems to be suitable for modeling architected cellular materials as it was able to catch negative *Poisson's* ratios, transverse contractions, and volume changes. Further work will include the modeling of other auxetic microstructures, a study of the influence of the local hardening rule on the homogenized plastic behavior and the simulation of an indentation test using the macroscopic model developed in this work. For industrial applications, non-linear phenomena such as buckling will also have to be taken into account.

Résumé

Dans cette seconde partie, l'homogénéisation numérique à l'aide des éléments finis est implémentée dans le cas de matériaux périodiques à coefficient de *Poisson* négatif. Une introduction à ce type de matériaux est donnée. Les formules de moyennes pour les champs mécaniques sont adaptées pour le cas des matériaux cellulaires. Les différentes microstructures considérées sont ensuite présentées et leurs propriétés effectives déterminées. Une étude de l'anisotropie élastique est réalisée pour ces microstructures. L'extension au domaine élastoplastique est réalisée pour la cellule hexachirale, ainsi que pour le nid d'abeilles classique : la comparaison est faite entre ces deux motifs. Une modélisation macroscopique du comportement plastique compressible est proposée en utilisant un critère anisotrope généralisé de *Hill*. En se basant sur les résultats obtenus, une nouvelle cellule 3D est proposée et étudiée. L'application structurale des auxétiques est validée par la simulation d'essais d'indentation sphérique et cylindrique. Enfin la caractérisation expérimentale d'échantillons obtenus par fusion laser sélective est décrite et les résultats sont confrontés à la simulation.

Application to random media Part III

6 Poisson fibers

*L'homme est capable de faire ce qu'il est incapable d'imaginer.
Sa tête sillonne la galaxie de l'absurde.*

— René Char, *Feuillets d'Hypnos, Fureur et mystère* (1948)

Part II was dedicated to periodic microstructures. We will now focus our attention on the homogenization of random media. We have introduced the problem of the representativity of samples in Section 2.1 and presented the statistical approach for determining RVE sizes of heterogeneous materials in Section 4.2. This method was implemented as is in several contributions such as [Kanit et al., 2003, Pelissou et al., 2009, Jean et al., 2011b] and has proved to be quite effective. However, all the microstructures considered in these 3 references are morphologically periodic. For the sake of efficiency, [Pelissou et al., 2009] and [Jean et al., 2011b] resort to periodic boundary conditions (PBC) since [Kanit et al., 2003] showed from computational experiments that apparent properties obtained with PBC converge towards the effective properties more rapidly than those obtained with KUBC and SUBC. The rate of convergence of apparent properties towards the effective properties, with respect to the volume of the system, informs us on the size of the RVE. If one considers a given microstructure for which this rate of convergence is slow, this would give rise to large RVE sizes, especially if this medium is not morphologically periodic (or periodizable) and if PBC cannot be used. It would thus be a challenge to homogenize such media, this is the purpose of the present chapter. Some extreme, or pathological, candidate morphologies could give rise to gigantic RVE sizes. This is the case of *Poisson* fibers, which correspond to a particular type of 3D stochastic networks composed by randomly oriented and distributed infinite rectilinear interpenetrating fibers. There are many studies in the literature regarding finite-length fibrous media and strongly oriented infinite-fiber media, likely due to the industrial relevance of such materials. For instance, [Delisée et al., 2001] and [Peyrega et al., 2009] dealt with the morphology of 3D long-fiber media randomly oriented in-plane, [Schladitz et al., 2006] used a 3D random model of randomly oriented long-fibers for the design of an acoustic absorber, and [Barbier et al., 2009b, Barbier et al., 2009a] used virtual samples of long but finite fibers,

for modeling the mechanics of entangled materials. None of these studies accounted for the representativity of samples. [Oumarou et al., 2012] computed RVE sizes for 2D random arrays of fibers, using the statistical method of [Kanit et al., 2003]. We also acknowledge the work of Picu et al. on 2D fibrous fractal networks, as it deals with the homogenization of such, yet self-similar, fibrous media. See for instance [Soare and Picu, 2007, Hatami-Marbini and Picu, 2009, Picu and Hatami-Marbini, 2010, Picu, 2011]. To our knowledge, no one ever assessed the question of RVE size for 3D infinite randomly oriented fibrous media.

When dealing with the computational homogenization of random media, one has to consider virtual specimens or models. In order for the model to be realistic, the microstructural heterogeneities have to be taken into account in the simulation. Mathematical morphology provides powerful tools to do so (*cf.* Appendix B). For the case of real microstructures the method consists of the digitization and reconstruction from actual physical measurements of the microstructure obtained using techniques such as microscopic contrast tomography (μ CT), transmission electron microscopy (TEM), scanning electron microscopy (SEM), confocal microscopy (CM), electron back scattering diffraction (EBSD), synchrotron light beam source, etc. Virtual samples obtained in this way can be used, without much change, for computational homogenization with Fast Fourier Transform (FFT), which is voxel-based, or FE, thus adding an intermediate meshing step. Nevertheless, it would be a pity not to access the underlying morphological information present in any realistic sample. The data acquired earlier should thus be quantitatively characterized by means of a two-step morphological measurements procedure: first, a morphological transformation is applied on the data; then a measure performed on the resulting object. Typical morphological measurements include stereological data (volume fraction, integral of mean curvature, etc.), size distribution, spatial distribution (clustering, scales, anisotropy) and connectivity. Knowing this information allows one to generate realistic virtual samples based on models of random structures as it was done in [Kanit et al., 2006, Schladitz et al., 2006, Madi et al., 2007, Peyrega et al., 2009, Escoda et al., 2011, Jean et al., 2011a] for instance. Based on morphological arguments, one can also define a specific model of random structures that does not necessarily correspond to a realistic medium. This kind of models could present interest for testing theories and to further our understanding of the physics of random media.

This is the main goal of the present chapter, as well as examining the statistical RVE approach of Kanit et al. in the light of a quite unfavorable case. The morphology considered here, *Poisson* fibers, correspond to a particular type of 3D stochastic network composed by randomly oriented and distributed infinitely-long rectilinear interpenetrating fibers. This specific model of random structure exhibits an infinite integral range [Jeulin, 1991a], *i.e.* an infinite correlation length; the statistical RVE method would thus have to be updated. Besides, *Poisson* fibers exhibit two percolating phases with an infinite contrast of properties. This medium does not respect the principle of scale separation and it is non-periodizable without modifying its morphology, thus falling beyond the spectrum of periodic homogenization and the definition of RVE proposed by [Sab and Nedjar, 2005]. Although infinite fibers do not exist in nature, they could be a limit case representative of sintered long-fiber non-woven materials, such as those studied in [Mezeix et al., 2009]. Throughout this paper, we implement a computational homogenization

scheme based on finite element (FE) simulations. This will require virtual samples generated using a specific mathematical morphology model, which is described in [Jeulin, 2012] along with a review on the determination of effective properties for random sets, including *Poisson* fibers.

The approach adopted in this work is quite original, considering that we are trying to homogenize a rather unrealistic material in order to show the robustness of the proposed approach for realistic materials. It is intended to compute the effective properties of a pathological type of models of random structures, for which periodic homogenization is helpless. First, the microstructural model is presented in Section 6.1 along with the virtual samples generation procedure. Numerical simulation setup and parameters, and boundary conditions for the thermal and mechanical problems are discussed in Section 6.2. Results coming from the simulation are shown in Section 6.3. Morphological, thermal and elastic isotropy is checked for in Section 6.4.1. In Section 6.5, we determine the RVE size for this kind of microstructure regarding thermal and mechanical properties using the generalized statistical method presented in Section 4.2.5. Discussion is postponed to Section 6.4.

6.1 Microstructural model

The microstructural model considered for *Poisson* fibers is made of a Boolean model on a *Poisson* variety. Firstly, we will clarify the notion of *Poisson* point process, then present the *Poisson* linear varieties and finally we will define a Boolean model on *Poisson* lines in 3D. In this section we will use vocabulary and notation specific to mathematical morphology that are explained in Appendix B.

6.1.1 Poisson point process

The *Poisson* point process is a random point process on which many stochastic models are based, *cf.* for instance [Serra, 1982], it is the prototype for random processes without any order. It consists in implanting points x_i in \mathbb{R}^n according to a *Poisson* law [Poisson, 1837]. The intensity of the *Poisson* law is equal to its mathematical expectation and its variance. For instance, $P_2(m)$ is the probability for m *Poisson* points to be implanted with intensity θ on a surface S :

$$P_2(m) = \frac{(\theta S)^m}{m!} \exp(-\theta S) \quad (6.1)$$

This type of random point process is illustrated on Figure 6.1:

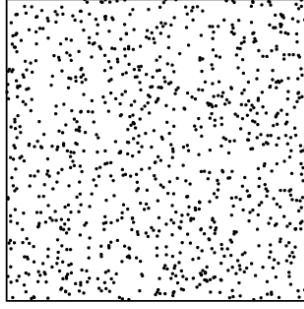


Figure 6.1: Realization of a *Poisson* point process in \mathbb{R}^2

6.1.2 Linear Poisson varieties

Let us now consider a *Poisson* point process $\{x_i(\omega)\}$, with intensity $\theta_k(d\omega)$ on the variety of dimension $(n - k)$ containing the origin O , and with orientation ω . For every point $x_i(\omega)$ there is a variety of dimension k , called $V_k(\omega)_{x_i}$, that is orthogonal to the direction ω . Let us consider the set V_k , which is the union over $\{x_i(\omega)\}$ of all varieties, such that:

$$V_k = \cup_{x_i(\omega)} V_k(\omega)_{x_i} \quad (6.2)$$

Using this definition in \mathbb{R}^3 , one can for instance generate a network of *Poisson* hyperplanes ($k = 2$) or *Poisson* lines ($k = 1$).

The number of varieties of dimension k hit by a compact set K is a *Poisson* variable with parameter $\theta(K)$, and as proved in [Jeulin, 1991a, Jeulin, 1991b, Jeulin, 2011] for the stationary case:

$$\theta(K) = \int_{\mathbb{R}^n} \theta_k(d\omega) \mu_{n-k}(K(\omega)) \quad (6.3)$$

where $K(\omega)$ is the orthogonal projection of K on the space orthogonal to $V_k(\omega)$, $V_{k\perp}(\omega)$. In the isotropic (θ_k being constant), stationary case of *Poisson* lines in \mathbb{R}^3 ($n = 3$, $k = 1$), for a convex set K , we can prove that the number of varieties of dimension k hit by a compact set K is a *Poisson* variable, with parameter $\theta(K)$:

$$\theta(K) = \frac{\pi}{4} \theta \mathcal{S}(K) \quad (6.4)$$

where \mathcal{S} is the measure of surface.

6.1.3 Boolean random sets

Boolean random sets can be built from *Poisson* varieties and a primary grain A' , as described in [Jeulin, 1991a, Jeulin, 1991b, Jeulin, 2011]. A Boolean model built on *Poisson* lines generates a fibrous network, with a possible overlap of fibers. According to [Jeulin, 1991a], the *Choquet*

capacity of a Boolean random model built on a *Poisson* variety of dimension k reads as:

$$T(K) = 1 - \exp\left(-\int \theta_k(d\omega) \bar{\mu}_{n-k}(A'(\omega) \oplus \check{K}(\omega))\right) \quad (6.5)$$

In the case of isotropic *Poisson* lines, for a convex set $A' \oplus \check{K}$, the *Choquet* capacity simplifies to:

$$T(K) = 1 - \exp\left(-\theta \frac{\pi}{2} \bar{\mathcal{F}}(A' \oplus \check{K})\right) \quad (6.6)$$

Thus, for *Poisson* fibers resulting from the dilation of isotropic *Poisson* lines by a sphere of radius R :

$$T(0) = P\{x \in A\} = 1 - \exp\left(-\theta \frac{\pi^2 R^2}{2}\right) \quad (6.7)$$

Hence, for a given volume fraction V_V of *Poisson* fibers, we obtain θ that is:

$$\theta = \frac{-2 \ln(1 - V_V)}{\pi^2 R^2} \quad (6.8)$$

Based on Equation 6.8, one can compute the average number of *Poisson* fibers \bar{N} for a given set of parameters in the model: the fiber radius R , the volume fraction of fibers V_V and the volume considered $V = L^3$:

$$\bar{N} = S\theta = \pi \left(\frac{\sqrt{3}L}{2}\right)^2 \frac{-2 \ln(1 - V_V)}{\pi^2 R^2} = \frac{-3 \ln(1 - V_V)}{2\pi} \frac{L^2}{R^2} \quad (6.9)$$

with $\frac{L^2}{R^2}$ ratio of characteristic lengths.

6.1.4 Generation of Poisson fiber virtual models

Using the aforementioned definition of *Poisson* fibers, we can use the morphological description to generate virtual models (realizations) with the help of a structure-generating software. In this work we relied on `vtkSim`¹ which is developed at the Centre de Morphologie Mathématique of MINES-ParisTech in Fontainebleau. This software is able to generate tridimensional random structures based on a morphological description. It is programmed in C++ and based on the `vtk`² graphics library [Schroeder et al., 2006]. The main advantages of using this software compared to an acquired data-based approach is that `vtkSim` operates on a vectorial framework making the

¹<http://cmm.ensmp.fr/~faessel/vtkSim/demo/>

²<http://vtk.org>

computation time for generating a random structure almost size-independent until discretization, and its ability to generate very large random structures in comparison with voxel-based software.

Hereafter is the algorithm we developed for generating *Poisson* fibers using `vtkSim`, illustrated in Figure 6.2.

1. Input : volume fraction of isotropic fibers V_V , fibers radius R , sample size L ($V = L^3$)
2. Compute the theoretical number of germs for implanting fibers $n_{\text{theo}} = \pi \left(\frac{\sqrt{3}L}{2} \right)^2 \theta = \frac{-3L^2 \ln(1 - V_V)}{2\pi R^2}$
3. Monte-Carlo type simulation for determining the random number of germs n_{simul} according to a *Poisson* law
4. Generate and implant the n^{th} *Poisson* line
 - Randomize angles ρ and ϕ accounting for the fiber orientation
 - Rotate the equatorial plan $\Pi \rightarrow \Pi' \rightarrow \Gamma$ after angles ρ and ϕ
 - Randomize coordinates $\{x, y\}$ of the germ on the disc Γ and trace the normal of Γ in $\{x, y\}$
5. Repeat step 4 while $n \leq n_{\text{simul}}$
6. Dilate the ensemble of *Poisson* lines by the sphere of radius R
7. Write geometric data file

On Figure 6.3 is presented a vectorial (non-discretized) realization of *Poisson* fibers.

6.1.5 Discretization of microstructural models

Our aim is to use finite element analysis for determining effective properties, we thus have to discretize the generated realizations. `vtkSim` uses the meshing tools of the `vtk` library, which provides 3D regular triangular meshes attached to a Cartesian grid. The spacing of the grid is a parameter for the generation. Those meshes cannot be used directly for FE computations for two reasons: they are only 3D surface meshes; they are not optimized at all. In order to obtain a 3D volume mesh based on a 3D closed surface mesh, one needs to fill the latter with tetrahedra. In this work, this was done using the Z-Set FE package³ interfaced with the meshing tools developed at INRIA. This procedure first consists in a shape optimization of the 3D surface mesh using YAMS software [Frey, 2001]. The resulting closed surface mesh is then

³<http://www.zset-software.com/>

filled with TetMesh-GHS3D software [SIMULOG, 2003] using a *Voronoi–Delaunay* algorithm [Voronoi, 1908, Delaunay, 1934]. Finally, the meshes obtained in this way are compatible with the Z-Set standards, they can thus be used for computational homogenization.

6.1.6 Parameters of the simulation

There are several parameters to be set for the simulation, they are summarized in Table 6.1.

Volume fraction

Volume fraction V_V of fibers was chosen to be 15%. This value corresponds to an average number of fibers large enough to compute mechanical properties on reasonably small volumes. Unfortunately, by increasing the mesh density in `vtkSim`, *i.e.* enhancing the morphological description, we ended up with an average volume fraction of fibers close to 16% for the same *Poisson* intensity.

Fibres radius

Fibres radius R is kept constant and equal to 1 as a convention, hence setting the unit-length for the computation of elementary volumes.

Simulation size

Many simulation sizes L are considered. It corresponds to the edge length of the simulation cube of volume V . This length ranges from 10 to 200. Examples of virtual sample realizations are shown for different sizes on Figure 6.4.

Mesh density

In order to assess the impact of mesh refinement on the results, 5 different mesh densities d are considered. The mesh density is approximately equal to a normalized quantity of finite elements per unit-length. The higher this value, the larger the number of elements in the mesh and the better the description of the morphological model. The effect of mesh density is investigated and computations are performed, when possible, with the 5 densities shown in Figure 6.5.

6.1.7 Computational strategy

Since a vectorial framework was used for generating samples, binarization was avoided in order to keep the number of degrees of freedom (DOFs) low for a given morphological description. Voxel-based computational homogenization methods were put aside, such as Fast-Fourier Transform-

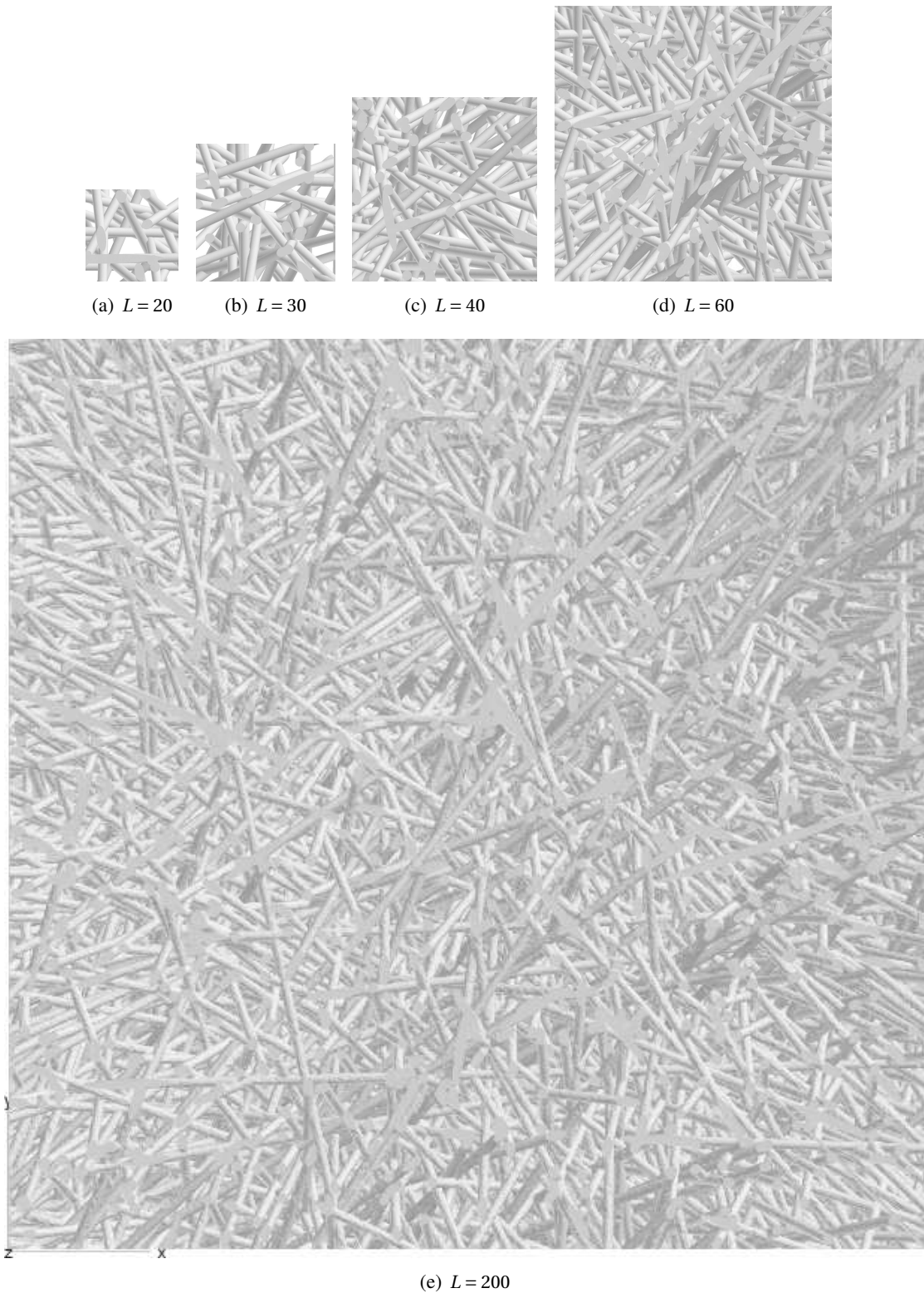


Figure 6.4: 3D rendering of *Poisson* fibers models (a) $L = 20$, (b) $L = 30$, (c) $L = 40$, (d) $L = 60$ and (e) $L = 200$

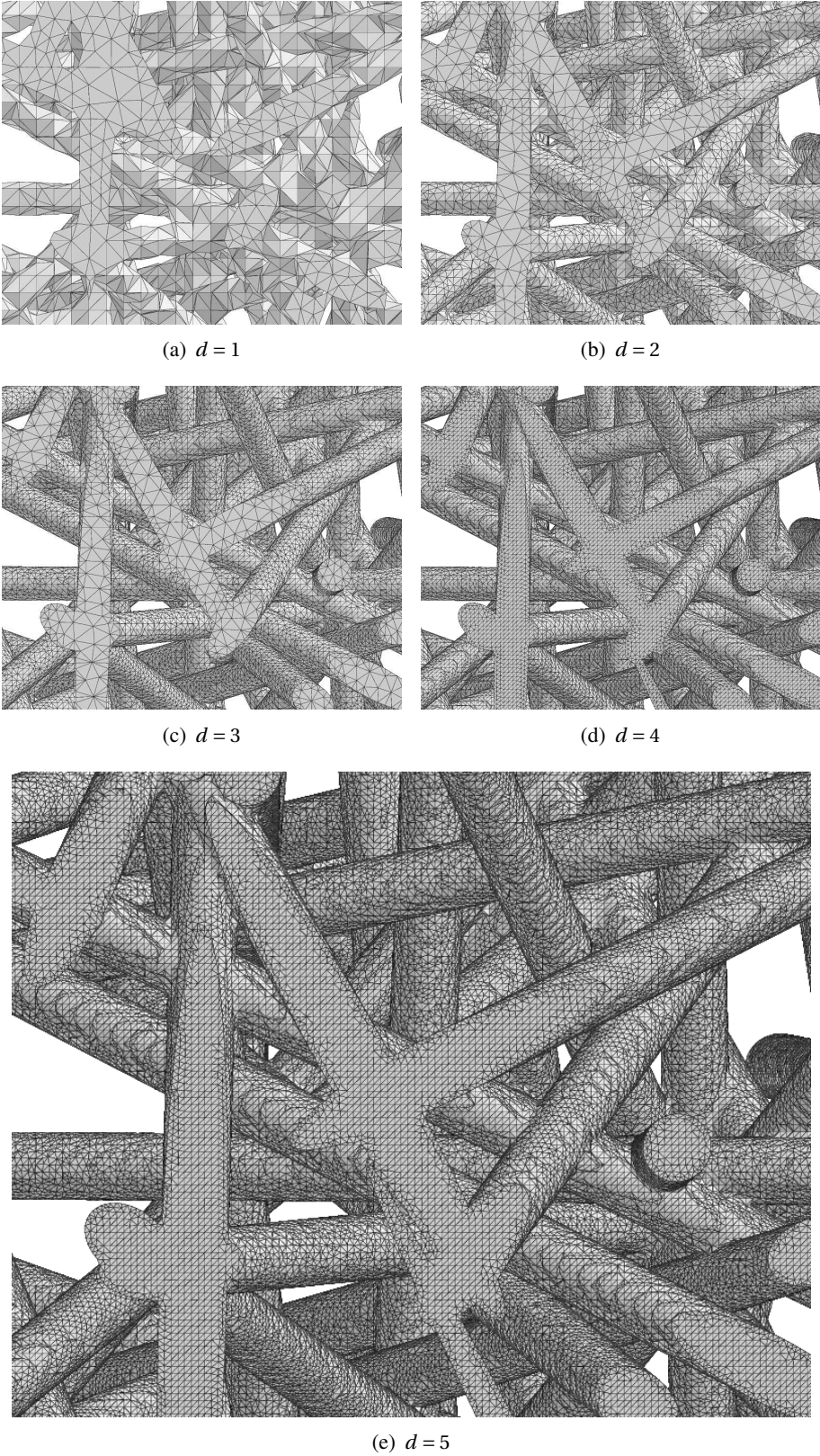


Figure 6.5: Mesh densities (a) $d = 1$, (b) $d = 2$, (c) $d = 3$, (d) $d = 4$ and (e) $d = 5$

6.2. Boundary conditions

Simulation size (L)	Mesh density (d)	Fiber radius	Volume fraction	Boundary conditions
[10;200]	[1;5]	1	0.16	Uniform & mixed

Table 6.1: Simulation parameters for computing effective properties

based (FFT) [Moulinec and Suquet, 1994] and FE with multi-phase elements [Barbe et al., 2001]. We opted for volumic FE with free meshes using linear tetrahedra for efficiency. Sequential computations were considered for the sake of simplicity. FE package Z-Set 8.5 was used for the computation as it is developed in-house and has previously been used with success for computing properties of heterogeneous microstructures [Barbe et al., 2001, Cailletaud et al., 2003, Kanit et al., 2003, Madi et al., 2005, Jean et al., 2011b, Dirrenberger et al., 2012].

The many simulations considered in this work were performed on the computing cluster of the Centre des Matériaux, allowing us to run many sequential computations in a parallel manner. The largest computation considered in this paper corresponds to a volume $V = 10^6$ including *ca.* 800 Poisson fibers. The associated mesh includes 11 million linear tetrahedral elements, *i.e.* 7.6 million DOFs. The MUMPS linear solver [Amestoy et al., 2000] was used as it was the most efficient available. For comparison, about 128 GB of RAM were necessary for the whole resolution of a linear elastic problem with the largest mesh using the default DSC_Pack linear solver, whereas MUMPS only needed 54 GB. In terms of time, the computation itself takes about 2.5 hours for an elastic problem on a AMD Opteron 6134 single-core @ 2.3 GHz, while the post-processing takes another half hour. All the data considered in this paper has been generated over a duration of 4 months; this does not include meshing.

6.2 Boundary conditions

Based on the microstructural model defined in Section 6.1, we compute the effective elastic and thermal properties of *Poisson* fibers. After discussing and adapting the averaging relations for the thermal and mechanical fields to the case of *Poisson* fibers, we will specify the boundary value problems considered in the simulations.

As shown on Figure 6.6, the elementary volume considered here is the volume V that is composed of two complementary phases V_f and V_p , respectively accounting for the *Poisson* fibers and the porous phase, such that:

$$V = V_f \cup V_p \tag{6.10}$$

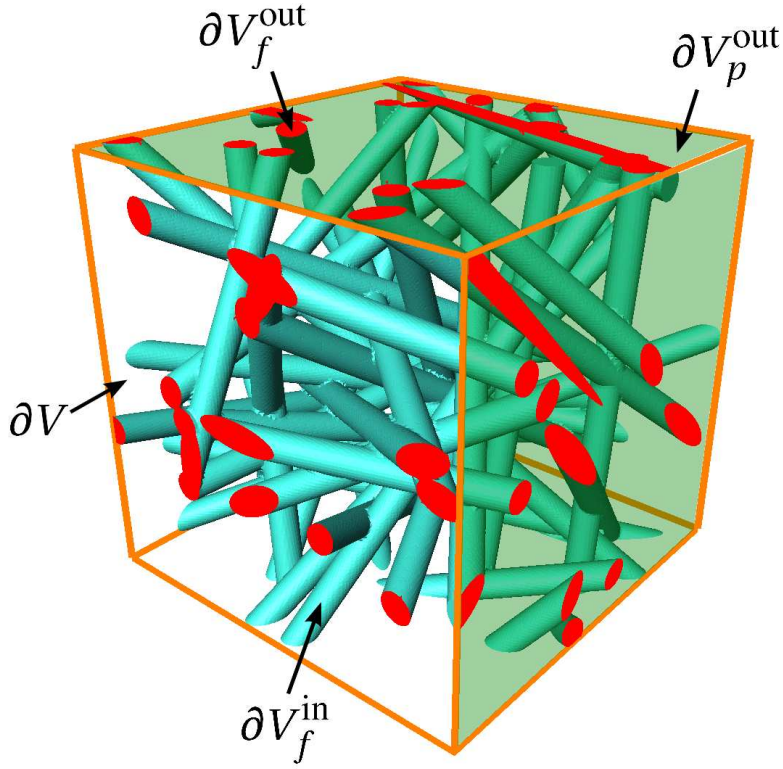


Figure 6.6: Example of elementary volume of *Poisson* fibers used in simulations

Let us consider the boundary of each phase:

$$\partial V_f = \partial V_f^{\text{in}} \cup \partial V_f^{\text{out}} \quad (6.11)$$

$$\partial V_p = \partial V_p^{\text{in}} \cup \partial V_p^{\text{out}} \quad (6.12)$$

with exponent ⁱⁿ and ^{out}, respectively accounting for the internal and external boundaries of the phases. For instance, $\partial V_f^{\text{out}}$ corresponds to the set of red surfaces in Figure 6.6. Moreover,

$$\underline{n}_f^{\text{in}} = -\underline{n}_p^{\text{in}} \quad \forall \underline{x} \in \partial V_{f,p}^{\text{in}} \quad (6.13)$$

Finally, the boundary ∂V of the elementary volume considered is made of the 6 faces of the cube F_1^+ , F_1^- , F_2^+ , F_2^- , F_3^+ and F_3^- . ∂V can also be defined as the union of the external boundaries of each phase:

$$\partial V = \partial V_f^{\text{out}} \cup \partial V_p^{\text{out}} \quad (6.14)$$

6.2.1 Thermal properties

The temperature T and heat flux $\underline{\mathbf{q}}$ fields are defined on the elementary volume V : they are computed on V_f only; on V_p , fields T and $\underline{\mathbf{q}}$ may be considered as extensions of T and $\underline{\mathbf{q}}$ on V_f using suitable interpolations assuming continuity for T and $\underline{\mathbf{q}} \cdot \underline{\mathbf{n}}$ on $\partial V_{f,p}^{\text{in}}$. We adopt the following extension of the $\underline{\mathbf{q}}$ field on V_p :

$$\underline{\mathbf{q}}(\underline{\mathbf{x}}) = \underline{\mathbf{0}} \quad \forall \underline{\mathbf{x}} \in V_p \quad (6.15)$$

This choice requires that,

$$\underline{\mathbf{q}}(\underline{\mathbf{x}}) \cdot \underline{\mathbf{n}} = 0 \quad \forall \underline{\mathbf{x}} \in \partial V_f^{\text{in}} \quad (6.16)$$

This is compatible with the condition of fibers free boundaries used in the computation.

For thermal effective properties of *Poisson* fibers, we use boundary conditions that have been introduced in Section 2.3.1 (UTG), which we recall hereafter, as well as new boundary conditions: the mixed thermal boundary conditions (MTBC). First, the averaging relations given for ∇T and $\underline{\mathbf{q}}$, respectively in Equations 2.2 and 2.3, have to be adapted for the homogenization of *Poisson* fibers. Let us consider the volume V , made of two complementary phases of volume V_f and V_p , respectively accounting for the fibers and the porous phase. Thus, if one considers the spatial average over V of the gradient of temperature ∇T :

$$\begin{aligned} \langle \nabla T \rangle &= \frac{1}{V} \int_V \nabla T dV = \frac{1}{V} \int_{V_f} \nabla T dV + \frac{1}{V} \int_{V_p} \nabla T dV \\ &= \frac{1}{V} \int_{V_f} T_{,i} dV \underline{\mathbf{e}}_i + \frac{1}{V} \int_{V_p} T_{,i} dV \underline{\mathbf{e}}_i \\ &= \frac{1}{V} \int_{\partial V_f} T n_i dS \underline{\mathbf{e}}_i + \frac{1}{V} \int_{\partial V_p} T n_i dS \underline{\mathbf{e}}_i \\ &= \frac{1}{V} \int_{\partial V_f} T \underline{\mathbf{n}} dS + \frac{1}{V} \int_{\partial V_p} T \underline{\mathbf{n}} dS \\ &= \frac{1}{V} \int_{\partial V_f^{\text{out}}} T \underline{\mathbf{n}} dS + \frac{1}{V} \int_{\partial V_p^{\text{out}}} T \underline{\mathbf{n}} dS \end{aligned} \quad (6.17)$$

The value of $\langle \nabla T \rangle$ depends on the interpolation chosen for T on ∂V_p .

If one considers now the spatial average over V of a steady-state heat flux vector $\underline{\mathbf{q}}^*$, i.e. $\text{Div} \underline{\mathbf{q}}^* =$

0 in V , it yields:

$$\begin{aligned}
 \langle \underline{\mathbf{q}}^* \rangle &= \frac{1}{V} \int_{V_f} \underline{\mathbf{q}}^* dV + \underbrace{\frac{1}{V} \int_{V_p} \underline{\mathbf{q}}^* dV}_{=0 \text{ cf. Equation 6.15}} \\
 &= \frac{1}{V} \int_{V_f} q_i^* dV \underline{\mathbf{e}}_i \\
 &= \frac{1}{V} \int_{V_f} (q_j^* x_i)_{,j} dV \underline{\mathbf{e}}_i \\
 &= \frac{1}{V} \int_{V_f} q_j^* n_j x_i dS \underline{\mathbf{e}}_i \\
 &= \frac{1}{V} \int_{\partial V_f} (\underline{\mathbf{q}}^* \cdot \underline{\mathbf{n}}) \underline{\mathbf{x}} dS \\
 &= \frac{1}{V} \int_{\partial V_f^{\text{out}}} (\underline{\mathbf{q}}^* \cdot \underline{\mathbf{n}}) \underline{\mathbf{x}} dS + \underbrace{\frac{1}{V} \int_{\partial V_f^{\text{in}}} (\underline{\mathbf{q}}^* \cdot \underline{\mathbf{n}}) \underline{\mathbf{x}} dS}_{=0 \text{ cf. Equation 6.16}} \\
 &= \frac{1}{V} \int_{\partial V_f^{\text{out}}} (\underline{\mathbf{q}}^* \cdot \underline{\mathbf{n}}) \underline{\mathbf{x}} dS \tag{6.18}
 \end{aligned}$$

From a practical viewpoint, $\langle \underline{\mathbf{q}} \rangle$ is computed on the fibers in this way:

$$\langle \underline{\mathbf{q}} \rangle = \frac{1}{V} \int_{V_f} \underline{\mathbf{q}} dV = \frac{V_f}{V} \frac{1}{V_f} \int_{V_f} \underline{\mathbf{q}} dV = V_V^f \langle \underline{\mathbf{q}} \rangle_f \tag{6.19}$$

Finally, let us consider the thermal dissipation rate density \mathcal{D}^{th} that arises from the fields $\underline{\mathbf{q}}^*$ and

∇T in the porous linear case for a reference temperature T_0 (linearized theory):

$$\begin{aligned}
 T_0 \mathcal{D}^{\text{th}} &= \langle -\underline{\mathbf{q}}^* \cdot \nabla T \rangle \\
 &= \frac{1}{V} \int_{V_f} -\underline{\mathbf{q}}^* \cdot \nabla T dV + \underbrace{\frac{1}{V} \int_{V_p} -\underline{\mathbf{q}}^* \cdot \nabla T dV}_{=0} \\
 &= \frac{1}{V} \int_{V_f} -q_i^* T_{,i} dV \\
 &= \frac{1}{V} \int_{V_f} -(q_i^* T)_{,i} dV \\
 &= \frac{1}{V} \int_{\partial V_f} -q_i^* n_i T dS \\
 &= \frac{1}{V} \int_{\partial V_f^{\text{out}}} -T \underline{\mathbf{q}}^* \cdot \underline{\mathbf{n}} dS + \underbrace{\frac{1}{V} \int_{\partial V_f^{\text{in}}} -T \underline{\mathbf{q}}^* \cdot \underline{\mathbf{n}} dS}_{=0} \\
 &= \frac{1}{V} \int_{\partial V_f^{\text{out}}} -T \underline{\mathbf{q}}^* \cdot \underline{\mathbf{n}} dS
 \end{aligned} \tag{6.20}$$

Practically, $T_0 \mathcal{D}^{\text{th}}$ is computed this way:

$$T_0 \mathcal{D}^{\text{th}} = \langle -\underline{\mathbf{q}} \cdot \nabla T \rangle = \frac{1}{V} \int_{V_f} -\underline{\mathbf{q}} \cdot \nabla T dV = V_V^f \langle -\underline{\mathbf{q}} \rangle_f \cdot \langle \nabla T \rangle \tag{6.21}$$

Uniform temperature gradient boundary conditions – UTG

The macroscopic gradient of temperature $\underline{\mathbf{G}}$ is prescribed at the boundary of the simulation domain, such that:

$$T = \underline{\mathbf{G}} \cdot \underline{\mathbf{x}} \quad \forall \underline{\mathbf{x}} \in \partial V = \partial V_f^{\text{out}} \cup \partial V_p^{\text{out}} \tag{6.22}$$

which yields from Equation 6.17,

$$\langle \nabla T \rangle = \frac{1}{V} \int_{\partial V} (\underline{\mathbf{G}} \cdot \underline{\mathbf{x}}) \underline{\mathbf{n}} dS = \underline{\mathbf{G}} \tag{6.23}$$

The macroscopic heat flux field $\underline{\mathbf{Q}}$ is computed in this way:

$$\underline{\mathbf{Q}} = \langle \underline{\mathbf{q}} \rangle = V_V^f \langle \underline{\mathbf{q}} \rangle_f \tag{6.24}$$

Finally, the apparent thermal conductivity $\underline{\lambda}^{\text{app}}$ is estimated using the following relation:

$$\underline{\mathbf{Q}} = -\underline{\lambda}^{\text{app}} \cdot \underline{\mathbf{G}} \tag{6.25}$$

Let us consider the thermal dissipation rate density \mathcal{D}^{th} , computed in this way:

$$\begin{aligned}
 T_0 \mathcal{D}^{\text{th}} &= \frac{1}{V} \int_V -\underline{\mathbf{q}} \cdot \nabla T dV \\
 &= \frac{1}{V} \int_{\partial V} -(\underline{\mathbf{q}} \cdot \underline{\mathbf{n}}) T dS \\
 &= \frac{1}{V} \int_{\partial V} -(\underline{\mathbf{q}} \cdot \underline{\mathbf{n}}) (\underline{\mathbf{G}} \cdot \underline{\mathbf{x}}) dS \\
 &= \frac{1}{V} \int_{\partial V} -(q_i G_j x_j) n_i dS \\
 &= \frac{1}{V} \int_V -q_i G_j x_{j,i} dV \\
 &= \frac{1}{V} \int_V -\underline{\mathbf{q}} \cdot \underline{\mathbf{G}} dV \\
 &= \langle -\underline{\mathbf{q}} \rangle \cdot \underline{\mathbf{G}} \\
 &= -\underline{\mathbf{Q}} \cdot \underline{\mathbf{G}} \\
 &= (\underline{\lambda}^{\text{app}} \cdot \underline{\mathbf{G}}) \cdot \underline{\mathbf{G}}
 \end{aligned} \tag{6.26}$$

Assuming that the homogeneous equivalent medium is isotropic, we use $-\langle \underline{\mathbf{q}} \cdot \nabla T \rangle$ as an estimate of $\lambda^{\text{eff}} \underline{\mathbf{G}} \cdot \underline{\mathbf{G}}$. The following macroscopic gradient of temperature is considered:

$$\underline{\mathbf{G}} = \begin{bmatrix} -1 \\ 0 \\ 0 \end{bmatrix} \tag{6.27}$$

so that,

$$T_0 \mathcal{D}^{\text{th}} = \langle -\underline{\mathbf{q}} \cdot \nabla T \rangle = V_V^f \langle -\underline{\mathbf{q}} \cdot \nabla T \rangle_f = -\underline{\mathbf{Q}} \cdot \underline{\mathbf{G}} = -Q_1 G_1 = Q_1 \tag{6.28}$$

is an estimate of λ^{eff} .

Uniform heat flux boundary conditions – UHF

Let us now consider the case of a macroscopic heat flux $\underline{\mathbf{Q}} \cdot \underline{\mathbf{n}}$ prescribed at the boundary ∂V of the simulation domain, such that:

$$\underline{\mathbf{q}} \cdot \underline{\mathbf{n}} = \underline{\mathbf{Q}} \cdot \underline{\mathbf{n}} \quad \forall \underline{\mathbf{x}} \in \partial V \tag{6.29}$$

In the case of *Poisson fibers*, this condition is in conflict with extension of the heat flux field:

$$\underline{\mathbf{q}} = 0 \quad \forall \underline{\mathbf{x}} \in V_p \tag{6.30}$$

so that,

$$\underline{\mathbf{q}} \cdot \underline{\mathbf{n}} = 0 \quad \forall \underline{\mathbf{x}} \in \partial V_p \quad (6.31)$$

We can only prescribe:

$$\underline{\mathbf{q}} \cdot \underline{\mathbf{n}} = \underline{\mathbf{Q}} \cdot \underline{\mathbf{n}} \quad \forall \underline{\mathbf{x}} \in \partial V_f^{\text{out}} \quad (6.32)$$

but in the case of a random microstructure, these boundary conditions do not ensure the following balance equation:

$$\int_{\partial V} \underline{\mathbf{q}} \cdot \underline{\mathbf{n}} dS = 0 \quad (6.33)$$

That is why we propose the following alternative boundary conditions.

Mixed thermal boundary conditions – MTBC

Temperature is prescribed on a pair of opposite faces $F_1 = F_1^+ \cup F_1^-$ (normal to direction 1) of the boundary ∂V of the simulation domain, such that:

$$T = \underline{\mathbf{G}} \cdot \underline{\mathbf{x}} \quad \forall \underline{\mathbf{x}} \in F_1 \cap \partial V_f^{\text{out}} \quad (6.34)$$

The temperature field T is extended on $F_1 \cap \partial V_p^{\text{out}}$ following the same expression $T = \underline{\mathbf{G}} \cdot \underline{\mathbf{x}}$.

On the other pairs of faces F_2 and F_3 , the heat flux is prescribed such that:

$$\underline{\mathbf{q}} \cdot \underline{\mathbf{n}} = 0 \quad \forall \underline{\mathbf{x}} \in (F_2 \cap \partial V_f^{\text{out}}) \cup (F_3 \cap \partial V_f^{\text{out}}) \quad (6.35)$$

Let us consider the spatial average of the temperature gradient:

$$\begin{aligned} \langle \nabla T \rangle &= \frac{1}{V} \int_V \nabla T dV \\ &= \frac{1}{V} \int_{\partial V} T \underline{\mathbf{n}} dS \\ &= \frac{1}{V} \int_{F_1} T \underline{\mathbf{n}} dS + \frac{1}{V} \int_{F_2 \cup F_3} T \underline{\mathbf{n}} dS \end{aligned} \quad (6.36)$$

For a coordinates system with its origin at the center of the simulation cube, let us consider each

component of the temperature gradient, it yields:

$$\begin{aligned}
 \langle T_{,1} \rangle &= \frac{1}{V} \int_{F_1} T n_1 dS \\
 &= \frac{1}{V} \int_{F_1^+} T n_1 dS - \frac{1}{V} \int_{F_1^-} T n_1 dS \\
 &= \frac{1}{V} \int_{F_1} \underline{\mathbf{G}} \cdot \underline{\mathbf{x}} n_1 dS \\
 &= \frac{1}{V} \underline{\mathbf{G}} \int_{F_1} \underline{\mathbf{x}} n_1 dS \\
 &= \frac{1}{V} \left(G_1 \int_{F_1} x_1 n_1 dS + G_2 \underbrace{\int_{F_1} x_2 n_1 dS}_{=0} + G_3 \underbrace{\int_{F_1} x_3 n_1 dS}_{=0} \right) \\
 &= G_1
 \end{aligned} \tag{6.37}$$

$$\begin{aligned}
 \langle T_{,2} \rangle &= \frac{1}{V} \int_{F_2} T n_2 dS \\
 &= \frac{1}{V} \int_{F_2^+} T n_2 dS - \frac{1}{V} \int_{F_2^-} T n_2 dS \\
 &= \frac{1}{V} \int_{F_2^+ \cap \partial V_f^{\text{out}}} T n_2 dS + \int_{F_2^+ \cap \partial V_p^{\text{out}}} T n_2 dS - \int_{F_2^- \cap \partial V_f^{\text{out}}} T n_2 dS - \int_{F_2^- \cap \partial V_p^{\text{out}}} T n_2 dS
 \end{aligned} \tag{6.38}$$

In our computations the surface integral over $\partial V_f^{\text{out}} \cap F_2$ can be evaluated. However, a suitable extrapolation of T on $\partial V_p^{\text{out}} \cap F_2$ is needed for the full evaluation of $\langle T_{,2} \rangle$. The same argument holds for $\langle T_{,3} \rangle$.

Let us now consider the macroscopic heat flux, using Equation 6.18:

$$\underline{\mathbf{Q}} = V_V^f \langle \underline{\mathbf{q}} \rangle_f = \frac{1}{V} \int_{\partial V_f^{\text{out}}} (\underline{\mathbf{q}} \cdot \underline{\mathbf{n}}) \underline{\mathbf{x}} dS \tag{6.39}$$

So for each components:

$$\begin{aligned}
 Q_i &= \frac{1}{V} \int_{\partial V_f^{\text{out}}} (\underline{\mathbf{q}} \cdot \underline{\mathbf{n}}) x_i dS \\
 &= \frac{1}{V} \int_{F_1 \cap \partial V_f^{\text{out}}} (\underline{\mathbf{q}} \cdot \underline{\mathbf{n}}) x_i dS \\
 &= \frac{1}{V} \int_{F_1^+} q_1 x_i dS - \frac{1}{V} \int_{F_1^-} q_1 x_i dS
 \end{aligned} \tag{6.40}$$

which yields,

$$Q_1 = \frac{1}{V} L \int_{F_1^+} q_1 dS \tag{6.41}$$

In our computation, Q_1 is actually post-processed by means of the following spatial average:

$$Q_1 = V_V^f \langle q_1 \rangle_f \tag{6.42}$$

Components Q_2 and Q_3 are estimated in the same fashion. They do not vanish in general.

Finally, let us consider the thermal dissipation rate density, computed in this way:

$$\begin{aligned}
 T_0 \mathcal{D}^{\text{th}} &= \frac{1}{V} \int_{\partial V} -T (\underline{\mathbf{q}} \cdot \underline{\mathbf{n}}) dS \\
 &= \frac{1}{V} \int_{F_1} -G_i x_i q_j n_j dS
 \end{aligned} \tag{6.43}$$

Assuming that the homogeneous equivalent medium is isotropic, we use $\langle -\underline{\mathbf{q}} \cdot \nabla T \rangle$ as an estimate of $\lambda^{\text{eff}} \underline{\mathbf{G}} \cdot \underline{\mathbf{G}}$. The following macroscopic gradient of temperature is considered:

$$\underline{\mathbf{G}} = \begin{bmatrix} -1 \\ 0 \\ 0 \end{bmatrix} \tag{6.44}$$

so that,

$$\begin{aligned}
 T_0 \mathcal{D}^{\text{th}} &= \langle -\underline{\mathbf{q}} \cdot \nabla T \rangle \\
 &= \frac{1}{V} \int_{\partial V} -(\underline{\mathbf{q}} \cdot \underline{\mathbf{n}}) (\underline{\mathbf{G}} \cdot \underline{\mathbf{x}}) dS \\
 &= \frac{G_1}{V} \int_{\partial V} -(\underline{\mathbf{q}} \cdot \underline{\mathbf{n}}) x_1 dS \\
 &= \frac{G_1}{V} \int_V -(q_i x_1)_{,i} dV \\
 &= \frac{G_1}{V} \int_V -q_1 dV \\
 &= -G_1 Q_1 \\
 &= Q_1
 \end{aligned} \tag{6.45}$$

is an estimate of λ^{eff} . For an isotropic material, Q_2 and Q_3 should converge towards zero for the macroscopic gradient of temperature considered here. This is a useful tool to check for isotropy, as it will be done in Section 6.4.1.

6.2.2 Mechanical properties

The displacement $\underline{\mathbf{u}}$ and stress $\underline{\boldsymbol{\sigma}}$ fields are defined on the elementary volume V : they are computed on V_f only. Over V_p , the fields $\underline{\mathbf{u}}$ and $\underline{\boldsymbol{\sigma}}$ may be considered as extensions of $\underline{\mathbf{u}}$ and $\underline{\boldsymbol{\sigma}}$ on V_f using suitable interpolations assuming continuity for $\underline{\mathbf{u}}$ and $\underline{\boldsymbol{\sigma}} \cdot \underline{\mathbf{n}}$ on $\partial V_{f,p}^{\text{in}}$. We adopt the following extension of the $\underline{\boldsymbol{\sigma}}$ field on V_p :

$$\underline{\boldsymbol{\sigma}}(\underline{\mathbf{x}}) = \underline{\mathbf{0}} \quad \forall \underline{\mathbf{x}} \in V_p \tag{6.46}$$

This choice requires that,

$$\underline{\boldsymbol{\sigma}}(\underline{\mathbf{x}}) \cdot \underline{\mathbf{n}} = \underline{\mathbf{0}} \quad \forall \underline{\mathbf{x}} \in \partial V_f^{\text{in}} \tag{6.47}$$

This is compatible with the condition of fibers free boundaries used in the computation.

For mechanical effective properties of *Poisson* fibers, we use boundary conditions that have been introduced in Section 2.3.2 (KUBC), which we recall hereafter, as well as new boundary conditions: the mixed boundary conditions (MBC). First, the averaging relations given for $\underline{\boldsymbol{\epsilon}}$ and $\underline{\boldsymbol{\sigma}}$, respectively in Equations 2.5 and 2.6, have to be adapted for the homogenization of *Poisson* fibers. Let us consider the volume V , made of two complementary phases of volume V_f and V_p , respectively accounting for the fibers and the porous phase. Thus, if one considers the spatial average over V of the kinematically compatible strain field $\underline{\boldsymbol{\epsilon}}'$, which is defined as the symmetric

part of the gradient of the displacement field $\underline{\mathbf{u}}'$:

$$\begin{aligned}
 \langle \underline{\boldsymbol{\varepsilon}}' \rangle &= \frac{1}{V} \int_V \underline{\boldsymbol{\varepsilon}}' dV = \frac{1}{V} \int_{V_f} \underline{\boldsymbol{\varepsilon}}' dV + \frac{1}{V} \int_{V_p} \underline{\boldsymbol{\varepsilon}}' dV \\
 &= \frac{1}{V} \int_{V_f} u'_{(i,j)} dV \underline{\mathbf{e}}_i \otimes \underline{\mathbf{e}}_j + \frac{1}{V} \int_{V_p} u'_{(i,j)} dV \underline{\mathbf{e}}_i \otimes \underline{\mathbf{e}}_j \\
 &= \frac{1}{V} \int_{\partial V_f} u'_{(i n_j)} dS \underline{\mathbf{e}}_i \otimes \underline{\mathbf{e}}_j + \frac{1}{V} \int_{\partial V_p} u'_{(i n_j)} dS \underline{\mathbf{e}}_i \otimes \underline{\mathbf{e}}_j \\
 &= \frac{1}{V} \int_{\partial V_f} \underline{\mathbf{u}}' \overset{s}{\otimes} \underline{\mathbf{n}} dS + \frac{1}{V} \int_{\partial V_p} \underline{\mathbf{u}}' \overset{s}{\otimes} \underline{\mathbf{n}} dS \\
 &= \frac{1}{V} \int_{\partial V_f^{\text{out}}} \underline{\mathbf{u}}' \overset{s}{\otimes} \underline{\mathbf{n}} dS + \frac{1}{V} \int_{\partial V_p^{\text{out}}} \underline{\mathbf{u}}' \overset{s}{\otimes} \underline{\mathbf{n}} dS
 \end{aligned} \tag{6.48}$$

The value of $\langle \underline{\boldsymbol{\varepsilon}}' \rangle$ depends on the interpolation chosen for $\underline{\mathbf{u}}'$ on ∂V_p .

If one considers now the spatial average over V of a statically admissible stress field $\underline{\boldsymbol{\sigma}}^*$, i.e. $\text{Div} \underline{\boldsymbol{\sigma}}^* = \underline{\mathbf{0}}$ in V , it yields:

$$\begin{aligned}
 \langle \underline{\boldsymbol{\sigma}}^* \rangle &= \frac{1}{V} \int_{V_f} \underline{\boldsymbol{\sigma}}^* dV + \underbrace{\frac{1}{V} \int_{V_p} \underline{\boldsymbol{\sigma}}^* dV}_{=0 \text{ cf. Equation 6.46}} \\
 &= \frac{1}{V} \int_{V_f} \sigma^*_{ij} dV \underline{\mathbf{e}}_i \otimes \underline{\mathbf{e}}_j \\
 &= \frac{1}{V} \int_{V_f} \sigma^*_{(ik\delta_j)k} dV \underline{\mathbf{e}}_i \otimes \underline{\mathbf{e}}_j \\
 &= \frac{1}{V} \int_{V_f} \sigma^*_{(ikx_j),k} dV \underline{\mathbf{e}}_i \otimes \underline{\mathbf{e}}_j \\
 &= \frac{1}{V} \int_{\partial V_f} \sigma^*_{(ikn_k x_j)} dS \underline{\mathbf{e}}_i \otimes \underline{\mathbf{e}}_j \\
 &= \frac{1}{V} \int_{\partial V_f^{\text{out}}} (\underline{\boldsymbol{\sigma}}^* \cdot \underline{\mathbf{n}}) \overset{s}{\otimes} \underline{\mathbf{x}} dS + \underbrace{\frac{1}{V} \int_{\partial V_f^{\text{in}}} (\underline{\boldsymbol{\sigma}}^* \cdot \underline{\mathbf{n}}) \overset{s}{\otimes} \underline{\mathbf{x}} dS}_{=0 \text{ cf. Equation 6.47}} \\
 &= \frac{1}{V} \int_{\partial V_f^{\text{out}}} (\underline{\boldsymbol{\sigma}}^* \cdot \underline{\mathbf{n}}) \overset{s}{\otimes} \underline{\mathbf{x}} dS
 \end{aligned} \tag{6.49}$$

From a practical viewpoint, $\langle \underline{\boldsymbol{\sigma}} \rangle$ is computed on the fibers in this way:

$$\langle \underline{\boldsymbol{\sigma}} \rangle = \frac{1}{V} \int_{V_f} \underline{\boldsymbol{\sigma}} dV = \frac{V_f}{V} \frac{1}{V_f} \int_{V_f} \underline{\boldsymbol{\sigma}} dV = V_f^f \langle \underline{\boldsymbol{\sigma}} \rangle_f \tag{6.50}$$

Finally, let us consider the elastic energy density \mathcal{E}^{el} that arises from the fields $\underline{\boldsymbol{\sigma}}^*$ and $\underline{\boldsymbol{\varepsilon}}'$ in the

porous case:

$$\begin{aligned}
 2\mathcal{E}^{\text{el}} &= \langle \underline{\boldsymbol{\sigma}}^* : \underline{\boldsymbol{\varepsilon}}' \rangle \\
 &= \frac{1}{V} \int_{V_f} \underline{\boldsymbol{\sigma}}^* : \underline{\boldsymbol{\varepsilon}}' dV + \underbrace{\frac{1}{V} \int_{V_p} \underline{\boldsymbol{\sigma}}^* : \underline{\boldsymbol{\varepsilon}}' dV}_{=0} \\
 &= \frac{1}{V} \int_{V_f} \sigma_{ij}^* u'_{(i,j)} dV \\
 &= \frac{1}{V} \int_{V_f} (\sigma_{ij}^* u'_i)_{,j} dV \\
 &= \frac{1}{V} \int_{\partial V_f} \sigma_{ij}^* u'_i n_j dS \\
 &= \frac{1}{V} \int_{\partial V_f} (\underline{\boldsymbol{\sigma}}^* \cdot \underline{\mathbf{n}}) \cdot \underline{\mathbf{u}}' dS \\
 &= \frac{1}{V} \int_{\partial V_f^{\text{out}}} (\underline{\boldsymbol{\sigma}}^* \cdot \underline{\mathbf{n}}) \cdot \underline{\mathbf{u}}' dS + \underbrace{\frac{1}{V} \int_{\partial V_f^{\text{in}}} (\underline{\boldsymbol{\sigma}}^* \cdot \underline{\mathbf{n}}) \cdot \underline{\mathbf{u}}' dS}_{=0} \\
 &= \frac{1}{V} \int_{\partial V_f^{\text{out}}} (\underline{\boldsymbol{\sigma}}^* \cdot \underline{\mathbf{n}}) \cdot \underline{\mathbf{u}}' dS \tag{6.51}
 \end{aligned}$$

Practically, \mathcal{E}^{el} is computed this way:

$$2\mathcal{E}^{\text{el}} = \langle \underline{\boldsymbol{\sigma}} : \underline{\boldsymbol{\varepsilon}} \rangle = \frac{1}{V} \int_{V_f} \underline{\boldsymbol{\sigma}} : \underline{\boldsymbol{\varepsilon}} dV = V_V^f \langle \underline{\boldsymbol{\sigma}} \rangle_f : \langle \underline{\boldsymbol{\varepsilon}} \rangle \tag{6.52}$$

Kinematic uniform boundary conditions – KUBC

The macroscopic strain tensor $\underline{\mathbf{E}}$ is prescribed at the boundary ∂V of the simulation domain, such that:

$$\underline{\mathbf{u}} = \underline{\mathbf{E}} \cdot \underline{\mathbf{x}} \quad \forall \underline{\mathbf{x}} \in \partial V = \partial V_f^{\text{out}} \cup \partial V_p^{\text{out}} \tag{6.53}$$

which yields,

$$\langle \underline{\boldsymbol{\varepsilon}} \rangle = \frac{1}{V} \int_{\partial V} (\underline{\mathbf{E}} \cdot \underline{\mathbf{x}}) \underline{\mathbf{n}} dS = \underline{\mathbf{E}} \tag{6.54}$$

The macroscopic stress field $\underline{\boldsymbol{\Sigma}}$ is computed in this way:

$$\underline{\boldsymbol{\Sigma}} = \langle \underline{\boldsymbol{\sigma}} \rangle = V_V^f \langle \underline{\boldsymbol{\sigma}} \rangle_f \tag{6.55}$$

Finally, the apparent elastic moduli $\underline{\underline{C}}^{\text{app}}$ are estimated using the following relation:

$$\underline{\underline{\Sigma}} = \underline{\underline{C}}^{\text{app}} : \underline{\underline{E}} \quad (6.56)$$

Elastic moduli Using the linear relationships arising from Equation 1.10, 6 different computations have to be performed to determine the full elastic moduli tensor. For instance, in order to compute the components C_{2I}^{app} , the following macroscopic strain tensor $\underline{\underline{E}}$ is considered:

$$\underline{\underline{E}} = \begin{bmatrix} 0 & 0 & 0 \\ 0 & 1 & 0 \\ 0 & 0 & 0 \end{bmatrix} \quad (6.57)$$

so that,

$$2\mathcal{E}^{\text{el}} = \langle \underline{\underline{\sigma}} : \underline{\underline{\epsilon}} \rangle = V_V^f \langle \underline{\underline{\sigma}} : \underline{\underline{\epsilon}} \rangle_f = \underline{\underline{\Sigma}} : \underline{\underline{E}} \quad (6.58)$$

Using Equation 6.56, the following linear relationships arise for C_{2I}^{app} :

$$\begin{aligned} \Sigma_{11} &= C_{12}^{\text{app}} E_{22} \\ \Sigma_{22} &= C_{22}^{\text{app}} E_{22} \\ \Sigma_{33} &= C_{23}^{\text{app}} E_{22} \\ \Sigma_{23} &= C_{24}^{\text{app}} E_{22} \\ \Sigma_{31} &= C_{25}^{\text{app}} E_{22} \\ \Sigma_{12} &= C_{26}^{\text{app}} E_{22} \end{aligned} \quad (6.59)$$

The other components of C_{IJ}^{app} are computed the same way.

Bulk modulus Assuming that the homogeneous equivalent medium is isotropic, we use $\langle \underline{\underline{\sigma}} : \underline{\underline{\epsilon}} \rangle$ as an estimate of $\left(\underline{\underline{C}}^{\text{eff}} : \underline{\underline{E}} \right) : \underline{\underline{E}}$, with $\underline{\underline{C}}^{\text{eff}}$ that can be rewritten in this way:

$$\underline{\underline{C}}^{\text{eff}} = 3k^{\text{eff}} \underline{\underline{J}} + 2\mu^{\text{eff}} \underline{\underline{K}} \quad (6.60)$$

Hence, for a hydrostatic macroscopic strain tensor,

$$\underline{\underline{E}} = \begin{bmatrix} 1 & 0 & 0 \\ 0 & 1 & 0 \\ 0 & 0 & 1 \end{bmatrix} \quad (6.61)$$

it yields:

$$2\mathcal{E}^{\text{el}} = \langle \underline{\sigma} : \underline{\epsilon} \rangle = V_V^f \langle \underline{\sigma} : \underline{\epsilon} \rangle_f = \underline{\Sigma} : \underline{E} = \left(\underline{C}^{\text{eff}} : \underline{E} \right) : \underline{E} = 3k^{\text{eff}} \underline{E} : \underline{J} : \underline{E} = 9k^{\text{eff}} \quad (6.62)$$

$\frac{1}{9} \langle \underline{\sigma} : \underline{\epsilon} \rangle$ is then an estimate of k^{eff} .

Shear modulus Assuming that the homogeneous equivalent medium is isotropic, we use $\langle \underline{\sigma} : \underline{\epsilon} \rangle$ as an estimate of $\left(\underline{C}^{\text{eff}} : \underline{E} \right) : \underline{E}$, with $\underline{C}^{\text{eff}}$ that can be rewritten using Equation 6.60.

So, for a deviatoric macroscopic strain tensor,

$$\underline{E} = \begin{bmatrix} 0 & \frac{1}{2} & 0 \\ \frac{1}{2} & 0 & 0 \\ 0 & 0 & 0 \end{bmatrix} \quad (6.63)$$

it yields:

$$2\mathcal{E}^{\text{el}} = \langle \underline{\sigma} : \underline{\epsilon} \rangle = V_V^f \langle \underline{\sigma} : \underline{\epsilon} \rangle_f = \underline{\Sigma} : \underline{E} = \left(\underline{C}^{\text{eff}} : \underline{E} \right) : \underline{E} = 2\mu^{\text{eff}} \underline{E} : \underline{K} : \underline{E} = \mu^{\text{eff}} \quad (6.64)$$

$\langle \underline{\sigma} : \underline{\epsilon} \rangle$ is then an estimate of μ^{eff} .

Static uniform boundary conditions – SUBC

Let us now consider the case of a macroscopic traction vector $\underline{\Sigma} \cdot \underline{n}$ prescribed at the boundary ∂V of the simulation domain, such that:

$$\underline{\sigma} \cdot \underline{n} = \underline{\Sigma} \cdot \underline{n} \quad \forall \underline{x} \in \partial V \quad (6.65)$$

In the case of *Poisson* fibers, this condition is in conflict with extension of the stress field:

$$\underline{\sigma} = 0 \quad \forall \underline{x} \in V_p \quad (6.66)$$

so that,

$$\underline{\sigma} \cdot \underline{n} = 0 \quad \forall \underline{x} \in \partial V_p \quad (6.67)$$

We can only prescribe:

$$\underline{\sigma} \cdot \underline{n} = \underline{\Sigma} \cdot \underline{n} \quad \forall \underline{x} \in \partial V_f^{\text{out}} \quad (6.68)$$

but in the case of a random microstructure, these boundary conditions do not ensure the following balance equation:

$$\int_{\partial V} \boldsymbol{\sigma} \cdot \underline{\mathbf{n}} \, dS = \underline{\mathbf{0}} \quad (6.69)$$

That is why we propose the following alternative boundary conditions.

Mixed boundary conditions – MBC

A non-uniform type of boundary conditions is proposed here, instead of SUBC, in order to compute values that we can compare with those obtained using KUBC. Mixed boundary conditions are “softer” than KUBC, only certain DOFs are prescribed at the boundary ∂V . They differ from the mixed uniform boundary conditions proposed (MUBC) in [Hazanov and Huet, 1994] and [Hazanov, 1998], or the normal mixed boundary conditions (NMBC) proposed by [Gélébart et al., 2009]. As a matter of fact, in the case of *Poisson* fibers, the existence of a porous phase intersecting the limit ∂V of the elementary volume is incompatible with MUBC and NMBC. Nevertheless, considering that the mechanical work is happening within the fibers, we defined boundary conditions on ∂V_f only. Isotropic elastic behavior is assumed for determining the bulk and shear moduli from the following mixed loading.

Triaxial loading Let us consider the case of a triaxial loading in order to estimate the bulk modulus k . Displacement $\underline{\mathbf{u}}$ is prescribed along normals on ∂V , as illustrated on Figure 6.7, such that:

$$\begin{aligned} u_1 &= E_{11} x_1 & \forall \underline{\mathbf{x}} \in F_1 \\ u_2 &= E_{22} x_2 & \forall \underline{\mathbf{x}} \in F_2 \\ u_3 &= E_{33} x_3 & \forall \underline{\mathbf{x}} \in F_3 \end{aligned} \quad (6.70)$$

The traction vector $\boldsymbol{\sigma} \cdot \underline{\mathbf{n}}$ is prescribed in this way:

$$\begin{aligned} \sigma_{21} n_1 &= \sigma_{31} n_1 = 0 & \forall \underline{\mathbf{x}} \in F_1 \\ \sigma_{12} n_2 &= \sigma_{32} n_2 = 0 & \forall \underline{\mathbf{x}} \in F_2 \\ \sigma_{13} n_3 &= \sigma_{23} n_3 = 0 & \forall \underline{\mathbf{x}} \in F_3 \end{aligned} \quad (6.71)$$

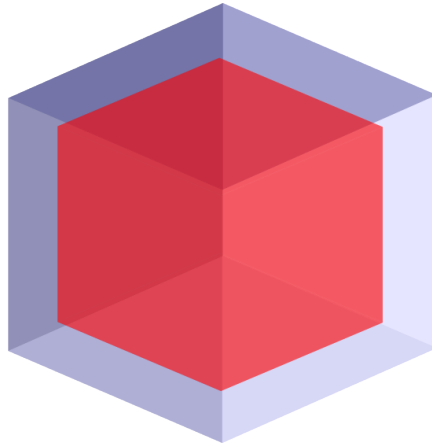


Figure 6.7: Deformed shape (red) of an elementary volume under hydrostatic compression

Let us consider the spatial average of the strain:

$$\begin{aligned}\langle \underline{\boldsymbol{\varepsilon}} \rangle &= \frac{1}{V} \int_V \underline{\boldsymbol{\varepsilon}} dV \\ &= \frac{1}{V} \int_{\partial V} \underline{\boldsymbol{u}} \otimes \underline{\boldsymbol{n}} dS \\ &= \frac{1}{V} \int_{\partial V} u_i n_j dS \underline{\boldsymbol{e}}_i \otimes \underline{\boldsymbol{e}}_j\end{aligned}\tag{6.72}$$

If we now consider each component of the strain field for the case of a coordinates system with

its origin at the center of the cube, it yields:

$$\begin{aligned}
 \langle \varepsilon_{11} \rangle &= \frac{1}{V} \int_V \varepsilon_{11} dV \\
 &= \frac{1}{V} \int_V u_{1,1} dV \\
 &= \frac{1}{V} \int_{\partial V} u_1 n_1 dS \\
 &= \frac{1}{V} \left(\int_{F_1} u_1 n_1 dS + \underbrace{\int_{F_2} u_1 n_1 dS}_{=0} + \underbrace{\int_{F_3} u_1 n_1 dS}_{=0} \right) \\
 &= \frac{1}{V} \int_{F_1} u_1 n_1 dS \\
 &= \frac{1}{V} \int_{F_1} E_{11} x_1 n_1 dS \\
 &= \frac{1}{V} \int_{F_1^+} E_{11} x_1 dS - \frac{1}{V} \int_{F_1^-} E_{11} x_1 dS \\
 &= \frac{E_{11}}{V} L^3 \\
 &= E_{11}
 \end{aligned} \tag{6.73}$$

The spatial averages $\langle \varepsilon_{22} \rangle = E_{22}$ and $\langle \varepsilon_{33} \rangle = E_{33}$ are determined similarly. Let us now consider other components, for instance:

$$\begin{aligned}
 \langle \varepsilon_{12} \rangle &= \frac{1}{V} \int_V \varepsilon_{12} dV \\
 &= \frac{1}{V} \int_V u_{1,2} dV \\
 &= \frac{1}{V} \int_{\partial V} u_1 n_2 dS \\
 &= \frac{1}{V} \left(\underbrace{\int_{F_1} u_1 n_2 dS}_{=0} + \int_{F_2} u_1 n_2 dS + \underbrace{\int_{F_3} u_1 n_2 dS}_{=0} \right) \\
 &= \frac{1}{V} \int_{F_2} u_1 n_2 dS \\
 &= \frac{1}{V} \left(\int_{F_2^+} u_1 dS - \int_{F_2^-} u_1 dS \right) \\
 &= \frac{1}{V} \left(\int_{F_2^+ \cap \partial V_f^{\text{out}}} u_1 dS + \int_{F_2^+ \cap \partial V_p^{\text{out}}} u_1 dS - \int_{F_2^- \cap \partial V_f^{\text{out}}} u_1 dS - \int_{F_2^- \cap \partial V_p^{\text{out}}} u_1 dS \right) \tag{6.74}
 \end{aligned}$$

Chapter 6. Poisson fibers

In our computations the surface integral over $\partial V_f^{\text{out}} \cap F_2$ can be evaluated. However, a suitable extrapolation of \underline{u} on $\partial V_p^{\text{out}} \cap F_2$ is needed for the full evaluation of $\langle \varepsilon_{12} \rangle$. This holds for every component $\langle \varepsilon_{ij} \rangle \quad \forall i \neq j$.

Let us now consider the macroscopic stress field. From Equation 6.49, it yields:

$$\underline{\Sigma} = V_V^f \langle \underline{\sigma} \rangle_f = \frac{1}{V} \int_{\partial V_f^{\text{out}}} \sigma_{(ik} n_k x_j) dS \quad (6.75)$$

If we now consider each component of the stress field:

$$\Sigma_{11} = V_V^f \langle \sigma_{11} \rangle_f \quad (6.76)$$

In our computations, Σ_{11} is computed as a spatial average. Other components Σ_{ij} are computed in the same way. If we consider another example:

$$\begin{aligned} \Sigma_{12} &= \frac{1}{2V} \int_{\partial V_f^{\text{out}}} \sigma_{1k} n_k x_2 + \sigma_{2k} n_k x_1 dS \\ &= \frac{1}{2V} \left(\int_{F_1} \left(\sigma_{11} n_1 x_2 + \underbrace{\sigma_{21} n_1 x_1}_{=0} \right) dS + \int_{F_2} \left(\underbrace{\sigma_{12} n_2 x_2}_{=0} + \sigma_{22} n_2 x_1 \right) dS \right. \\ &\quad \left. + \int_{F_3} \left(\underbrace{\sigma_{13} n_3 x_2}_{=0} + \underbrace{\sigma_{23} n_3 x_1}_{=0} \right) dS \right) \\ &= \frac{1}{2V} \left(\int_{F_1} \sigma_{11} n_1 x_2 dS + \int_{F_2} \sigma_{22} n_2 x_1 dS \right) \end{aligned} \quad (6.77)$$

which does not vanish in general.

Assuming that the homogeneous equivalent medium is isotropic, we use $\langle \underline{\sigma} : \underline{\varepsilon} \rangle$ as an estimate of $\left(\underline{\mathbb{C}}^{\text{eff}} : \underline{E} \right) : \underline{E}$, with $\underline{\mathbb{C}}^{\text{eff}}$ that can be rewritten using Equation 6.60.

Hence, for a hydrostatic macroscopic strain tensor,

$$\underline{E} = \begin{bmatrix} 1 & 0 & 0 \\ 0 & 1 & 0 \\ 0 & 0 & 1 \end{bmatrix} \quad (6.78)$$

$\frac{1}{9} \langle \underline{\sigma} : \underline{\varepsilon} \rangle$ is an estimate of k^{eff} . For an isotropic material, $\underline{\mathbb{K}} : \underline{\Sigma}$ should tend towards zero for the macroscopic strain tensor considered here. This will be used to check for isotropy in Section 6.4.1.

Shear loading Let us now consider the case of the shear loading for determining the shear modulus μ . Displacement \underline{u} is prescribed along direction 1 on F_2 and direction 2 on F_1 , as

illustrated on Figure 6.8, such that:

$$\begin{aligned} u_2 &= E_{12}x_1 \quad \forall \underline{\mathbf{x}} \in F_1 \\ u_1 &= E_{12}x_2 \quad \forall \underline{\mathbf{x}} \in F_2 \end{aligned} \tag{6.79}$$

The traction vector $\boldsymbol{\sigma} \cdot \underline{\mathbf{n}}$ is prescribed in this way:

$$\begin{aligned} \sigma_{11}n_1 &= \sigma_{31}n_1 = 0 \quad \forall \underline{\mathbf{x}} \in F_1 \\ \sigma_{22}n_2 &= \sigma_{32}n_2 = 0 \quad \forall \underline{\mathbf{x}} \in F_2 \\ \sigma_{33}n_3 &= \sigma_{13}n_3 = \sigma_{23}n_3 = 0 \quad \forall \underline{\mathbf{x}} \in F_3 \end{aligned} \tag{6.80}$$

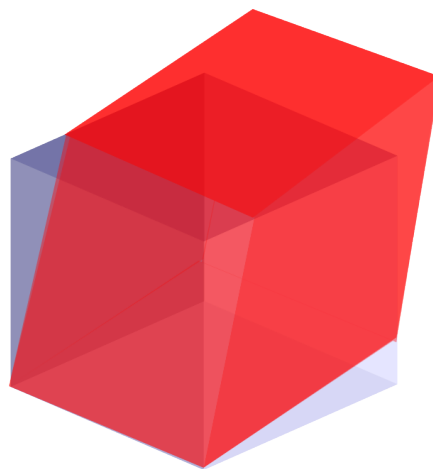


Figure 6.8: Deformed shape (red) of an elementary volume under shear

Let us consider the spatial average of the strain using Equation 6.72. If we now consider each

component of the strain field, it yields:

$$\begin{aligned}
 \langle \varepsilon_{12} \rangle &= \frac{1}{V} \int_V \varepsilon_{12} dV \\
 &= \frac{1}{V} \int_V u_{1,2} dV \\
 &= \frac{1}{V} \int_{\partial V} u_1 n_2 dS \\
 &= \frac{1}{V} \left(\underbrace{\int_{F_1} u_1 n_2 dS}_{=0} + \int_{F_2} u_1 n_2 dS + \underbrace{\int_{F_3} u_1 n_2 dS}_{=0} \right) \\
 &= \frac{1}{V} \int_{F_2} u_1 n_2 dS \\
 &= \frac{1}{V} \int_{F_2} E_{12} x_1 n_2 dS \\
 &= \frac{1}{V} \int_{F_1^+} E_{12} \frac{L}{2} dS - \frac{1}{V} \int_{F_1^-} \left(-E_{12} \frac{L}{2} \right) dS \\
 &= \frac{E_{12}}{V} L^3 \\
 &= E_{12}
 \end{aligned} \tag{6.81}$$

Let us now consider other components, for instance:

$$\begin{aligned}
 \langle \varepsilon_{11} \rangle &= \frac{1}{V} \int_V \varepsilon_{11} dV \\
 &= \frac{1}{V} \int_V u_{1,1} dV \\
 &= \frac{1}{V} \int_{\partial V} u_1 n_1 dS \\
 &= \frac{1}{V} \left(\int_{F_1} u_1 n_1 dS + \underbrace{\int_{F_2} u_1 n_1 dS}_{=0} + \underbrace{\int_{F_3} u_1 n_1 dS}_{=0} \right) \\
 &= \frac{1}{V} \int_{F_1} u_1 n_1 dS \\
 &= \frac{1}{V} \left(\int_{F_1^+} u_1 dS - \int_{F_1^-} u_1 dS \right) \\
 &= \frac{1}{V} \left(\int_{F_1 \cap \partial V_f^{\text{out}}} u_1 dS + \int_{F_1 \cap \partial V_p^{\text{out}}} u_1 dS \right)
 \end{aligned} \tag{6.82}$$

In our computations the surface integrals over $\partial V_f^{\text{out}} \cap F_1$ can be evaluated. However, a suitable

extrapolation of $\underline{\mathbf{u}}$ on $\partial V_p^{\text{out}} \cap F_1$ is needed for the full evaluation of $\langle \varepsilon_{11} \rangle$. This holds for every component $\langle \varepsilon_{ij} \rangle$.

Let us now consider the macroscopic stress field. From Equation 6.49, it yields:

$$\underline{\underline{\Sigma}} = V_V^f \langle \underline{\underline{\sigma}} \rangle_f = \frac{1}{V} \int_{\partial V_f^{\text{out}}} \sigma_{(ik} n_k x_j) dS \quad (6.83)$$

If we now consider each component of the stress field:

$$\Sigma_{12} = V_V^f \langle \sigma_{12} \rangle_f \quad (6.84)$$

In our computations, Σ_{12} is computed as a spatial average. Other components Σ_{ij} are computed in the same way. If we consider another example:

$$\begin{aligned} \Sigma_{11} &= \frac{1}{V} \int_{\partial V_f^{\text{out}}} \sigma_{1k} n_k x_1 dS \\ &= \frac{1}{V} \left(\underbrace{\int_{F_1} \sigma_{11} n_1 x_1 dS}_{=0} + \int_{F_2} \sigma_{12} n_2 x_1 dS + \underbrace{\int_{F_3} \sigma_{13} n_3 x_1 dS}_{=0} \right) \\ &= \frac{1}{V} \int_{F_2} \sigma_{12} n_2 x_1 dS \end{aligned} \quad (6.85)$$

which does not vanish in general.

Finally, by computing the elastic energy density using Equation 6.51, and assuming that the homogeneous equivalent medium is isotropic, we use $\langle \underline{\underline{\sigma}} : \underline{\underline{\varepsilon}} \rangle$ as an estimate of $\left(\underline{\underline{\mathbf{C}}}^{\text{eff}} : \underline{\underline{\mathbf{E}}} \right) : \underline{\underline{\mathbf{E}}}$, with $\underline{\underline{\mathbf{C}}}^{\text{eff}}$ that can be rewritten using Equation 6.60: $\underline{\underline{\mathbf{C}}}^{\text{eff}} = 3k^{\text{eff}} \underline{\underline{\mathbf{J}}} + 2\mu^{\text{eff}} \underline{\underline{\mathbf{K}}}$.

Hence, for a deviatoric macroscopic strain tensor,

$$\underline{\underline{\mathbf{E}}} = \begin{bmatrix} 0 & \frac{1}{2} & 0 \\ \frac{1}{2} & 0 & 0 \\ 0 & 0 & 0 \end{bmatrix} \quad (6.86)$$

$\langle \underline{\underline{\sigma}} : \underline{\underline{\varepsilon}} \rangle$ is an estimate of μ^{eff} . For an isotropic material, $\underline{\underline{\mathbf{J}}} : \underline{\underline{\Sigma}}$ should tend towards zero for the macroscopic strain tensor considered here. This will be used to check for isotropy in Section 6.4.1.

Young's modulus (GPa)	210
Poisson's ratio	0.3
Shear modulus (GPa)	81
Bulk modulus (GPa)	175
Thermal conductivity (W.[L] ⁻¹ .K ⁻¹)	100
Volume fraction	0.16

Table 6.2: Constitutive material parameters for *Poisson* fibers

6.3 Results

The computation of elastic and thermal properties has been performed on hundreds of realizations of *Poisson* fibers. Fibres were attributed the constitutive material properties listed in Table 6.2. Each realization gives rise to different results for apparent morphological, thermal and mechanical properties. Mean values over n realizations of the same size and mesh density are considered in this section. The number of realizations n fluctuates depending on the size and boundary conditions, these values are gathered in Table 6.3 for $d = 2$, with the relative error associated, determined using Equation 4.33. Results presented in this section are only shown for a given mesh density $d = 2$. Results for all mesh densities are postponed to Appendix D.

6.3.1 Morphological properties

The volume fraction of fibers $\overline{V_V^f}$ over n realizations for a given volume size V is computed using FE as follows:

$$\overline{V_V^f} = \frac{1}{n} \sum_{i=1}^n \langle V_V^f \rangle_i = \frac{1}{n} \sum_{i=1}^n \left(\frac{1}{V} \int_V 1_{V_f} dV \right)_i \quad (6.87)$$

with 1_{V_f} the indicator function of the fiber phase.

The number of realizations considered corresponds to the highest number in each column of Table 6.3. These mean values are then plotted as a function of the volume of simulation. Results are shown on Figure 6.9 for the volume fraction of *Poisson* fibers. The mean value obtained for $V = 10^6$ is $\overline{V_V^f} = 16.2\% \pm 1.3\%$. Fluctuations are inherent to morphological stochastic modeling, but there is also a bias due to the mesh density, as explained in Section 6.1.6.

BC \ Size	10	20	30	40	50	60	70	80	90	100
$n - \text{UTG} - \overline{\lambda^{\text{app}}}$	64	64	62	60	56	56	53	58	39	21
$\epsilon_{\text{rel}} - \text{UTG} - \overline{\lambda^{\text{app}}}$	12.2%	5.6%	4.2%	3.1%	2.7%	2.3%	2.0%	1.7%	1.9%	2.3%
$n - \text{MTBC} - \overline{\lambda^{\text{app}}}$	51	63	60	56	50	46	48	46	30	19
$\epsilon_{\text{rel}} - \text{MTBC} - \overline{\lambda^{\text{app}}}$	17.0%	8.0%	5.8%	4.1%	3.6%	3.0%	2.5%	2.3%	2.5%	2.8%
$n - \text{KUBC} - \overline{k^{\text{app}}}$	63	63	61	60	56	54	44	51	32	13
$\epsilon_{\text{rel}} - \text{KUBC} - \overline{k^{\text{app}}}$	9.9%	4.9%	3.7%	2.9%	2.5%	2.1%	2.0%	1.7%	1.9%	2.6%
$n - \text{KUBC} - \overline{\mu^{\text{app}}}$	63	63	61	60	54	54	47	50	27	14
$\epsilon_{\text{rel}} - \text{KUBC} - \overline{\mu^{\text{app}}}$	11.9%	6.2%	4.7%	3.7%	3.3%	2.7%	2.6%	2.2%	2.7%	3.3%
$n - \text{MBC} - \overline{k^{\text{app}}}$	40	60	53	55	45	48	37	46	28	13
$\epsilon_{\text{rel}} - \text{MBC} - \overline{k^{\text{app}}}$	25.6%	11.7%	8.8%	6.0%	5.3%	4.1%	3.9%	3.0%	3.3%	4.2%
$n - \text{MBC} - \overline{\mu^{\text{app}}}$	41	62	58	59	48	49	45	41	11	12
$\epsilon_{\text{rel}} - \text{MBC} - \overline{\mu^{\text{app}}}$	51.6%	21.8%	14.7%	9.8%	8.8%	6.8%	5.6%	5.4%	8.9%	7.1%

Table 6.3: Number of realizations n considered and associated relative error ϵ_{rel} depending on boundary conditions and simulation size

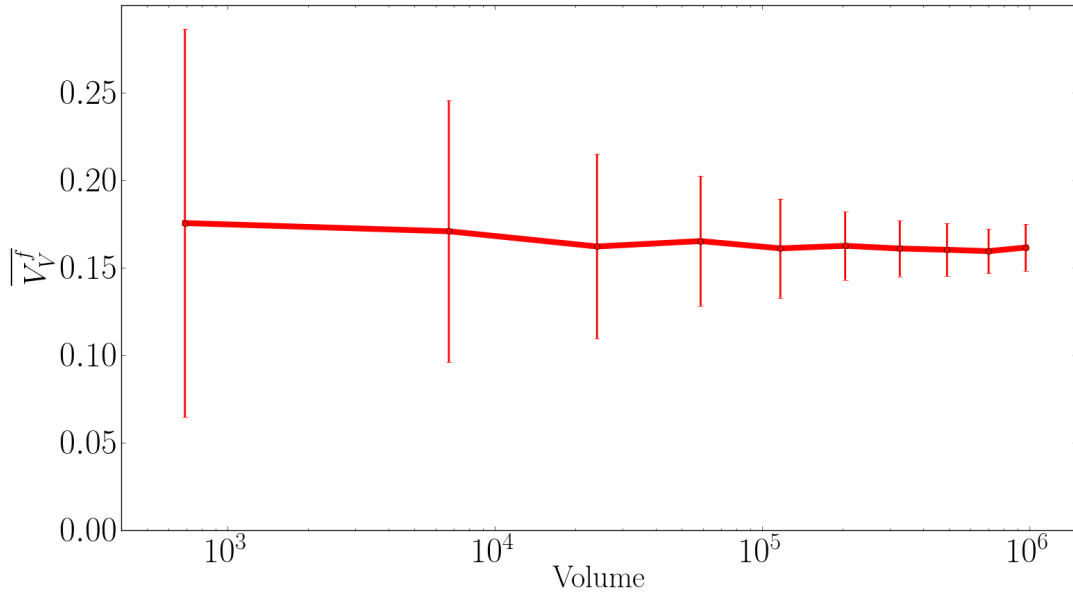


Figure 6.9: Mean values for the volume fraction depending on the volume size V

6.3.2 Thermal properties

Results for the thermal properties are obtained over a large number of realizations. Assuming isotropy of the thermal behavior, the thermal conductivity $\overline{\lambda^{\text{app}}}$ is computed in this way:

$$\overline{\lambda^{\text{app}}} = \frac{1}{n} \sum_{i=1}^n \langle \lambda^{\text{app}} \rangle_i = \frac{1}{n} \sum_{i=1}^n \left(\langle -\underline{q} \rangle_f : \langle \nabla T \rangle_i \right) \quad (6.88)$$

	$\overline{\lambda^{\text{app}}} \text{ (W.[L]}^{-1}.\text{K}^{-1})$
FE-UTG	7.07 ± 0.93
FE-MTBC	6.07 ± 0.97
<i>Hashin–Shtrikman</i> upper bound	11.27
<i>Wiener</i> upper bound	16.00

Table 6.4: Results for the thermal conductivity

Results are shown on Figure 6.10 for the thermal conductivity $\overline{\lambda^{\text{app}}}$ of *Poisson* fibers. The *Hashin–Shtrikman* and *Wiener* lower bounds, along with *Bruggeman’s* self-consistent estimate, are equal to zero since the thermal conductivity of the porous matrix is considered to be zero. There are discrepancies that are decreasing with volume down to an amount of about 16% between UTG and MTBC regarding the estimated value for thermal conductivity for the largest volume, this advocates for larger RVE sizes than the elementary volumes considered in this study. It can also be seen that mesh density does not influence the average values obtained, except for small elementary volume sizes, for which boundary effects are strongly affecting the results. The values obtained for the larger size considered ($\overline{N} \approx 800$), with mesh density $d = 2$, are shown with their corresponding intervals of confidence $[\overline{Z} - 2D_Z, \overline{Z} + 2D_Z]$ in Table 6.4 and compared with analytical bounds.

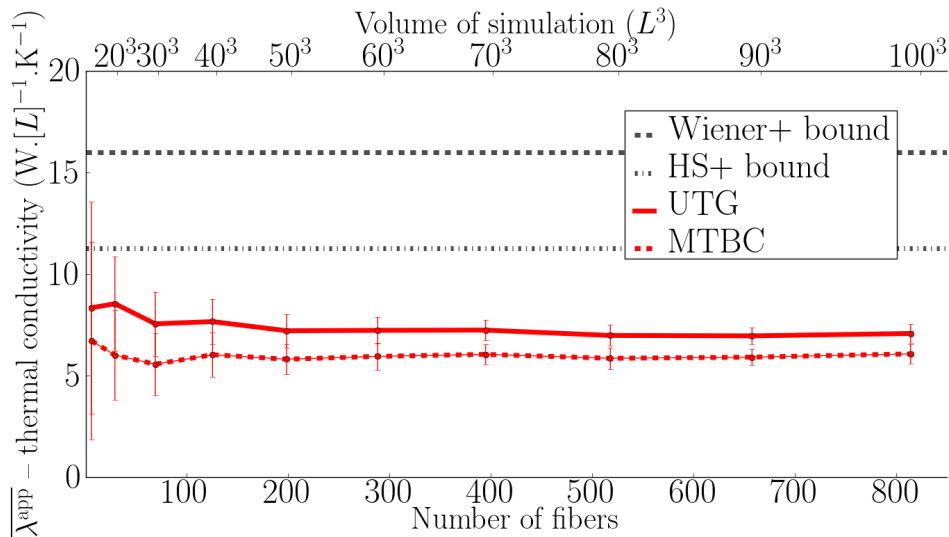


Figure 6.10: Mean values for the thermal conductivity depending on the number of fibers \overline{N}

	$\overline{k^{\text{app}}}$ (MPa)	$\overline{\mu^{\text{app}}}$ (MPa)
FE-KUBC	4763 ± 624	3270 ± 394
FE-MBC	2527 ± 413	1097 ± 272
<i>Hashin–Shtrikman</i> upper bound	11839	7328
<i>Voigt</i> bound	28000	12923

Table 6.5: Results for the bulk and shear moduli

6.3.3 Elastic properties

As for the thermal conductivity, elastic properties are obtained as mean values over hundreds of realizations. Assuming isotropy of the elastic behavior, the bulk modulus $\overline{k^{\text{app}}}$ is computed in this way:

$$\overline{k^{\text{app}}} = \frac{1}{n} \sum_{i=1}^n \langle k^{\text{app}} \rangle_i = \frac{1}{n} \sum_{i=1}^n \left(\frac{1}{9} \langle \boldsymbol{\sigma} \rangle_f : \langle \boldsymbol{\varepsilon} \rangle \right)_i \quad (6.89)$$

On the other hand, still assuming elastic isotropy, the shear modulus $\overline{\mu^{\text{app}}}$ is obtained as follows:

$$\overline{\mu^{\text{app}}} = \frac{1}{n} \sum_{i=1}^n \langle \mu^{\text{app}} \rangle_i = \frac{1}{n} \sum_{i=1}^n \left(\langle \boldsymbol{\sigma} \rangle_f : \langle \boldsymbol{\varepsilon} \rangle \right)_i \quad (6.90)$$

Results for the bulk modulus $\overline{k^{\text{app}}}$ and shear modulus $\overline{\mu^{\text{app}}}$ are shown respectively on Figures 6.11 and 6.12 against the volume and corresponding number of fibers considered, which is proportional to $V^{\frac{2}{3}}$. The *Hashin–Shtrikman* and *Reuss* lower bounds, as well as the self-consistent estimate, are equal to zero since the elastic moduli of the porous matrix are considered to be zero. The values obtained for the largest system size considered ($\overline{N} \approx 800$) are shown with their corresponding intervals of confidence [$\overline{Z} \pm 2D_Z$] in Table 6.5 and compared with analytical bounds. Boundary layer effects are important for small elementary volume sizes, for both types of boundary conditions. Mesh density has a limited impact on the average values obtained for elastic moduli, except for small volumes. There are very strong discrepancies for mean values obtained with KUBC and MBC for both bulk and shear moduli, even for the largest volume considered: 213% for $\overline{k^{\text{app}}}$ and 66% for $\overline{\mu^{\text{app}}}$. These results advocate for an RVE size dramatically larger than the elementary volume sizes studied here.

6.4 Discussion

In the results presented above, isotropy is assumed for elastic and thermal properties, however this question should be assessed with measurements: this is the purpose of this section. First, we will consider morphological isotropy with the analysis of the covariance. Then we will compute thermal and elastic properties without assuming isotropy, and we will draw conclusions from

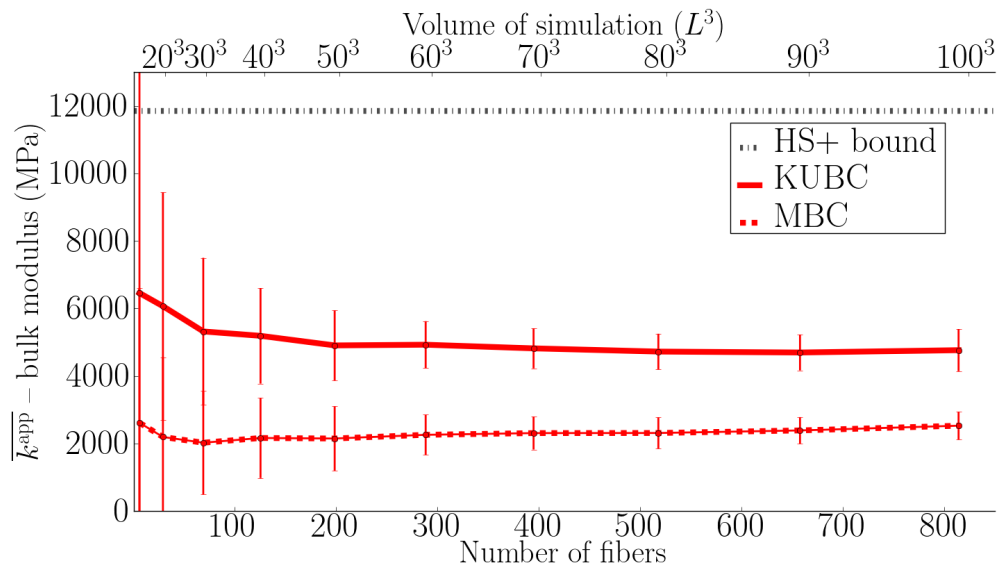


Figure 6.11: Mean values for the bulk modulus depending on the number of fibers

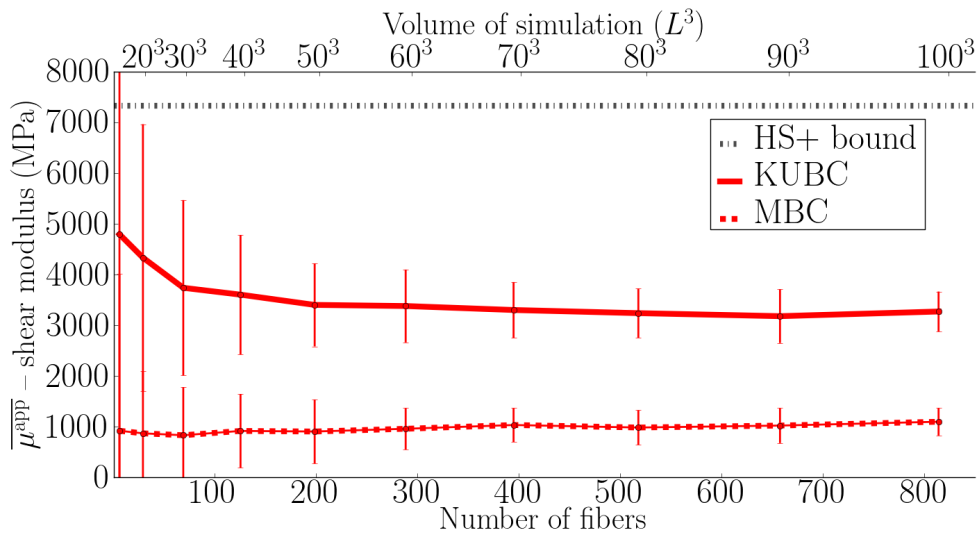


Figure 6.12: Mean values for the shear modulus depending on the number of fibers

these results.

6.4.1 Morphological isotropy

Let us consider the elementary volume of *Poisson* fibers of volume 40^3 , with approximately $\bar{N} = 127$ fibers, as shown on Figure 6.13.

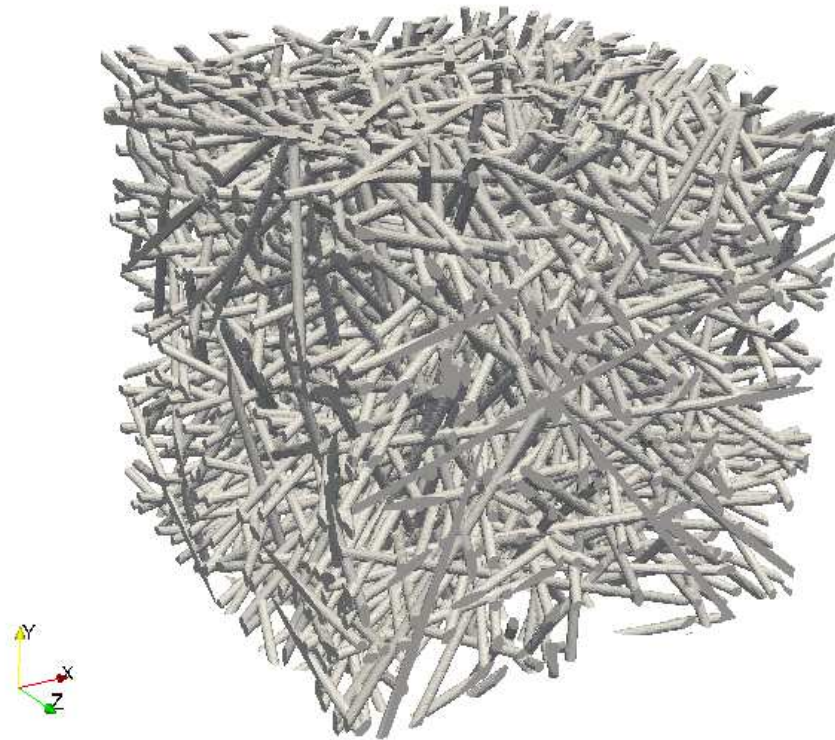


Figure 6.13: Elementary volume of fibers on which the covariance is computed ($L = 40$)

This virtual sample has been sliced and voxelized. Covariance was then computed on different slices. Results have been averaged over all the slices, they are plotted on Figure 6.14. For 4 different orientations ω of the vector \underline{h} , the covariance reaches its sill for a separation close to 10 pixels. One would expect the covariance to converge for longer correlation lengths in the case of *Poisson* fibers, this is true if an infinite medium is considered. In the case of a limited sample like this one, the probability for fibers to be aligned with \underline{h} is very small, the larger the sample, the higher the probability for this to occur.

Thermal conductivity

Firstly, the data computed for determining $\overline{\lambda^{\text{app}}}$ is used to check for isotropy. This is done by checking that $\overline{Q_2} \rightarrow 0$ and $\overline{Q_3} \rightarrow 0$. In order to characterize this vanishing, a discriminating

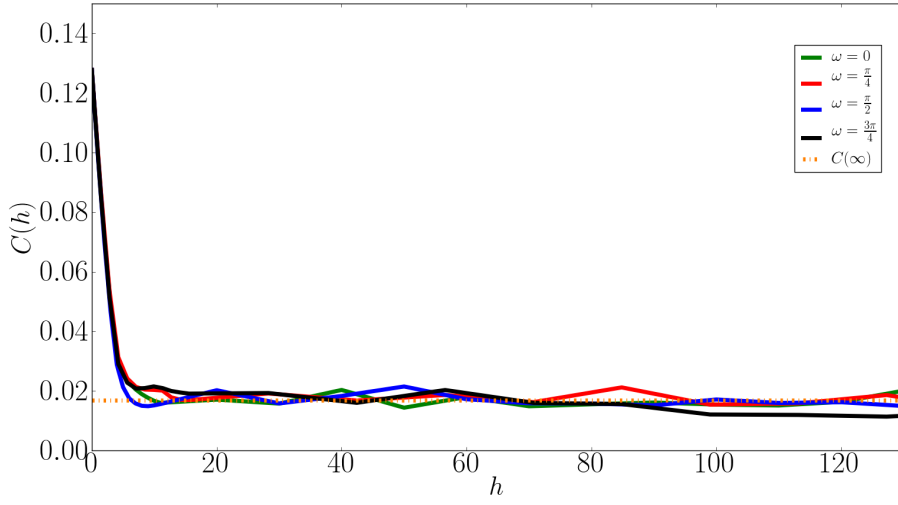


Figure 6.14: Covariance of the *Poisson* fibers determined on 2D slices for several orientations ω

BC \ Size	10	20	30	40	50	60	70	80	90	100
UTG – δ^λ	0.027	0.021	0.004	0.007	0.001	0.011	0.003	0.004	0.003	0.003
MTBC – δ^λ	0.084	0.008	0.008	0.007	0.002	0.001	0.003	0.004	0.003	0.002

Table 6.6: Thermal isotropy with respect to the thermal conductivity for Poisson fibers

criterion δ^λ , which is homogeneous to a temperature gradient, is defined as follows:

$$\delta^\lambda = \frac{|\overline{Q_2}| + |\overline{Q_3}|}{\overline{\lambda^{\text{app}}}} \quad (6.91)$$

The values for δ^λ have been computed and shown in Table 6.6 for the volumes of samples considered. δ^λ values have to be compared with the value of the macroscopic temperature gradient prescribed $G_1 = 1$. Isotropy can be assumed as soon as $\delta^\lambda \ll 1$. δ^λ fluctuates between 1×10^{-3} and 2.7×10^{-2} for UTG and 2×10^{-3} and 8.4×10^{-2} for MTBC, yielding a very low degree of anisotropy, depending on the considered realizations.

6.4.2 Elastic isotropy

Finally, let us consider the elastic isotropy of *Poisson* fibers. Using arguments presented in Section 6.2.2, we analyze the data that were already computed for determining the bulk and shear moduli. We will consider two separate analyses.

BC \ Size	10	20	30	40	50	60	70	80	90	100
KUBC – δ^k	0.093	0.055	0.032	0.008	0.012	0.050	0.005	< 0.001	0.019	0.014
MBC – δ^k	0.041	0.048	0.034	0.006	0.035	0.025	0.006	0.025	0.008	0.022

Table 6.7: Elastic isotropy with respect to the bulk modulus for Poisson fibers

Bulk modulus

First, we will use the data computed for determining $\overline{k^{\text{app}}}$. To check for isotropy is to check that $\overline{\underline{\Sigma}} : \underline{\underline{K}} : \overline{\underline{\Sigma}} \rightarrow 0$, with $\overline{\underline{\Sigma}}$ mean macroscopic stress tensor and $\underline{\underline{K}}$ the deviatoric projector for 2nd-order symmetric tensors. In order to characterize this vanishing, a discriminating criterion δ^k , which is homogeneous to strain, is defined as follows:

$$\delta^k = \frac{\sqrt{\overline{\underline{\Sigma}} : \underline{\underline{K}} : \overline{\underline{\Sigma}}}}{3\overline{k^{\text{app}}}} = \frac{\sqrt{\overline{\underline{\Sigma}^{\text{dev}}} : \underline{\underline{\Sigma}^{\text{dev}}}}}{3\overline{k^{\text{app}}}} \quad (6.92)$$

The values for δ^k have been computed and shown in Table 6.7 for the volumes of the samples considered. δ^k values have to be compared with the value of the macroscopic strain prescribed $E_{11} = E_{22} = E_{33} = 1$. Isotropy can assumed as soon as $\delta^k \ll 1$. δ^k fluctuates between $< 10^{-3}$ and 9.3×10^{-2} for KUBC and 6×10^{-3} and 4.8×10^{-2} for MBC, yielding a relatively low degree of anisotropy, depending on the considered realizations.

Shear modulus

We will now use the data computed for determining $\overline{\mu^{\text{app}}}$. To check for isotropy is to check that $\overline{\underline{\Sigma}} : \underline{\underline{J}} : \overline{\underline{\Sigma}} \rightarrow 0$, with $\underline{\underline{J}}$ the spherical projector for 2nd-order symmetric tensors. In order to characterize this vanishing, a discriminating criterion δ^μ is defined as follows:

$$\delta^\mu = \frac{\sqrt{\overline{\underline{\Sigma}} : \underline{\underline{J}} : \overline{\underline{\Sigma}}}}{2\overline{\mu^{\text{app}}}} = \frac{\sqrt{3\overline{\underline{\Sigma}^{\text{sph}}} : \underline{\underline{\Sigma}^{\text{sph}}}}}{2\overline{\mu^{\text{app}}}} \quad (6.93)$$

The values for δ^μ have been computed and plotted on Figure 6.8 against the volume of the samples considered. As for δ^k , δ^μ is homogeneous to strain, its values thus have to be compared with the value of the macroscopic strain prescribed $E_{12} = 0.5$. Isotropy can assumed as soon as $\delta^\mu \ll 0.5$. It appears that δ^μ is fluctuating between $< 10^{-3}$ and 2.9×10^{-2} for KUBC, and 2×10^{-3} and 2×10^{-1} for MBC. These results show that for MBC, there is a higher degree of anisotropy when considering the shear modulus than for the bulk modulus. Interestingly, this statement is inversed for KUBC. Discrepancies are observed on the elastic response for very small volumes

BC \ Size	10	20	30	40	50	60	70	80	90	100
KUBC - δ^μ	0.010	0.029	0.002	< 0.001	0.015	0.024	0.008	0.004	0.014	0.005
MBC - δ^μ	0.199	0.045	0.031	0.022	0.016	0.006	0.015	0.002	0.015	0.009

Table 6.8: Elastic isotropy with respect to the shear modulus for Poisson fibers

with inherent fluctuation due to boundary layer effects and very large volumes for which not enough realizations are available. They seem to be reinforced for MBC, due to a slightly smaller number of realizations.

Tensor of elastic moduli

Finally, we determined using KUBC the full elastic moduli tensor $\overset{\text{app}}{\underset{\approx E}{\mathbf{C}}}$ for 50 realizations of Poisson fibers with a volume of simulation $V = 50^3$ which corresponds to $\bar{N} \approx 180$ fibers for each sample. Details regarding the boundary value problems for determining the components of the elastic moduli tensor are given in Section 6.2.2. The elastic moduli tensor averaged over $n = 10$, $n = 20$ and $n = 50$ realizations are presented respectively in Equations 6.94, 6.95 and 6.96. Values obtained for $n = 50$ are presented in Equation 6.96 with their corresponding intervals of confidence $[\bar{C}_{IJ} \pm 2D_{C_{IJ}}]$. The averaged tensor components obtained for $n = 50$ are characteristic of isotropic elasticity since $\bar{C}_{11} \approx \bar{C}_{22} \approx \bar{C}_{33}$ with a maximal error of 12%, $\bar{C}_{12} \approx \bar{C}_{13} \approx \bar{C}_{23}$ with $\epsilon_{\text{rel}} = 20\%$, $\bar{C}_{44} \approx \bar{C}_{55} \approx \bar{C}_{66}$ with $\epsilon_{\text{rel}} = 17\%$ and are approximately equal to $\frac{\bar{C}_{11} - \bar{C}_{12}}{2}$ with a relative error of 14% at worst, also $\bar{C}_{14} \approx \bar{C}_{15} \approx \bar{C}_{16} \approx \bar{C}_{24} \approx \bar{C}_{25} \approx \bar{C}_{26} \approx \bar{C}_{34} \approx \bar{C}_{35} \approx \bar{C}_{36} \approx \bar{C}_{45} \approx \bar{C}_{46} \approx \bar{C}_{56}$ and they represent in the worst case less than 1% of \bar{C}_{11} .

$$[\bar{\mathbf{C}}]_{10} = \begin{bmatrix} 10032 & 3118 & 3122 & 33 & -100 & 50 \\ \bullet & 9272 & 2573 & -13 & 55 & 94 \\ \bullet & \bullet & 8773 & 150 & -74 & -58 \\ \bullet & \bullet & \bullet & 2977 & -57 & 49 \\ \bullet & \bullet & \bullet & \bullet & 3528 & 26 \\ \bullet & \bullet & \bullet & \bullet & \bullet & 3539 \end{bmatrix} \quad (6.94)$$

$$[\bar{\mathbf{C}}]_{20} = \begin{bmatrix} 9814 & 3067 & 3032 & 33 & -35 & 44 \\ \bullet & 9029 & 2583 & -1 & 36 & 59 \\ \bullet & \bullet & 8551 & 51 & 24 & -40 \\ \bullet & \bullet & \bullet & 2976 & -40 & 30 \\ \bullet & \bullet & \bullet & \bullet & 3418 & 27 \\ \bullet & \bullet & \bullet & \bullet & \bullet & 3469 \end{bmatrix} \quad (6.95)$$

$$[\bar{\mathbf{C}}]_{50} = \begin{bmatrix} 9627 \pm 2820 & 3002 \pm 740 & 3028 \pm 709 & 14 \pm 342 & -64 \pm 714 & 85 \pm 890 \\ \bullet & 8715 \pm 2401 & 2530 \pm 639 & 14 \pm 664 & 24 \pm 307 & 44 \pm 934 \\ \bullet & \bullet & 8630 \pm 2445 & 48 \pm 697 & -24 \pm 841 & 15 \pm 298 \\ \bullet & \bullet & \bullet & 2910 \pm 763 & 13 \pm 310 & 21 \pm 314 \\ \bullet & \bullet & \bullet & \bullet & 3408 \pm 836 & 13 \pm 344 \\ \bullet & \bullet & \bullet & \bullet & \bullet & 3389 \pm 872 \end{bmatrix} \quad (6.96)$$

6.4.3 Thermal and mechanical fields

In order to explain the discrepancies observed on the apparent properties, let us analyze the thermal and mechanical fields coming out of the simulation. In the case of thermal conduction, the heat flux within the fibers percolating in-between F_1^+ and F_1^- is the same for UTG and MTBC. The only difference comes from the thermal conduction taking place in the fibers intersecting F_2 and F_3 when considering UTG. This has a limited impact on the homogenized value λ^{app} . On the other hand, in the case of elasticity, discrepancies in the macroscopic results can be explained from the mechanical fields. For the hydrostatic load, mapping of $\frac{\text{Tr}(\boldsymbol{\epsilon})}{\text{Tr}(\boldsymbol{E})}$ is presented on Figure 6.16 for KUBC and MBC with a sample realization of $V = 50^3$. From this figure, localization of strain on certain fibers seems to be more pronounced with MBC than KUBC. This is likely due to the more restrictive KUBC for a imposed macroscopic strain that is the same that for MBC. This is confirmed on Figure 6.17, mapping only ϵ_{33} , with $E_{33} = 1$. The localization is clearly confined to the both ends of preferentially oriented fibers, here along the vertical direction. For KUBC, most of the deformation takes place all over the boundary ∂V , including within fibers that are not preferentially oriented.

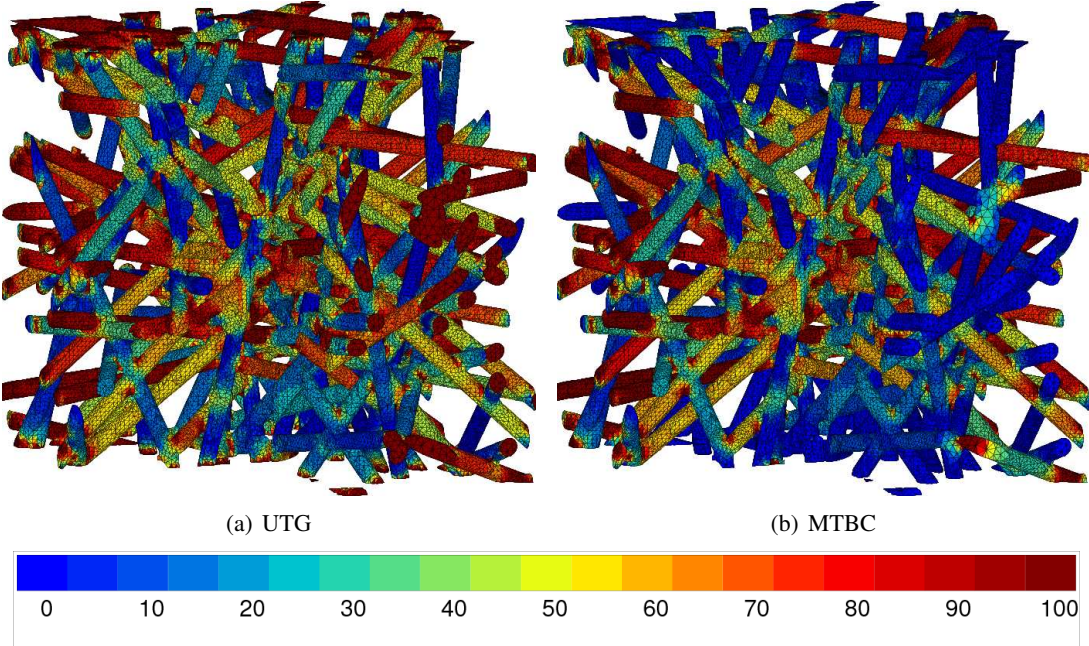


Figure 6.15: Q_1 mapping for a $V = 50^3$ realization using (a) UTG and (b) MTBC

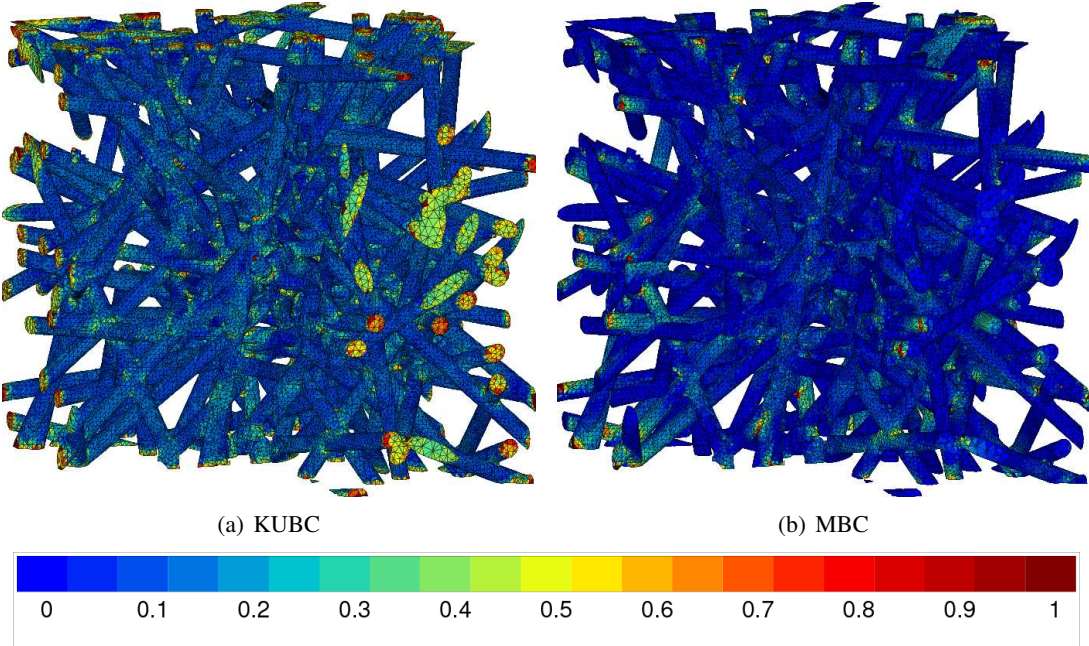


Figure 6.16: $\frac{\text{Tr}(\boldsymbol{\epsilon})}{\text{Tr}(\boldsymbol{E})}$ mapping for a $V = 50^3$ realization under hydrostatic load with (a) KUBC and (b) MBC

6.5 Determination of the statistical RVE size

6.5.1 Variance from simulation

In order to determine RVE sizes, variance of the mean value for each properties is studied, based on the approach we introduced in Section 4.2. For the case of *Poisson* fibers, [Jeulin, 2011] gave the theoretical value of $\frac{2}{3}$ for γ in Equation 4.31, which is recalled hereafter:

$$D_Z^2(V) = D_Z^2\left(\frac{A_3^*}{V}\right)^\gamma \quad (6.97)$$

The theoretical value $\gamma = \frac{2}{3}$ given by [Jeulin, 2011] holds only for the indicator function of the *Poisson* fibers and its mean value, the volume fraction. Anyway, we will consider, as a 1st-order approximation, that the elastic energy density and thermal dissipation rate density are dependent of the indicator function of the fibers, since the evolution of its variance with the volume is the only theoretical result available. γ exponents of the scaling-law for each physical property was estimated from the results of simulations and are gathered in Table 6.9. Only the data points for volumes $V \geq 40^3$ are considered here to avoid any bias due to boundary effects. However, in order to be able to compare representativity of samples for different properties, we will indeed consider $\gamma = \frac{2}{3}$ for fitting all the results. As a matter of fact, it is the only theoretical value available for *Poisson* fibers and it is not too far apart from the values obtained from computational experiments. Since we have no information about the convergence of the point variance D_Z^2 for the effective properties, except for the volume fraction V_V for which the theoretical value is given in Equation 4.25, we use the alternative form of the ensemble variance given in Equation 4.35, recalled hereafter:

$$D_Z^2(V) = KV^{-\gamma} \quad (6.98)$$

γ being fixed, K is the only parameter left for fitting the data.

Results regarding the volume fraction are presented on Figure 6.18. Variance for the bulk and shear moduli as functions of the volume are shown on Figures 6.20 and 6.21. Similar results for the thermal conductivity are obtained on Figure 6.19. For the sake of clarity, only one mesh density ($d = 2$) is shown, but similar results are obtained for other mesh densities, making the variance on apparent properties mesh-independent.

6.5.2 Results

Using Equation 4.34, it is now possible to determine statistical RVE sizes from computational simulations. A_3^* or K are estimated numerically from Equation 6.97 and 6.98, for different properties Z and boundary conditions. Estimates for RVE sizes are presented in Table 6.10. RVE sizes presented in this table are way larger than elementary volume sizes achieved throughout

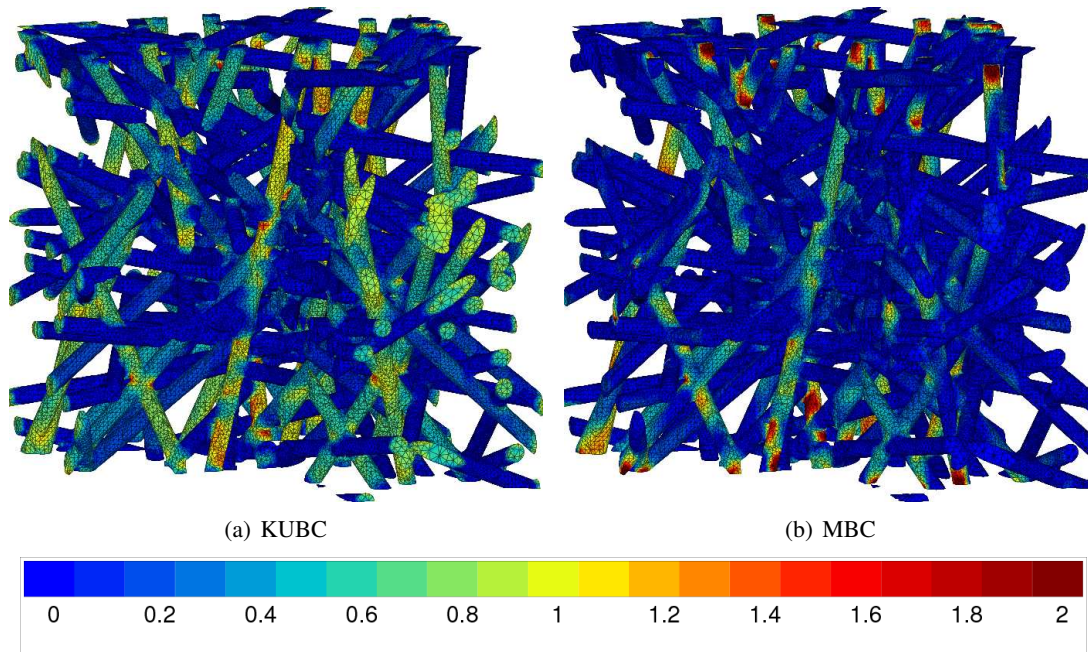


Figure 6.17: ε_{33} mapping for a $V = 50^3$ realization under hydrostatic load with (a) KUBC and (b) MBC

	γ
$\overline{\lambda^{\text{app}}}$ -UTG	0.68
$\overline{\lambda^{\text{app}}}$ -MTBC	0.64
$\overline{k^{\text{app}}}$ -KUBC	0.51
$\overline{k^{\text{app}}}$ -MBC	0.77
$\overline{\mu^{\text{app}}}$ -KUBC	0.64
$\overline{\mu^{\text{app}}}$ -MBC	0.66
$\overline{V_V^f}$	0.67

Table 6.9: Values for γ exponent estimated from the simulation

6.5. Determination of the statistical RVE size

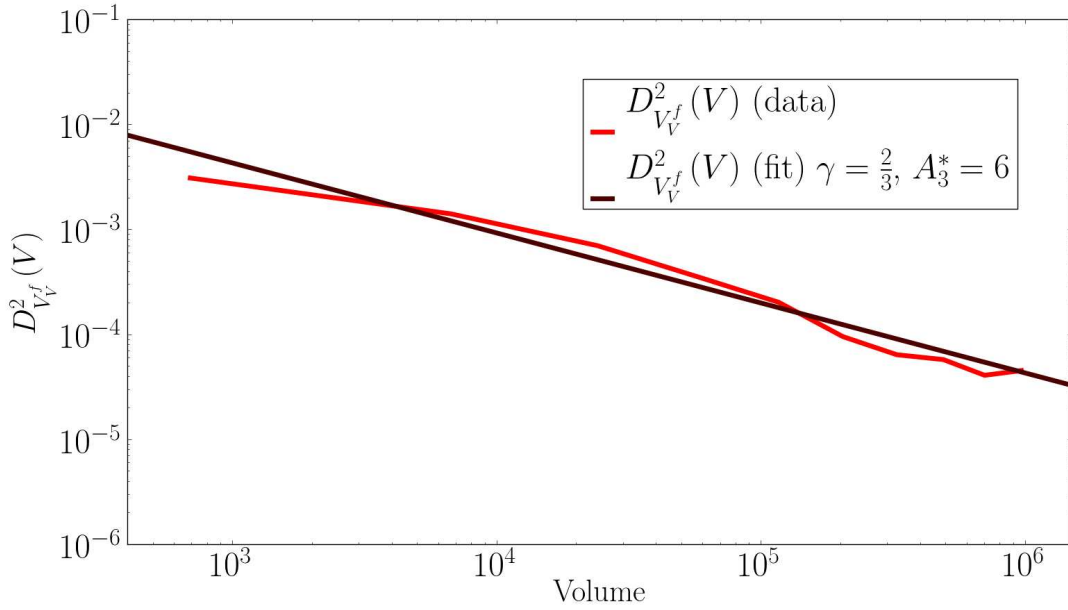


Figure 6.18: Variance for the volume fraction of fibers depending on the volume of simulation V

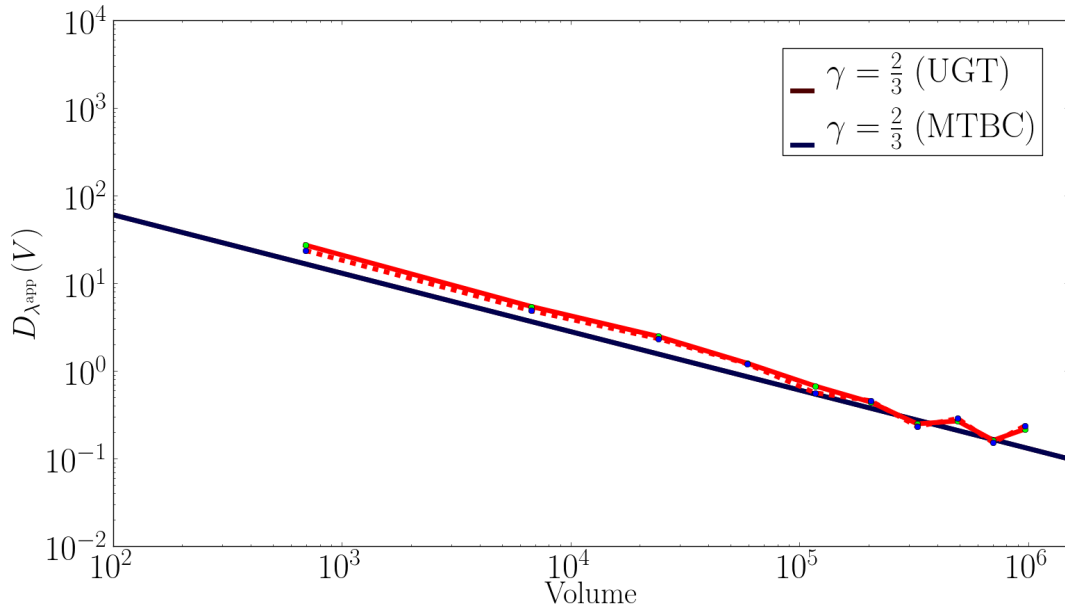


Figure 6.19: Variance for the thermal conductivity depending on the volume of simulation V

this work. This concurs with the discrepancies observed on the elastic moduli; as a matter of fact, the response over an elementary volume should be independent of the boundary conditions once the RVE size is reached. Nevertheless, the same precision, *i.e.* relative error, can be obtained from multiple realizations of smaller volumes. As an example, for k^{app} with KUBC, if $V = 50^3$, and $\epsilon_{\text{rel}} = 5\%$, one must compute 18 realizations to attain the same statistical convergence as

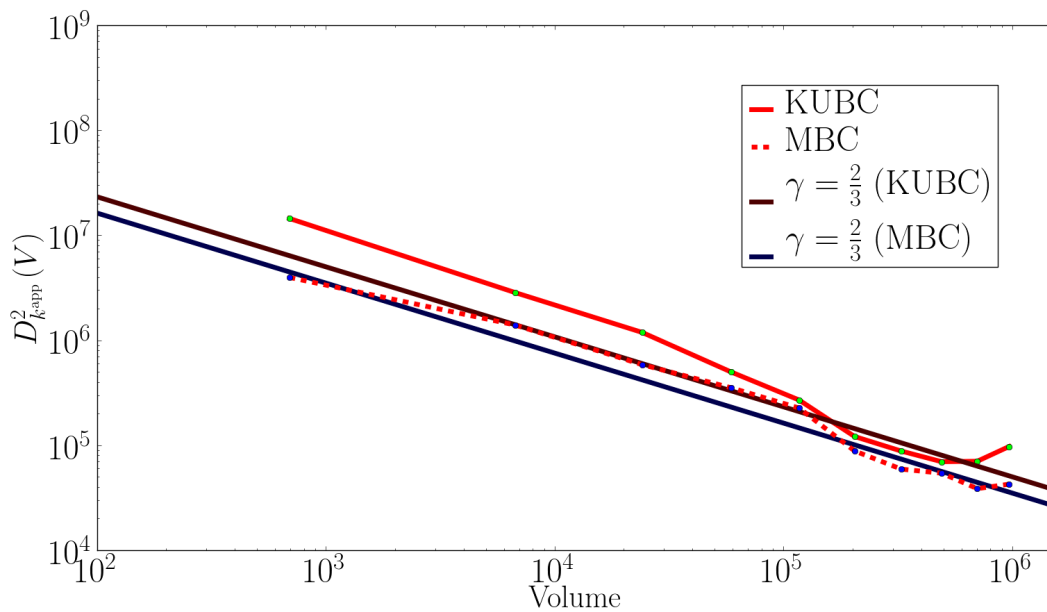


Figure 6.20: Variance for the bulk modulus depending on the volume of simulation V

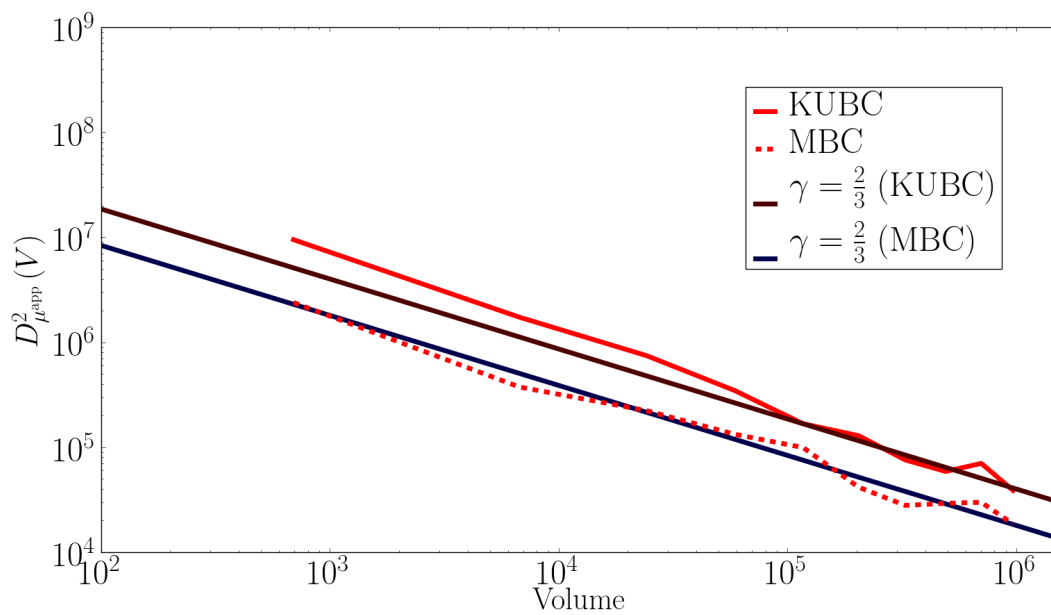


Figure 6.21: Variance for the shear modulus depending on the volume of simulation V

for 1 realization of $V = 188^3$. One should however be careful and consider the bias induced by boundary layer effects on mean values when choosing smaller elementary volumes: virtual samples that are too small should be avoided.

Z	BC	ϵ_{rel}	K	D_Z^2	A_3^*	V_{RVE}	\bar{N}
V_V	N/A	5%	–	1.3×10^{-1}	6.	171^3	2.3×10^3
λ^{app}	UTG	5%	1.3×10^3	–	–	205^3	3.3×10^3
λ^{app}	MTBC	5%	1.3×10^3	–	–	242^3	4.6×10^3
k^{app}	KUBC	5%	5.0×10^8	–	–	188^3	2.8×10^3
k^{app}	MBC	5%	3.5×10^8	–	–	296^3	7.0×10^3
μ^{app}	KUBC	5%	4.0×10^8	–	–	241^3	4.6×10^3
μ^{app}	MBC	5%	1.8×10^8	–	–	499^3	2.0×10^4

Table 6.10: RVE sizes estimated from computations with $\gamma = \frac{2}{3}$ and $n = 1$

6.6 Conclusion

A microstructural model was designed in order to create virtual samples of *Poisson* fibers. The statistical approach for determining RVE sizes was then implemented for *Poisson* fibers based on data obtained from FE simulations using uniform and mixed boundary conditions. First, mean values for morphological, thermal and elastic properties were obtained after averaging over a significant number of sample realizations, and this for 10 different sizes of simulation. For the volume fraction, the convergence of the mean value is independent of the simulation size, only the associated variance is decreasing with respect to the volume. For the case of heat transfer and elasticity, effective properties were bounded by the apparent values obtained for uniform and mixed boundary conditions. UHF and SUBC being incompatible with the microstructure considered, mixed boundary conditions were proposed as an alternative. A slow but steady convergence of the mean values for thermal conductivity and elastic moduli was observed. Unfortunately, even for the largest volumes considered, discrepancies persist between mean values obtained for both types of boundary conditions. This could mean that the RVE size should be quite larger according to [Sab, 1992], but the demonstration given in this reference does not necessarily hold in the case of an elementary volume including a porous phase intersecting the limit ∂V ; this is an open question. Anyway, even if the mixed BC used in this work differ from the MUBC proposed by [Hazanov and Huet, 1994], one could consider that the MBC estimates are closer than the KUBC estimates to the effective values, this was shown experimentally in [Hazanov and Amieur, 1995]. Further computations on samples including a meshed porous phase with asymptotically weaker thermal and elastic properties will have to be done for comparison. UHF and SUBC should then be applicable and results would be compared respectively with MTBC and MBC. Isotropy was investigated from a morphological, thermal and elastic viewpoint. Results in Section 6.4.1 yielded isotropy in average for most realizations, except in the worst case such as very small volumes that are highly inhomogeneous, and the very large ones for which only a few realizations are available. Isotropy is attained statistically but each sample is anisotropic. Finally, the evolution of ensemble variance for homogenized properties was investigated and

Chapter 6. Poisson fibers

fitted with a power-law of exponent $\frac{2}{3}$ which is a theoretical value for *Poisson* fibers. The fitting parameter used was then the value K . RVE sizes were determined for a given relative error of 5%. As expected, the obtained values were quite large for a single realization, but attainable with full-field approaches if many realizations are considered.

Résumé

Dans cette partie, un exemple de milieu aléatoire non-périodisable est considéré : les fibres de *Poisson*. Un modèle microstructural, basé sur la théorie des ensembles aléatoires, est formulé. Des échantillons virtuels sont ainsi créés et maillés de façon à pouvoir être utilisés dans un code de calcul par éléments finis. L'homogénéisation numérique est ici à nouveau implémentée, mais à l'aide de conditions aux limites différentes par rapport à l'étude des auxétiques. Les différents types de conditions limites (KUBC et MBC en mécanique, UTG et MTBC en thermique) considérées sont présentées et analysées. Les résultats obtenus pour de telles conditions limites permettent d'estimer les propriétés effectives des fibres de *Poisson*. Une analyse statistique des données obtenues sur des centaines de simulations nous permet notamment de définir une taille de volume élémentaire représentatif pour une erreur de mesure relative donnée.

Conclusions & Outlook Part IV

General conclusions

*The circle of our understanding
Is a very restricted area.
Except for a limited number
Of strictly practical purposes
We do not know what we are doing;
And even then, when you think of it,
We do not know much about thinking.*

— T. S. Eliot, *The Family Reunion* (1939)

In this thesis, existing homogenization tools were adapted in order to study architected materials. In many cases, architected materials are imagined as periodic materials, as we did for instance for auxetics. We also proposed to design random architected materials in order to reach isotropy of the effective behavior. First, an introduction to homogenization was presented and a description of a computational approach using the finite element method was given. This approach was applied for the specific case of periodic auxetic microstructures. Determining the effective elastic properties of periodic auxetics is straightforward, considering the availability of periodic boundary conditions in FE commercial packages. This gave us the opportunity to explore new auxetic patterns, but also the effect of plasticity on auxeticity, as well as structural applications. The main results we obtained regarding negative *Poisson's* ratio materials can be summarized as follows:

- 2D auxetic lattices, especially the hexachiral one, are plausible candidates for replacing honeycomb-core within sandwich panels. There are at least two reasons for that: all things being equal, the hexachiral cell exhibits a higher in-plane shear modulus than the honeycomb. Also, negative *Poisson's* ratio materials yield synclastic curvature when bended, which allows the design of dome-shaped or bent panels.
- A new tridimensional auxetic microstructure was proposed, homogenized, manufactured and characterized mechanically, yielding promising results in terms of mechanical strength in comparison with the honeycomb lattice for the same volume fraction. The use of such a microstructure, optimally oriented along the [110] or [111] direction for solicitation, would

dramatically increase the crashworthiness of structures subject to impact.

- Elastoplasticity of auxetics has been explored, showing that the auxetic effect persists and becomes even stronger with a confined plastic zone. The larger spread of the plastic zone, the smaller the strengthening of auxeticity due to plastic yielding. Transverse isotropy was preserved within the plastic regime for the hexachiral lattice unlike the honeycomb. Nevertheless, the plastic anisotropy for the honeycomb lattice is becoming weaker with hardening. All these considerations make auxetics good candidates for energy absorption in impacted structures.
- Macroscopic modeling using an anisotropic compressible plasticity framework was performed for the auxetic hexachiral lattice. The proposed fully anisotropic *Hill* criterion seems to be suitable for modeling 2D architected cellular materials as it was able to catch negative *Poisson's* ratios, transverse contractions, and volume changes.
- Manufacturing is the key technological lock for the development of auxetics in the industry: except for the most simple 2D patterns, most auxetics are currently being produced using direct manufacturing, which is the industrial version of rapid prototyping, based on additive powder metallurgy or polymer sintering processes, all of which are quite expensive.

A second application was considered for computational homogenization: random media. One could then have considered periodized random media, as it was done in [Kanit, 2003] for *Voronoi* polyhedra and [Jean, 2009] for Boolean random models of spheres, or consider random media with no constraint of periodicity, or even unperiodizable random media. The latter seemed the most challenging for us in terms of assessing the long-standing question of representativity. As a matter of fact, *Poisson* fibers are undoubtedly one of the worst case scenario one could think of in terms of homogenizing biphasic materials: this microstructure is "unperiodizable", presents an infinite contrast of properties, includes a porous phase that is intersecting with the outer limits of the samples considered, and has an infinite integral range. These features are also what makes this type of random media interesting for testing the robustness of the statistical approach that was introduced in [Kanit et al., 2003] for determining RVE sizes. A microstructural model of *Poisson* fibers was developed and implemented numerically. The meshed virtual samples obtained in this way were then filled and optimized in order to be used in finite element simulations. Hundreds of realizations were performed, generating a large amount of data to be analyzed statistically. The main results arising from the study of *Poisson* fibers can be summarized as follows:

- When considering mean values for the volume fraction, the mean value is independent of the simulation size, only the associated variance is decreasing with respect to the volume size.
- Uniform heat flux boundary conditions (UHF) and static uniform boundary conditions (SUBC) are incompatible with the microstructure considered, mixed boundary conditions were proposed as an alternative.

-
- For the case of heat transfer, effective properties were estimated by the apparent values obtained for uniform temperature gradient boundary conditions (UGT) and mixed thermal boundary conditions (MTBC). A slow but steady convergence of the mean values for thermal conductivity was observed for an increasing volume of simulation. Even for the largest volumes considered, discrepancies persist between mean values obtained for UGT and MTBC (about 16%). This could be symptomatic of gigantic RVE sizes.
 - For the case of elasticity, effective properties were estimated by the apparent values obtained for kinematic uniform boundary conditions (KUBC) and mixed boundary conditions (MBC). The same trend was observed as for thermal properties, but with a larger gap: $\sim 213\%$ discrepancy for the bulk modulus and $\sim 66\%$ discrepancy for the shear modulus. This advocates for quite larger RVE sizes according to [Sab, 1992]. Even if the MBC differ from the MUBC proposed by [Hazanov and Huet, 1994], it should give a better estimate than the KUBC, as it was shown experimentally in [Hazanov and Amieur, 1995].
 - Isotropy of the microstructural model used was verified on the morphology, on the thermal conductivity tensor and on the elastic moduli tensor. This allowed us to thin down to 1 instead of 3 the number of computations needed to estimate the thermal properties, and from 6 to 2 per realization for the elastic properties.
 - The study of the ensemble variance for apparent properties gave rise to scaling power-laws of exponents close to $\frac{2}{3}$. We obtained this exponent from computational experiments and verified the theoretical value given in [Jeulin, 2011]. The value $\gamma = \frac{2}{3}$ was then used for comparison between RVE sizes determined for different properties.
 - Values for A_3^* or K were fitted from the data, allowing us to determine RVE sizes for a given relative error. The values obtained are quite large for a single realization only, but attainable with full-field approaches if many realizations are considered.

As a synthesis, let us answer the questions asked in Chapter 0:

- How to determine the effective properties of architected materials?
There are plenty of approximate analytical models for determining the effective properties of architected materials. For simple configurations in terms of morphology and phases, these models can probably give a good estimate of the properties, but they will not be sufficient to account for anisotropy, nonlinear behavior, multiple scales, etc. This is why we advocate for computational methods, such as finite element analysis, to be a pertinent tool for designing architected materials, as we have hopefully shown for auxetic cellular materials.
- How could we adapt existing computational tools for this purpose?
In the case of periodic architected materials, the now classical periodic homogenization approaches are readily available, but attention should be paid to contrasts of properties

between phases which are often very large, infinite indeed, and should then be taken into account carefully. From a practical viewpoint, eccentric architected microstructures can be challenging to mesh; advanced meshing tools should thus be operational in order to avoid falling into a computational nightmare.

- Can rapid prototyping be useful to develop architected materials?

Definitely. The ability to extend one's microstructural design space from 2D to 3D is priceless. This calls for advanced shape optimization tools in order to efficiently exploit the rapid prototyping technology. The negative aspect of such manufacturing processes is obviously the financial cost, even if competitive with other powder metallurgy processes, and the scalability of the process which does not allow to produce materials larger than a few hundred cubic centimeters.

- What can be expected from negative *Poisson's* ratio materials?

Unusual properties. Based on the study we have conducted on auxetics, we think that their enhanced strength in shear could be used smartly in impacted structures. More generally, this new class of materials may not have direct applications, anyhow studying auxetics is fundamental for understand the link between microstructure and macroscopic behavior. Counterintuitive *Poisson* effects may inspire one to think of new ways for architecting materials.

- How could we assess the representativity of elementary volumes?

As it was presented and implemented in this work, there is a rational way to evaluate the representativity of elementary volumes for heterogeneous media based on statistical arguments. We used this method to determine the RVE size of a quite unfavorable case of random structures, in order to successfully test the robustness of the approach. It is a powerful tool for determining effective properties from samples smaller than the predicted RVE size for a given relative error on the results. However, the statistical method supposes convergence towards the same limit for each boundary condition. This is not the case in our study. As a consequence, the actual RVE sizes may actually be way larger, gigantic even, than the ones we determined from the parcellar information obtained throughout this work.

Further work

*The world of the future will be an even more demanding
struggle against the limitations of our intelligence,
not a comfortable hammock in which we can lie down
to be waited upon by our robot slaves.*

— Norbert Wiener, *The Human Use of Human Beings: Cybernetics and Society* (1954)

Regarding auxetics, further work should include the modeling of other auxetic microstructures, especially tridimensional ones. A deeper study of the influence of the local hardening rule on the homogenized plastic behavior should also be attempted. Taking into account non-linear phenomena such as elastic buckling and damage would be necessary before using such materials in actual structures. Also, the simulation of structural applications should include aluminium skins in addition to the macroscopic model developed in this work. More mechanical experiments should be conducted on auxetics, in order to feed the models.

Negative *Poisson's* ratio materials are undoubtedly fascinating, mainly because of their counter-intuitive mechanical behavior. Unfortunately, this fascination sometimes overshadow the fact that most auxetics are strongly anisotropic, an aspect that is often omitted in the literature, hence limiting the use of auxetics in structural applications. One goal for auxetics research should be to achieve isotropy, this was done by [Lakes, 1987] with his reentrant random copper foam, with $\nu = -0.7$, and [Milton, 1992] with his multiscale laminate that theoretically reaches $\nu = -1$ but that was never fabricated for obvious technological reasons. One possible way for further research would be to develop a periodic cell that is shape-optimized for exhibiting the most isotropic mechanical behavior and for presenting a *Poisson* ratio close to -1 , a reentrant truss-like structure based on a tetrakaidecahedron for instance. Besides, the association of auxetics with classical materials would probably give rise to some interesting new composites.

Concerning the study of *Poisson* fibers, more simulations should be done to obtain a base of data points that is more representative statistically, larger samples should also be investigated. To do so, parallel computing could be an interesting way. For instance, considering the high-performance computing cluster of the Centre des Matériaux, and the largest volume studied ($V = 100^3$, which took up to 100 GB of RAM for the mesh density $d = 3$), one could theoretically compute an

elementary volume $V = 300^3$ using domain decomposition on 27 cluster nodes, which represents about $\bar{N} \approx 7000$ fibers, using the same parameters as in our study. Unfortunately, meshing such a virtual sample is currently out of reach with the computational means available in our laboratory, yielding at least 100 million elements as an optimistic estimate. However, there is no theoretical limit *a priori* regarding mesh sizes, only contingent obstacles. In order to conclude about bounding of effective properties, computations on samples including a meshed porous phase with asymptotically weak thermal and elastic properties could be done for comparison. UHF and SUBC would then be applicable and results could be compared respectively with MTBC and MBC. Even if the microstructure is not periodic, comparison should be made with results coming from FFT computations. In that case, using a regular grid-mesh, artificial periodic boundary conditions could also be used for FE. The FFT method was proposed by [Moulinec and Suquet, 1994] and was subsequently enhanced by [Moulinec and Suquet, 1998, Michel et al., 2001]. It was used for instance for the homogenization of polycrystals [Lebensohn, 2001] and composites [Willot et al., 2008, Willot and Jeulin, 2009]. From a materials science viewpoint, the influence of the volume fraction of fibers should also be investigated, as well as a *Poisson* fibers hard-core random model, which would be closer to what real fibrous media actually look like. *Poisson* fibers samples could be manufactured using rapid prototyping and be mechanically characterized. Finally, in order to go one step further, one could apply the same statistical approach to *Poisson* planes, which are another *Poisson* linear variety, but with a scaling power-law of exponent $\gamma = \frac{1}{3}$.

We showed in this work the universality of the statistical RVE size determination method by applying it successfully to a medium with non-finite integral range. This advocates for a systematic use of the method whenever sampling of random media is involved. The method is indeed very powerful when considering arbitrary models of random structures but really is a powerful tool for assessing the representativity of actual samples. For instance, this method would be useful in the context of the mechanical characterization of concrete samples since the characteristic lengths of such materials are often quite large, while samples are limited in size. Hopefully, applications of this method to many different classes of materials will provide a positive feedback for improving the approach.

The use of architected materials in industrial applications is conditional upon the development of appropriate models for such materials. This thesis dealt with the determination of the effective properties of architected materials as infinite media, not as finite materials within structures. While our approach, which is based on micromechanics, is valid for microstructures, it probably lacks answers for the case of macrostructures. A way of development are the higher-order models of continua, that are able to render the non-separability of scales that occurs often within architected materials. For instance, plate and shell models for architected materials have been studied recently in [Lebée, 2010, Trinh, 2011, Forest and Trinh, 2011, Laszczyk, 2011], as well as models for bio-inspired architected actuators [Turcaud et al., 2011].

Architected materials do bring up new challenges for scientists, but they also provide new opportunities for engineers. A healthy partnership between the academic research and the industry on the topic of architected materials could be beneficial for both parties. We strongly believe

that architected materials could be a factor of innovation since they are *reshuffling the card deck* of materials properties, yielding the possibility of coexistence of what used to be antagonistic physical properties within a single material. For this to happen, an effort on education is necessary.

Hopefully, this work will contribute to *architecturing* our knowledge of such materials.

Appendices **Part V**

A Finite element method for periodic homogenization

The effective properties of heterogeneous materials can be determined using computational simulation based on the finite element method combined with the homogenization technique. The purpose of this appendix is to present, with two case studies, computational homogenization using the Z-Set finite element code in the case of linear elasticity for a periodic unit-cell.

A.1 Case study #1: fiber-reinforced composite material

The first case study consists in homogenizing a fiber-reinforced composite material. Both phases are considered isotropic linear elastic. Volume fraction of fibers is approximately of 13%: the periodic cell is of length 10 while the fiber radius is 2.

Cell geometry exhibits a quadratic symmetry. The tensor of elastic moduli \mathbf{C}_{IJ} will thus be as follows:

$$\begin{bmatrix} \mathbf{C}_{11} & \mathbf{C}_{12} & \mathbf{C}_{13} & 0 & 0 & 0 \\ \mathbf{C}_{12} & \mathbf{C}_{11} & \mathbf{C}_{13} & 0 & 0 & 0 \\ \mathbf{C}_{13} & \mathbf{C}_{13} & \mathbf{C}_{33} & 0 & 0 & 0 \\ 0 & 0 & 0 & \mathbf{C}_{44} & 0 & 0 \\ 0 & 0 & 0 & 0 & \mathbf{C}_{44} & 0 \\ 0 & 0 & 0 & 0 & 0 & \mathbf{C}_{66} \end{bmatrix} \quad (\text{A.1})$$

	Matrix	Fiber
<i>Young's modulus (GPa)</i>	3	50
<i>Poisson's ratio</i>	0.3	0.3

Table A.1: Constitutive material parameters

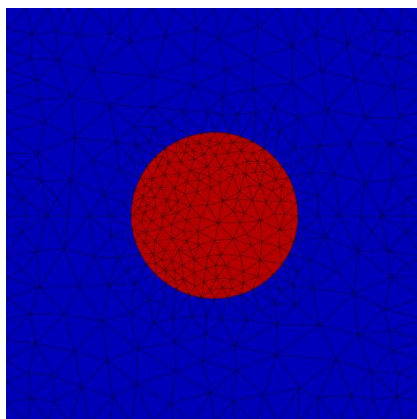


Figure A.1: FE mesh of the periodic cell with the matrix (blue) reinforced by the fiber (red)

In this appendix, we intend on presenting 3 methods for computing the effective properties of the periodic cell:

- The **MPC_periodic** method
- The **element DOF** method:
 - with prescribed macroscopic strain
 - with prescribed macroscopic stress

A.1.1 The MPC_periodic method

This method, which uses standard finite elements, allows one to prescribe an average strain \underline{E} with periodic boundary conditions corresponding to affine relationships between DOFs at the boundary of the periodic cell, such that:

$$\underline{\mathbf{u}}(\underline{\mathbf{x}}^+) - \underline{\mathbf{u}}(\underline{\mathbf{x}}^-) = \underline{\mathbf{E}}(\underline{\mathbf{x}}^+ - \underline{\mathbf{x}}^-) \quad (\text{A.2})$$

In 2D, 4 components of \underline{E} have to be prescribed (3 components for the average strain + 1 component for the average rotation), while in 3D, 9 components have to be prescribed (6 components for the average strain + 3 components for the average rotation). "MPC" means Multi-Point Constraint, *i.e.* prescribing linear relationships between certain DOFs on several mesh nodes, themselves defined by sets of nodes (nsets). In order to use the **MPC_periodic** it is mandatory to distinguish and label properly, using appropriate nsets, mesh nodes included on faces, edges and

A.1. Case study #1: fiber-reinforced composite material

vertices of the periodic cell.

The definition of nsets can be performed using Z-Set meshing tools *via* functions and Boolean operations. For example,

```
****mesher
****mesh periodic_mesh.geof
**open mesh.geof
**nset faceBottom
*function (z<=0.01)*(x>=0.01)*(x<=9.99)*(y>=0.01)*(y<=9.99);
**nset faceTop
*function (z>=0.49)*(x>=0.01)*(x<=9.99)*(y>=0.01)*(y<=9.99);
**nset faceLeft
*function (x<=0.01)*(z>=0.01)*(z<=0.49)*(y>=0.01)*(y<=9.99);
**nset faceRight
*function (x>=9.99)*(z>=0.01)*(z<=0.49)*(y>=0.01)*(y<=9.99);
**nset faceFront
*function (y<=0.01)*(x>=0.01)*(x<=9.99)*(z>=0.01)*(z<=0.49);
**nset faceBack
*function (y>=9.99)*(x>=0.01)*(x<=9.99)*(z>=0.01)*(z<=0.49);
****return
```

Here, we are considering a hexahedron of dimension 10 by 10 by 0.5.

The **AND** operation reads `function1*function2`, while the **OR** operation reads `function1||function2`. Furthermore, the `**rotate` and `**remove_nodes_from_nset` commands can become very handy when it is needed to exclude nodes from nsets, *e.g.* nodes from faces belonging to edges, or nodes from edges belonging to vertices.

Periodic boundary conditions, here for the case of an average strain of 1.0 along direction 1, are implemented within the input file (.inp):

```
****calcul
****mesh
**file periodic_mesh.geof % MESH LOADING
***bc % PRESCRIBING RIGID MOTION
**impose_nodal_dof center U1 0.
**impose_nodal_dof center U2 0.
**impose_nodal_dof center U3 0.
***table
**name tab
*time 0. 1.
*value 0. 1.
***resolution % LINEAR ELASTICITY
**sequence
*time 1.
*increment 1
*ratio absolu 0.001
*algorithm eeeee
***material % CONSTITUTIVE PARAMETERS
**elset fiber
*file fiber.mat
**elset matrix
*file matrix.mat
***equation % MPC_PERIODIC : DOF + NSET COUPLE + AVERAGE STRAIN COMPONENT
**mpc_periodic U1 faceBack faceFront E11 1.0 E22 0.0 E33 0.0 E12 0.0 E21 0.0 E13 0.0 E31 0.0 E23 0.0 E32 0.0 tab
**mpc_periodic U2 faceBack faceFront E11 1.0 E22 0.0 E33 0.0 E12 0.0 E21 0.0 E13 0.0 E31 0.0 E23 0.0 E32 0.0 tab
**mpc_periodic U3 faceBack faceFront E11 1.0 E22 0.0 E33 0.0 E12 0.0 E21 0.0 E13 0.0 E31 0.0 E23 0.0 E32 0.0 tab
...
**mpc_periodic U1 edge09 edge12 E11 1.0 E22 0.0 E33 0.0 E12 0.0 E21 0.0 E13 0.0 E31 0.0 E23 0.0 E32 0.0 tab
```

Appendix A. Finite element method for periodic homogenization

```

**mpc_periodic U2 edge09 edge12 E11 1.0 E22 0.0 E33 0.0 E12 0.0 E21 0.0 E13 0.0 E31 0.0 E23 0.0 E32 0.0 tab
...
**mpc_periodic U2 vertex01 vertex08 E11 1.0 E22 0.0 E33 0.0 E12 0.0 E21 0.0 E13 0.0 E31 0.0 E23 0.0 E32 0.0 tab
**mpc_periodic U3 vertex01 vertex08 E11 1.0 E22 0.0 E33 0.0 E12 0.0 E21 0.0 E13 0.0 E31 0.0 E23 0.0 E32 0.0 tab
****return

```

Results can be visualized *via* Z-Set GUI, here for equivalent *von Mises* stresses:

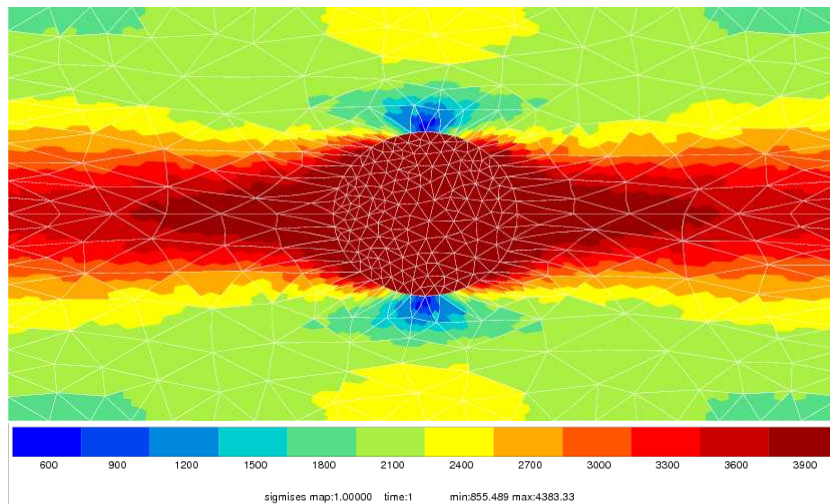


Figure A.2: Deformed FE mesh and equivalent von Mises stress map (MPa) for $E_{11} = 1.0$

Post-processing necessary for determining the homogenized elastic moduli tensor $\tilde{\mathbf{C}}$ consists in a spatial average over the periodic cell of the local stress tensor $\boldsymbol{\sigma}$. Applying the same average operation on the local strain tensor $\boldsymbol{\varepsilon}$ enables one to verify the macroscopic strain applied to the cell. It can be done using the post-processor of Z-Set as follows:

```

****post_processing
**precision 6
**global_post_processing
**file integ
**elset ALL_ELEMENT
**process volume
**process average
*list_var sig11 sig22 sig33 sig12 sig23 sig13 eto11 eto22 eto33 eto12 eto23 eto13
****return

```

Using linear relationships defined previously between stress and strain (*Hooke's law*) one can deduce the numerical value of each components of $\tilde{\mathbf{C}}$. Hence, it yields (in MPa):

A.1. Case study #1: fiber-reinforced composite material

$$[C_{ij}] = \begin{bmatrix} 4822 & 2001 & 2047 & 0 & 0 & 0 \\ 2001 & 4822 & 2047 & 0 & 0 & 0 \\ 2047 & 2047 & 10134 & 0 & 0 & 0 \\ 0 & 0 & 0 & 1365 & 0 & 0 \\ 0 & 0 & 0 & 0 & 1443 & 0 \\ 0 & 0 & 0 & 0 & 0 & 1443 \end{bmatrix}$$

This method might feel tedious since one needs to define manually all the nsets on the boundary of the cell. Moreover, there is a risk for the nset couples not to be numbered in the right order, especially with free meshes. It is advised to check the mesh and nsets before starting any computation. In order to avoid these complications, there are 2 alternatives. The first one is to create nsets using Z-Set GUI, which is quite efficient in 2D, but a nightmare in 3D. Anyway, the mesher will number nsets properly. In 3D, it can be useful to define nsets using the functions presented previously, also the `**match_nset` function is renumbering nodes within a nset in order to make them correspond to those of the homologous nset. Here is an example:

```
****mesher
**match_nset
*n1 front %NAME OF NSET #1
*n2 back %NAME OF NSET #2
*distance 10. %DISTANCE BETWEEN NSETS
*no_x %ONLY Y COORDINATES
*no_z %ARE CONSIDERED HERE
****return
```

The second option consists in using the periodic element method along with the `**nset_for_cell` command, as explained hereafter.

A.1.2 The element DOF method with prescribed macroscopic strain

This method has been presented in Section .

We will now describe the procedure for implementing the method, starting with meshing. Z-Set developers fortunately coded the `**nset_for_cell` function which allows to define periodic boundary conditions automatically for the periodic cell. This function needs the definition of periodicity vectors, up to 3 (b_0, b_1, b_2) in its initial version. These vectors correspond to Cartesian components of directions of replication of the initial pattern, using the axes of the structure. For a cubic cell, this is the length of the cube along directions x, y and z . It may be needed to have more than 3 vectors of periodicity, as for a tetrakaïdecahedral cell: 14 faces, 7 vectors of periodicity. One then needs the extended version of the `**nset_for_cell` function. Nevertheless, one can always go down to 3 vectors of periodicity in 3D, but for practical purpose, using more vectors is often easier. Here is an example of implementation:

Appendix A. Finite element method for periodic homogenization

```
****mesher
***mesh periodic_mesh.geof
**open mesh.geof
**nset_for_cell
  *name cell %NSETS NAME PREFIX
  *prec 0.001 %PRECISION
  *b0 (10. 0. 0.) %COORDINATES OF THE
  *b1 (0. 10. 0.) %PERIODICITY VECTORS
  *b2 (0. 0. 0.5)
****return
```

As an output, Z-Set will generate the input mesh with added periodic nsets, as well as a list of equations to be added within the input file. They correspond to the periodicity equations of the generated mesh and nsets

For instance, `**mpc1 cell14 U1` means that all nodes within nset `cell14` are prescribed the same value for their U1 DOF;

`**mpc2 cell181 U3 cell182 U3` means that all nodes within nset `cell181` are prescribed the same value for their U3 DOF as their homologous nodes within nset `cell182`.

Once these equations have been copied under `***equation` in the input file, the loading has to be set, *i.e.* the macroscopic strain prescribed over the periodic cell:

```
****calcul
***mesh periodic % FE WITH ADDITIONAL DOF
**file periodic_mesh.geof
***bc
**impose_elset_dof ALL_ELEMENT E11 1.0 tab
**impose_elset_dof ALL_ELEMENT E22 0.0 tab
**impose_elset_dof ALL_ELEMENT E33 0.0 tab
**impose_elset_dof ALL_ELEMENT E12 0.0 tab
**impose_elset_dof ALL_ELEMENT E23 0.0 tab
**impose_elset_dof ALL_ELEMENT E31 0.0 tab
***table
**name tab
  *time 0. 1.
  *value 0. 1.
***equation
  *mpc1 cell1 U1
...
  *mpc2 cell181 U3 cell182 U3
...
****return
```

The element type is defined by `***mesh periodic` for the volumic periodic element. There are 2D element formulation for plane stress and plane strain conditions, respectively activated by `***mesh periodic_plane_stress` and `***mesh periodic_plane_strain`.

Using Z-Set GUI, we check the deformed mesh and equivalent *von Mises* stress map:

Post-processing is the same as for the **MPC_periodic** method. This yields:

A.1. Case study #1: fiber-reinforced composite material

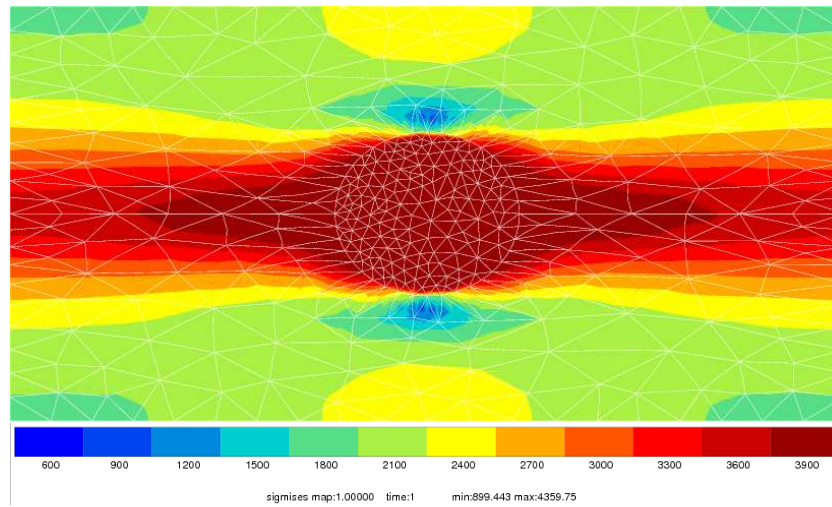


Figure A.3: Deformed FE mesh and equivalent von Mises stress map (MPa) for $E_{11} = 1.0$

$$[C_{ij}] = \begin{bmatrix} 4822 & 2001 & 2047 & 0 & 0 & 0 \\ 2001 & 4822 & 2047 & 0 & 0 & 0 \\ 2047 & 2047 & 10134 & 0 & 0 & 0 \\ 0 & 0 & 0 & 1365 & 0 & 0 \\ 0 & 0 & 0 & 0 & 1443 & 0 \\ 0 & 0 & 0 & 0 & 0 & 1443 \end{bmatrix}$$

This method has the advantage of being very quick to implement and to work in many situations. Nevertheless, for complex periodic microstructures, the use of the `**nset_for_cell` function might be a drawback.

A.1.3 The element DOF method with prescribed macroscopic stress

The method above is presented for prescribed macroscopic stress. It is an interesting approach when homogenizing nonlinear mechanical behavior, *e.g.* creep, and for computing homogenized compliance tensor $\underline{\underline{S}}$ directly. Let us prescribe macroscopic reactions $\mathbf{R}E_{ij} = V\Sigma_{ij}$ at the scale of the element.

For a macroscopic stress (1 MPa) prescribed along direction 1:

Appendix A. Finite element method for periodic homogenization

$$\begin{aligned}
 \mathbf{R}\mathbf{E}_{11} &= V\Sigma_{11} = V\langle\sigma_{11}\rangle = 1.0 \\
 \Rightarrow \mathbf{E}_{11} &= \mathbf{S}_{11}\Sigma_{11} \\
 &\dots \\
 2\mathbf{E}_{12} &= \mathbf{S}_{14}\Sigma_{11} \\
 &\text{By computing } \langle\varepsilon_{ij}\rangle, \text{ it yields:} \\
 \mathbf{S}_{11} &= \frac{\mathbf{E}_{11}}{\Sigma_{11}} = \frac{V\langle\varepsilon_{11}\rangle}{\mathbf{R}\mathbf{E}_{11}} = \frac{V\langle\varepsilon_{11}\rangle}{1.0} \\
 &\dots \\
 \mathbf{S}_{16} &= \frac{2\mathbf{E}_{12}}{\Sigma_{11}} = \frac{2V\langle\varepsilon_{12}\rangle}{\mathbf{R}\mathbf{E}_{11}} = \frac{2V\langle\varepsilon_{12}\rangle}{1.0}
 \end{aligned}$$

When prescribing $\mathbf{R}\mathbf{E}_{12}$:

$$\begin{aligned}
 \mathbf{R}\mathbf{E}_{12} &= 2V\Sigma_{12} = V\langle\sigma_{12}\rangle = 1.0 \\
 \Rightarrow \mathbf{E}_{11} &= \mathbf{S}_{61}\Sigma_{12} \\
 &\dots \\
 2\mathbf{E}_{12} &= \mathbf{S}_{66}\Sigma_{12} \\
 &\text{By computing } \langle\varepsilon_{ij}\rangle, \text{ it yields:} \\
 \mathbf{S}_{61} &= \frac{\mathbf{E}_{11}}{\Sigma_{12}} = \frac{2V\langle\varepsilon_{12}\rangle}{1.0} \\
 &\dots \\
 \mathbf{S}_{66} &= \frac{2\mathbf{E}_{12}}{\Sigma_{12}} = \frac{4V\langle\varepsilon_{12}\rangle}{1.0}
 \end{aligned}$$

From Equation 4.14, it is worth noting that $\mathbf{R}\mathbf{E}_{ij} = \mathbf{R}\mathbf{E}_{ji} = \frac{1}{2}V\Sigma_{ij}$.

The macroscopic stress is computed as the spatial average of the local stress field:

$$\underline{\underline{\Sigma}} = \frac{1}{V} \int_V \underline{\underline{\sigma}} dV \tag{A.3}$$

For cellular materials, the prescribed stress has to be balanced by the volume fraction of the solid phase:

$$\underline{\underline{\Sigma}} = \frac{1}{V} \int_{V_{\text{sol}}} \underline{\underline{\sigma}} dV = \frac{V_{\text{sol}}}{V} = \frac{1}{V_{\text{sol}}} \int_{V_{\text{sol}}} \underline{\underline{\sigma}} dV = \frac{V_{\text{sol}}}{V} \langle\underline{\underline{\sigma}}\rangle_{\text{sol}} \tag{A.4}$$

with V_{sol} , volume of solid phase within the periodic cell of volume V .

A.1. Case study #1: fiber-reinforced composite material

The prescribed value corresponds to the macroscopic stress multiplied by the volume of the cell, *i.e.* $10 \times 10 \times 0.5 = 50$ for this example. The input file reads as follows:

```

***bc
**impose_elset_dof_reaction ALL_ELEMENT E11 1.0 tab
**impose_elset_dof_reaction ALL_ELEMENT E22 0.0 tab
**impose_elset_dof_reaction ALL_ELEMENT E33 0.0 tab
**impose_elset_dof_reaction ALL_ELEMENT E12 0.0 tab
**impose_elset_dof_reaction ALL_ELEMENT E23 0.0 tab
**impose_elset_dof_reaction ALL_ELEMENT E31 0.0 tab
***table **name tab
*time 0. 1.
*value 0. 50.

```

The small macroscopic stress applied (1 MPa) results in a slightly deformed FE mesh:

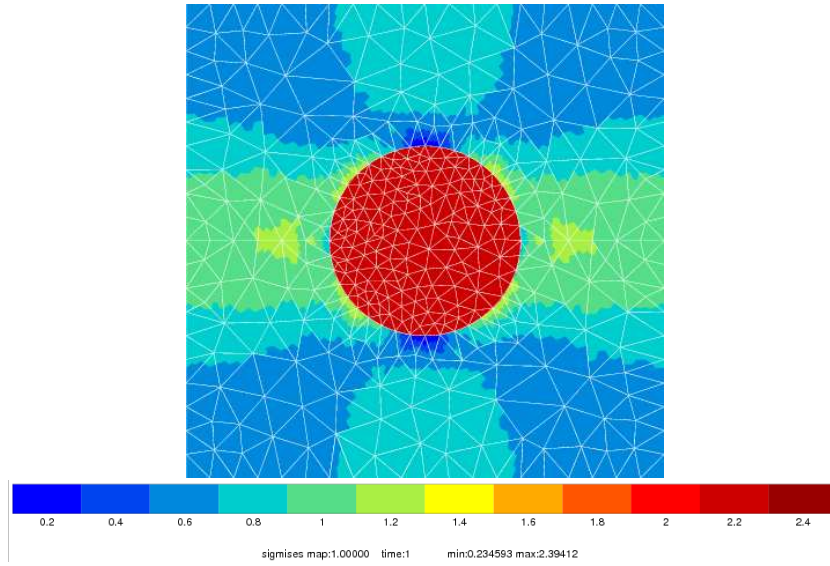


Figure A.4: Deformed FE mesh and equivalent von Mises stress map (MPa) for $\mathbf{RE}_{11} = 1 \times V$

After post-processing, *i.e.* spatial averaging of the local fields, the components of the compliance tensor $\underline{\underline{S}}$ (expressed in MPa^{-1}) are obtained from $\langle \underline{\underline{\epsilon}} \rangle$:

$$[S_{ij}] = \begin{bmatrix} 2,6 \cdot 10^{-4} & -9,4 \cdot 10^{-5} & -3,4 \cdot 10^{-5} & 0 & 0 & 0 \\ -9,4 \cdot 10^{-5} & 2,6 \cdot 10^{-4} & -3,4 \cdot 10^{-5} & 0 & 0 & 0 \\ -3,4 \cdot 10^{-5} & -3,4 \cdot 10^{-5} & 1,1 \cdot 10^{-4} & 0 & 0 & 0 \\ 0 & 0 & 0 & 7,3 \cdot 10^{-4} & 0 & 0 \\ 0 & 0 & 0 & 0 & 6,9 \cdot 10^{-4} & 0 \\ 0 & 0 & 0 & 0 & 0 & 6,9 \cdot 10^{-4} \end{bmatrix}$$

The elastic moduli tensor $\underline{\underline{C}}$ is obtained by inverting $\underline{\underline{S}}$. The values are exactly the same as for the approach with prescribed macroscopic strain:

Appendix A. Finite element method for periodic homogenization

	Grid
<i>Young's modulus</i> (GPa)	210
<i>Poisson's ratio</i>	0.3

Table A.2: Constitutive material parameters for case study #2

$$[C_{ij}] = \begin{bmatrix} 4822 & 2001 & 2047 & 0 & 0 & 0 \\ 2001 & 4822 & 2047 & 0 & 0 & 0 \\ 2047 & 2047 & 10134 & 0 & 0 & 0 \\ 0 & 0 & 0 & 1365 & 0 & 0 \\ 0 & 0 & 0 & 0 & 1443 & 0 \\ 0 & 0 & 0 & 0 & 0 & 1443 \end{bmatrix}$$

A.2 Case study #2: 3D grid

Let us now consider a grid-type material, or a solid/air composite. Both phases are considered isotropic linear elastic. The volume fraction of solid phase, the grid, is 36%: a periodic cell of length 10 with a grid width of 1.

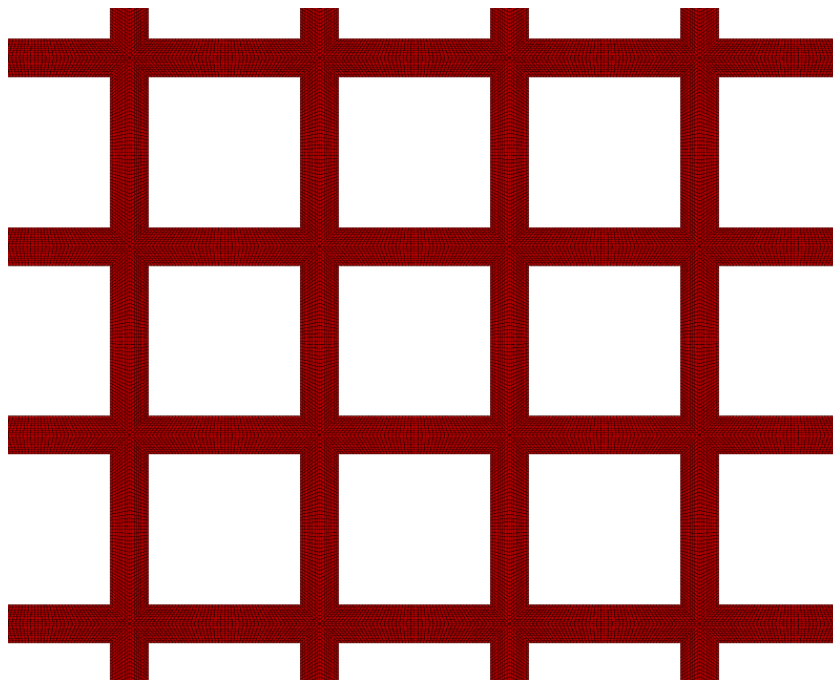


Figure A.5: Replicated FE mesh of the periodic cell with the grid (red)

As for the case study #1, the cell geometry exhibits quadratic symmetry. The elastic moduli tensor will have the same shape as before.

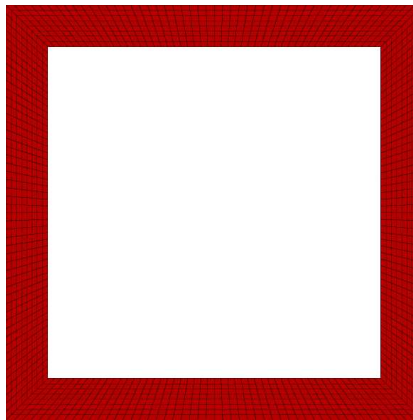


Figure A.6: FE mesh of the periodic unit cell with the grid (red)

Let us implement the 3 methods presented in case study #1.

A.2.1 The MPC_periodic method

Let us implement the **MPC_periodic** method as described earlier. The input file is prepared in the same way as before. Results can be visualized through the Z-Set GUI:

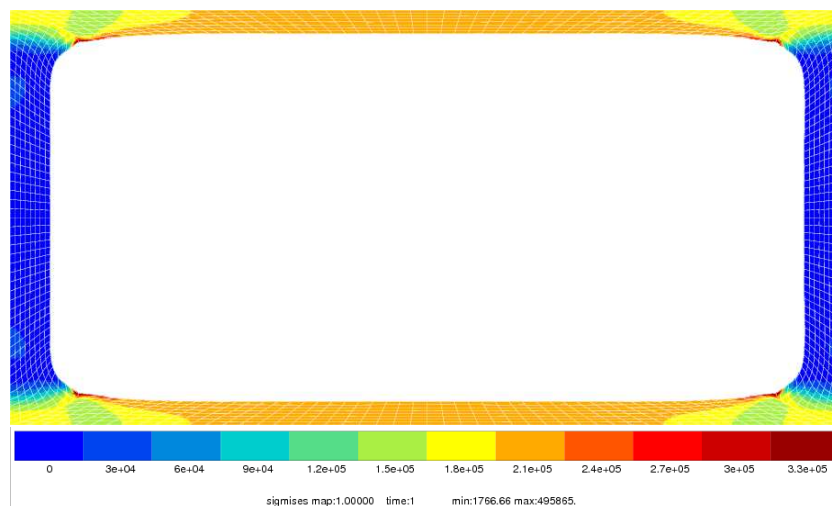


Figure A.7: Deformed FE mesh and equivalent von Mises stress map (MPa) for $E_{11} = 1.0$

Post-processing still consists in a spatial averaging the local stress tensor in order to determine the components of the elastic moduli tensor $\underline{\underline{C}}$. Nevertheless, there is a critical difference: the averaged stress components have to be weighed by the volume fraction of solid phase, thus yielding the following values:

Appendix A. Finite element method for periodic homogenization

$$[C_{ij}] = \begin{bmatrix} 48096 & 4917 & 15904 & 0 & 0 & 0 \\ 4917 & 48096 & 15904 & 0 & 0 & 0 \\ 15904 & 15904 & 85142 & 0 & 0 & 0 \\ 0 & 0 & 0 & 1142 & 0 & 0 \\ 0 & 0 & 0 & 0 & 17125 & 0 \\ 0 & 0 & 0 & 0 & 0 & 17125 \end{bmatrix}$$

These values are characteristic of quadratic elasticity. However, there is an issue still: if one wants to verify the applied load, here a macroscopic strain, the spatial average will not be correct. As a matter of fact, the strain of the void phase is not taken into account. In order to verify the macroscopic strain of the periodic cell, one can use either the **element DOF** method, or the nodal displacement measurements, *cf.* Section A.2.3.

A.2.2 The element DOF method with prescribed macroscopic strain

The ****nset_for_cell** function allows one to define automatically the periodic boundary conditions of the problem, as well as their corresponding node sets. The implementation is similar to the first case study #1.

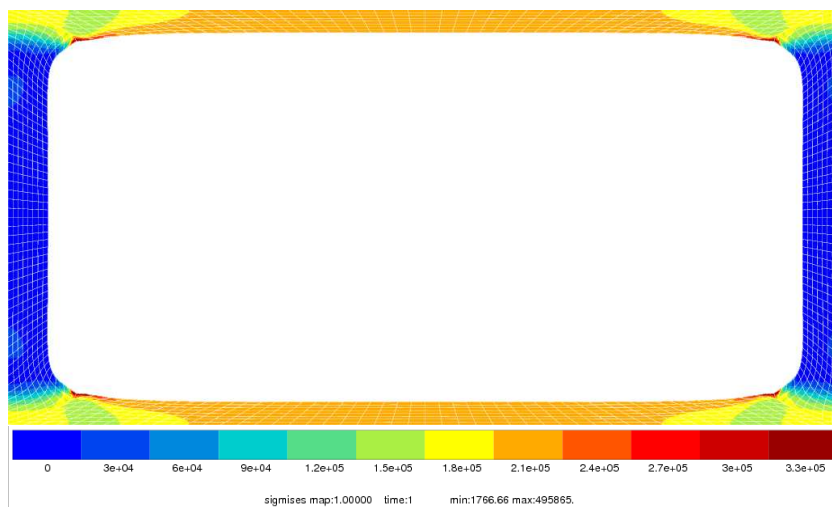


Figure A.8: Deformed FE mesh and equivalent von Mises stress map (MPa) for $E_{11} = 1.0$

Post-processing is the same as for the **MPC_periodic** method:

$$[C_{ij}] = \begin{bmatrix} 48096 & 4917 & 15904 & 0 & 0 & 0 \\ 4917 & 48096 & 15904 & 0 & 0 & 0 \\ 15904 & 15904 & 85142 & 0 & 0 & 0 \\ 0 & 0 & 0 & 1142 & 0 & 0 \\ 0 & 0 & 0 & 0 & 17125 & 0 \\ 0 & 0 & 0 & 0 & 0 & 17125 \end{bmatrix}$$

This method is as quick to implement as for the first case study and yields results that are exactly the same as for the **MPC_periodic** method. As is, it does not allow one to verify the prescribed loading. Let us try the same method but with a prescribed macroscopic stress.

A.2.3 The element DOF method with prescribed macroscopic stress

The procedure is now different from the first case study. It is mandatory to account for the strain of the void phase when computing the macroscopic strain of the cell. There are 3 solutions to that:

- Mesh the void phase, even roughly, so that the spatial average strain field can be computed. It can be very costly to do so in the case of very porous microstructures. Anyway, additional meshing will always cost more in terms of computation time.
- Measure the local displacements of certain nodes of the mesh, which enables one to compute the macroscopic strain tensor over the periodic cell.
- Compute the DOF of the element instead of the nodal ones. This method is limited to the linear elastic case and does not help one to verify the loading of the periodic cell.

Mesh of the void phase

Let us consider a new mesh, including the void phase:

Once again, one has to prescribe the value of the macroscopic stress multiplied by the volume of the cell, but

$$\underline{\Sigma} = \frac{1}{V} \int_V \underline{\sigma} dV \tag{A.5}$$

Appendix A. Finite element method for periodic homogenization

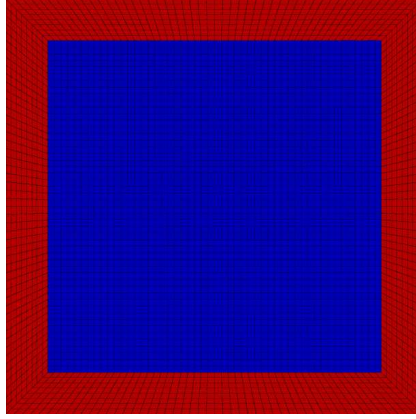


Figure A.9: FE mesh of the periodic unit cell with the grid (red) and the void (blue)

Stress in void phase are equal to zero, this yields:

$$\underline{\Sigma} = \frac{1}{V} \int_{V_{grid}} \underline{\sigma} dV \quad (A.6)$$

$$= \frac{V_{grid}}{V} \frac{1}{V_{grid}} \int_{V_{grid}} \underline{\sigma} dV \quad (A.7)$$

$$= \frac{V_{grid}}{V} \langle \underline{\sigma} \rangle_{grid} \quad (A.8)$$

with V_{grid} , volume of the in the periodic unit cell of volume V . In this example, for a cell of dimension $10 \times 10 \times 0.2$ and a grid volume per cell of 7.2, the prescribed value for $V_{grid} \langle \underline{\sigma} \rangle_{grid} = V \underline{\Sigma}$ is $10 \times 10 \times 0.2 \times 7.2 \div 20 = 7.2$, which corresponds to $1 \times V_{grid}$. Constitutive parameters of the void phase are chosen as follows: $E = 0.1$ MPa, $\nu = 0.3$.

Components of the compliance tensor $\underline{\mathbb{S}}$ (expressed in MPa^{-1}) are obtained by post-processing and weighing of the average by the inverse of the volume fraction of solid phase:

$$[S_{ij}] = \begin{bmatrix} 2,2 \cdot 10^{-5} & -9,6 \cdot 10^{-7} & -4,0 \cdot 10^{-6} & 0 & 0 & 0 \\ -9,6 \cdot 10^{-7} & 2,2 \cdot 10^{-5} & -4,0 \cdot 10^{-6} & 0 & 0 & 0 \\ -4,0 \cdot 10^{-6} & -4,0 \cdot 10^{-6} & 1,3 \cdot 10^{-5} & 0 & 0 & 0 \\ 0 & 0 & 0 & 8,8 \cdot 10^{-4} & 0 & 0 \\ 0 & 0 & 0 & 0 & 5,8 \cdot 10^{-5} & 0 \\ 0 & 0 & 0 & 0 & 0 & 5,8 \cdot 10^{-5} \end{bmatrix}$$

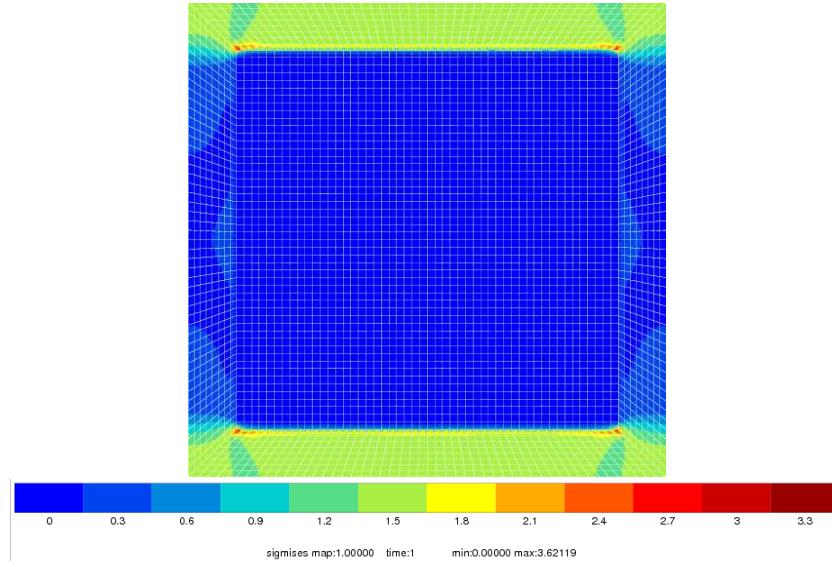


Figure A.10: Deformed FE mesh and equivalent von Mises stress map (MPa) for $\mathbf{RE}_{11} = 1 \times V_{grid}$

By inverting $\underline{\underline{\mathbf{S}}}$, one obtains the components of the elastic moduli tensor $\underline{\underline{\mathbf{C}}}$ (MPa):

$$[C_{ij}] = \begin{bmatrix} 48096 & 4917 & 15904 & 0 & 0 & 0 \\ 4917 & 48096 & 15904 & 0 & 0 & 0 \\ 15904 & 15904 & 85142 & 0 & 0 & 0 \\ 0 & 0 & 0 & 1142 & 0 & 0 \\ 0 & 0 & 0 & 0 & 17125 & 0 \\ 0 & 0 & 0 & 0 & 0 & 17125 \end{bmatrix}$$

The elastic properties of the void phase are taken into account here hence increasing the values slightly (+0,02%) in comparison with the previous examples.

Average strain method

We describe a simple method for determining macroscopic strain for a stress-loaded periodic cell without using element DOFs. It is based on a direct measure of the homogenized compliance tensor $\underline{\underline{\mathbf{S}}}$. Let us define 3 pairs of nodes defining vectors $\underline{\mathbf{x}}^i$ that are collinear to the periodicity vectors of the cell. For the trivial case of a rectangular parallelepiped defined within basis (x, y, z) , it yields $\{\underline{\mathbf{x}}^a \parallel \vec{x}; \underline{\mathbf{x}}^b \parallel \vec{y}; \underline{\mathbf{x}}^c \parallel \vec{z}\}$. For the sake of simplicity, let us use vectors $\underline{\mathbf{x}}^i$ as basis, with nodes located at the vertices of the periodic cell so that the norms of vectors correspond to the dimensions of the cell. Hence, knowing the initial location of the considered nodes and by measuring their local displacements one can compute the macroscopic strain using the following relationship:

$$\underline{\mathbf{u}}^i = \underline{\mathbf{E}} \cdot \Delta \underline{\mathbf{x}}^i \quad (\text{A.9})$$

Appendix A. Finite element method for periodic homogenization

with,

$$\Delta \underline{\mathbf{x}}^i = \underline{\mathbf{x}}^i - \underline{\mathbf{x}}^{i+1} = [\Delta x_1^i; \Delta x_2^i; \Delta x_3^i] \quad (\text{A.10})$$

Equation A.9 can be rewritten as follows:

$$\begin{bmatrix} u_1^a \\ u_2^a \\ u_3^a \\ u_1^b \\ u_2^b \\ u_3^b \\ u_1^c \\ u_2^c \\ u_3^c \end{bmatrix} = \begin{bmatrix} \Delta x_1^a & 0 & 0 & \Delta x_2^a & 0 & 0 & \Delta x_3^a & 0 & 0 \\ 0 & \Delta x_2^a & 0 & 0 & \Delta x_3^a & 0 & 0 & \Delta x_1^a & 0 \\ 0 & 0 & \Delta x_3^a & 0 & 0 & \Delta x_1^a & 0 & 0 & \Delta x_2^a \\ \Delta x_1^b & 0 & 0 & \Delta x_2^b & 0 & 0 & \Delta x_3^b & 0 & 0 \\ 0 & \Delta x_2^b & 0 & 0 & \Delta x_3^b & 0 & 0 & \Delta x_1^b & 0 \\ 0 & 0 & \Delta x_3^b & 0 & 0 & \Delta x_1^b & 0 & 0 & \Delta x_2^b \\ \Delta x_1^c & 0 & 0 & \Delta x_2^c & 0 & 0 & \Delta x_3^c & 0 & 0 \\ 0 & \Delta x_2^c & 0 & 0 & \Delta x_3^c & 0 & 0 & \Delta x_1^c & 0 \\ 0 & 0 & \Delta x_3^c & 0 & 0 & \Delta x_1^c & 0 & 0 & \Delta x_2^c \end{bmatrix} \begin{bmatrix} \mathbf{E}_{11} \\ \mathbf{E}_{22} \\ \mathbf{E}_{33} \\ \mathbf{E}_{12} \\ \mathbf{E}_{23} \\ \mathbf{E}_{31} \\ \mathbf{E}_{13} \\ \mathbf{E}_{21} \\ \mathbf{E}_{32} \end{bmatrix} \quad (\text{A.11})$$

For the case of a rectangular parallelepiped, as shown on Figure A.11, let us consider the vertex O of the periodic cell and 3 homologous nodes $\{A; B; C\}$. Three vectors $\underline{\mathbf{OA}}$, $\underline{\mathbf{OB}}$ and $\underline{\mathbf{OC}}$ can be defined:

$$\begin{aligned} \underline{\mathbf{OA}} &= \underline{\mathbf{x}}^A - \underline{\mathbf{x}}^O = \underline{\mathbf{X}}^A + \underline{\mathbf{u}}^A - \underline{\mathbf{X}}^O - \underline{\mathbf{u}}^O \\ &= (\underline{\mathbf{X}}^A - \underline{\mathbf{X}}^O) + (\underline{\mathbf{u}}^A - \underline{\mathbf{u}}^O) \\ &= (\underline{\mathbf{X}}^A - \underline{\mathbf{X}}^O) + \underline{\mathbf{E}} \cdot (\underline{\mathbf{X}}^A - \underline{\mathbf{X}}^O) \end{aligned} \quad (\text{A.12})$$

Also,

$$\underline{\mathbf{OB}} = \underline{\mathbf{x}}^B - \underline{\mathbf{x}}^O = (\underline{\mathbf{X}}^B - \underline{\mathbf{X}}^O) + \underline{\mathbf{E}} \cdot (\underline{\mathbf{X}}^B - \underline{\mathbf{X}}^O) \quad (\text{A.13})$$

$$\underline{\mathbf{OC}} = \underline{\mathbf{x}}^C - \underline{\mathbf{x}}^O = (\underline{\mathbf{X}}^C - \underline{\mathbf{X}}^O) + \underline{\mathbf{E}} \cdot (\underline{\mathbf{X}}^C - \underline{\mathbf{X}}^O) \quad (\text{A.14})$$

It yields a system of 9 equations with 9 unknown variables:

$$\underline{\mathbf{u}}^A - \underline{\mathbf{u}}^O = \underline{\mathbf{E}} \cdot (\underline{\mathbf{X}}^A - \underline{\mathbf{X}}^O) \quad (\text{A.15})$$

$$\underline{\mathbf{u}}^B - \underline{\mathbf{u}}^O = \underline{\mathbf{E}} \cdot (\underline{\mathbf{X}}^B - \underline{\mathbf{X}}^O) \quad (\text{A.16})$$

$$\underline{\mathbf{u}}^C - \underline{\mathbf{u}}^O = \underline{\mathbf{E}} \cdot (\underline{\mathbf{X}}^C - \underline{\mathbf{X}}^O) \quad (\text{A.17})$$

The macroscopic strain tensor $\underline{\mathbf{E}}$ can thus be easily obtained from the displacement measure of a few nodes. This measure is simple done by a local post-processing.

Using this method, one can compute the macroscopic strain tensor $\underline{\mathbf{E}}$ just by measuring the displacement of certain nodes of the mesh. Nevertheless, a local post-processing is necessary in order to obtain the nodal displacements, here is an example:

```
****post_processing
***precision 6
***local_post_processing
```

```

**output_number 1
**file node
**nset vertices
**process format
*file nodes_displacement
*list_var U1 U2 U3

****return

```

The displacements U_1 , U_2 and U_3 of the nodes included within the `nset vertices` are written in the `nodes_displacement` file.

Coming back to our case study, this yields the components of the compliance tensor $\underline{\underline{S}}$, in MPa^{-1} :

$$[S_{ij}] = \begin{bmatrix} 2,2 \cdot 10^{-5} & -9,6 \cdot 10^{-7} & -4,0 \cdot 10^{-6} & 0 & 0 & 0 \\ -9,6 \cdot 10^{-7} & 2,2 \cdot 10^{-5} & -4,0 \cdot 10^{-6} & 0 & 0 & 0 \\ -4,0 \cdot 10^{-6} & -4,0 \cdot 10^{-6} & 1,3 \cdot 10^{-5} & 0 & 0 & 0 \\ 0 & 0 & 0 & 8,8 \cdot 10^{-4} & 0 & 0 \\ 0 & 0 & 0 & 0 & 5,8 \cdot 10^{-5} & 0 \\ 0 & 0 & 0 & 0 & 0 & 5,8 \cdot 10^{-5} \end{bmatrix}$$

By inverting $\underline{\underline{S}}$, one obtains $\underline{\underline{C}}$, in MPa:

$$[C_{ij}] = \begin{bmatrix} 48096 & 4917 & 15904 & 0 & 0 & 0 \\ 4917 & 48096 & 15904 & 0 & 0 & 0 \\ 15904 & 15904 & 85142 & 0 & 0 & 0 \\ 0 & 0 & 0 & 1142 & 0 & 0 \\ 0 & 0 & 0 & 0 & 17125 & 0 \\ 0 & 0 & 0 & 0 & 0 & 17125 \end{bmatrix}$$

These values are identical to those obtained using the `MPC_periodic` and the `element DOF` methods with prescribed macroscopic strain.

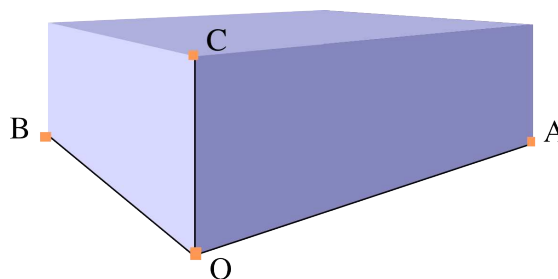


Figure A.11: Parallelepipedic periodic cell

Appendix A. Finite element method for periodic homogenization

Make use of the additional element DOF

In this last method, the spatial average of the local strain field is not computed anymore. Instead, it makes use of the duality between the macroscopic strain DOF \mathbf{E}_{ij} and their associated reactions \mathbf{RE}_{ij} . Thus, the values of \mathbf{E}_{ij} obtained after the computation correspond to the effective values of macroscopic strain over the periodic cell. By default, these values are not kept during the computation, it has to be specified in the input file using the following commands:

```
****calcul
...
****output
**test
*elset_var ALL_ELEMENT E11 E22 E33 E12 E23 E31 RE11 RE22 RE33 RE12 RE23 RE31
...
****return
```

These values are written in a .test file after the computation. One can then obtain the compliance tensor $\underline{\underline{S}}$. We obtain the same values as before:

$$[S_{ij}] = \begin{bmatrix} 2,2.10^{-5} & -9,6.10^{-7} & -4,0.10^{-6} & 0 & 0 & 0 \\ -9,6.10^{-7} & 2,2.10^{-5} & -4,0.10^{-6} & 0 & 0 & 0 \\ -4,0.10^{-6} & -4,0.10^{-6} & 1,3.10^{-5} & 0 & 0 & 0 \\ 0 & 0 & 0 & 8,8.10^{-4} & 0 & 0 \\ 0 & 0 & 0 & 0 & 5,8.10^{-5} & 0 \\ 0 & 0 & 0 & 0 & 0 & 5,8.10^{-5} \end{bmatrix}$$

This method is straightforward and avoids post-processing, however it does not allow one to verify the applied load over the periodic cell.

B Basics of mathematical morphology

This appendix is a selective synthesis of the mathematical morphology courses given by Prof. Dominique Jeulin at the École Nationale Supérieure des Mines de Paris, where this discipline was created in the 1960s by Profs. *Georges Matheron* and *Jean Serra*. I am completely indebted to Prof. *Jeulin* for the content of this part, everything here can be found in a more detailed manner in both the *Models of Random Structures* and *Physics & Mechanics of Random Media* graduate courses he taught at ENSMP, as well as in [[Bornert et al., 2001](#)]. Only the concepts useful in the context of this work are presented hereafter, for a more exhaustive description please check the aforementioned references.

The purpose of the present appendix is to sum up and clarify notations used and results given previously in this work. Hopefully, this can also serve as an introduction for the inquiring reader to go deeper in the established literature of a subject that is often overlooked but always beneficial.

In Part III, we make use of models of random structures to simulate materials. There are many morphological models that are useful for simulating materials, for instance realizations stochastic point processes can account for dispersions of particles in a matrix, polycrystalline materials can be assimilated to random tessellations of space, biphasic or multiphasic media can be modeled by binary or multicomponent random sets. When considering measurements, chemical concentration mappings or gray level images for instance can be modeled by random functions or multivariate random function models; random graphs can be used to model porous networks, cracks, etc. In this work we considered Boolean random models using *Poisson* linear varieties in order to simulate a medium made of interpenetrating randomly oriented and distributed infinite rectilinear fibres, *Poisson* fibres. Random structures need to be characterized in order to build models accordingly. First, the characterization of random structures is introduced, followed by a presentation of some models of random structures, namely the *Poisson* point process, *Poisson* linear varieties and the Boolean scheme.

B.1 Characterization of random structures

B.1.1 Minkowski functionals

The morphological characterization of random structures is a two-step process [Serra, 1982]: first a morphological transformation is applied to a random structure (obtained from experiments for instance), then a measure is done on the resulting structure. The choice of the morphological transformation is related to the morphological criterion chosen for characterizing the random structure. Measures performed for morphological characterization must have the following properties: invariance by translation, continuity, locality, additivity and stereology. In integral geometry, it is shown [Matheron, 1975, Serra, 1982] that in \mathbb{R}^n , $n + 1$ measures satisfy these constraints: *Minkowski* functionals W_i , homogeneous and of degree i :

$$W_i(\lambda A) = \lambda^{n-i} W_i(A) \quad (\text{B.1})$$

Also for a given set A in \mathbb{R}^3 , the *Minkowski* functionals read as follows:

$$W_0(A) = \mathcal{V}(A) \quad (\text{B.2})$$

$$3W_1(A) = \mathcal{S}(A) \quad (\text{B.3})$$

$$3W_2(A) = \mathcal{M}(A) = \frac{1}{2} \int_{\partial A} \left(\frac{1}{R_1} + \frac{1}{R_2} \right) dS \quad (\text{B.4})$$

$$3W_3(A) = 4\pi(N - G) = \mathcal{N}(A) = \int_{\partial A} \left(\frac{1}{R_1 R_2} \right) dS \quad (\text{B.5})$$

with $\mathcal{V}(A)$ volume of A , $\mathcal{S}(A)$ its surface, $\mathcal{M}(A)$ its integral of mean curvature, $\mathcal{N}(A)$ its integral of total curvature (connectivity number in \mathbb{R}^3), R_1 and R_2 maximum and minimum radii of curvature on ∂A , N , number of connected components of A , and G , genus of A (maximal number of closed curves to be drawn on its boundary ∂A without disconnecting it into two parts).

In the case of random sets, the *Minkowski* functionals become random variables. For stationary random sets, average measures are invariant by translation. Specific values such as the volume fraction V_V or specific surface S_V are obtained by normalizing by the volume unit. These specific quantities exhibit stereological properties relating one to another using the Crofton relationships (cf. [Bornert et al., 2001]), thus meaning that for instance the volume fraction V_V of a stationary random structure can be obtained from 2D or 1D cuts.

B.1.2 Basic operations of mathematical morphology

The morphology of random structures can be described using structuring elements. A structuring element K is a compact set implanted in every point x of the Euclidean space \mathbb{R}^n . It is necessary to know if both K_x and the set A are mutually located in every point x . This yields the indicator function $\Phi(A)$, obtained by transforming set A . By answering the question "Is K hitting A ?" or

" $K \cap A \neq \emptyset$ ", the dilation operation can be defined:

$$A \oplus \check{K} = \{x, K_x \cap A \neq \emptyset\} = \cup_{y \in K} A_{-y} = \cup_{x \in A, y \in K} \{x - y\} \quad (\text{B.6})$$

with $K_x = \{x + y, y \in K\}$, translated of K to point x and $\check{K} = \{-x, x \in K\}$, obtained by transposition of K . By answering the question "Is K included in A ?" or " $K \subset A$ ", the erosion operation can be defined:

$$A \ominus \check{K} = \{x, K_x \subset A\} = \cap_{y \in K} A_{-y} = (A^c \oplus \check{K})^c \quad (\text{B.7})$$

In Equations B.6 and B.7, the symbols \oplus and \ominus denote the *Minkowski* addition and subtraction respectively:

$$A \oplus K = \cup_{x \in A, y \in K} \{x + y\} = \cup_{y \in K} A_y = \cup_{x \in A} K_x \quad (\text{B.8})$$

$$A \ominus K = \cap_{y \in K} A_y = (A^c \oplus K)^c \quad (\text{B.9})$$

As shown in Equation B.9, dilation and erosion are not independent operations. The following rules apply:

$$(A \ominus \check{K}_1) \ominus \check{K}_2 = A \ominus (\check{K}_1 \oplus \check{K}_2) \quad (\text{B.10})$$

$$(A \cap B) \ominus \check{K} = (A \ominus \check{K}) \cap (B \ominus \check{K}) \quad (\text{B.11})$$

$$A \oplus (\check{K}_1 \cup \check{K}_2) = (A \oplus \check{K}_1) \cup (A \oplus \check{K}_2) \quad (\text{B.12})$$

B.1.3 Steiner formulae

Relationships between the *Minkowski* functionals of a convex set A dilated by a convex set K and the *Minkowski* functionals of A and K are given by the *Steiner* formulae. For $A \subset \mathbb{R}^3$ and $K \subset \mathbb{R}^3$, they read as follows:

$$E\{\mathcal{V}(A \oplus \check{K})\} = \mathcal{V}(A) + \frac{\mathcal{M}(K)}{4\pi} \mathcal{S}(A) + \frac{\mathcal{M}(A)}{4\pi} \mathcal{S}(K) + \mathcal{V}(K) \quad (\text{B.13})$$

$$E\{\mathcal{S}(A \oplus \check{K})\} = \mathcal{S}(A) + \frac{\mathcal{M}(A)\mathcal{M}(K)}{2\pi} + \mathcal{S}(K) \quad (\text{B.14})$$

$$E\{\mathcal{M}(A \oplus \check{K})\} = \mathcal{M}(A) + \mathcal{M}(K) \quad (\text{B.15})$$

Appendix B. Basics of mathematical morphology

For $A \subset \mathbb{R}^3$ and $K \subset \mathbb{R}^2$, $\mathcal{M}(K) = \frac{\pi}{2} \mathcal{L}(K)$, thus yielding the following *Steiner* formulae:

$$E\{\mathcal{V}(A \oplus \check{K})\} = \mathcal{V}(A) + \frac{\mathcal{L}(K)}{8} \mathcal{S}(A) + \frac{\mathcal{M}(A)}{2\pi} \mathcal{A}(K) \quad (\text{B.16})$$

$$E\{\mathcal{S}(A \oplus \check{K})\} = \mathcal{S}(A) + \frac{\mathcal{M}(A) \mathcal{L}(K)}{4} + 2\mathcal{A}(K) \quad (\text{B.17})$$

with $\mathcal{A}(K)$, area of compact set K and $\mathcal{L}(K)$, perimeter of compact set K in \mathbb{R}^2 .

B.1.4 Covariance

There are several morphological criteria (granulometry, anisotropy, etc.) that can be used to characterize random structures. We focus here on the spatial arrangement of a given random structure. It is characterized by, at least, three properties: covariance, distance function and anisotropy. Since this work does not deal with multiscale and/or anisotropic models of random structures, we will only consider the covariance. The covariance $C(x, x+h)$ of random set A is given by:

$$C(x, x+h) = P\{x \in A, x+h \in A\} \quad (\text{B.18})$$

If A is a stationary random set, $C(x, x+h) = C(h)$. If A is ergodic, $C(h)$ can be estimated from the volume fraction of $A \cap A_{-h}$:

$$C(h) = V_V(A \cap A_{-h}) = V_V(A \ominus \check{h}) \quad (\text{B.19})$$

The erosion by $\{x, x+h\}$ results in variations in $C(h)$ which depend on vector h (modulus $|h|$ and orientation α). The covariance $Q(h)$ of the complementary random set A^c can also be considered, although it does not give any information compared to $C(h)$:

$$Q(0) = q = 1 - p \quad (\text{B.20})$$

$$Q(h) = P\{x \in A^c, x+h \in A^c\} = 1 - 2C(0) + C(h) \quad (\text{B.21})$$

The covariance of a random set in \mathbb{R}^3 is subject to the following properties:

- $C(0) = P\{x \in A\} = p$;
- $\frac{1}{\pi} \int_0^{4\pi} - \left(\frac{\partial C(h, \alpha)}{\partial |h|} \right)_{h=0} d\alpha = S_V(A)$ when the partial derivative remains finite;
- if $C(0) - C(h) \simeq |h|^\beta$ for $h \rightarrow 0$, with $0 < \beta < 1$, the boundary of A has a non integer *Haussdorf* dimension $d = 3 - \beta$, and A is a fractal set;

- $C(\infty) = p^2$, the covariance of a stationary ergodic random set reaches a sill, the events are independent;
- For a given orientation α , $C(h)$ reaches a sill at a certain distance a_α , or range, that we consider as the characteristic length scale of the random structure: $C(a_\alpha) = C(\infty) = V_V(A)^2 = p^2$;
- The presence of multiple scales in the random structure is characterized inflections of the experimental covariance;
- Periodicity of the structure results in periodicity of the covariance.

Correlation functions are useful for studying physical properties within random structures. The centered second-order correlation function can be deduced from the covariance. For the case of a two-phase medium with properties $Z = Z_1$ when $x \in A$ and $Z = Z_2$ when $x \in A^c$, it yields:

$$\begin{aligned}
 \overline{W}_2(h) &= E\{(Z(x+h) - E\{Z\})(Z(x) - E\{Z\})\} \\
 &= (Z_1 - Z_2)^2 (C(h) - p^2) \\
 &= (Z_1 - Z_2)^2 (Q(h) - q^2)
 \end{aligned} \tag{B.22}$$

The integral range A_n presented in Section 4.2.4 is obtained from the centered second-order correlation function in this way:

$$A_n = \frac{1}{D_Z^2} \int_{\mathbb{R}^n} \overline{W}_2(h) dh \tag{B.23}$$

The characterization of random structures has been presented, let us now introduce models of random structures.

B.2 Models of random structures

B.2.1 Choquet capacity

Models of random structures are derived from the theory of random sets by *G. Matheron* [Matheron, 1975]. A random closed set A (RACS) is characterized by its *Choquet* capacity $T(K)$, which is a functional defined on the compact sets K , such that:

$$T(K) = P\{K \cap A \neq \emptyset\} = 1 - P\{K \subset A^c\} = 1 - Q(K) \tag{B.24}$$

The *Choquet* capacity exhibits the following properties:

- $T(K_x) = T(K)$, invariant by translation for a stationary RACS;

Appendix B. Basics of mathematical morphology

- $T(K)$ is invariant by rotation for an isotropic RACS;
- $T(K)^* = P\{x \in A \oplus \check{K}\}^* = V_V(A \oplus \check{K})^*$, $T(K)$ can be estimated ($*$ denotes estimation) from the measure of the volume fraction on a single realization for an ergodic RACS.

This last property is due to the following equation:

$$\frac{1}{\mu_n(B)} \int_B 1_A(x) dx = \frac{\mu_n(A \cap B)}{\mu_n(B)} \xrightarrow{B \rightarrow \mathbb{R}^n} P\{x \in A\} = p \quad (\text{B.25})$$

The construction consists in the choice of basic assumptions regarding the model, and in the computation of the *Choquet* capacity $T(K)$. For a given model, $T(K)$ is obtained by theoretical calculation or by estimation from either simulations or real structures.

B.2.2 Poisson point process

Let us now consider the *Poisson* point process. It is the prototype model for random processes without any order. For a non-homogeneous Poisson point process in \mathbb{R}^n with a regionalized intensity $\theta(x)$ with $x \in \mathbb{R}^n$ and $\theta \geq 0$, the numbers $N(K_i)$ are independent random variables for any family of disjoint compact sets K_i . $N(K)$ is a *Poisson* random variable with parameter $\theta(K)$ such that:

$$\theta(K) = \int_K \theta(dx) \quad (\text{B.26})$$

$$P_n(K) = P\{N(K) = m\} = \frac{\theta(K)^m}{m!} \quad (\text{B.27})$$

The *Choquet* capacity of a *Poisson* point process is given by:

$$T(K) = 1 - Q(K) = 1 - P_0(K) = 1 - \exp(-\theta(K)) \quad (\text{B.28})$$

which yields for the stationary case:

$$T(K) = 1 - \exp(-\theta \mu_n(K)) \quad (\text{B.29})$$

The Poisson point process, like other point processes, can be used to generate more general models, known as the grain models (Boolean models, dead leaves models, random function models). No spatial interaction is considered in the Poisson point process. By introducing a repulsion distance d_R , hard core processes can be derived from the *Poisson* point process. For instance, in a realization of a *Poisson* point process, delete every pair of points separated by a distance $d \leq d_R$. Other point processes can be derived from the *Poisson* point process, such as the *Cox* point process [Cox, 1955].

B.2.3 Poisson linear varieties

Poisson linear varieties are also derived from the *Poisson* point process. Here is a definition of *Poisson* linear varieties taken from [Jeulin, 1991b, Jeulin, 1991a, Jeulin, 2011], based on [Matheron, 1975]:

“*Poisson linear varieties can be introduced as follows: a Poisson point process $\{x_i(\omega)\}$, with intensity $\theta_k(d\omega)$ is considered on the variety of dimension $(n - k)$ containing the origin O , and with orientation ω . On every point $x_i(\omega)$ is given a variety of dimension k , $V_k(\omega)_{x_i}$, orthogonal to the direction ω . By construction, we have $V_k = \cup_{x_i(\omega)} V_k(\omega)_{x_i}$. For instance in \mathbb{R}^3 [...] a network of Poisson lines in every plane Π_ω containing the origin.*”

The *Poisson* point process is actually a *Poisson* linear variety of dimension $k = 0$. In \mathbb{R}^n , $k = n - 1$ yields *Poisson* hyperplanes. For any dimension $k \geq 1$, a network of *Poisson* linear varieties of dimension k can be considered as a *Poisson* point process in the space $S_k \times \mathbb{R}^{n-k}$, with intensity $\theta_k(d\omega) \mu_{n-k}(dx)$. θ_k is a positive *Radon* measure for the set of subspaces of dimension k , S_k , and μ_{n-k} is the *Lebesgue* measure on \mathbb{R}^{n-k} . If $\theta_k(d\omega)$ is any *Radon* measure, the obtained varieties are anisotropic, whereas if $\theta_k(d\omega) = \theta_k d\omega$, they are isotropic. If $\mu_{n-k}(dx)$ is replaced by $\omega_{n-k}(dx)$ in the intensity formula, the varieties are non-stationary.

The number of *Poisson* linear varieties of dimension k hit by a compact set K is a *Poisson* variable [Jeulin, 1991b, Jeulin, 1991a, Jeulin, 2011], with parameter $\theta(K)$ such that,

$$\theta(K) = \int \theta_k(d\omega) \int_{K(\omega)} \theta_{n-k}(dx) = \int \theta_k(d\omega) \theta_{n-k}(K(\omega)) \quad (\text{B.30})$$

where $K(\omega)$ is the orthogonal projection of K on the orthogonal space to $V_k(\omega)$, $V_{k^\perp}(\omega)$. For the stationary case,

$$\theta(K) = \int \theta_k(d\omega) \mu_{n-k}(K(\omega)) \quad (\text{B.31})$$

The *Choquet* capacity of the *Poisson* linear varieties of dimension k is thus obtained as follows:

$$T(K) = 1 - \exp\left(- \int \theta_k(d\omega) \int_{K(\omega)} \theta_{n-k}(dx)\right) \quad (\text{B.32})$$

which reads as follows for the stationary case:

$$T(K) = 1 - \exp\left(- \int \theta_k(d\omega) \mu_{n-k}(K(\omega))\right) \quad (\text{B.33})$$

For the isotropic (θ_k being constant) and stationary case, the number of *Poisson* linear varieties of dimension k hit by a compact set K (convex) is a *Poisson* variable, with parameter $\theta(K)$ such

Appendix B. Basics of mathematical morphology

that:

$$\theta(K) = \theta_k \int \mu_{n-k}(K(\omega)) d\omega = \theta_k \frac{b_{n-k} b_{k+1}}{b_n} \frac{k+1}{2} W_k(K) \quad (\text{B.34})$$

where $W_k(K)$ is the *Minkowski* functional of K , homogeneous and of degree $n - k$, and b_k the volume of the unit-ball in \mathbb{R}^k , given by the following formula:

$$b_k = \frac{\pi^{\frac{k}{2}}}{\Gamma\left(1 + \frac{k}{2}\right)} \quad (\text{B.35})$$

with $\Gamma(x)$, the *Euler* gamma function, defined in this way:

$$\Gamma(x) = \int_0^{\infty} e^{-u} u^{x-1} du \quad (\text{B.36})$$

The *Euler* gamma function exhibits the following properties:

- $\Gamma(1+x) = x\Gamma(x)$;
- $\Gamma(1+n) = n!$ for $n \in \mathbb{N}$;
- $\Gamma(x)\Gamma(1-x) = \frac{\pi}{\sin \pi x}$ for $x \in \mathbb{R}^-$;
- $\Gamma\left(\frac{1}{2}\right) = \sqrt{\pi}$;
- $\Gamma(2x) = \Gamma(x)\Gamma\left(x + \frac{1}{2}\right) \frac{2^{2x-1}}{\sqrt{\pi}}$.

Using this function in Equation B.35, it yields:

- $b_1 = 2$ for $k = 1$;
- $b_2 = \pi$ for $k = 2$;
- $b_3 = \frac{4}{3}\pi$ for $k = 3$.

In \mathbb{R}^3 , *Poisson* lines are obtained for $k = 1$, this yields the following parameter for the *Poisson* process:

$$\theta(K) = \frac{\pi}{4} \theta \mathcal{S}(K) \quad (\text{B.37})$$

B.2.4 Boolean model

The Boolean model [Matheron, 1967] is obtained by implanting random primary grains A' , possibly with overlapping, on *Poisson* points $\{x_k\}$ with intensity θ , such that $A = \cup_{x_k} A'_{x_k}$. Any shape can be used for the grain A' .

The number of primary grains of the Boolean model hit by a compact set K , $N(K)$, follows a *Poisson* distribution with parameter $E\{\theta(\check{A}' \oplus K)\}$. In the stationary case, the parameter of the *Poisson* distribution is given by $\theta\bar{\mu}_n(A' \oplus \check{K})$.

The *Choquet* capacity of the Boolean model with primary grain A' reads as follows:

$$T(K) = 1 - \exp(-E\{\theta(\check{A}' \oplus K)\}) \quad (\text{B.38})$$

which becomes, for the stationary case:

$$T(K) = 1 - \exp(-\theta\bar{\mu}_n(A' \oplus \check{K})) \quad (\text{B.39})$$

with $\bar{\mu}_n(A' \oplus \check{K}) = E\{\mu_n(A' \oplus \check{K})\}$. For the stationary case, let us consider the *Choquet* capacity $T(K)$ with $q = P\{x \in A^c\} = \exp(-\theta\bar{\mu}_n(A'))$:

$$T(K) = 1 - Q(K) = 1 - \exp(-\theta\bar{\mu}_n(A' \oplus \check{K})) = 1 - q^{\frac{\bar{\mu}_n(A' \oplus \check{K})}{\bar{\mu}_n(A')}} \quad (\text{B.40})$$

If A' is a ball of radius r , $q = \exp\left(-\theta\frac{4}{3}\pi r^3\right)$. If one considers m balls of radii r_m , $q = \exp\left(-\theta\frac{4}{3}\pi E\{r_m^3\}\right)$.

The covariance of the Boolean model is given by the following expression:

$$Q(h) = P\{x \in A^c, x+h \in A^c\} = q^2 \exp(\theta K(h)) = q^{2-r(h)} \quad (\text{B.41})$$

with the geometrical covariogram given by:

$$K(h) = \bar{\mu}_n(A' \cap A'_{-h}) \text{ and } r(h) = \frac{K(h)}{K(0)} \quad (\text{B.42})$$

The Boolean model exhibits the following stereological properties:

- For sections of a Boolean model in \mathbb{R}^n by a subspace S_k with $k < n$, it yields a Boolean model in S_k with intensity θ_k and the induced primary grain A'_k satisfying for any $K \subset S_k$, $\theta\bar{\mu}_n(A' \oplus \check{K}) = \theta_k\bar{\mu}_k(A'_k \oplus \check{K})$;
- The property above yields also a particular case: $\theta\bar{\mu}_n(A') = \theta_k\bar{\mu}_k(A'_k)$;
- A 3D Boolean model induces in \mathbb{R}^2 a Boolean model with intensity $\theta_2 = \theta\frac{\overline{\mathcal{M}}(A')}{2\pi}$;

Appendix B. Basics of mathematical morphology

- A Boolean model of spherical primary grains in \mathbb{R}^3 induces a Boolean model of discs in \mathbb{R}^2 , and a Boolean model of segments in \mathbb{R} , hence allowing the reconstruction of the distribution function of radii in \mathbb{R}^3 from the covariance $Q(h)$ obtained on sections.

A Boolean model can be built using *Poisson* linear varieties, we will refer to this model as Boolean random varieties.

B.2.5 Boolean random varieties

Boolean random varieties [Jeulin, 1991b, Jeulin, 1991a, Jeulin, 2011] with primary grain A' are built on *Poisson* linear varieties in this way: a network of *Poisson* linear varieties V_k is considered. Each *Poisson* linear variety $V_{k\alpha}$ is dilated by an independent realization of the primary grain A' . The resulting Boolean random varieties are a Boolean random closed set A such that:

$$A = \cup_{\alpha} V_{k\alpha} \oplus A' \quad (\text{B.43})$$

The *Choquet* capacity of the Boolean random varieties of dimension k is given by this expression:

$$T(K) = 1 - \exp\left(-\int \theta_k(d\omega) \bar{\mu}_{n-k}(A'(\omega) \oplus \check{K}(\omega))\right) \quad (\text{B.44})$$

For isotropic Boolean random varieties, the *Choquet* capacity reads as follows:

$$T(K) = 1 - \exp\left(-\theta_k \frac{b_{n-k} b_{k+1}}{b_n} \frac{k+1}{2} \bar{W}_k(A' \oplus \check{K})\right) \quad (\text{B.45})$$

with b_k , volume of the unit-ball in \mathbb{R}^k (cf. Equation B.35).

When $K = \{x\}$, the probability q yields:

$$q = P\{x \in A^c\} = \exp\left(-\int \theta_k(d\omega) \mu_{n-k}(A'(\omega))\right) \quad (\text{B.46})$$

Finally, when $K = \{x, x+h\}$, the covariance of A^c , $Q(h)$ yields:

$$Q(h) = q^2 \exp\left(\int \theta_k(d\omega) K_{n-k}(\omega, h)\right) \quad (\text{B.47})$$

where $K_{n-k}(\omega, h) = \bar{\mu}_{n-k}(A'(\omega) \cap A'_{-h}(\omega))$ and $h = \underline{\mathbf{h}} \cdot \underline{\mathbf{u}}(\omega)$, with $\underline{\mathbf{u}}(\omega)$ unit-vector along direction ω .

For a compact primary grain A' and for any h , there is an angular sector $K_{n-k}(\omega, h) \neq 0$, so that the covariance generally does not reach a sill, and the integral range defined in Equation B.23 is infinite.

B.2.6 Poisson fibres

Poisson fibres are obtained when considering a *Poisson* linear variety of dimension $k = 1$ in \mathbb{R}^3 , i.e. a network of *Poisson* lines, that is dilated by the compact set of primary grains A' . For isotropic *Poisson* lines, with a convex set $A' \oplus \check{K}$, the following *Choquet* capacity is obtained using Equation B.45:

$$T(K) = 1 - \exp\left(-\theta \frac{\pi}{2} \overline{\mathcal{F}}(A' \oplus \check{K})\right) \quad (\text{B.48})$$

In the event of $A' \oplus \check{K}$ not being convex, the *Choquet* capacity can be expressed as a function of the area \mathcal{A} of the projection on the planes Π_ω using this formula:

$$T(K) = 1 - \exp\left(-\theta \int_{2\pi\text{ster}} \overline{\mathcal{A}}(A'(\omega) \oplus \check{K}(\omega)) d\omega\right) \quad (\text{B.49})$$

If A' is a random sphere with a random radius R and K is a sphere with radius r , the *Choquet* capacity becomes:

$$T(r) = 1 - \exp\left(-\frac{\pi^2}{2} \theta \left(E\{R^2\} + 2r\bar{R} + r^2\right)\right) \quad (\text{B.50})$$

$$T(0) = P\{x \in A\} = 1 - \exp\left(-\frac{\pi^2}{2} \theta E\{R^2\}\right) \quad (\text{B.51})$$

When considering a single spherical primary grain A' with radius R , the *Choquet* capacity is finally expressed in this way:

$$T(0) = P\{x \in A\} = 1 - \exp\left(-\theta \frac{\pi^2 R^2}{2}\right) \quad (\text{B.52})$$

Equation B.52 gives the *Choquet* capacity characterizing the model of *Poisson* fibres used in Part III.

C Experimental characterization of auxetics

Experiments on auxetics were not planned at the beginning of this work. Anyhow, the availability of samples made using SLM coincided with a call for students research projects, making these experiments happen. I would like to acknowledge the interest of two students for this work: *Lenaïc Chizat* and *Valentin Vermeulen*. I would also like to thank Prof. *Gourgues-Lorenzon* for accepting my project, and Dr. *Mazière*, as well as Mmes. *Betbeder* and *Heurtel* for their precious help with the experiments. What could be more satisfactory for an aspiring academic than having his spectrum of understanding broaden by doing projects with students? First, an investigation of the microstructure was done on a bulk cube made of 316L stainless steel using SLM. Then force-displacement curves obtained for uniaxial compression testing are presented for hexatruss 316L samples processed with SLM.

C.1 Microstructural characterization

Appendix C. Experimental characterization of auxetics

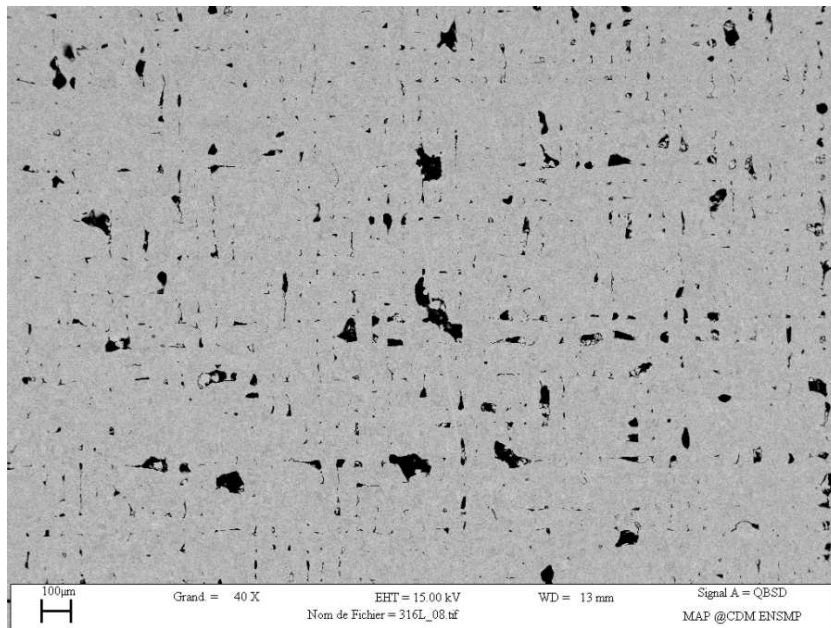


Figure C.1: SEM-BSE micrograph of a 316L stainless steel bulk sample made using SLM

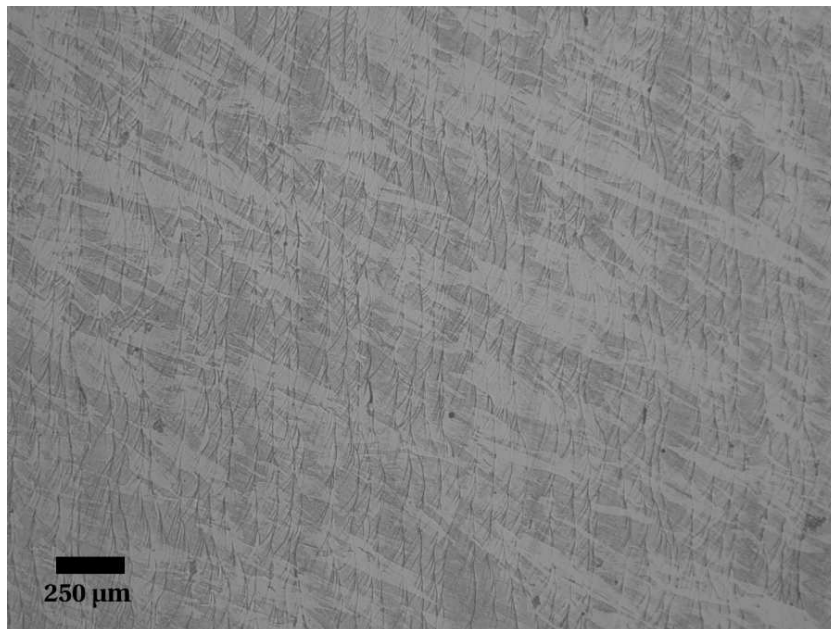


Figure C.2: Optical micrograph (x10) of a 316L stainless steel bulk sample made using SLM

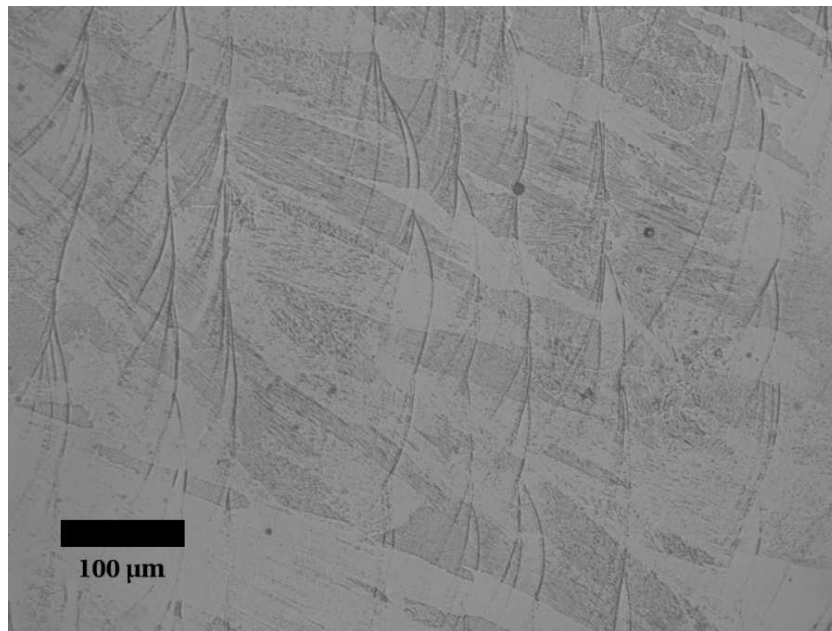


Figure C.3: Optical micrograph (x50) of a 316L stainless steel bulk sample made using SLM

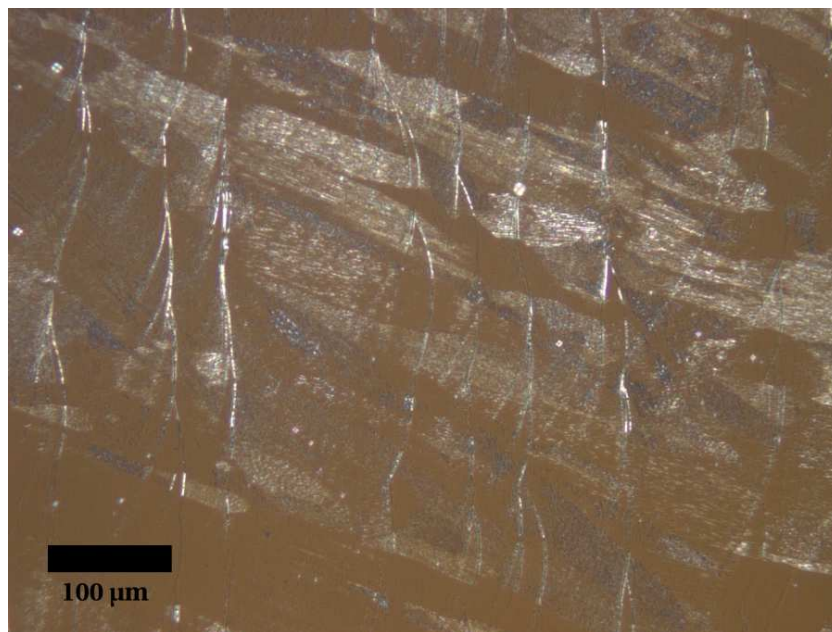


Figure C.4: Polarized optical micrograph (x50) of a 316L stainless steel bulk sample made using SLM

C.2 Macroscopic mechanical testing

Samples were made from 316L stainless steel powders using SLM. These samples were tested in compression. Photographs of the compressive experimental settings are shown in Figure C.5

Appendix C. Experimental characterization of auxetics

for the hexachiral sample and Figure C.6 for the hexatruss one. In order to ensure that the stress state would be mostly compressive uniaxially, we ran a linear elastic FE simulation of the compressive test of the homogenized material. Maps of the principal stress components during compression can be found in Figures C.7 and C.8, showing evidence of a homogeneous uniaxial stress field in the region of interest. Results for the hexatruss samples are shown on Figure C.9. In that case, samples were compressed along direction [110], which is the direction of sollicitation yielding the lowest *Poisson* ratio. Discrepancies arise from the two tests but the trend is similar: heterogeneous deformation is happening, as it was shown on Figure 5.44, which is coming from the same set of experiments. *Young's* modulus was estimated from the fit of the linear part of the curves: $E_{\text{exp}}^* = 8$ MPa. This value is quite comparable to the value obtained from the simulation, that can also be estimated for direction [110] from Figure 5.32: $E_{\text{sim}}^* = 210000 \times 0.02 \times 0.0033 = 13.9$ MPa. Results from the experiments are in the same order of magnitude. The same test was done on hexachiral samples, along the principal direction [010] in order to measure the in-plane *Young's* modulus. Its value was estimated from the results shown on Figure C.10: $E_{\text{exp}}^* = 815$ MPa. This value is comparable with the value obtained from simulation (*cf.* Table 5.1): $E_{\text{sim}}^* = 210000 \times 0.15 \times 0.023 = 725$ MPa. The experimental value is higher than the one predicted from simulation, this is likely due to localized plasticity happening at the very beginning of the experiment. As a matter of fact, the deformation taking place in the hexachiral cell is confined to small zones at the junction between beams and circular nodes; this was shown with the simulations done in Section 5.5.

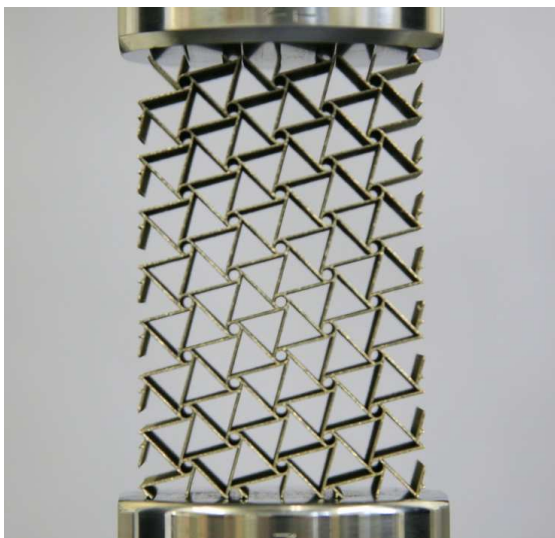


Figure C.5: Experimental setting for the compressive test of the hexachiral cell along [100]

C.3 X-ray microtomography

A sample of the hexatruss lattice material made using SLM was scanned using X-ray microtomography by Prof. *Maire* at MATEIS/INSA Lyon. Analysis of the micrograph obtained in this way (*cf.* Figure C.11) reveals porosities of about 40 μm in diameter, thus justifying our suspicions



Figure C.6: Experimental setting for the compressive test of the hexatruss cell along [110]

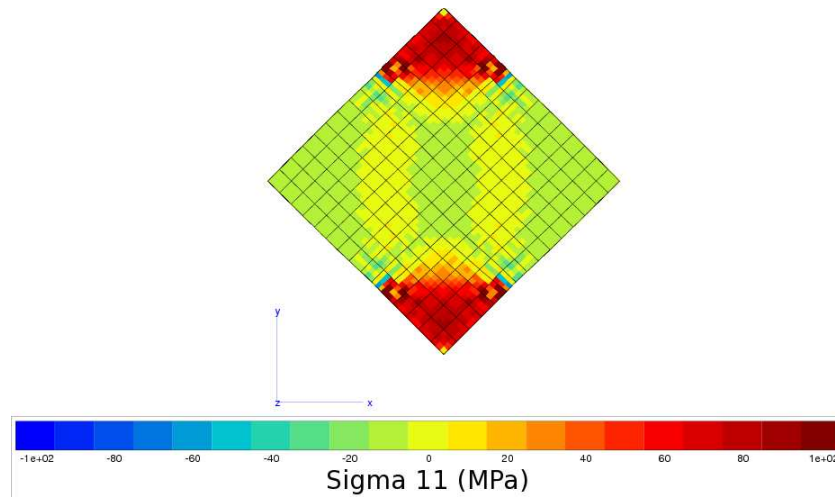


Figure C.7: Deformed shape and σ_{11} stress map for the hexatruss homogeneous equivalent medium

of larger porosity in truss structures made using SLM, in comparison with bulk samples. X-ray spot size used here is 20 μm .

Appendix C. Experimental characterization of auxetics

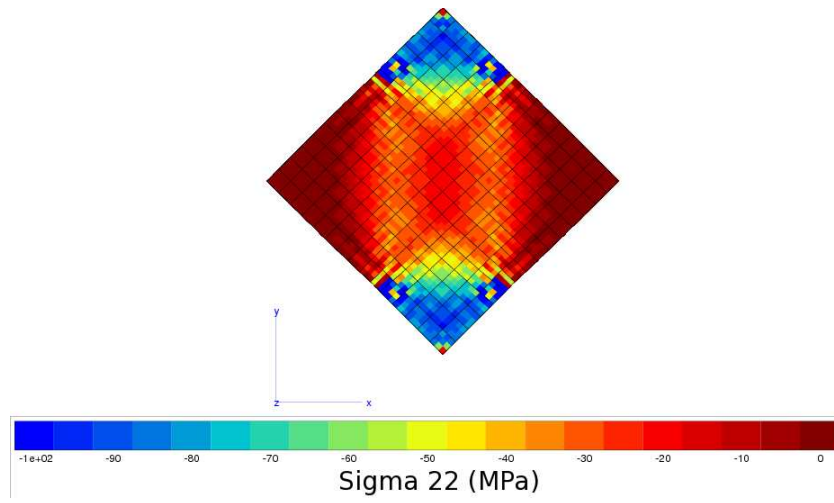


Figure C.8: Deformed shape and σ_{22} stress map for the hexatruss homogeneous equivalent medium

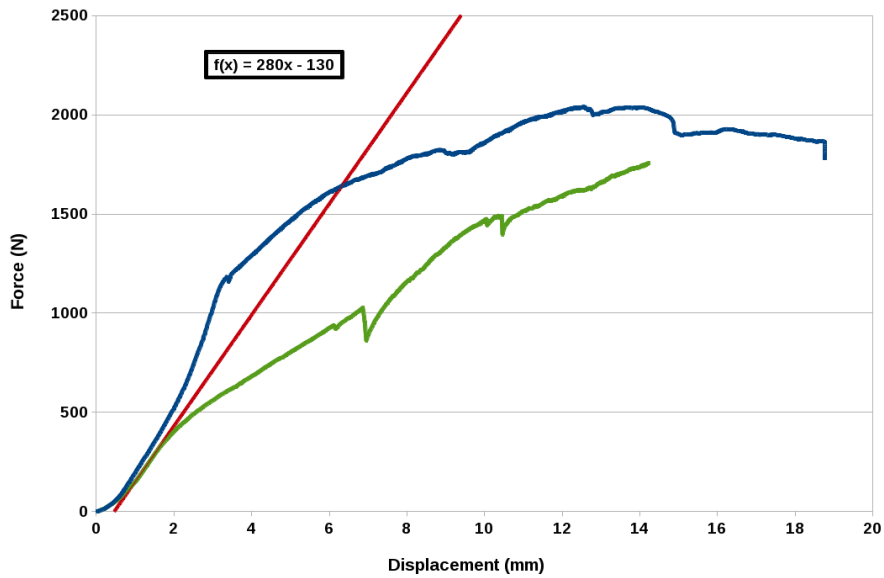


Figure C.9: Force vs. displacement curves for the compression of hexatruss samples

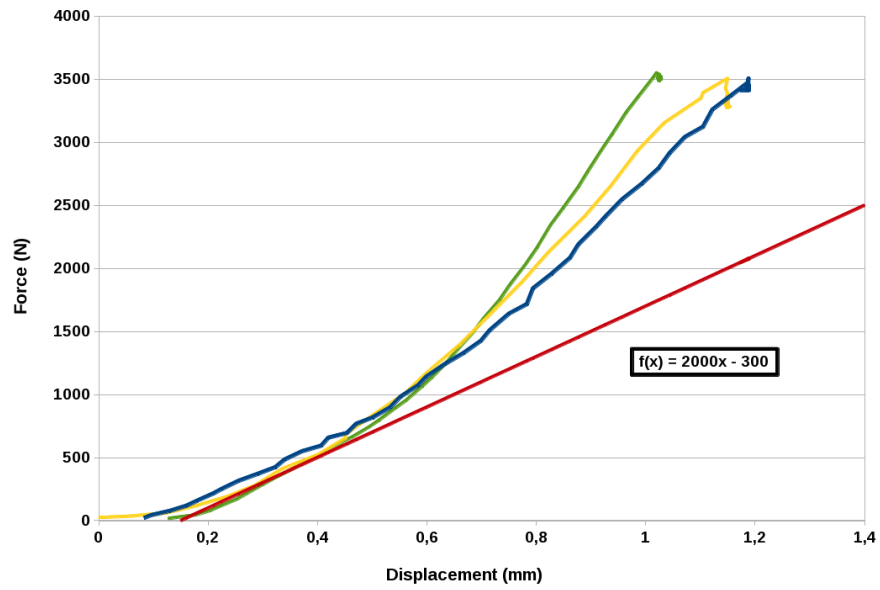


Figure C.10: Force vs. displacement curves for the compression of hexachiral samples

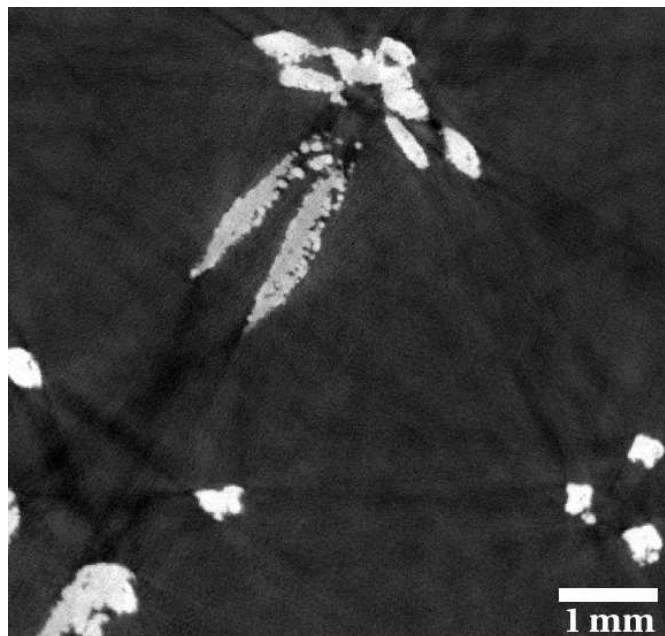


Figure C.11: X-ray micrograph of a hexatruss lattice sample made using SLM

D Simulation results for Poisson fibers

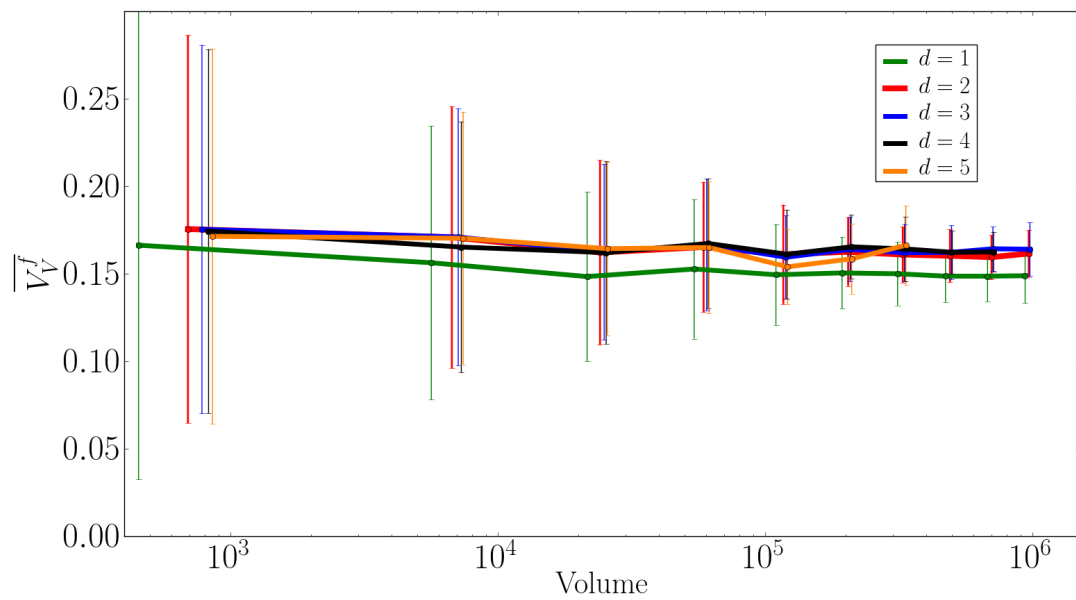


Figure D.1: Mean values for the volume fraction depending on the volume size V

Appendix D. Simulation results for Poisson fibers

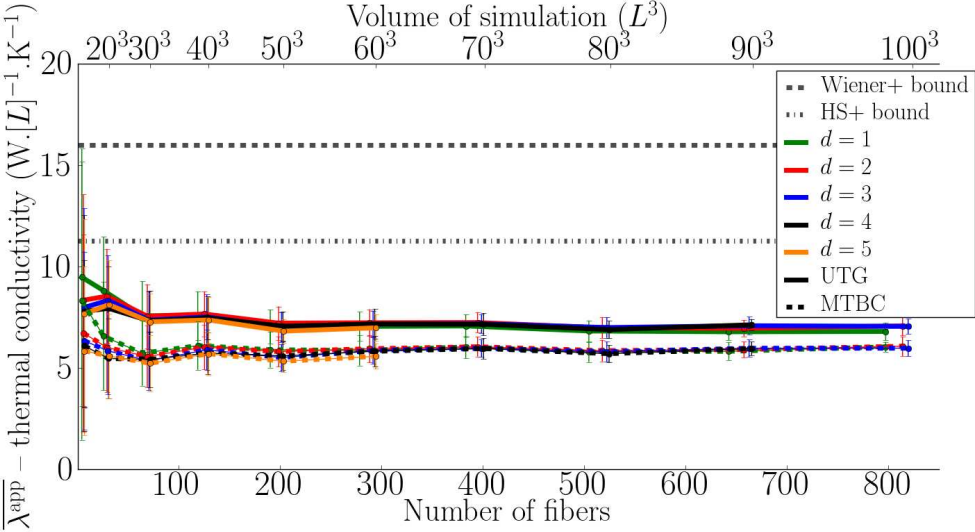


Figure D.2: Mean values for the thermal conductivity depending on the number of fibers \overline{N}

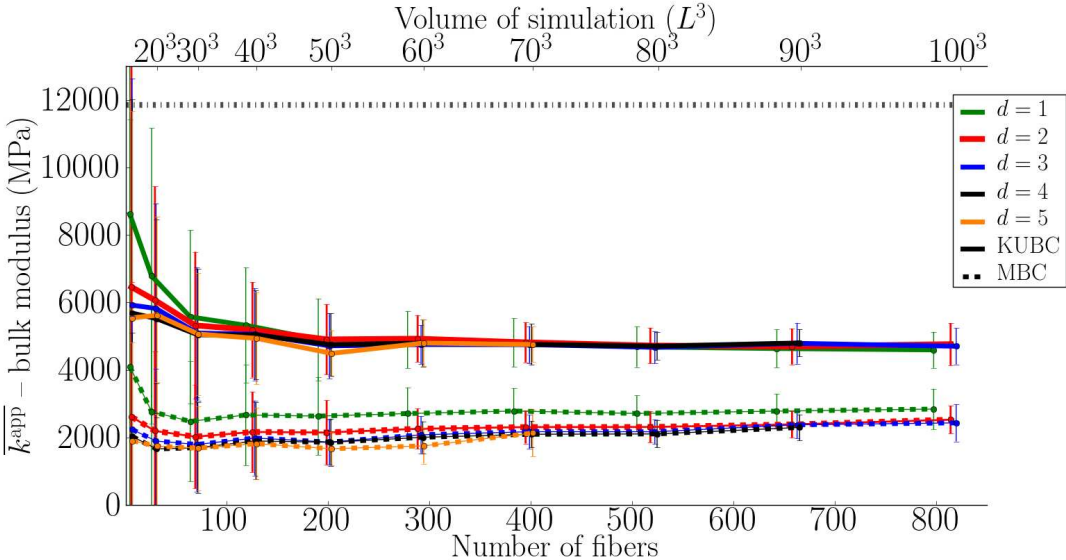


Figure D.3: Mean values for the bulk modulus depending on the number of fibers

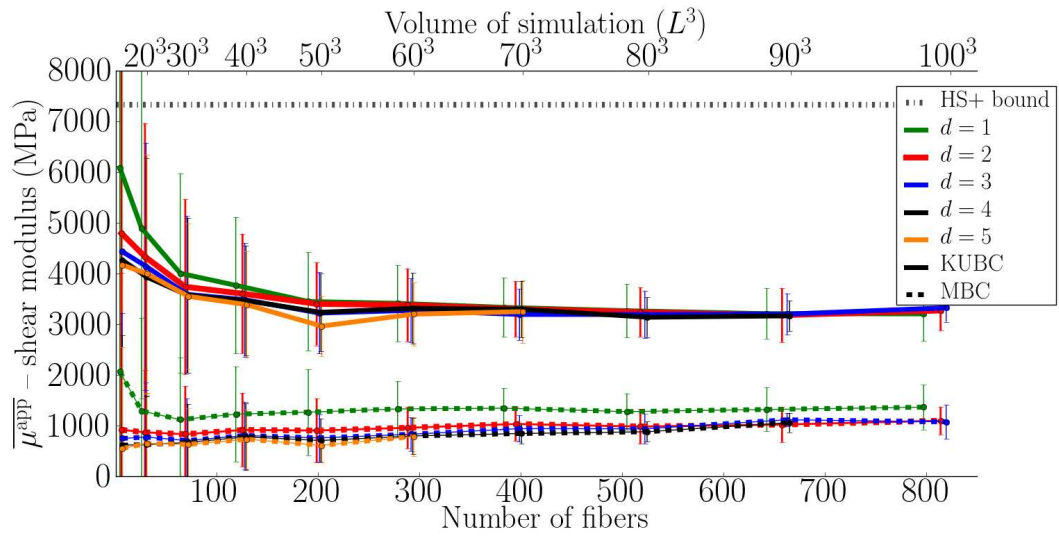


Figure D.4: Mean values for the shear modulus depending on the number of fibers

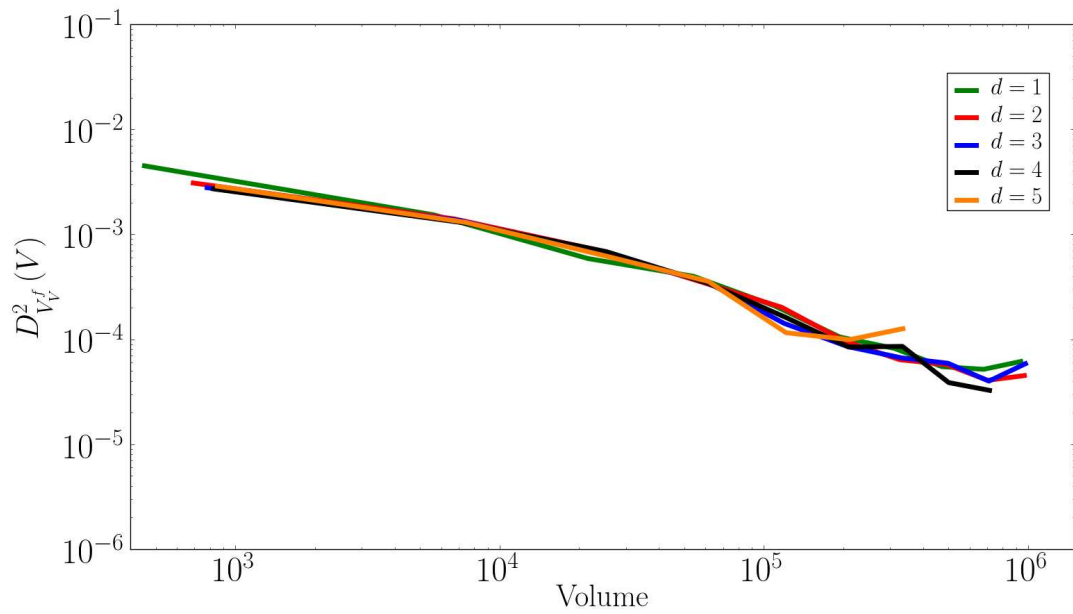


Figure D.5: Variance for the volume fraction of fibers depending on the volume of simulation V

Appendix D. Simulation results for Poisson fibers

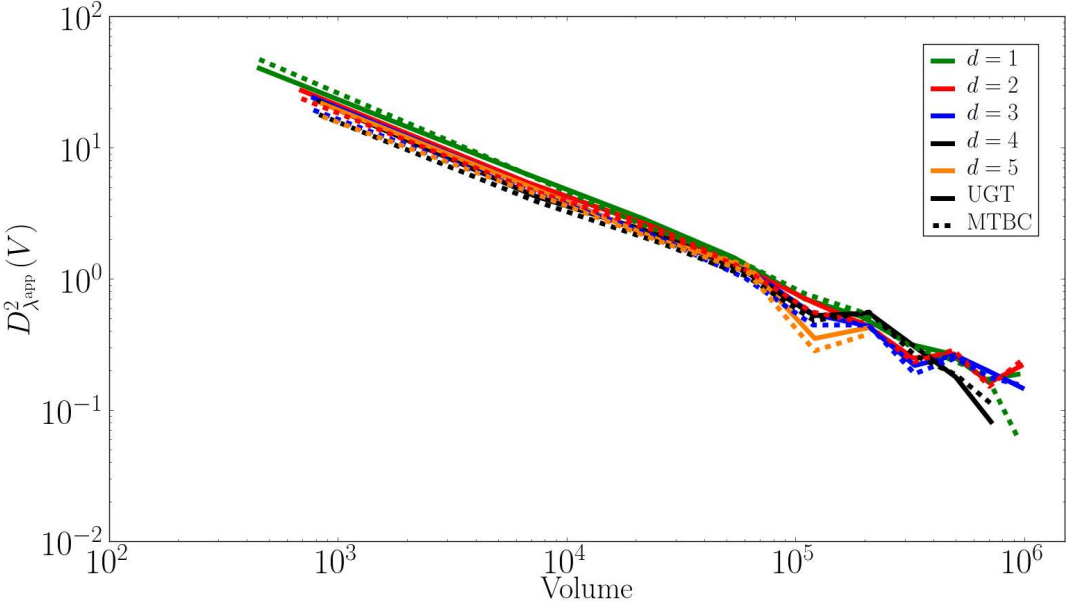


Figure D.6: Variance for the thermal conductivity depending on the volume of simulation V

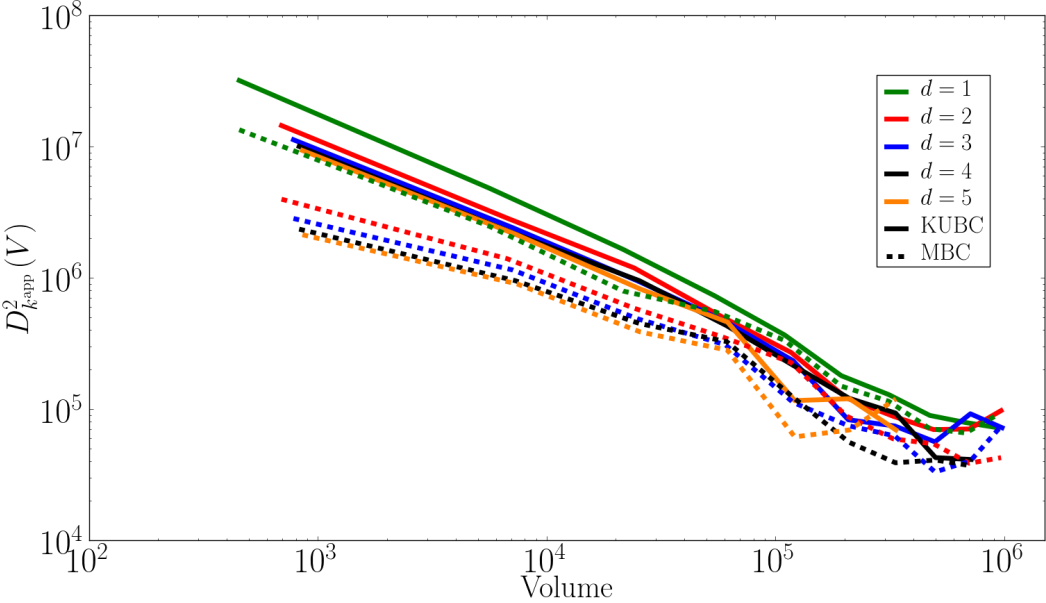


Figure D.7: Variance for the bulk modulus depending on the volume of simulation V

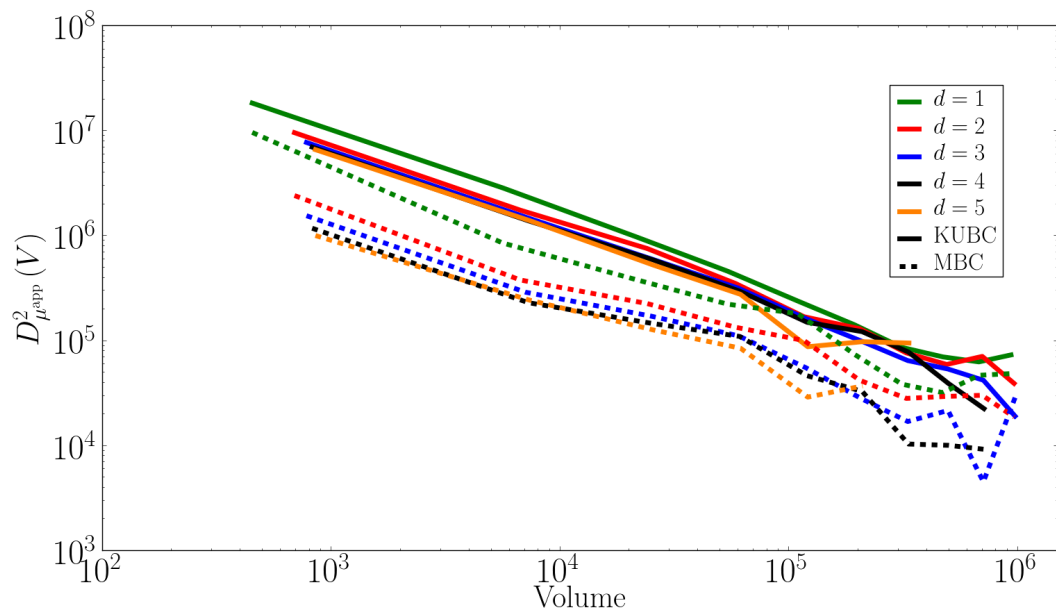


Figure D.8: Variance for the shear modulus depending on the volume of simulation V

References

- [Abouaf et al., 1988] Abouaf M., Chenot J.-L., Raison G., and Bauduin P. (1988). *Finite element simulation of hot isostatic pressing of metal powders*. International Journal for Numerical Methods in Engineering, vol. 25, pp 191–212. [88]
- [Alderson et al., 2010] Alderson A., Alderson K. L., Attard D., Evans K. E., Gatt R., Grima J. N., Miller W., Ravirala N., Smith C. W., and Zied K. (2010). *Elastic constants of 3-, 4- and 6-connected chiral and anti-chiral honeycombs subject to uniaxial in-plane loading*. Composites Science and Technology, vol. 70 n° 7, pp 1042–1048. [68, 70, 71, 75, 76, 80, 81]
- [Alderson et al., 2000] Alderson K. L., Fitzgerald A., and Evans K. E. (2000). *The strain dependent indentation resilience of auxetic microporous polyethylene*. Journal of Materials Science, vol. 35 n° 16, pp 4039–4047. [68]
- [Alderson et al., 1994] Alderson K. L., Pickles A. P., Neale P. J., and Evans K. E. (1994). *Auxetic Polyethylene - The Effect of a Negative Poisson Ratio on Hardness*. Acta Metallurgica et Materialia, vol. 42 n° 7, pp 2261–2266. [68]
- [Almgren, 1985] Almgren R. F. (1985). *An isotropic three-dimensional structure with Poisson's ratio=-1*. Journal of Elasticity, vol. 15, pp 427–430. [68]
- [Altendorf, 2011] Altendorf H. (2011). *3D Morphological Analysis and Modeling of Random Fiber Networks*. Thèse de Doctorat, MINES-ParisTech, Paris. [60, 61]
- [Alvarez Elipe and Diaz Lantada, 2012] Alvarez Elipe J. C. and Diaz Lantada A. (2012). *Comparative study of auxetic geometries by means of computer-aided design and engineering*. Smart Materials and Structures, vol. 21. (105004). [72]
- [Amestoy et al., 2000] Amestoy P. R., Duff I. S., and L'Excellent J.-Y. (2000). *Multifrontal parallel distributed symmetric and unsymmetric solvers*. Computer Methods in Applied Mechanics and Engineering, vol. 184, pp 501–520. [119]
- [Ashby, 1999] Ashby M. F. (1999). *Materials selection in mechanical design*. Butterworth Heinemann, 2nd edition. [3]
- [Ashby, 2013] Ashby M. F. (2013). *Designing architected materials*. Scripta Materialia, vol. 68 n° 1, pp 4–7. [3, 4, 5]

References

- [Ashby and Bréchet, 2003] Ashby M. F. and Bréchet Y. (2003). *Designing hybrid materials*. Acta Materialia, vol. 51, pp 5801–5821. [3, 4, 5, 6]
- [Auffray, 2008a] Auffray N. (2008a). *Comportement des matériaux cellulaires ; élaboration, caractérisation et modélisation prédictive des propriétés*. Thèse de Doctorat, Institut National Polytechnique de Grenoble. [71]
- [Auffray, 2008b] Auffray N. (2008b). *Démonstration du théorème d’Hermann à partir de la méthode Forte-Vianello*. Comptes-Rendus de l’Académie des Sciences - Serie IIB : Mécanique, vol. 336, pp 458–463. [71]
- [Badiche et al., 2000] Badiche X., Forest S., Guibert T., Bienvenu Y., Bartout J.-D., Ienny P., Croset M., and Bernet H. (2000). *Mechanical properties and non-homogeneous deformation of open-cell nickel foams: application of the mechanics of cellular solids and of porous materials*. Materials Science and Engineering, vol. A289, pp 276–288. [88]
- [Barbe et al., 2001] Barbe F., Decker L., Jeulin D., and Cailletaud G. (2001). *Intergranular and intragranular behavior of polycrystalline aggregates. Part I: F.E. model*. International Journal of Plasticity, vol. 17, pp 513–536. [119]
- [Barbier et al., 2009a] Barbier C., Dendievel R., and Rodney D. (2009a). *Numerical study of 3D-compressions of entangled materials*. Computational Materials Science, vol. 45, pp 593–596. [109]
- [Barbier et al., 2009b] Barbier C., Dendievel R., and Rodney D. (2009b). *Role of friction in the mechanics of nonbounded fibrous materials*. Physical Review E, vol. 80 n° 1, pp 016115. [109]
- [Bathurst and Rothenburg, 1988] Bathurst R. J. and Rothenburg L. (1988). *Note on a random isotropic granular material with negative Poisson’s ratio*. International Journal of Engineering Science, vol. 26 n° 4, pp 373–383. [68]
- [Bensoussan et al., 1978] Bensoussan A., Lions J.-L., and Papanicolaou G. (1978). *Asymptotic Analysis for Periodic Structures*. Studies in Mathematics and its Applications. North-Holland. [33]
- [Beran, 1965] Beran M. J. (1965). *Use of the vibrational approach to determine bounds for the effective permittivity in random media*. Il Nuovo Cimento, vol. 38 n° 2, pp 771–782. [37]
- [Beran, 1968] Beran M. J. (1968). *Statistical Continuum Theories*. Wiley. [17, 33]
- [Beran and Molyneux, 1966] Beran M. J. and Molyneux J. (1966). *Use of classical variational principles to determine bounds for the effective bulk modulus in heterogeneous media*. Quarterly of Applied Mathematics, vol. 24, pp 107–118. [46]
- [Besson et al., 2001] Besson J., Cailletaud G., Chaboche J.-L., and Forest S. (2001). *Mécanique Non Linéaire des Matériaux*. Hermès. [33, 47, 51]

- [Bornert et al., 2001] Bornert M., Bretheau T., and Gilormini P. (2001). *Homogénéisation en mécanique des matériaux, Tome 1 : Matériaux aléatoires élastiques et milieux périodiques*. Hermès. [[33](#), [47](#), [189](#), [190](#)]
- [Bréchet and Embury, 2013] Bréchet Y. and Embury J. D. (2013). *Architected materials: Expanding materials space*. Scripta Materialia, vol. 68 n° 1, pp 1–3. [[3](#)]
- [Brinker et al., 1994] Brinker C. J., Sehgal R., Hietala S. L., Deshpande R., Smith D. M., Loy D., and Ashley C. S. (1994). *Sol-gel strategies for controlled porosity inorganic materials*. Journal of Membrane Science, vol. 94 n° 1, pp 85–102. [[3](#)]
- [Bruggeman, 1935] Bruggeman D. A. G. (1935). *Berechnung verschiedener physikalischer Konstanten von heterogenen Substanzen. I. Dielektrizitätskonstanten und Leitfähigkeiten der Mischkörper aus isotropen Substanzen*. Annalen der Physik, vol. 416 n° 7, pp 636–664. [[34](#)]
- [Budiansky, 1965] Budiansky B. (1965). *On the elastic moduli of some heterogeneous materials*. Journal of the Mechanics and Physics of Solids, vol. 13, pp 223–227. [[41](#)]
- [Bunge, 1982] Bunge H. J. (1982). *Texture Analysis in Materials Science*. Butterworths. [[74](#)]
- [Caddock and Evans, 1989] Caddock B. D. and Evans K. E. (1989). *Microporous materials with negative Poisson's ratios: I. Microstructure and mechanical properties*. Journal of Physics D: Applied Physics, vol. 22, pp 1877–1882. [[68](#)]
- [Cailletaud et al., 2003] Cailletaud G., Forest S., Jeulin D., Feyel F., Galliet I., Mounoury V., and Quilici S. (2003). *Some elements of microstructural mechanics*. Computational Materials Science, vol. 27, pp 351–374. [[51](#), [119](#)]
- [Cailletaud et al., 1994] Cailletaud G., Jeulin D., and Rolland P. (1994). *Size effect on elastic properties of random composites*. Engineering Computations, vol. 11 n° 2, pp 99–110. [[56](#), [57](#)]
- [Cauchy, 1827] Cauchy A.-L. (1827). *De la pression ou tension dans un corps solide*, vol. 2 of *Exercices de Mathématiques*, pp 42–59. De Bure, Paris. [[12](#)]
- [Chekkal et al., 2010] Chekkal I., Bianchi M., Remillat C., Becot F.-X., Jaouen L., and Scarpa F. (2010). *Vibro-Acoustic Properties of Auxetic Open Cell Foam: Model and Experimental Results*. Acta Acustica united with Acustica, vol. 96 n° 2, pp 266–274. [[69](#)]
- [Chen and Lakes, 1996] Chen C. P. and Lakes R. S. (1996). *Micromechanical analysis of dynamic behavior of conventional and negative Poisson's ratio foams*. Journal of Engineering Materials and Technology, vol. 118 n° 3, pp 285–288. [[69](#)]
- [Choi and Lakes, 1991] Choi J. B. and Lakes R. S. (1991). *Design of a Fastener Based on Negative Poisson's Ratio Foam*. Cellular Polymers, vol. 10 n° 3, pp 205–212. [[68](#)]

References

- [Choi and Lakes, 1996] Choi J. B. and Lakes R. S. (1996). *Fracture toughness of re-entrant foam materials with a negative Poisson's ratio: experiment and analysis*. International Journal of Fracture, vol. 80, pp 73–83. [68]
- [Courtois et al., 2011] Courtois L., Maire E., Perez M., Bréchet Y., and Rodney D. (2011). *Mechanical Properties of Monofilament Entangled Materials*. In : Optical Measurements, Modeling and Metrology, Volume 5, ed. Proulx T., vol. 5 of *Conference Proceedings of the Society for Experimental Mechanics Series*, pp 33–38. Springer. [6]
- [Cox, 1955] Cox D. R. (1955). *Some Statistical Methods Connected with Series of Events*. Journal of the Royal Statistical Society, vol. 17 n° 2, pp 129–164. [194]
- [Delaunay, 1934] Delaunay B. (1934). *Sur la sphère vide*. Izvestia Akademii Nauk SSSR, Otdelenie Matematicheskikh i Estestvennykh Nauk, vol. VII n° 6, pp 793–800. [116]
- [Delisée et al., 2001] Delisée C., Jeulin D., and Michaud F. (2001). *Morphological Characterization and Porosity in 3D of Cellulosic Fibrous Materials*. Comptes-Rendus de l'Académie des Sciences - Serie IIB : Mécanique, vol. 329 n° 3, pp 179–185. [109]
- [Deshpande and Fleck, 2000] Deshpande V. S. and Fleck N. A. (2000). *Isotropic constitutive models for metallic foams*. Journal of the Mechanics and Physics of Solids, vol. 48, pp 1253–1283. [82, 88]
- [di Paola, 2010] di Paola F. (2010). *Modélisation multi-échelles du comportement thermo-élastique de composites à particules sphériques*. Thèse de Doctorat, Ecole Centrale Paris. [59]
- [Dirrenberger et al., 2012] Dirrenberger J., Forest S., and Jeulin D. (2012). *Elastoplasticity of auxetic materials*. Computational Materials Science, vol. 64, pp 57–61. [92, 119]
- [Dirrenberger et al., 2013] Dirrenberger J., Forest S., and Jeulin D. (2013). *Effective elastic properties of auxetic microstructures: anisotropy and structural applications*. International Journal of Mechanics and Materials in Design, vol. 9 n° 1, pp 21–33. [92]
- [Dirrenberger et al., 2011] Dirrenberger J., Forest S., Jeulin D., and Colin C. (2011). *Homogenization of periodic auxetic materials*. Procedia Engineering, vol. 10, pp 1847–1852. 11th International Conference on the Mechanical Behavior of Materials (ICM11). [70, 72]
- [Doyoyo and Hu, 2006] Doyoyo M. and Hu J. W. (2006). *Plastic failure analysis of an auxetic foam or inverted strut lattice under longitudinal and shear loads*. Journal of the Mechanics and Physics of Solids, vol. 54, pp 1479–1492. [92]
- [Drugan and Willis, 1996] Drugan W. J. and Willis J. R. (1996). *A Micromechanics-Based Nonlocal Constitutive Equation and Estimates of Representative Volume Element Size for Elastic Composites*. Journal of the Mechanics and Physics of Solids, vol. 44 n° 4, pp 497–524. [18]

- [Einstein, 1906] Einstein A. (1906). *Eine neue Bestimmung der Moleküldimensionen*. Annalen der Physik, vol. 324 n° 2, pp 289–306. [38]
- [Einstein, 1911] Einstein A. (1911). *Berichtigung zu meiner Arbeit: “Eine neue Bestimmung der Moleküldimensionen”*. Annalen der Physik, vol. 339 n° 3, pp 591–592. [38]
- [Embury and Bouaziz, 2010] Embury D. and Bouaziz O. (2010). *Steel-Based Composites: Driving Forces and Classifications*. Annual Review of Materials Research, vol. 40, pp 213–241. [3]
- [Escoda et al., 2011] Escoda J., Willot F., Jeulin D., Sanahuja J., and Toulemonde C. (2011). *Estimation of local stresses and elastic properties of a mortar sample by FFT computation of fields on a 3D image*. Cement and Concrete Research, vol. 41, pp 542–556. [110]
- [Eshelby, 1957] Eshelby J. D. (1957). *The Determination of the Elastic Field of an Ellipsoidal Inclusion, and Related Problems*. Proceedings of the Royal Society of London. Series A, Mathematical and Physical Sciences, vol. 241 n° 1226, pp 376–396. [38]
- [Evans, 1991] Evans K. E. (1991). *The Design of Doubly Curved Sandwich Panels with Honeycomb Cores*. Composite Structures, vol. 17 n° 2, pp 95–111. [68, 69]
- [Evans and Alderson, 2000] Evans K. E. and Alderson A. (2000). *Auxetic Materials: Functional Materials and Structures from Lateral Thinking!* Advanced Materials, vol. 12 n° 9, pp 617–628. [68]
- [Evans et al., 1991] Evans K. E., Nkansah M. A., Hutchinson I. J., and Rogers S. C. (1991). *Molecular network design*. Nature, vol. 353, pp 124. [68]
- [Forest et al., 2005] Forest S., Blazy J.-S., Chastel Y., and Moussy F. (2005). *Continuum modeling of strain localization phenomena in metallic foams*. Journal of Materials Science, vol. 40, pp 5903–5910. [88]
- [Forest and Trinh, 2011] Forest S. and Trinh D.-K. (2011). *Generalized continua and non-homogeneous boundary conditions in homogenisation methods*. Zeitschrift für angewandte Mathematik und Mechanik, vol. 91, pp 90–109. [166]
- [Fourier, 1822] Fourier J. (1822). *Théorie analytique de la chaleur*. Firmin Didot, Paris. [11]
- [Freeman, 2002] Freeman A. J. (2002). *Materials by design and the exciting role of quantum computation/simulation*. Journal of Computational and Applied Mathematics, vol. 149 n° 1, pp 27–56. [3]
- [Frey, 2001] Frey P. J. (2001). *YAMS: A fully automatic adaptive isotropic surface remeshing procedure*. Technical Report 0252, INRIA, Domaine de Voluceau, Rocquencourt, BP 105, 78153 LE CHESNAY Cedex (France). [116]
- [Galerkin, 1915] Galerkin B. G. (1915). *Series solution of some problems of elastic equilibrium of rods and plates*. Wjstnik Ingenerow Petrograd, pp 897–908. [52]

References

- [Gaspar et al., 2005] Gaspar N., Ren X. J., Smith C. W., Grima J. N., and Evans K. E. (2005). *Novel honeycombs with auxetic behaviour*. *Acta Materialia*, vol. 53, pp 2439–2445. [68, 72]
- [Gélébart et al., 2009] Gélébart L., Chateau C., and Bornert M. (2009). *Conditions aux limites mixtes normales*. In : 19ème Congrès Français de Mécanique, 24-28 August 2009, Marseille. [133]
- [Gitman et al., 2007] Gitman I. M., Askes H., and Sluys L. J. (2007). *Representative volume: Existence and size determination*. *Engineering Fracture Mechanics*, vol. 74, pp 2518–2534. [17]
- [Green, 1972] Green R. J. (1972). *A Plasticity Theory for Porous Solids*. *International Journal of Mechanical Sciences*, vol. 14, pp 215–224. [88]
- [Hashin, 1983] Hashin Z. (1983). *Analysis of Composite Materials - A Survey*. *Journal of Applied Mechanics*, vol. 50, pp 481–505. [17]
- [Hashin and Shtrikman, 1962a] Hashin Z. and Shtrikman S. (1962a). *A Variational Approach to the Theory of the Effective Magnetic Permeability of Multiphase Materials*. *Journal of Applied Physics*, vol. 33, pp 3125–3131. [36]
- [Hashin and Shtrikman, 1962b] Hashin Z. and Shtrikman S. (1962b). *A Variational Approach to the Theory of the Elastic Behaviour of Polycrystals*. *Journal of the Mechanics and Physics of Solids*, vol. 10, pp 343–352. [33]
- [Hashin and Shtrikman, 1963] Hashin Z. and Shtrikman S. (1963). *A Variational Approach to the Theory of the Elastic Behaviour of Multiphase Materials*. *Journal of the Mechanics and Physics of Solids*, vol. 11, pp 127–140. [44]
- [Hatami-Marbini and Picu, 2009] Hatami-Marbini H. and Picu R. C. (2009). *Heterogeneous long-range correlated deformation of semiflexible random fiber networks*. *Physical Review E*, vol. 80 n° 4. [110]
- [Hazanov, 1998] Hazanov S. (1998). *Hill condition and overall properties of composites*. *Archive of Applied Mechanics*, vol. 68, pp 385–394. [133]
- [Hazanov and Amieur, 1995] Hazanov S. and Amieur M. (1995). *On overall properties of elastic heterogeneous bodies smaller than the representative volume*. *International Journal of Engineering Science*, vol. 33 n° 9, pp 1289–1301. [155, 163]
- [Hazanov and Huet, 1994] Hazanov S. and Huet C. (1994). *Order Relationships for Boundary Conditions Effect in Heterogeneous Bodies Smaller than the Representative Volume*. *Journal of the Mechanics and Physics of Solids*, vol. 42 n° 12, pp 1995–2011. [133, 155, 163]
- [Herakovich, 1984] Herakovich C. T. (1984). *Composite Laminates with Negative Through-the-Thickness Poisson's Ratios*. *Journal of Composite Materials*, vol. 18 n° 5, pp 447–455. [68]

- [Hertz, 1881] Hertz H. (1881). *Über die Berührung fester elastischer Körper*. Journal für die reine und angewandte Mathematik, vol. 92, pp 156–171. [68]
- [Hill, 1950] Hill R. (1950). *The Mathematical Theory of Plasticity*. Clarendon Press, Oxford. [90]
- [Hill, 1963] Hill R. (1963). *Elastic Properties of Reinforced Solids: Some Theoretical Principles*. Journal of the Mechanics and Physics of Solids, vol. 11, pp 357–372. [17]
- [Hill, 1965] Hill R. (1965). *A Self-Consistent Mechanics of Composite Materials*. Journal of the Mechanics and Physics of Solids, vol. 13, pp 213–222. [41]
- [Hill, 1967] Hill R. (1967). *The essential structure of constitutive laws for metal composites and polycrystals*. Journal of the Mechanics and Physics of Solids, vol. 15, pp 79–95. [24]
- [Hooke, 1678] Hooke R. (1678). *De Potentia Restitutiva*. John Martyn, London. [12]
- [Huang and Blackburn, 2002] Huang X. and Blackburn S. (2002). *Developing a New Processing Route to Manufacture Honeycomb Ceramics with Negative Poisson's Ratio*. Key Engineering Materials, vol. 206-213, pp 201–204. [102]
- [Huet, 1990] Huet C. (1990). *Application of Variational Concepts to Size Effects in Elastic Heterogeneous Bodies*. Journal of the Mechanics and Physics of Solids, vol. 38 n° 6, pp 813–841. [28]
- [Hughes et al., 2010] Hughes T. P., Marmier A., and Evans K. E. (2010). *Auxetic frameworks inspired by cubic crystals*. International Journal of Solids and Structures, vol. 47, pp 1469–1476. [68]
- [Irwin, 1957] Irwin G. R. (1957). *Analysis of Stresses and Strains Near the End of a Crack Traversing a Plate*. Journal of Applied Mechanics, vol. 24, pp 361–364. [68]
- [Jean, 2009] Jean A. (2009). *Étude d'un élastomère chargé, de sa nanostructure à son macro-comportement*. Thèse de Doctorat, MINES-ParisTech. [53, 61, 162]
- [Jean and Engelmayr, 2010] Jean A. and Engelmayr G. C. (2010). *Finite element analysis of an accordion-like honeycomb scaffold for cardiac tissue engineering*. Journal of Biomechanics, vol. 43, pp 3035–3043. [53]
- [Jean et al., 2011a] Jean A., Jeulin D., Forest S., Cantournet S., and N'Guyen F. (2011a). *A multiscale microstructure model of carbon black distribution in rubber*. Journal of Microscopy, vol. 241 n° 3, pp 243–260. [61, 110]
- [Jean et al., 2011b] Jean A., Willot F., Cantournet S., Forest S., and Jeulin D. (2011b). *Large-scale Computations of Effective Elastic Properties of Rubber with Carbon Black Fillers*. International Journal for Multiscale Computational Engineering, vol. 9 n° 3, pp 271–303. [109, 119]

References

- [Jeulin, 1991a] Jeulin D. (1991a). *Modèles de Fonctions Aléatoires Multivariées*. Sciences de la Terre, vol. 30, pp 225–256. [60, 110, 112, 195, 198]
- [Jeulin, 1991b] Jeulin D. (1991b). *Modèles Morphologiques de Structures Aléatoires et de Changement d'Échelle*. Thèse de Doctorat d'État, Université de Caen. [112, 195, 198]
- [Jeulin, 2001] Jeulin D. (2001). *Caractérisation Morphologique et Modèles de Structures Aléatoires*, vol. 1 of *Homogénéisation en Mécanique des Matériaux*, chapter 4, pp 95–132. Hermès. [57]
- [Jeulin, 2011] Jeulin D. (2011). *Variance scaling of Boolean random varieties*. Technical report, Centre de Morphologie Mathématique. [60, 112, 151, 163, 195, 198]
- [Jeulin, 2012] Jeulin D. (2012). *Morphology and effective properties of multi-scale random sets: a review*. Comptes-Rendus de l'Académie des Sciences - Serie IIb : Mécanique, vol. 340 n° 4-5, pp 219–229. [111]
- [Jeulin and Ostoja-Starzewski, 2001] Jeulin D. and Ostoja-Starzewski M. (2001). *Mechanics of Random and Multiscale Microstructures*. CISM Courses. Springer. [46, 47, 57]
- [Kanit, 2003] Kanit T. (2003). *Notion de Volume Élémentaire Représentatif pour les Matériaux Hétérogènes : Approches Statistique et Numérique*. Thèse de Doctorat, MINES-ParisTech. [53, 61, 162]
- [Kanit et al., 2003] Kanit T., Forest S., Galliet I., Mounoury V., and Jeulin D. (2003). *Determination of the Size of the Representative Volume Element for Random Composites: Statistical and Numerical Approach*. International Journal of Solids and Structures, vol. 40, pp 3647–3679. [18, 19, 28, 53, 56, 59, 60, 61, 109, 110, 119, 162]
- [Kanit et al., 2006] Kanit T., N'Guyen F., Forest S., Jeulin D., Reed M., and Singleton S. (2006). *Apparent and effective physical properties of heterogeneous materials: Representativity of samples of two materials from food industry*. Computer Methods in Applied Mechanics and Engineering, vol. 195, pp 3960–3982. [28, 53, 61, 110]
- [Kolopp et al., 2011] Kolopp A., Rivallant S., and Bouvet C. (2011). *Impact Testing of Composite Sandwich Structures for Aircraft Armor Applications*. In : JNC 17 - 17èmes Journées Nationales sur les Composites, 15-17 June 2011, Poitiers, France. [6]
- [Lakes, 1987] Lakes R. S. (1987). *Foam Structures with a Negative Poisson's Ratio*. Science, vol. 235, pp 1038–1040. [68, 165]
- [Lakes, 1991] Lakes R. S. (1991). *Deformation mechanisms in negative Poisson's ratio materials: structural aspects*. Journal of Materials Science, vol. 26, pp 2287–2292. [68, 70]
- [Lakes, 1993] Lakes R. S. (1993). *Materials with structural hierarchy*. Nature, vol. 361, pp 511–515. [68]

- [Lantuéjoul, 1991] Lantuéjoul C. (1991). *Ergodicity and Integral Range*. Journal of Microscopy, vol. 161, pp 387–403. [57, 60]
- [Lantuéjoul, 2002] Lantuéjoul C. (2002). *Geostatistical Simulation: Models and Algorithms*. Springer. [57]
- [Laszczyk, 2011] Laszczyk L. (2011). *Homogénéisation et optimisation topologique de panneaux architecturés*. Thèse de Doctorat, Université de Grenoble. [166]
- [Lebée, 2010] Lebée A. (2010). *Homogénéisation de plaques périodiques épaisses : application aux panneaux sandwichs à ame pliables en chevrons*. Thèse de Doctorat, Université Paris-Est. [166]
- [Lebensohn, 2001] Lebensohn R. A. (2001). *N-site modeling of a 3D viscoplastic polycrystal using Fast Fourier Transform*. Acta Materialia, vol. 49, pp 2723–2737. [166]
- [Leite et al., 2012a] Leite P., Thomas M., and Bréchet Y. (2012a). *Optimal design of a lightweight sandwich panel for mechanical and thermal properties*. In : MS&T '12, Proceedings of the Materials Science and Technology Conference, Pittsburgh, Pennsylvania, USA, 7-11 October 2012. [6]
- [Leite et al., 2012b] Leite P., Thomas M., Simon F., and Bréchet Y. (2012b). *Optimal design of an asymmetrical sandwich panel for acoustical and mechanical properties*. In : Proceedings of the ESDA2012, 11th Biennial conference on Engineering Systems Design and Analysis, Nantes, France, 1-4 July 2012. [6]
- [Lemaitre and Chaboche, 1994] Lemaitre J. and Chaboche J.-L. (1994). *Mechanics of Solid Materials*. Cambridge University Press. [15]
- [Lewandowski et al., 2012] Lewandowski M., Amiot M., and Perwuelz A. (2012). *Development and Characterization of 3D Nonwoven Composites*. Materials Science Forum, vol. 714, pp 131–137. [6]
- [Lipsett and Beltzer, 1988] Lipsett A. W. and Beltzer A. I. (1988). *Reexamination of Dynamic Problems of Elasticity for Negative Poisson's Ratio*. Journal of the Acoustical Society of America, vol. 84 n° 6, pp 2179–2186. [69]
- [Madi, 2006] Madi K. (2006). *Influence de la morphologie tridimensionnelle des phases sur le comportement mécanique de réfractaires électrofondus*. Thèse de Doctorat, MINES-ParisTech. [53, 61]
- [Madi et al., 2007] Madi K., Forest S., Boussuge M., Gailliègue S., Lataste E., Buffière J.-Y., Bernard D., and Jeulin D. (2007). *Finite element simulations of the deformation of fused-cast refractories based on X-ray computed tomography*. Computational Materials Science, vol. 39, pp 224–229. [61, 110]

References

- [Madi et al., 2005] Madi K., Forest S., Cordier P., and Boussuge M. (2005). *Numerical study of creep in two-phase aggregates with a large rheology contrast: implications for the lower mantle*. Earth and Planetary Science Letters, vol. 237 n° 1-2, pp 223–238. [[53](#), [61](#), [119](#)]
- [Martin et al., 2008] Martin J., Heyder-Bruckner J.-J., Remillat C., Scarpa F., Potter K., and Ruzzene M. (2008). *The hexachiral prismatic wingbox concept*. Physica Status Solidi (b), vol. 245 n° 3, pp 570–577. [[68](#)]
- [Matheron, 1967] Matheron G. (1967). *Éléments pour une Théorie des Milieux Poreux*. Masson. [[197](#)]
- [Matheron, 1971] Matheron G. (1971). *The Theory of Regionalized Variables and its Applications*, vol. Fascicule 5 of *Les Cahiers du Centre de Morphologie Mathématique de Fontainebleau*. Ecole des Mines de Paris. [[56](#), [58](#)]
- [Matheron, 1975] Matheron G. (1975). *Random Sets and Integral Geometry*. J. Wiley. [[57](#), [190](#), [193](#), [195](#)]
- [Matheron, 1989] Matheron G. (1989). *Estimating and Choosing*. Springer-Verlag, Berlin. [[59](#)]
- [Maxwell, 1873] Maxwell J. C. (1873). *Treatise on Electricity and Magnetism*. Clarendon Press. [[33](#)]
- [Maxwell Garnett, 1904] Maxwell Garnett J. C. (1904). *Colours in metal glasses and in metallic films*. Philosophical Transactions of the Royal Society A, vol. 203, pp 385–420. [[34](#)]
- [McCoy, 1970] McCoy J. J. (1970). *On the displacement field in an elastic medium with random variations of material properties*. In : Recent Advances in Engineering Sciences, vol. 5, pp 235–254. Gordon and Breach. [[46](#)]
- [Mezeix et al., 2009] Mezeix L., Bouvet C., Huez J., and Poquillon D. (2009). *Mechanical behavior of entangled fibers and entangled cross-linked fibers during compression*. Journal of Materials Science, vol. 44 n° 14, pp 3652–3661. [[111](#)]
- [Michel et al., 1999] Michel J.-C., Moulinec H., and Suquet P. (1999). *Effective properties of composite materials with periodic microstructure: a computational approach*. Computer Methods in Applied Mechanics and Engineering, vol. 172, pp 109–143. [[24](#)]
- [Michel et al., 2001] Michel J.-C., Moulinec H., and Suquet P. (2001). *A computational scheme for linear and non-linear composites with arbitrary phase contrast*. International Journal for Numerical Methods in Engineering, vol. 52 n° 1-2, pp 139–158. [[166](#)]
- [Miller, 2000] Miller R. E. (2000). *A continuum plasticity model for the constitutive and indentation behaviour of foamed metals*. International Journal of Mechanical Sciences, vol. 42, pp 729–754. [[88](#)]
- [Milton, 1992] Milton G. W. (1992). *Composite Materials with Poisson's Ratios Close to -1*. Journal of the Mechanics and Physics of Solids, vol. 40 n° 5, pp 1105–1137. [[68](#), [165](#)]

- [Milton, 2002] Milton G. W. (2002). *The Theory of Composites*. Cambridge Monographs on Applied and Computational Mathematics. Cambridge University Press, 1st edition. [33, 47]
- [Milton and Phan-Thien, 1982] Milton G. W. and Phan-Thien N. (1982). *New Bounds on Effective Elastic Moduli of Two-Component Materials*. Proceedings of the Royal Society of London. Series A, Mathematical and Physical Sciences, vol. 380 n° 1779, pp 305–331. [37, 47]
- [Mitschke et al., 2011] Mitschke H., Schwerdtfeger J., Schury F., Stingl M., Körner C., Singer R. F., Robins V., Mecke K., and Schröder-Turk G. E. (2011). *Finding Auxetic Frameworks in Periodic Tessellations*. Advanced Materials, vol. 23, pp 2669–2674. [76, 102]
- [Mori and Tanaka, 1973] Mori T. and Tanaka K. (1973). *Average Stress in Matrix and Average Elastic Energy of Materials with Misfitting Inclusions*. Acta Metallurgica, vol. 21 n° 5, pp 571–574. [46]
- [Moulinec and Suquet, 1994] Moulinec H. and Suquet P. (1994). *A fast numerical method for computing the linear and nonlinear mechanical properties of composites*. Comptes-Rendus de l'Académie des Sciences, vol. 318 n° Série II, pp 1417–1423. [119, 166]
- [Moulinec and Suquet, 1998] Moulinec H. and Suquet P. (1998). *A numerical method for computing the overall response of nonlinear composites with complex microstructure*. Computer Methods in Applied Mechanics and Engineering, vol. 157, pp 69–94. [166]
- [Mura, 1987] Mura T. (1987). *Micromechanics of defects in solids*. Springer, 2nd edition. [47]
- [Olson, 2001] Olson G. B. (2001). *Beyond discovery: design for a new material world*. Calphad, vol. 25 n° 2, pp 175–190. [3]
- [Ostoja-Starzewski, 2002] Ostoja-Starzewski M. (2002). *Microstructural Randomness Versus Representative Volume Element in Thermomechanics*. Journal of Applied Mechanics, vol. 69 n° 1, pp 25–35. [17]
- [Oumarou et al., 2011] Oumarou M., Jeulin D., and Renard J. (2011). *Etude statistique multi-échelle du comportement élastique et thermique d'un composite thermoplastique*. Revue des composites et des matériaux avancés, vol. 21, pp 221–254. [61]
- [Oumarou et al., 2012] Oumarou M., Jeulin D., Renard J., and Castaing P. (2012). *Multi-Scale Statistical Approach of the Elastic and Thermal Behavior of a Thermoplastic Polyamid-Glass Fiber Composite*. Technische Mechanik, vol. 32 n° 2-5, pp 484–506. [110]
- [Pascal et al., 2010] Pascal S., di Paola F., and Berdin C. (2010). *Analyse de VER : une idée pour s'affranchir des effets de bords*. In : Journées thématiques MECAMAT organisées par les Groupes de Travail 'Approches probabilistes en mécanique des milieux hétérogènes - Rhéologie des matériaux hétérogènes - Traitements thermomécaniques', 3-4 May 2010, Université Paris-Est, Marne-la-Vallée, pp 23–24. [59]

References

- [Pelissou et al., 2009] Pelissou C., Baccou J., Monerie Y., and Perales F. (2009). *Determination of the size of the representative volume element for random quasi-brittle composites*. International Journal of Solids and Structures, vol. 46, pp 2842–2855. [109]
- [Peyrega et al., 2009] Peyrega C., Jeulin D., Delisée C., and Malvestio J. (2009). *3D Morphological Modelling of a Random Fibrous Network*. Image Analysis & Stereology, vol. 28, pp 129–141. [109, 110]
- [Picu, 2011] Picu R. C. (2011). *Mechanics of random fiber networks—a review*. Soft Matter, vol. 7, pp 6768–6785. [110]
- [Picu and Hatami-Marbini, 2010] Picu R. C. and Hatami-Marbini H. (2010). *Long-range correlations of elastic fields in semi-flexible fiber networks*. Computational Mechanics, vol. 46, pp 635–640. [110]
- [Poisson, 1837] Poisson S.-D. (1837). *Recherches sur la probabilité des jugements en matière criminelle et en matière civile*. Bachelier, Paris. [111]
- [Prager, 1949] Prager W. (1949). *Recent Developments in the Mathematical Theory of Plasticity*. Journal of Applied Physics, vol. 20 n° 3, pp 235–241. [15]
- [Prall and Lakes, 1997] Prall D. and Lakes R. S. (1997). *Properties of a Chiral Honeycomb with a Poisson's Ratio of -1*. International Journal of Mechanical Sciences, vol. 39 n° 3, pp 305–314. [68, 70, 72]
- [Reuss, 1929] Reuss A. (1929). *Berechnung der Fließgrenze von Mischkristallen auf Grund der Plastizitätsbedingung für Einkristalle*. Zeitschrift für angewandte Mathematik und Mechanik, vol. 9 n° 1, pp 49–58. [43]
- [Rothenburg et al., 1991] Rothenburg L., Berlin A. A., and Bathurst R. J. (1991). *Microstructure of isotropic materials with negative Poisson's ratio*. Nature, vol. 354, pp 470–472. [68]
- [Sab, 1992] Sab K. (1992). *On the homogenization and the simulation of random materials*. European Journal of Mechanics, A/Solids, vol. 11 n° 5, pp 585–607. [17, 18, 28, 155, 163]
- [Sab and Nedjar, 2005] Sab K. and Nedjar B. (2005). *Periodization of random media and representative volume element size for linear composites*. Comptes-Rendus de l'Académie des Sciences - Serie IIb : Mécanique, vol. 333, pp 187–195. [110]
- [Salmi et al., 2012a] Salmi M., Auslender F., Bornert M., and Fogli M. (2012a). *Apparent and effective mechanical properties of linear matrix-inclusion random composites: Improved bounds for the effective behavior*. International Journal of Solids and Structures, vol. 49, pp 1195–1211. [28]
- [Salmi et al., 2012b] Salmi M., Auslender F., Bornert M., and Fogli M. (2012b). *Various estimates of Representative Volume Element sizes based on a statistical analysis of the apparent behavior of random linear composites*. Comptes-Rendus de l'Académie des Sciences - Serie IIb : Mécanique, vol. 340, pp 230–246. [28]

- [Sanchez-Palencia, 1974] Sanchez-Palencia E. (1974). *Comportements local et macroscopique d'un type de milieux physiques hétérogènes*. International Journal of Engineering Science, vol. 12 n° 4, pp 331–351. [33]
- [Sanchez-Palencia and Zaoui, 1987] Sanchez-Palencia E. and Zaoui A. (1987). *Homogenization techniques for composite media*, vol. 272 of *Lecture Notes in Physics*. Springer-Verlag. [28, 47]
- [Scarpa et al., 2002] Scarpa F., Yates J. R., Ciffo L. G., and Patsias S. (2002). *Dynamic crushing of auxetic open-cell polyurethane foam*. Proceedings of the Institution of Mechanical Engineers Part C-Journal of Mechanical Engineering Science, vol. 216 n° 12, pp 1153–1156. [69]
- [Schaedler et al., 2011] Schaedler T. A., Jacobsen A. J., Torrents A., Sorensen A. E., Lian J., Greer J. R., Valdevit L., and Carter W. B. (2011). *Ultralight Metallic Microlattices*. Science, vol. 334 n° 6058, pp 962–965. [4]
- [Schladitz et al., 2006] Schladitz K., Peters S., Reinel-Bitzer D., Wiegmann A., and Ohser J. (2006). *Design of acoustic trim based on geometric modeling and flow simulation for non-woven*. Computational Materials Science, vol. 38, pp 56–66. [109, 110]
- [Schroeder et al., 2006] Schroeder W., Martin K., and Lorensen B. (2006). *The Visualization Toolkit An Object-Oriented Approach To 3D Graphics*. Kitware, Inc. publishers, 4th edition edition. [113]
- [Schwerdtfeger et al., 2010] Schwerdtfeger J., Heintl P., Singer R. F., and Körner C. (2010). *Auxetic cellular structures through selective electron-beam melting*. Physica Status Solidi (b), vol. 247 n° 2, pp 269–272. [102]
- [Serra, 1982] Serra J. (1982). *Image Analysis and Mathematical Morphology*. Academic Press. [111, 190]
- [SIMULOG, 2003] SIMULOG (2003). *TetMesh-GHS3D User's Manual*, 4th edition edition. [116]
- [Soare and Picu, 2007] Soare M. A. and Picu R. C. (2007). *An approach to solving mechanics problems for materials with multiscale self-similar microstructure*. International Journal of Solids and Structures, vol. 44, pp 7877–7890. [110]
- [Spadoni, 2008] Spadoni A. (2008). *Application of Chiral Cellular Materials for the Design of Innovative Components*. Thèse de Doctorat, Georgia Institute of Technology. [68, 70]
- [Spadoni et al., 2009] Spadoni A., Ruzzene M., Gonella S., and Scarpa F. (2009). *Phononic properties of hexagonal chiral lattices*. Wave Motion, vol. 46 n° 7, pp 435–450. [69]
- [Timoshenko and Goodier, 1951] Timoshenko S. and Goodier J. N. (1951). *Theory of elasticity*. Engineering Societies Monographs. McGraw-Hill, 2nd edition. [68, 69]
- [Torquato, 2001] Torquato S. (2001). *Random Heterogeneous Materials*. Springer. [33, 47]

References

- [Trinh, 2011] Trinh D.-K. (2011). *Méthodes d'homogénéisation d'ordre supérieur pour les matériaux architecturés*. Thèse de Doctorat, MINES-ParisTech. [166]
- [Turcaud et al., 2011] Turcaud S., Guiducci L., Fratzl P., Dunlop J. W. C., and Bréchet Y. (2011). *An excursion into the design space of biomimetic architected biphasic actuators*. International Journal of Materials Research, vol. 102 n° 6, pp 607–612. [166]
- [Voigt, 1887] Voigt W. (1887). *Theoretische Studien über die Elastitätsverhältnisse der Krystalle*. Abhandlungen der Königlichen Gesellschaft der Wissenschaften zu Göttingen, vol. 34, pp 3–51. [13]
- [Voigt, 1889] Voigt W. (1889). *Ueber die Beziehung zwischen den beiden Elasticitätsconstanten isotroper Körper*. Annalen der Physik und Chemie, vol. 38, pp 573–587. [43]
- [von Mises, 1913] von Mises R. (1913). *Mechanik der festen Körper im plastisch deformablen Zustand*. Nachrichten von der Gesellschaft der Wissenschaften zu Göttingen, vol. Mathematisch-Physikalische Klasse n° 4, pp 582–592. [15]
- [von Mises, 1928] von Mises R. (1928). *Mechanik der plastischen Formänderung von Kristallen*. Zeitschrift für angewandte Mathematik und Mechanik, vol. 8 n° 3, pp 161–185. [90]
- [Voronoi, 1908] Voronoi G. (1908). *Nouvelles applications des paramètres continus à la théorie des formes quadratiques*. Journal für die reine und angewandte Mathematik, vol. 133, pp 97–178. [116]
- [Wiener, 1912] Wiener O. (1912). *Die Theorie des Mischkörpers für das Feld der stationären Strömung. I. Abhandlung: Die Mittelwertsätze für Kraft, Polarisation und Energie*. Abhandlungen der Königlich Sächsischen Gesellschaft der Wissenschaften, vol. 32 n° 6. [35]
- [Willot and Jeulin, 2009] Willot F. and Jeulin D. (2009). *Elastic behavior of composites containing Boolean random sets of inhomogeneities*. International Journal of Engineering Science, vol. 47, pp 313–324. [166]
- [Willot et al., 2008] Willot F., Pellegrini Y.-P., and Ponte Castañeda P. (2008). *Localization of elastic deformation in strongly anisotropic, porous, linear materials with periodic microstructures: Exact solutions and dilute expansions*. Journal of the Mechanics and Physics of Solids, vol. 56, pp 1245–1268. [166]
- [Yang et al., 2004] Yang W. et al. (2004). *Review on auxetic materials*. Journal of Materials Science, vol. 39, pp 3269–3279. [68]

Index

- Analytical estimates, 33, 38
- Anisotropy, 81, 83, 88, 89, 92, 94, 102
- Anti-tetrachiral, 71, 72, 75, 76, 81, 95, 96, 102, 103
- Apparent properties, 25
- Architected materials, 104
- Associated plasticity, 89
- Auxetics, 7, 67, 75, 81, 83, 92–94, 102–104
- Averaging relations, 19

- Boolean model, 113, 197
- Boolean random varieties, 198
- Boundary conditions, 21, 80, 94
 - KUBC, 23, 130
 - MBC, 133
 - MTBC, 125
 - PBC, 23, 81
 - PTBC, 22
 - SUBC, 23, 81, 132
 - UHF, 22, 124
 - UTG, 21, 123
- Bounds, 33, 35, 43
 - Hashin–Shtrikman*, 34, 36, 44, 141
 - Reuss*, 28, 43
 - Voigt*, 28, 43
 - Wiener*, 35, 141
- Bruggeman*'s self-consistent model, 34, 141
- Bulk modulus, 30, 140

- Cellular materials, 88, 178
- Chirality, 70, 72, 76
- Choquet* capacity, 113, 193, 199
- Compressible plasticity, 88
- Computational homogenization, 51

- Constitutive behavior, 12
- Correlation function, 193
- Covariance, 145, 192, 198
- Crofton* relationships, 190
- Cumulative plastic strain, 83

- Deviatoric stress, 89, 90
- Divergence theorem, 19, 20

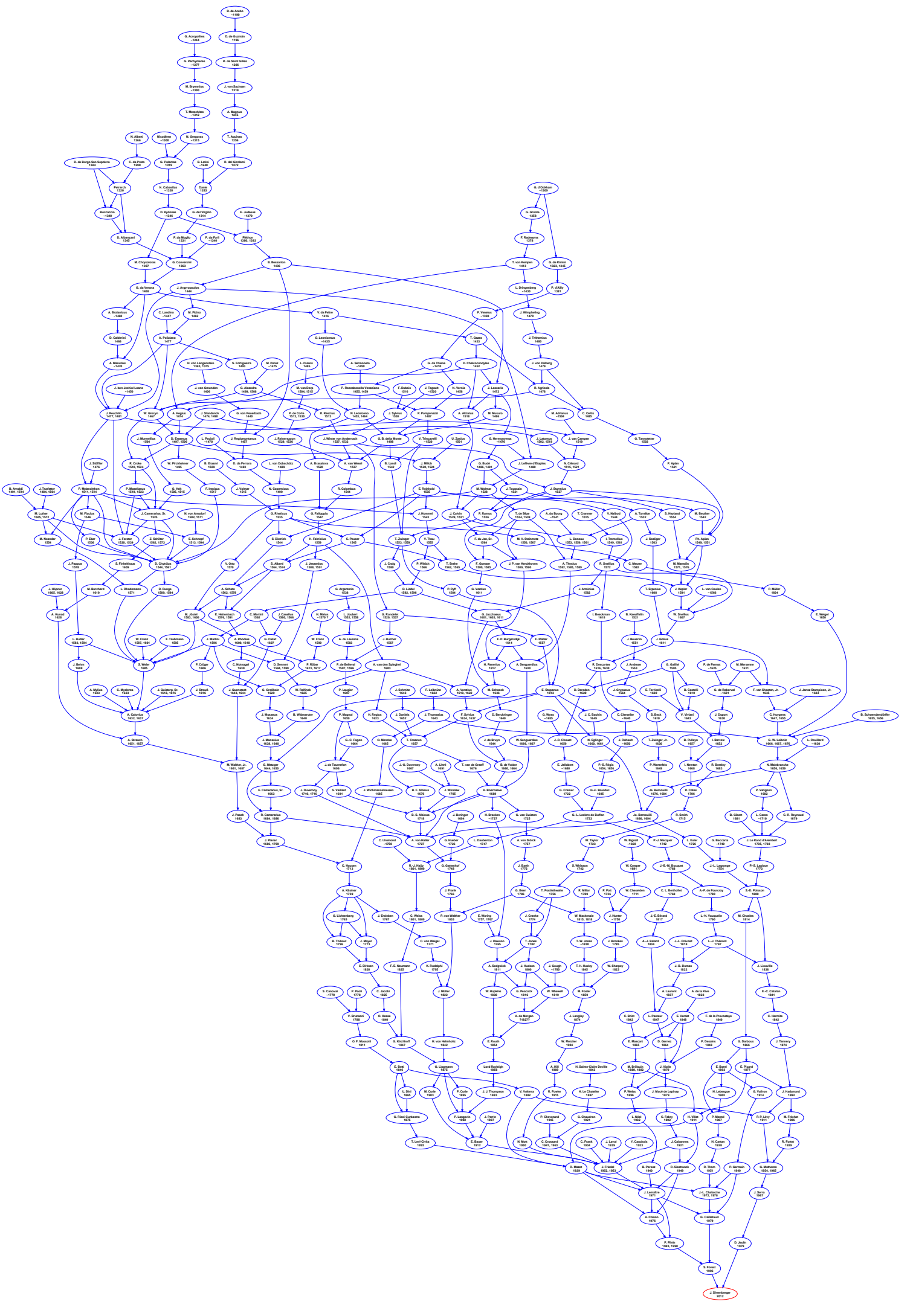
- Effective properties, 11, 25
- Einstein*'s estimate, 38
- Elastic energy density, 96
- Elastic moduli, 75, 78, 81, 82, 94, 102
- Elastic strain energy density, 27
- Elasticity
 - Cubic, 92
 - Isotropic, 83, 89
 - Quadratic, 71, 76, 103
 - Transversely isotropic, 70, 72, 78, 80, 104
- Elastoplasticity, 67, 82, 87, 104
- Engineering, 94
- Engineering strain, 13
- Ergodicity, 56, 57, 192, 193
- Eshelby*'s model, 38
- Euler* angles, 74
- Euler* angles, 74
- Euler* gamma function, 196
- Experimental characterization, 102

- Finite elements, 51, 67, 69, 73, 80, 94, 102
 - Mesh, 94, 96
- Foams, *see* Cellular materials
- Fourier*'s law, 11

Index

- Geometry, 70, 92
- Hardening modulus, 67, 83, 91
- Hardening rule, 83, 90
- Heat flux density field, 19
- Hexachiral, 71, 75, 77, 78, 81, 82, 86, 87, 92, 95, 96, 102, 104
- Hexatruss, 92, 96, 103
- Hill equivalent stress, 90
- Hill tensor, 90
- Hill–Mandel condition, 24
- Homogenization, 11, 17, 51, 67, 102
- Honeycomb, 67, 72, 73, 80, 81, 86, 87, 95, 96, 102–104
- Hooke’s law, 12
- Hydrostatic stress, 89, 90
- Identification, 90
- Indentation, 67, 92, 94, 95, 102, 103
 - Cylindrical, 96
 - Spherical, 94–96
- Integral range, 57, 60, 61, 193
- Isotropic hardening, 16
- Isotropy, 112, 195, 198
- J_2 plasticity, 15, 82
- Kinematic hardening, 16
- Linear elasticity, 26
- Macroscopic modeling, 67, 87
- Maxwell Garnett’s estimate, 33
- Microstructure, 94, 102
- Minkowski functionals, 190, 191
- Models of random structures, 193
- Morphological criterion, 192
- Morphology, 190
- Negative Poisson’s ratio, *see* Auxetics
- Objectivity principle, 12
- Optimization, 90
- Plane-strain condition, 96
- Plane-stress condition, 96
- Plastic Poisson’s ratio, 89
- Plastic strain rate, 89
- Plastic yield function, 82, 88
- Plastic yield stress, 83, 88
- Poisson fibers, 7, 60, 113
- Poisson fibres, 199
- Poisson linear varieties, 60, 112, 195
- Poisson point process, 7, 111, 194
- Poisson’s ratio, 74–76, 78, 80, 81, 86, 87, 90, 91, 140
- Porosity, 89
- Porous materials, 88
- Principle of local action, 12
- Principle of virtual work, 52
- Properties
 - Elastic, 93
 - In-plane, 75
 - Out-of-plane, 75
- Random sets, 190
- Random variables, 190
- Representative volume element, 17, 56, 61, 90
- Rotachiral, 72, 73, 78, 81, 82, 96, 102
- Sandwich materials, 103
- Scaling law, 60
- Selective laser melting, 103
- Self-consistent scheme, 41
- Shear, 90, 102
- Shear modulus, 31, 74–76, 78, 81, 140
- Simple material principle, 12
- Simulation, 90, 91, 94
- Small deformations hypothesis, 12
- Stationarity, 57, 112, 192, 194, 195, 197
- Statistical homogeneity, 57
- Steiner formulae, 191
- Stereology, 190, 197
- Strain field, 20
- Stress field, 20
- Structural application, 94
- Structuring element, 190

- Symmetry, 70–72, 85, 94, 95
- Temperature field, 19
- Thermal behavior, 11, 21
- Thermal conductivity, 21, 25, 29, 140, 141
- Thermal dissipation rate density, 19, 26
- Thermal field, 19
- Voigt* notation, 14
- Volume fraction, 70, 72, 75, 93, 96, 102, 103, 140
- von Mises* criterion, 15
- von Mises* equivalent stress, 82
- Young's* modulus, 74–76, 81, 103, 140



Propriétés effectives de matériaux architecturés

Résumé: Les matériaux architecturés font émerger de nouvelles possibilités en termes de propriétés structurales et fonctionnelles, repoussant ainsi les limites des cartes d'*Ashby*. Le terme "matériaux architecturés" inclut toute microstructure conçue de façon astucieuse, de sorte que certaines de ses propriétés soient optimisées. Les exemples sont nombreux : composites fibreux et particulaires, matériaux cellulaires, structures sandwiches, matériaux tissés, structures treillis, etc. Un enjeu de taille pour l'emploi de tels matériaux est la prédiction de leurs propriétés effectives. Dans ce travail, deux types de microstructures sont considérés: des structures auxétiques périodiques et des milieux fibreux aléatoires. Les auxétiques sont des matériaux apparus au milieu des années 1980, présentant un coefficient de *Poisson* négatif. On attend des auxétiques qu'ils présentent des propriétés mécaniques améliorées, comme le module de cisaillement ou la résistance à l'indentation. Les milieux fibreux aléatoires considérés dans ce travail sont constitués de fibres 3D infinies interpénétrantes aléatoirement distribuées et orientées. Ce type de structure aléatoire est très défavorable à la détermination d'une taille de volume élémentaire statistiquement représentatif. Pour les deux types de matériaux, l'homogénéisation numérique à l'aide de la méthode des éléments finis est implémentée dans le but d'estimer les propriétés thermiques et mécaniques effectives.

Mots-clés: Homogénéisation numérique, Volume élémentaire représentatif, Auxétiques, Milieux fibreux stochastiques, Propriétés effectives

Effective properties of architected materials

Abstract: Architected materials bring new possibilities in terms of structural and functional properties, filling gaps and pushing the boundaries of *Ashby's* materials maps. The term "architected materials" encompasses any microstructure designed in a thoughtful fashion, so that some of its materials properties have been improved. There are many examples: particulate and fibrous composites, foams, sandwich structures, woven materials, lattice structures, etc. One engineering challenge is to predict the effective properties of such materials. In this work, two types of microstructures are considered: periodic auxetic lattices and stochastic fibrous networks. Auxetics are materials with negative *Poisson's* ratio that have been engineered since the mid-1980s. Such materials have been expected to present enhanced mechanical properties such as shear modulus or indentation resistance. The stochastic fibrous networks considered in this work is made of 3D infinite interpenetrating fibers that are randomly distributed and oriented. This case of random structure is challenging regarding the determination of a volume element size that is statistically representative. For both materials, computational homogenization using finite element analysis is implemented in order to estimate the effective thermal and mechanical properties.

Keywords: Computational homogenization, Representative Volume Element, Auxetics, Random fibrous networks, Effective properties

